UNIVERSITÀ DEGLI STUDI DI CATANIA

IN CONVENZIONE CON

UNIVERSITÀ DEGLI STUDI DI PALERMO

DOTTORATO DI RICERCA IN

SCIENZA DEI MATERIALI E NANOTECNOLOGIE - XXIX CICLO

PIETRO CAMARDA

GROWTH AND PHOTOLUMINESCENCE DYNAMICS OF ZnO NANOPARTICLES PRODUCED BY PULSED LASER ABLATION IN LIQUID

TUTOR: PROF. M. CANNAS

CO-TUTOR: DR. F. MESSINA

COORDINATORE: PROF.SSA M. G. GRIMALDI

TESI PER IL CONSEGUIMENTO DEL TITOLO DI DOTTORE DI RICERCA

Contents

Introduction

Zinc oxide (ZnO) is a wide band-gap semiconductor material (E_g=3.37 eV) characterized by many promising properties which make it appealing for several technological applications such as blue/UV optoelectronics, transparent electronic devices, photovoltaics, piezoelectric system and sensors. One of the most attractive features of ZnO is its high exciton binding energy (60 meV) which allows the observation of the UV excitonic emission at room temperature and favors the excitation of defect-related emission bands in the visible spectral region. For these reasons ZnO has the potential to replace GaN as the next-generation white or blue light emitting diode materials. On the other hand, the presence of donor defects reduces the effective use of ZnO in LED system because they neutralize most of the introduced shallow acceptors, thus making difficult to obtain p-type ZnO. In recent years, there has been an increasing interest in ZnO nanostructures due to their variety of morphologies and availability of simple and low cost processing methods. Among the many techniques currently available, pulsed laser ablation in liquid (PLAL) offers a simple and versatile route to synthesize nanoparticles (NPs) of extremely high purity. This green method allows to obtain different morphologies and structures by acting on several experimental parameters such as laser photon energy, laser wavelength, pulse duration, solvent and solute.

The advent of nano-technologies has enriched the potentiality of ZnO NPs and nanostructures creating new application fields which exploit the enhancement of surface to volume ratio that favors the formation of luminescent defects and thus the luminescence intensity as well as increase the material reactivity with the surrounding environment. These circumstances, together with the intrinsic features such as low toxicity, chemical stability and good resistance to several external treatments, make ZnO NPs interesting for gas sensor devices and biological applications, including bioimaging and drug delivery systems for diagnostics and therapy. Interestingly, nanostructured ZnO can also offer a platform to study the fundamental aspects related to quantum confinement. Indeed, ZnO NPs having size comparable with that of exciton Bohr radius, have shown excellent quantum confinement effects in their optical and electrical properties.

Although several explanations have been proposed on the origin of emission properties of ZnO NPs, there are still unanswered questions concerning the specific structure of defects responsible of the visible emission. One of the most debated is a broad PL peaked at 2.2-2.4 eV, commonly called green band, which is often attributed to oxygen vacancies in the ZnO crys-

talline matrix. An obstacle to clarify its origin is due to the huge variety of intrinsic defects which generation strongly depends on the used synthesis method and from the lack of a detailed investigation combining together several complementary experimental techniques. In addition, the current knowledge is based on *ex situ* experiments, namely investigations that look at ZnO NPs and related defects mainly after the end of their formation. In contrast, we propose that kinetic investigations often provide additional information which can help us to deep understand physical processes involved giving rise to the stationary properties. Specialized research community debates on the origin of green emission both as an intriguing challenge from a basic point of view and as a keystone for the use of ZnO NPs in optical applications.

This Thesis reports an experimental research work on the structural and optical properties of ZnO NPs produced by PLAL of zinc in liquid and also deals with the formation processes involved during the synthesis. Our experimental approach is based on the combined use of several spectroscopic and microscopic techniques, as mandatory to perform a comprehensive study. In particular, some of the most valuable information come from the use of *in situ* optical spectroscopy which allow us to investigate the oxidation kinetics of Zn NPs and the generation mechanism of the oxygen vacancies during and after PLAL. On the other side, the use of external treatments in controlled environment is crucial to clarify the photophysics of defects leading the bright visible PL of ZnO NPs.

The Thesis is organized in 6 chapters.

- In Chapter 1 we present the structural and optical properties of ZnO, both in bulk and in nanometric form, focusing on the excitonic and point defects emission. We briefly discuss the effect of quantum confinement, in strong and weak regime, on the optical properties of ZnO NPs. Finally, we describe the potential applications for ZnO nanostructures in advanced technologies.

- In Chapter 2 we overview the various techniques that are used in the growth of ZnO nanostructures. However, we focus our attention on pulsed laser ablation in liquid, that is the production method used in this thesis work.

- In Chapter 3 we describe the materials and the experimental setups used for the present investigation. In particular, we describe the experimental setups used to perform laser ablation with Nd:YAG and Ti:Sapphire lasers, and the techniques used to study the ablation product: time resolved photoluminescence, optical absorption, transmission electron microscopy, atomic force microscopy, μRaman, thermal treatments in controlled atmospheres.

- In Chapter 4 we report the experimental results obtained by *ex situ* measurements on ZnO NPs produced by Nd:YAG pulsed laser ablation of a zinc plate in water. We show the optical, morphological and structural properties of NPs. Then, based on the effect of thermal annealing, we demonstrate that the green emission cames from oxygen vacancies

and propose a recombination mechanism leading to the photoluminescence emissions of ZnO NPs.

- In Chapter 5 we show results achieved by *in situ* measurements during Nd:YAG pulsed laser ablation of a zinc plate in liquid. This results allowed us to suggest an oxidation model that explains the growth of defective ZnO NPs due to aqueous oxidation of Zn NPs slowed down and hindered by water diffusion through the ZnO shell.

- In Chapter 6 we report the *ex situ* morphological and optical properties of ZnO NPs synthesized by Ti:Sapphire pulsed laser ablation. Our results show that by Ti:Sapphire laser we obtain smaller ZnO NPs affected by quantum confinement and we observe the presence of a further visible emission in the blue region of which we propose a tentative photoluminescence model.

- Finally, we draw the main conclusions and briefly sketch some proposals for further work. We report a list of papers, related to the results presented in this work, which have been published on scientific Journals.

Chapter 1

ZnO Materials and Nanostructures

In this work, the structural and optical properties of ZnO nanoparticles (NPs) produced by pulsed laser ablation in liquid were studied. To this aim in the first chapter, after a brief description of the structural and emission properties of Zinc oxide (ZnO) bulk materials, we discuss the effect of quantum confinement on the energy band gap and excitonic luminescence of ZnO NPs. We provide an overview of the main works on the defects related visible photoluminescence (PL) in ZnO nanostructures, focusing on the, so-called, green PL at 2.2-2.4 eV, the origin of which is currently debated. Finally, we provide a list of the promising technological applications for ZnO NPs and nanostructures.

1.1   Bulk ZnO

Zinc oxide (ZnO) is an oxidic compound naturally occurring as the rare mineral zincite, which crystallizes in the hexagonal wurtzite structure P63mc [1, 2]. The mineral zincite was discovered in 1810 and it is usually red- or orange-coloured by manganese impurities as shown in Fig. 1.1 (a). The pure ZnO powder is produced from metallic zinc, which is an abundant material in the earth's crust. Growth of zinc oxide bulk can be carried out by a variety of methods, including gas or vapor transport, hydrothermal and pressurized melt growth [3, 4]. These techniques involve different growth mechanisms, resulting in bulk crystals grown at different rates, with different impurity background concentrations and, consequently, different electrical and optical properties [5]. A synthetic zinc oxide crystal is shown in Fig. 1.1 (b). ZnO is a II-VI semiconductor material which has a direct band gap of 3.37 eV at 300 K in wurtzite structure that can be modified by dilute alloying with BeO, MgO, and CdO [7–9]. Up to now, most of the zinc oxide powder produced in the world is used for rubber production, paints, for ceramics. However, because ZnO is characterized by a wide range of useful properties, specially in the form of nanoparticles and nanostructures, it is a very promising material for a variety of technological applications such as piezoelectric systems, drug delivery, photovoltaic, transparent conductive contacts [2, 10, 11]. These properties include large piezoelectric constant, high electron mobilities, high thermal conductivity, as well as bio-compatibility and radiation hardness.
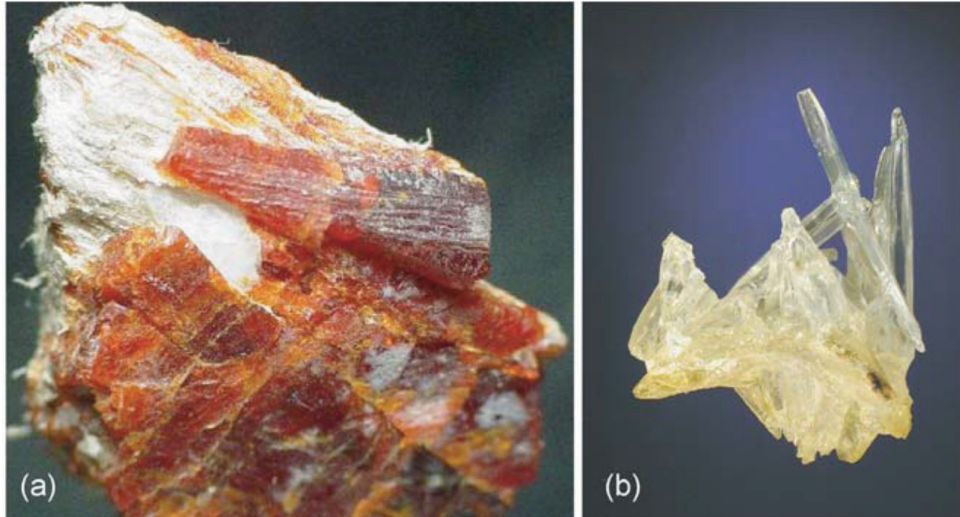
Figure 1.1: (a) An orange zincite crystal from Sterling Mine, Ogdensburg, USA and (b) a synthetic zinc oxide crystal [6].

Moreover, as shown in Fig. 1.2, the most tightly bound exciton in ZnO (60 meV) compared with other compound semiconductors (20 meV for GaN) opens the possibility for ZnO-based optoelectronic devices to operate well above 300 K. In fact, ZnO has the potential to replace GaN as the next-generation white or blue light emitting diode material [5, 12].
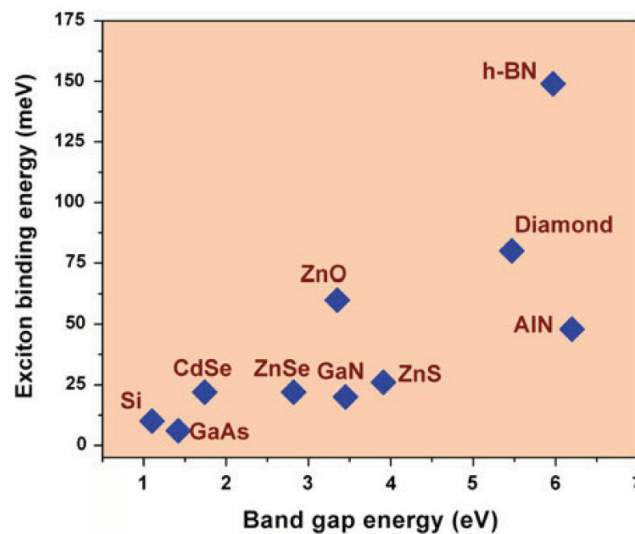
Figure 1.2: The exciton binding energy as a function of the band gap energy for compound semiconductors [13].

1.1.1 Structural Properties

Already in 1914, shortly after the discovery of X-ray diffraction, Bragg elucidated the crystal structure of wurtzite ZnO, which was published in 1920 [14]. The wurtzite structure belongs to the space group C_{6v}^4 and consists of four atoms per unit cell (2ZnO), the measured lattice param-

eters of the hexagonal wurtzite ZnO are a=0.3249 nm and c=0.5206 nm. Each atom of one kind is surrounded by four atoms of the other kind forming sp^3 hybrid bond in a nearly tetrahedral configuration, in which the Zn-O distance along the c-axis is smaller ($d_{Zn-O}[1]$=0.190 nm) than for the other three neighboring oxygen atoms ($d_{Zn-O}[2]$=0.198 nm). The hexagonal structure of ZnO is shown in Fig. 1.3 (a). The ratio of the wurtzite lattice constants c/a≈1.60 is close to the
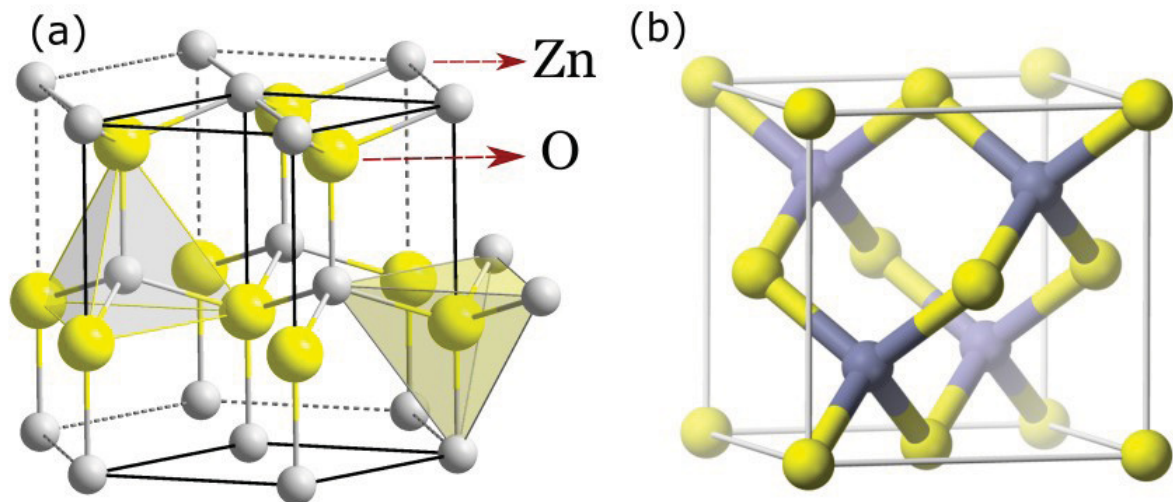
Figure 1.3: (a) Wurtzite structure of ZnO showing the tetrahedral coordination of the Zn and O atoms. (b) Zincblende structure [15].
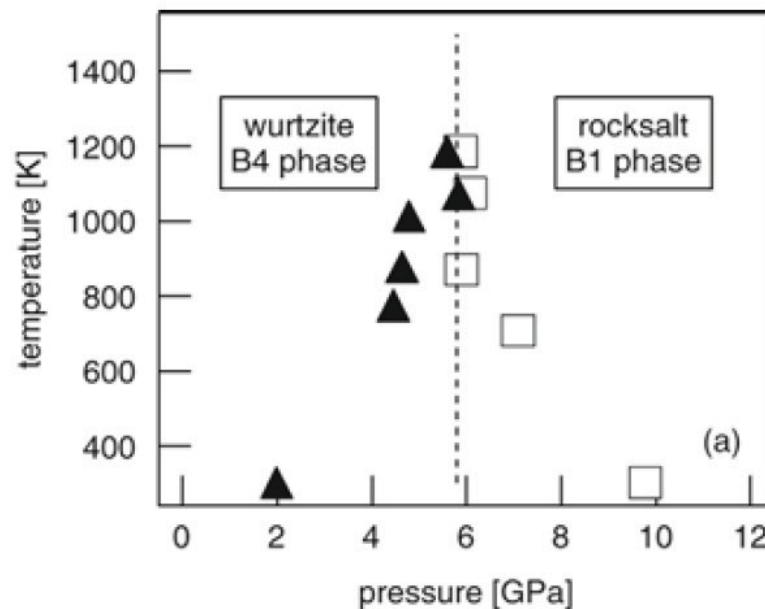
Figure 1.4: Phase diagram of ZnO. The squares mark the wurtzite (B4) - rocksalt (B1), the triangles the B1-B4 transition [20]. The hysteresis of the transition, which extends from 9.8 to 2 GPa at 300 K, depends on the temperature and is absent for T>1300 K [6].

ideal value for hexagonal cell c/a=1.633 and as in most group II-VI materials, the bonding in ZnO is largely ionic (Zn^{2+}-O^{2-}) with the corresponding radii of 0.074 nm for Zn^{2+} and 0.140 nm for O^{2-}. The tetrahedral coordination forms bi-layers consisting of alternate zinc and oxygen layers which, due to large bond ionicity, give rise to polar symmetry along the c-axis producing the strong piezoelectricity of ZnO. Moreover, the largely ionic Zn-O bonding also accounts for the preferential formation of wurtzite rather than other structures [16].

Notwithstanding wurtzite structure is thermodynamically the most stable phase under ambient conditions, ZnO can crystallize into other different structures, zinc blende, and rocksalt depending of different growth conditions. Zincblende structure (see Fig. 1.3 (b)) can be stabilized by growing on cubic substrates like MgO and $Pt/SiO_2/Si$ [8]. It can view as an arrangement of two interpenetrating face-centered cubic sub-lattices. The bonding orbital are directed along the four body diagonal axes. The primitive cell of zinc-blende crystal is an oblique parallelepiped (a=0.447 nm) and contains only one pair of ions Zn^{2+} and O^{2-}. Rocksalt (NaCl) structure can be realized only by applying very high pressures [17]. In fact, it was observed by Decremps et al. [18] using synchrotron radiation energy dispersive X-ray diffraction which measured the shrinking of the lattice cell of hexagonal ZnO up to hydrostatic pressures of 11 GPa. At a pressure of 9.8 GPa (at 300K) a phase transition to the cubic phase of ZnO that exhibits the rocksalt (NaCl) structure occurs. This can be explained considering that an enhancement of pressure produces a shrinking of cystalline structure leading to a stronger Coulomb interaction. Thereby, the interaction favors the ionicity rather than covalent nature of the bonds. Upon decreasing the hydrostatic pressure this phase transition is reversible in the range of 2-6 GPa, depending on temperature. Hence, the rocksalt structure is not metastable at normal pressure. The temperature-pressure phase diagram of ZnO is shown in Fig. 1.4. Since wurtzite ZnO compared with zincblende and rocksalt structures, shows intriguing optical, electrical, and optoelectronic properties in thin film and nanostructured form, a lot of research work has been mainly focused on the study of doped and undoped wurtzite ZnO thin films and nanostructures.

1.1.2 Phonon Modes

By evaluation of the phonon-mode frequencies, information about strain [19] or about the incorporation of doping or alloying atoms can be derived. Besides the phonon-mode frequency and broadening parameter provides information about crystal quality, because scattering due to a lower crystal quality or due to alloying makes the phonon-mode broadening parameter larger [6]. To this aim Raman scattering is often applied for studying the phonon modes of ZnO bulk samples [20–24], and has become a fast and reliable tool to study ZnO thin films [19, 24–27], and ZnO nano- and microstructures [28–30]. The optical phonons of the wurtzite structure at the Γ point of the Brillouin zone belong to the following irreducible representation:

$$\Gamma^{opt} = 1A_1 + 2B_1 + 1E_1 + 2E_2 \, . \tag{1.1}$$

Both A_1- and E_1-modes are polar, because the macroscopic electric fields is associated with the LO phonons, they split into transverse optical (TO) and longitudinal optical (LO) phonons with different frequencies ω_{TO} and ω_{LO}, respectively. For the lattice vibrations with A_1- and E_1-symmetry, the atoms move parallel and perpendicular to the c-axis, respectively (Fig. 1.5) [6].
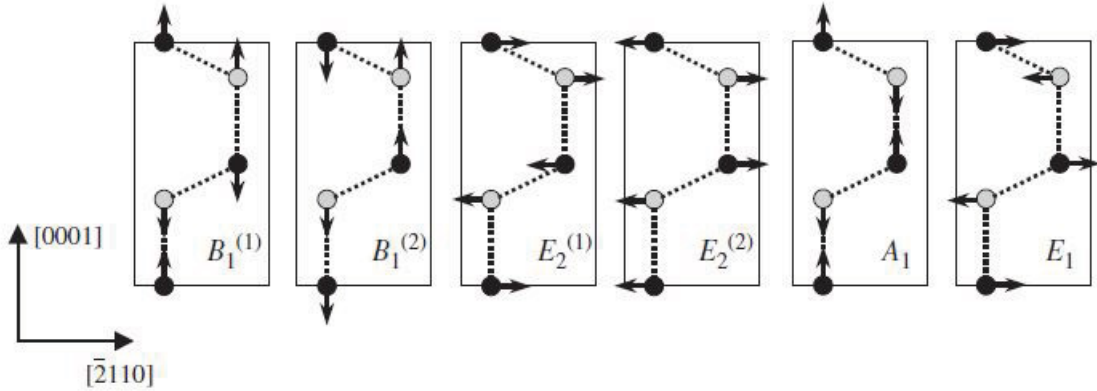
Figure 1.5: Displacement patterns of the optical phonons of a lattice with wurtzite crystal structure [6].
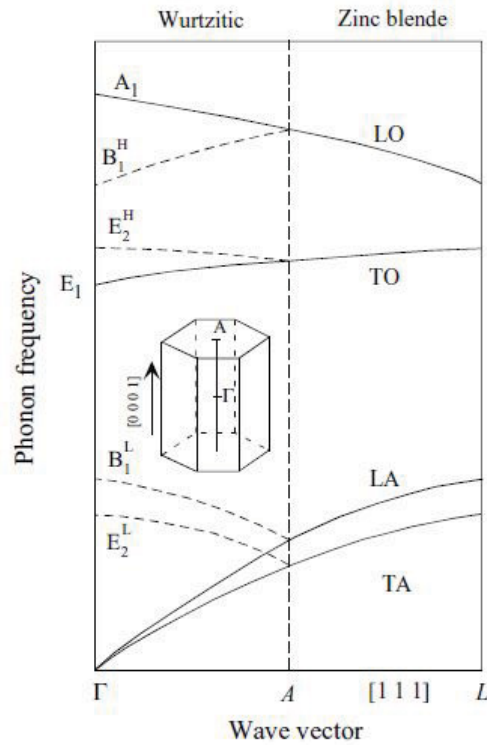
Figure 1.6: Schematic depiction of the phonon dispersion curves for zinc blende and Wurtzite structures [31].

Both A_1- and E_1 are Raman and IR active, whereas the two nonpolar $E_2^{(1)}$ and $E_2^{(2)}$ modes are only Raman active and the B_1 modes are IR and Raman inactive (silent modes). A schematic phonon dispersion curves of wurtzite and zinc blende structure ZnO throughout the Brillouin

Zone is reported in Fig. 1.6, where also the Γ and A points of the zone in relation to the real space of the hexagonal structure are shown. Phonon branches along the [1 1 1] direction (Miller index) in the zinc blende structure are folded to approximate those of the wurtzite structure along the [0 0 0 1] direction (Miller-Bravais index) because the unit cell length of the hexagonal structure along the [0 0 0 1] direction is twice that of the cubic structure along the [1 1 1] direction. Hence, for example, A_1 and B_1^H mode derive from a singly degenerate LO phonon branch of the zinc blende system by system folding, among them, the A_1 mode (solid line) is only present in zinc blende structure [31]. The frequencies of the Raman active phonon modes in cm^{-1} for bulk ZnO in wurtzite structure are presented in Tab. 1. 1. Data are a compilation of the results different studies reported by Alim et al. [32]. In Figs. 1.7 (a) and

E_2(low)	$A_1(TO)$	$E_1(TO)$	E_2(high)	$A_1(LO)$	$E_1(LO)$
102	379	410	439	574	591

Table 1.1: Raman active phonon mode frequencies in cm^{-1} for bulk ZnO in wurtzite structure [32].

(b) the unpolarized Raman spectra at various temperature and polarized Raman spectra are reported, respectively. The set of spectra collect the phonon modes at $\omega \approx$ 100 cm^{-1}, 380 cm^{-1}, 410 cm^{-1}, 437 cm^{-1}, 570 cm^{-1} and 590 cm^{-1} which can be assigned to phonon modes reported in Tab. 1.1, E_2(low), $A_1(TO)$, $E_1(TO)$, E_2(high), $A_1(LO)$, $E_1(LO)$ and some multiple phonon (MP) scattering like E_2(high)-E_2(low). It is worth noting that the intensity of the $A_1(LO)$ mode is almost negligible in all spectra because of its lower scattering cross section. In fact, its scattering cross-section is markedly smaller than other modes, which was explained by the destructive interference of the Frohlich interaction and the deformation potential contributions to the LO-scattering in ZnO [33]. However, point defects as oxygen vacancies or zinc interstitials or their complexes are assumed to enhance the A_1(LO) mode [34–37]. Fig. 1.7 (a) also reveals the stability of bulk ZnO under thermal annealing up to 690 K, while the polarized Raman spectra in Fig. 1.7 (b) evidence that the intensity of the phonon modes strongly depend on the different laser polarization because of hexagonal symmetry.

1.1.3 Band Structure and Excitons

Numerous theoretical calculations have been employed to calculate the band structure of ZnO [5]. Fig. 1.8 (a) shows the calculated band structure of wurtzite ZnO. It it possible to note that both the valence band maxima and the conduction band minima occur at the Γ point k=0 indicating that ZnO is a direct band gap semiconductor. The bottom bands occurring around -9 eV (not shown in figure), and around -20 eV come from the Zn 3d levels and the O 2s levels, respectively. The lowest conduction band (CB) is formed, from the empty 4s states of Zn^{2+} or the antibonding sp^3 hybrid states. The effective electron mass is almost isotropic, with a value around m$_e$=(0.28±0.02)m$_0$ [6]. The valence band (VB) originate from the occupied 2p orbitals of
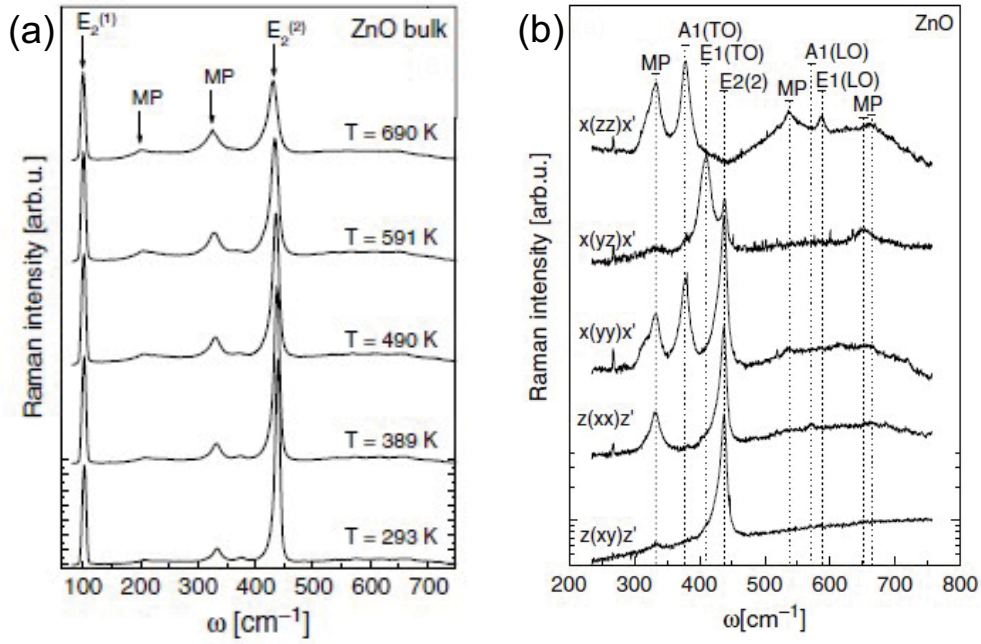
Figure 1.7: Temperature-dependent, unpolarized Raman spectra (a) [38] and polarized Raman spectra (b) [39] of a ZnO bulk sample. Excitation with Nd:YAG laser line $\lambda = 532$ nm and laser power P=40mW.
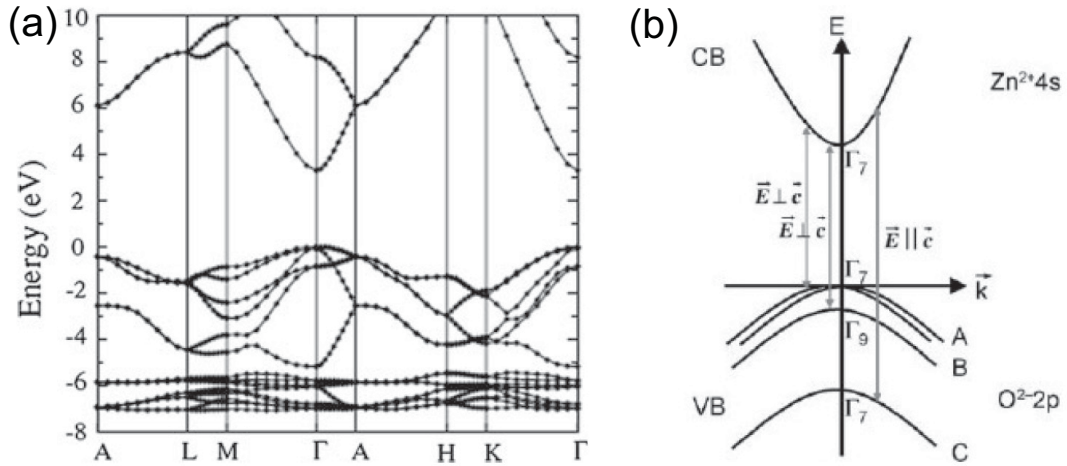
Figure 1.8: (a) Calculated band structure of the wurtzite ZnO using HSE hybrid functional method [5], (b) Schematic view of valence band (VB) and conduction band (CB) around of the Γ point [12].

O^{2-} or from the bonding sp^3 orbitals. It is split under the influence of the noncentrosymmetric hexagonal crystal field into two states. A further splitting is due to spin-orbit coupling into three double degenerate VBs. In all wurtzite-type semiconductors these VBs are labeled from highest to lowest energies as A (heavy hole), B (light hole) and C (crystal-field split band) bands (see Fig. 1.8 (b)). The symmetries of the A, B and C valence bands are still debated. However, since the splitting of the A and B valence bands is only of the order of 5 meV (40 meV with respect to the C VB), and since the selection rules are essentially the same, thus both A and B

VB are allowed transition only for E⊥c, whereas transition between C VB to CB are allowed for E∥c [12] as shown in Fig. 1.8 (b).The effective hole masses in ZnO are rather isotropic and similar for the A, B, and C VBs, with typical values of $m_{h\perp\|A,B}$=0.59m_0, $m_{h\|C}$=0.31m_0, and $m_{h\perp C}$ =0.55m_0 [6].
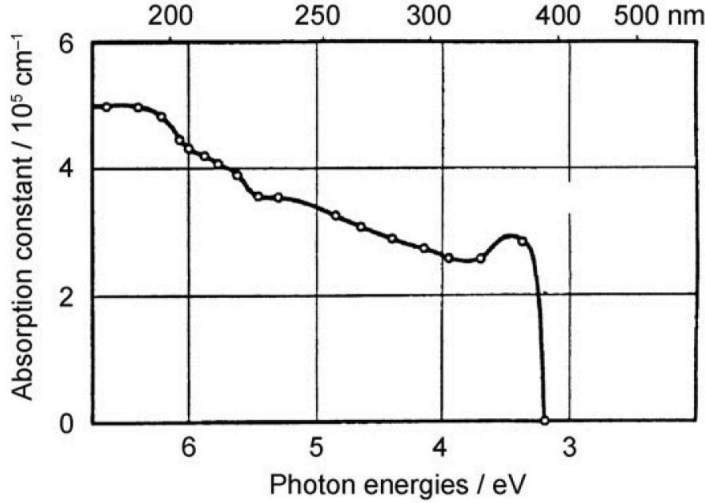
Figure 1.9: A room-temperature absorption spectrum of bulk ZnO [40].

As previously discussed, ZnO is a direct band-gap semiconductor with a dipole-allowed band-to-band transition, therefore, a photon with an energy larger than the band gap excites an electron from the VB to the CB. A pioneering plot of the absorption spectrum of bulk ZnO is reported in Fig. 1.9, it shows the typical absorption edge of ZnO. The photon absorption for ZnO and semiconductors or insulant in general leads an electron in the CB and a hole in the VB are created simultaneously. Similarly, they are annihilated in a radiative or nonradiative recombination process. If one carrier approaches the other, their Coulomb attraction is not negligible, and they may form a bound state (exciton) at an energy slightly below the band gap, in particular, they form a series of hydrogen-like states below the CB (Fig. 1.10). The excitons are called Wannier excitons when the average distance between electron and hole, that is, the excitonic Bohr radius r_B, is larger than the lattice constant, in contrast they are called Frenkel excitons, when electron and hole reside in the same unit cell. For bulk semiconductors, the exciton Bohr radius can be calculated by using the following equation [2, 6, 41]

$$r_B = \frac{\hbar\epsilon}{\mu e^2},$$

(1.2)

where $\hbar$ is the Planck constant, ϵ is the dielectric constant, $1/\mu = 1/\mu_e + 1/\mu_h$ is the exciton reduced mass. Fig. 1.10 (a) and (b) report the band structure and the exciton states consisting of the series of hydrogen-like states determined by quantum number n_B=1, 2, 3,... and is followed by the ionization continuum, starting at Eg. Taking into account the effective and reduced electron and hole masses and the dielectric constant (ϵ_r=8.75) it is possible to calculate the

energy of the hydrogen-like series by the expression

$$E_{ex} = \frac{\mu e^4}{2h^2\epsilon^2} \cdot \frac{1}{n^2} = -E_b \cdot \frac{1}{n^2} \; ; \qquad (1.3)$$

From Eq. (1.3) we obtain the excitonic binding energy in ZnO E_b=60 meV and from Eq. (1.2) the excitonic Bohr radius r_B= 2.23 nm [2,6]. For all the exciton series resulting from the transitions from the A, B, and C VB (Fig. 1.8) into the CB, the translational mass is given by the sum of effective electron-electron and electron-hole masses. At sufficiently high temperatures, $KT > E_b$, the excitons dissociate into free electrons and holes. The excitonic states can couple with photon
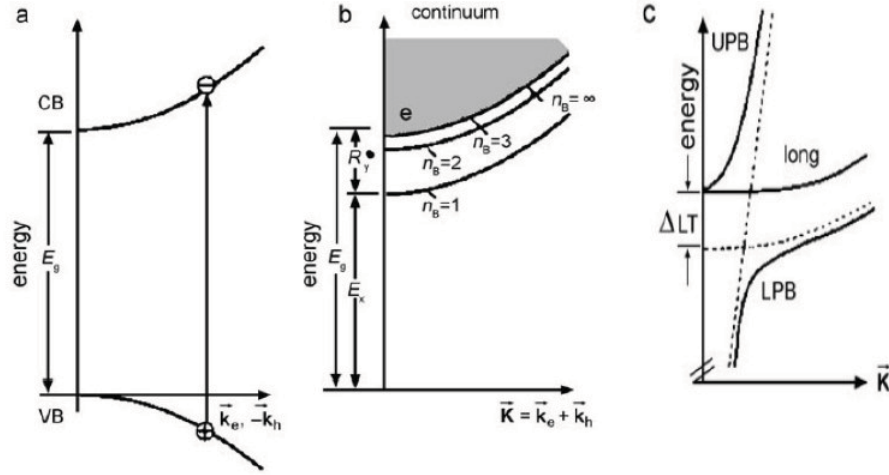
Figure 1.10: Schematic drawing of (a) the band-to-band transition and (b) the resulting exciton states. c) The exciton polariton resulting from the coupling of the exciton with light [42].

that, through the crystal producing the exciton polariton, a quasi-particle resulting from strong coupling between an electromagnetic wave and a electric dipole produced by excitation. The dashed lines in Fig. 1.10 (c) give the dispersion of the n_B=1 exciton and of the photon. A coupling between the two results in the dispersion curve (solid line) of the lower polariton branch (LPB) which starts photon-like, then bends over to an exciton-like behavior. A transverse-longitudinal splitting Δ_{LT}, separates the LPB from the upper polariton branch (UPB) which bends over again to photon-like behavior. The splitting Δ_{LT} is related to exchange term of the excitonic Hamiltonian and represents the difference between the transversal and longitudinal exciton dispersion curve, the latter doesn't interacts with photons thus remaining pure excitons. Since, the exciton or exciton-polariton states can be excited directly according to the selection rules, the splitting Δ_{LT} produces a homogeneous broadening ($\sim$1 meV) on the exciton absorption spectrum and related PL also at lowest temperature. Due to the presence of the excitons, the absorption spectrum at low temperature results in exciton series and relative exciton-polariton states with n_B=1, 2, 3,... with a width due to Δ_{LT} and by homogeneous broadening, finally absorption spectrum shows the continuum ionization which produces a sharp absorption edge. At higher temperature, there is scattering with phonons which results in broader absorption bands

Figure 1.11: Luminescence spectra of ZnO for various temperatures: (a) 110 K and (b) 290 K [43].

and in an exponential tail of the absorption. Such tail extends towards lower energies, forming the so called Urbach tail [12]. In Fig. 1.11, we show the excitonic luminescence spectra of a bulk ZnO acquired a 110 K and 290 K, respectively. It is possible noting the broadened peak of the A and B exciton polaritons at 110 K around 3.37 eV and their longitudinal-optical (LO) phonon replica around 3.30 eV and 3.225 eV, the secondary peak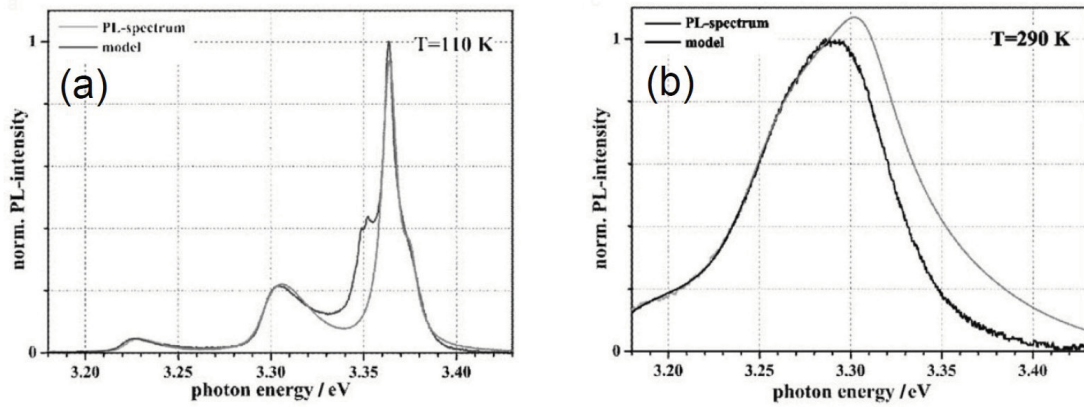 at 3.35 eV is due to bound exciton complex. The phonon replica result from an exciton recombination by emission of one or more LO phonons. With increasing temperature, the homogeneous broadening increases, resulting at room temperature in a structureless emission band (width~0.1 eV). It should be noted that its peak is not identical with the exciton energy and the discrepancy between measured spectra and models at higher temperatures results from reabsorption. In the absence of scattering, the nearly vertical transition due to photon absorption creates an exciton with $K = 0$ [44], in order to fulfill the conservation of crystalline momentum in photon absorption, and the excitonic emission presents a very sharp line shape only due to exciton-polariton coupling. Phonon-scattering processes of the excitons (illustrated in Fig. 1.12) can produce an homogeneous or inhomogeneous broadening of the excitonic emission. After a scattering event, the wavevector changes from the initial value K of a level to a final value K' either in the same level or in another discrete level or in the continuum states. If the interaction involves an acoustic phonon, the scattering event does not change the discrete level, whereas, process involving LO phonons can bring the exciton in another discrete level or can let it in the same initial energy level. Tokoyozawa theory predicts two different type of broadening (homogeneous and inhomogeneous) of the excitonic peak depending on interaction between exciton and the phonon bath. In particular, the exciton line shape is governed by the competition between the mobile nature of excitons and their tendency to be momentarily localize in the lattice due to interaction with phonons [45, 46]. Homogeneous broadening occurs when the mobile nature of the exciton prevail (weak scattering limit). Lorentzian width (FWHM) is due to the fact that the K=0 exciton remains a finite lifetime due to phonon-induced scattering toward K $\neq$ 0 levels, hence, its width is determined by energy-time uncertainly principle. In contrast, large thermal or structural disorder can induce to a completely localized, defect-like exciton, whose absorption line basically reproduces

the density of states with energy that thermally fluctuates with Gaussian statistics from site to site. Therefore, the excitonic line shape is characterized by a Gaussian. Obviously, these effects are expected to increase with growing temperature due to progressive thermal activation of the lattice, thus line shape and width are dependent on the temperature. The Urbach tail shown above, can be explain considering that scattering with phonons can induce the appearance of localized states below the bottom of the excitonic band, which can be regarded as temporary self trapped excitons states due to sufficiently great local lattice deformations.
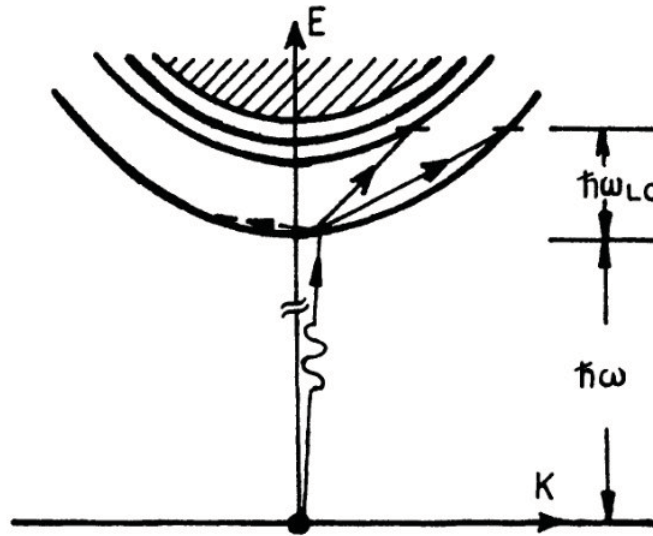
Figure 1.12: Scattering of excitons by acoustic (left) or LO (right) phonon scattering which brings it to the final state. The nearly vertical transition due to photon absorption creates an exciton with $K = 0$. The solid lines indicate the discrete excitons energy level discussed above [44].

The excitons are often bound to defects, then, the translational degrees of freedom are off and the spectral width of emission is very small. The binding energy is much smaller than that of the free exciton; therefore, they are observed at very low temperatures. In these conditions it is possible observe several peaks between 3.35 and 3.37 eV (see Fig. 1.11) due to bound excitons, but the attribution of the peaks to particular bound exciton is difficult because the energy region is very narrow and the emission energy of a particular complex can depend on synthesis method. The lifetimes of free and bound excitons in ZnO, as in other direct wide-gap semiconductors, are typically from 0.3 up to some ns, and especially for the free excitons, are generally determined by nonradiative recombination processes [12,47,48]. Fig. 1.13 reports the PL free exciton (FE) decay time for bulk ZnO and tetrapods. The decay of the free exciton emissions from the ZnO tetrapods is found to be bi-exponential with time constants of τ_1=14 ns and τ_2=1 ns at 280 K. In contrast, PL decay in bulk ZnO is much faster and is described by a single exponential with lifetime of 0.5 ns. In general the free excitonic emission is expected to have a single decay time determined by interplay of radiative and NR recombination processes as $1/\tau = 1/\tau_r + 1/\tau_{nr}$, where τ_r and τ_{nr} denote the intrinsic radiative and defect-mediated NR lifetimes of the exciton, respectively. A typical value of τ_r for bulk ZnO is about 300 ps, which is small compared to other
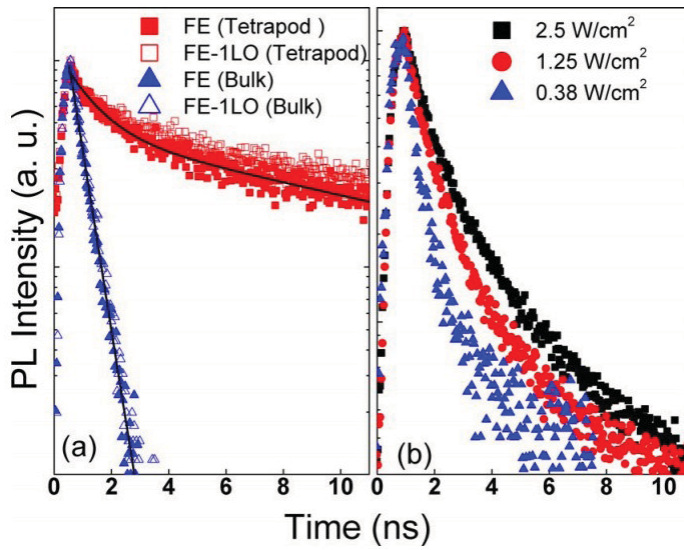
Figure 1.13: (a) PL decay measured for the free excitonic (FE) emissions at 280 K. Symbols represent experimental data for ZnO bulk and tetrapod, FE-1LO labels indicate data obtained monitoring the first longitudinal optical(LO)-phonon replica. The solid lines are fitting curves. (b) PL decays of the FE-1LO emission from the tetrapods measured at room temperature with the specified excitation powers [49].

semiconductors [50]; whereas, since in ZnO QDs excitons are confined the radiative lifetime is inversely proportional to the oscillator strength. In this case, was observed for ZnO QDs very small exciton radiative lifetimes of the order of tens of picoseconds [51].

1.1.4   Point Defects

Defects can strongly influence the electrical and optical properties of a semiconductor, affecting doping, carrier lifetime and luminescence efficiency [52, 53]. In addition, excitons could bind to defects, thus their dynamics and related luminescence are strongly influenced by their presence. Understanding the behavior of point defects in ZnO is therefore essential to its successful application in semiconductor devices. Native or intrinsic defects are imperfections in the crystal lattice that involve the constituent elements [52]. They include vacancies (missing atoms at regular lattice positions), interstitials (extra atoms occupying interstices in the lattice) and antisites (a Zn atom occupying an O lattice site or vice versa). Native defects play an even more important role in doping effect of ZnO. For example, oxygen vacancies and zinc interstitials have often been invoked as sources of n-type conductivity in ZnO [54–57]. Moreover, oxygen vacancies and other donor defects make difficult to obtain p-type ZnO because they neutralize most of the introduced shallow acceptors.

Density-functional calculations for native defects in ZnO have been reported in several groups, see for instance refs [59–61]. In particular, most of the calculations agree that oxygen vacancies (V_O) and zinc vacancies (V_{Zn}) are the lowest energy defects, followed by the Zn interstitial and the Zn_O antisite, whereas oxygen interstitials (O_i) and O_{Zn} antisites were found to be at higher energy. The defects that are favored under Zn-rich conditions (V_O, Zn_i and
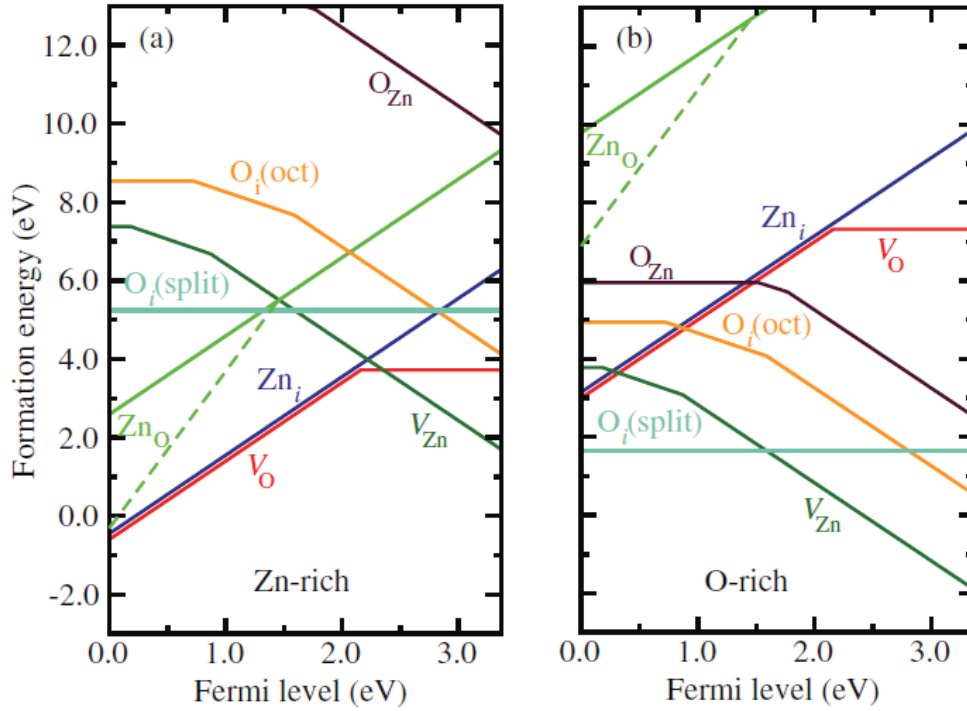
Figure 1.14: Formation energies as a function of Fermi-level position for native point defects in ZnO for (a) Zn-rich and (b) O-rich conditions. The zero of Fermi level corresponds to the valence-band maximum [58]. V_{Zn}, denote a zinc vacancy, respectively, Zn_i indicate zinc interstitial, V_O^o denote oxygen vacancy, O_i (oct) and O_i (split) represent oxygen interstitial in octahedral and split configuration, respectively; while O_{Zn} indicates antisite oxygen and Zn_O denotes antisite zinc.

Zn_O) act as donors, while those that are favored under O-rich conditions (V_{Zn}, O_i and O_{Zn}) act as acceptors. In Fig. 1.14 the calculated defect formation energies as a function of Fermi level [58] is shown. The lowest formation energy of V_O, indicates that these defects would be present in significant concentrations in ZnO under extreme Zn-rich conditions. For these reasons oxygen vacancy is the most investigated defect in the ZnO literature; it is therefore worthwhile devoting special attention to this defect. In general, V_O has been associated with unintentional n-type conductivity, but recent density-functional calculations indicate that V_O is a very deep rather than a shallow donor and, consequently, cannot contribute to n-type conductivity [58,62]. Although the calculations reported in the literature differ on the values for transition levels and formation energies due to the different approaches, they unanimously agree that V_O is a deep donor [58, 60, 62–66]. Fig. 1.15 shows that V_O in the neutral charge state induces a doubly occupied single-particle state at about 1 eV above the VB [66] confirming that V_O is a deep donor state that can not contribute to n-type conductivity. The electronic structure of an oxygen vacancy in ZnO can be viewed in a simple model within molecular orbital theory that involves four Zn dangling bonds sp_3 hybrids containing two electrons, which combine into a fully symmetric a_1 state located in the band gap and three almost degenerate states in CB. In the neutral charge state of the oxygen vacancy, the a_1 state is doubly occupied and the three states in CB are empty. Hence, oxygen vacancy in ZnO can exist in three charge states: neutral, +1
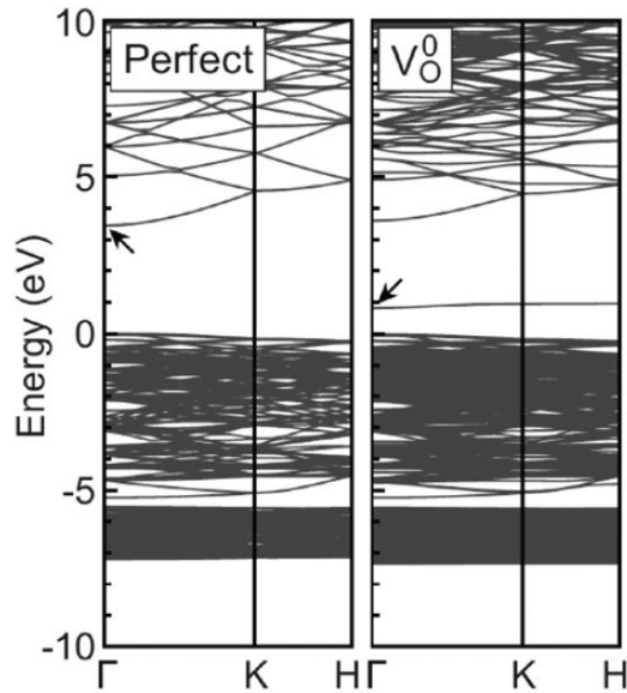
Figure 1.15: Band structure for the ZnO perfect crystal and for the oxygen vacancy (V_O) in the neutral charge state obtained using the HSE hybrid functional. The zero in energy corresponds to the valence-band maximum in the perfect crystal [66].

and +2, in which the a1 state is doubly occupied, singly occupied and empty, respectively. As shown in Fig. 1.16, the occupation of the a_1 state is directly related to the local lattice relaxation around the oxygen vacancy [58,62]. In the neutral charge state, the four Zn atoms strongly relax toward the vacancy by 12% of the equilibrium Zn-O bond length; in the +1 charge state they slightly relax outward by 3%; and in the +2 charge state, the four Zn atoms relax outward by 23%. These large differences in relaxations imply a significant reduction of the formation energies of V_O^{+2} and V_O^0 with respect to V_O^{+1}, which is never thermodynamically stable [58]. The calculated configuration diagram in Fig. 1.16 (d) show that V_O^{+1} is a metastable state because have a thermal barrier to escape out of 0.3 eV, that is larger then thermal energy at 300 K.

An important properties for point defects is the migration barrier (ΔE_m), which provides information about the mobility of defect as a function of temperature. During the migration of oxygen vacancy, a nearest-neighbor oxygen atom jumps from oxygen lattice into the original vacant site leaving a vacancy behind. The ΔE_m for this process can be calculated by considering the total energy at various intermediate configurations when moving a neighboring oxygen atom from its nominal lattice site along a path toward the vacancy. This ΔE_m does depend on the charge state of the oxygen vacancy. The calculated ΔE_m for V_O^0 is 2.4 eV and for V_O^{+2} is 1.7 eV [58]. These ΔE_ms indicate that V_O^0 will become mobile above temperatures of 900 K and V_O^{+2} will become mobile at temperatures above 650 K [58].

Other point defects of ZnO materials characterized by low formation energy (discussed above) are zinc vacancies (V_{Zn}) and zinc interstitial (Zn_i^{2+}). Fig. 1.14 evidences that the formation
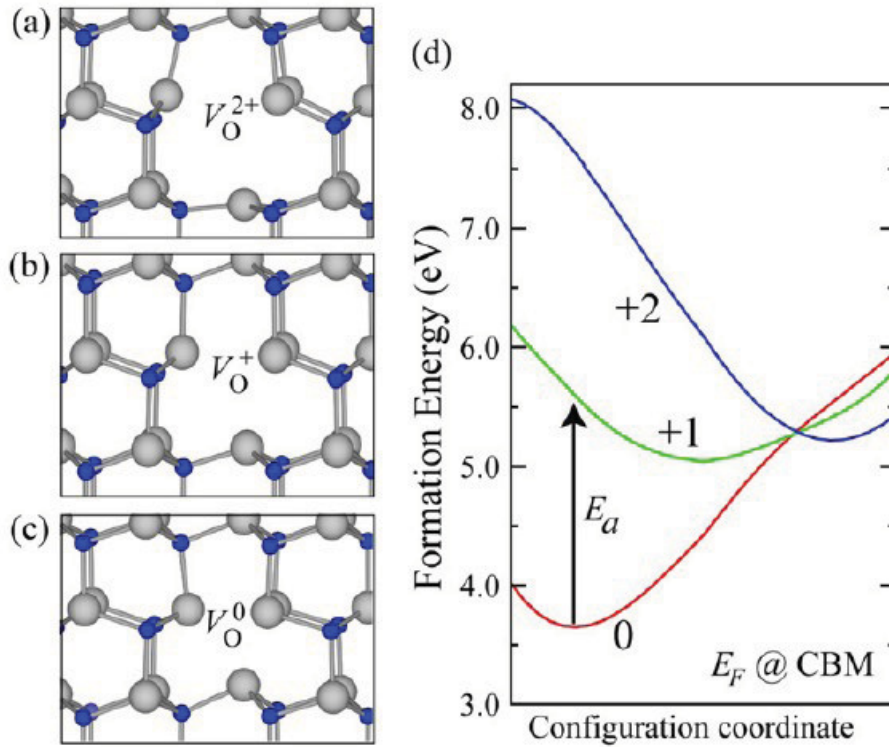
Figure 1.16: Ball and stick model of the local atomic relaxations around the oxygen vacancy in the (a) neutral, (b) +1 charge state and (c) +2 charge states. (d) Calculated configuration coordinate diagram for V_O^0, V_O^{+1} and V_O^{+2} for Fermi energy at the conduction-band minimum. The arrow represents an optical transition from V_O^0 to V_O^{+1} [62].

energy of a single V_{Zn} is 3.7 eV under p-type conditions (E_F at the maximum of the VB), in the most favorable extreme O-rich limit. The electronic structure of zinc vacancies can be understood considering that removing Zn atom from the ZnO lattice, we have four O dangling bonds and a total of six electrons from which four O dangling bonds combine into a doubly occupied symmetric a_1 state located deep in the valence band, and three almost degenerate states in the band gap, close to the VB [58]. These three states are partially occupied by four
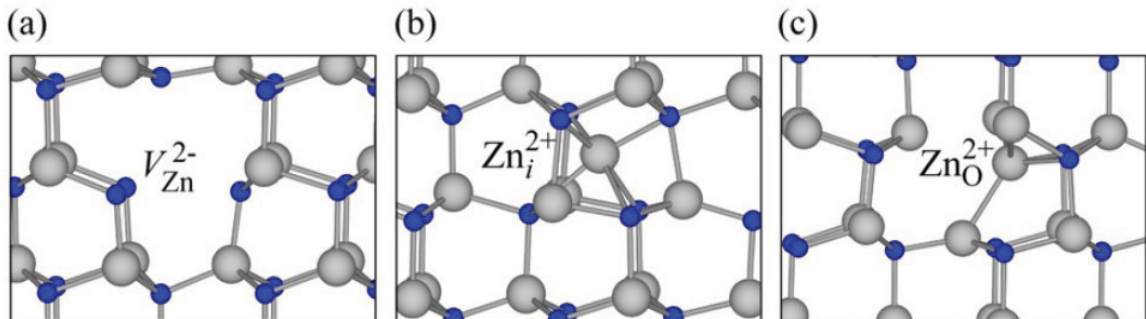
Figure 1.17: Calculated local atomic geometry for (a) the Zn vacancy in the -2 charge state V_{Zn}^{2-} ; (b) the zinc interstitial in the +2 charge state Zn_i^{2+}. (c) Calculated local atomic geometry of the zinc antisite in the +2 charge state Zn_O^{2+} [58].

electrons, therefore, can accept up to two additional electrons, thus explaining the acceptor behavior of V_{Zn} in ZnO. One can find V_{Zn} into three different charge state V_{Zn}^0, V_{Zn}^- and V_{Zn}^{2-}. In all cases, the oxygen atoms around V_{Zn} exhibit a large outward breathing relaxations of about 10% as compared to the equilibrium Zn-O bond length (figure 1.17 (a)). This suggests that the overlap between the oxygen $2p$ orbitals surrounding the zinc vacancy is too small to result in significant chemical bonding between the oxygen atoms. In fact, the calculated O-O distances are about 3.5 $\mathring{A}$, much larger than the sum of the covalent radii (1.46$\mathring{A}$) [58]. As the case of V_O, migration of V_{Zn} occurs when a nearest-neighbor Zn atom moves into the vacant site leaving a vacancy behind. The migration of V_{Zn}^{2-} in ZnO has been predicted to be isotropic with a ΔE_m of 1.4 eV corresponding at a temperature of 540 K [67].

A Zn_i atom could in principle occupy two site in the wurtzite ZnO: the tetrahedral site or the octahedral site. However, in octahedral site the Zn_i-neighbors distance are longer than tetrahedral site, hence, it is the most stable. At this state the Zn_i has three Zn and three O atoms as nearest neighbors at a distance of $\sim 1.07 \cdot d_0$ (d_0 is the Zn-O bond length along the c axis). Regarding its electronic structure, Zn_i induces an a_1 state with two electrons above the CB, which are transferred to conduction band states, stabilizing the $+2$ charge state (Zn_i^{2+}). Thereby, Zn_i will always donate electrons to the conduction band acting as a shallow donor [58]. Density functional calculations revealed that this defect have a low ΔE_m of 0.57 eV [58], accordingly to experimental results [68], this implies that Zn_i is highly mobile even at room temperature.
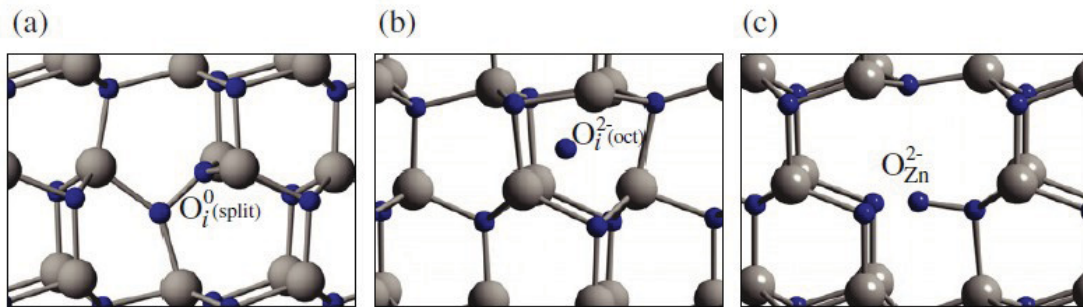
Figure 1.18: Local atomic geometries for (a) oxygen interstitial in the split-interstitial configuration O_i^0 (split); (b) oxygen interstitial in the octahedral configuration O_i^{2-} (oct); (c) oxygen antisite O_{Zn}^{2-}, showing a large displacement off the substitutional site [58].

The other native defects (oxygen interstitials, zinc antisites and oxygen antisites) have higher formation energies and, therefore, are not expected to play a role in ZnO under near-equilibrium conditions. As shown in Fig. 1.17, Zn_O produces a large displacement of the Zn atom by more than 1$\mathring{A}$ from the substitutional lattice site toward two nearest neighbor oxygen atoms [58,62], resulting in a Zn_O-O interatomic distances 8% larger than the equilibrium Zn-O bond length. One can think the structure of Zn_O as a complex of a Zn interstitial and an O vacancy [58].

Oxygen interstitial (O_i), as for Zn_i, can occupy the octahedral or tetrahedral interstitial sites, or form split interstitials. However, based on density functional calculations it is shown that more stable configuration are octahedral and split. In the O_i split configuration, the O-O

distance is 1.46Å (Fig. 1.18 (a)), suggesting the formation of an O-O chemical bond, with two almost degenerate and completely filled states in the band gap similar to the antibonding ppπ^* state in the molecular orbital of the isolated O_2 molecule. Oxygen interstitials, when occupy the octahedral site (O_i oct) introduces states in the lower part of the band gap that can accept two electrons (see Fig. 1.18 (b)). These states are derived from oxygen p orbitals and result in deep acceptor transition levels at 0.72 and 1.59 eV above the VB. The calculated migration energy barrier for O_i (split) is 0.9 eV, while the ΔE_m for O_i^{2-} (oct) through the hexagonal channel along the c axis is 1.1 eV. These values indicate that O_i (split) and O_i^{2-} (oct) will become mobile at T >340 K and T>440 K, respectively [67].

The oxygen antisite (O_{Zn}) is an acceptor-type defect with very high formation energy, even under the most favorable O-rich conditions as shown in Fig. 1.14 [58]; hence, it is very unlikely find O_{Zn} in equilibrium conditions. O_{Zn} are deep acceptors with transition levels at 1.77 eV above the VB [58].

1.2   Effect of Quantum Confinement (QC)

The term QC describes the confinement of electrons or holes within the physical boundaries of the semiconductor. Hence, low dimensional semiconductors such as quantum wells, quantum wires, and quantum dots describe confinement in 1, 2 and 3 dimensions respectively. When a nanostructure has one or more of its dimensions reduced to a nanometer length scale, this produces a quantization of the carrier energy corresponding to motion along these directions. For example, if the QC is along one direction, the carriers can have free motion in other two directions. To understand qualitatively the effect of QC one can image the Heisenberg's uncertainty principle, which infers that position X and momentum P of an electron cannot be precisely determined simultaneously, and the the corresponding uncertainties must satisfy the relation $\Delta X \Delta P \geq \hbar$. According to this principle an electron confined in one dimensional box (length L) has an uncertainty in the momentum $\Delta P = \hbar/L$. Since the energy E of a particle in the absence of a potential is related to the momentum by E=$< P^2 > /2m$, also in the case of electron "at rest" (P=0), we have an energy ground state E=$\Delta P^2/2m$. This implies that the kinetics energy of a electron confined in a linear box consists in a series of quantized energy levels with $E_n = n\hbar^2/2mL^2$ related to the box dimensions. In general, the total energy of electrons (or holes) will be the sum of allowed energies associated with the motion of these carriers along the confined direction and the kinetic energy due to free motion in the remaining unconfined directions.

QC in three dimensions, quantum dot (QD), occurs when the size of a semiconductor nanocrystal is reduced to the order or less than its exciton Bohr radius (<10 nm). In this case, the exciton will be strongly confined in this limited volume and the electronic structure of the three-dimensionally confined electrons and holes will be drastically modified. The r_B is often used to judge the degree of confinement in a QD with radius R, in three different regimes: R>r_B, R$\sim$$r_B$, and R<$r_B$, which are named as weak confinement, intermediate confinement and strong confinement regimes, respectively [2]. Taking into account that the exciton consists in a

electron hole pair which interact by Coulomb potential we can write the Schrodinger equation in spherical coordinates for one free exciton in a crystal

$$\left(-\frac{\hbar^2}{2m_e^*}\nabla_e^2 - \frac{\hbar^2}{2m_h^*}\nabla_h^2 + V_c \right)\phi(r) = E\phi(r)\,, \tag{1.4}$$

where m_e^* and m_h^* are effective masses of electron and hole, V_c is the Coulomb potential between electron and hole forming an exciton and $\phi(r)$ is the wave function of the exciton. The Schrodinger equation (1.4), can be solved analytically along with the corresponding boundary condition (ϕ(r=R)=0, in the absence of the Coulomb interaction, resulting in

$$E = E_h + E_e = E_g + \frac{\hbar^2}{2m_e^*}\left(\frac{\alpha_{n_e} l_e}{R} \right)^2 + \frac{\hbar^2}{2m_h^*}\left(\frac{\alpha_{n_h} l_h}{R} \right)^2\,, \tag{1.5}$$

Equation (1.5) shows that the absorption is blue-shifted with respect to the bulk band-gap E_g. The shift varies with crystal size like $1/R^2$, being larger for smaller sizes. Furthermore, this equation states that the energy spectrum consists of a series of lines corresponding to the electron-hole transitions. Thus, QC effects in QDs have a significant impact on the optical properties of the material. The selection rules for the dipole allowed interband transitions are Δl=0 in the absence of Coulomb interaction. When the Coulomb interaction is included, the problem also can be resolved by a numerical approach. However, in the case of strong confinement regime, in which the size of the quantum dot is smaller than r_B, the kinetic energy terms dominate and the absolute value of the pair states is only weakly shifted by Coulomb effects. Hence, the electrons and holes are largely represented by their quantized energy states obtained neglecting the coulomb interaction (Eq. (1.5)). Instead, in the weak confinement regime ($R > r_B$) the energy separation between the various levels becomes comparable to the exciton binding energy, thus the approximation made is not more possible.

1.3   ZnO Quantum Dots: Energy Gap and Excitonic Emission

Low-dimensional self-assembled ZnO nanostructures have shown a great advantage in fabrication of devices in the nanometer regime. In particular, one-dimensional (1D) ZnO nanowires/rods have been used to fabricate the field emission devices, piezoelectric nanogenerators, photonic devices, and light emitting diodes [2, 10, 67, 69, 70]. The high exciton binding energy (60 meV) of ZnO ensures the room temperature intense excitonic luminescence in the UV-blue spectral range. ZnO nanostructures having size comparable with r_B show excellent QC effects in their optical and electrical properties which make ZnO NPs promising to optical applications [10–12, 70]. In fact, QC not only modify properties of ZnO quantumdots (QDs) but also enhance the exciton oscillator strength and quantum efficiency. Hence, a study on ZnO QDs is important not only to understand the three dimensional QC effects on the excitonic transitions but also to create new forms of this material which could open more frontiers for its applications. Fig. 1.19 (a) shows typical TEM ensemble view of the ZnO QDs which are polydisperse and mostly of irregular

shape with a density of deposited NPs of the order of $10^{13} cm^{-2}$. The inset of Fig. 1.19 shows the selected area electron diffraction (SAED) pattern which confirms the formation of ZnO QDs. The size distribution of the ZnO QDs reveals that the mean radius was ∼2.23 nm, as shown in the histogram of Fig. 1.19 (b). This mean radius can be used for correlating the average band-edge of the ensemble of ZnO QDs with their corresponding mean size. Fig. 1.20 shows the room

Figure 1.19: A TEM image of a typical ensemble of the polydisperse ZnO QDs produced by pulsed laser deposition. Inset shows the selected area electron diffraction pattern of these dots. (b) Histogram showing size dispersion of the ZnO QDs [71].

temperature absorption spectra of ZnO QDs of different mean radii. These absorbance spectra do not show a series of sharp absorption edge rather each spectrum, corresponding to a particular mean size exhibits a broad absorption feature which is expected due to the broad distribution of ZnO QD sizes. Average values of the band-edges have been obtained from the first derivative of these spectra and plotted as function of mean size of the ZnO QDs as shown in the inset of

Figure 1.20: Optical absorption spectra of the ZnO QDs of different mean radii. Inset shows the first derivative of these spectra. Spectral position of the negative peak of these derivative spectra was taken as the average band-edge of the ZnO QDs ensemble [71].

Fig. 1.20. One can see that the QC causes a blue shift of the band-edge of these spectra with decreasing mean size of the ZnO QDs (Sec. 1.2). Moreover, it is worth noting a drastic increase in the band-gap with decreasing size of the ZnO QDs in the range smaller than r_B for ZnO ($\sim$2.23 nm), whereas in the size range greater than r_B, the variation of the band-gap is rather in a smaller extent. To understand the confinement effects on these two size-domains, one needs to consider the effective mass approximation with strong and weak confinement, respectively. In the size domain where the dot is smaller than r_B, it is plausible that the exciton may not exist and therefore holes and electrons will suffer a strong confinement with a characteristic reduced mass and a Coulombic interaction term. Under these circumstances, the optical band-gap can be calculated using the following expression [16, 72]:
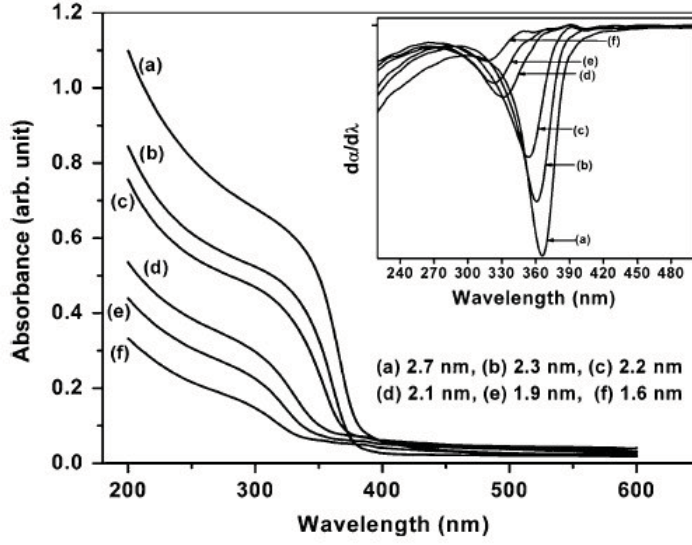
$$E = E_g + \frac{\hbar^2 \pi^2}{2eR^2}\left(\frac{1}{m_e^*} + \frac{1}{m_h^*}\right) - \frac{1.786e}{4\pi\epsilon_0\epsilon_r R} - 0.248E_{ex}\,, \tag{1.6}$$

where Eg is the bulk band-gap, R is the dot size, m_e^* and m_h^* are the effective masses of electron and hole, respectively. The last term $0.248E_{ex}$ represents the correlation energy, which can be expressed in terms of the excitonic binding energy E_{ex}. The used value are: m_e=0.24m_0, m_h=0.45m_0, Eg=3.369 eV, E_{ex}=59 meV, and ϵ_r=6.01 for ZnO [73]. The plot of the Eq. (1.6) is shown in Fig. 1.21 by solid lines. One can see that the agreement between the theoretical curve and the experimental data is reasonably good. In case of the dot size greater than r_B, the excitons can exist and therefore the Coulombic interaction term is replaced by the excitonic binding energy. Moreover, the exciton is free to move through the dot, thus, we need to replace the electron and hole effective mass into translational mass which is the algebraic sum of the electron and hole effective masses. In weak confinement region, the band-gap of the dots can be
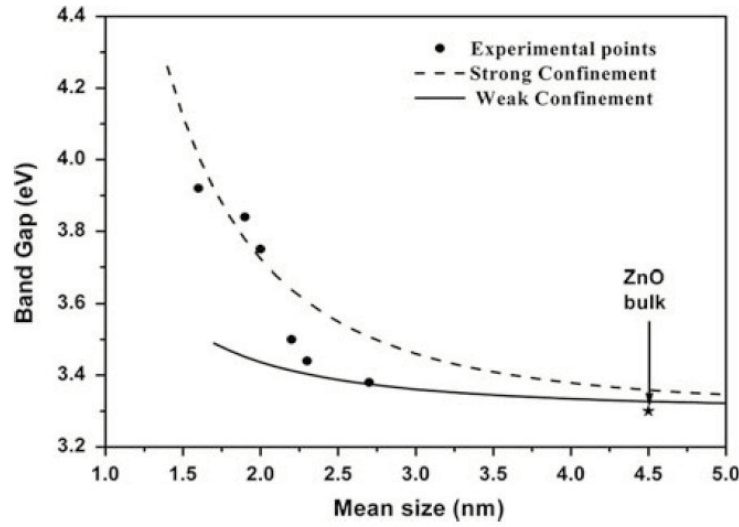
Figure 1.21: Variation of average band-edge of the ZnO QDs as a function of the mean radius. Experimental data are shown by filled circles while the fitting curves are plots of theoretically calculated values. The location of band-gap of bulk ZnO is also shown [71].

calculated using the following expression [72]:

$$E = E_g + \frac{\hbar^2 \pi^2}{2MeR^2} - E_{ex} \,, \tag{1.7}$$

where M is the translational mass of exciton and R is the mean dot size. It is worth noting that the blue shift in the band-gap as a function of R in this case is much weaker than in the strong confinement case. A plot of the Eq. (1.7) is shown in Fig. 1.21. In this case the measured band-edge of the ZnO QDs of mean size bigger than 2.3 nm lie in this curve, whereas for shorter size deviate from the theoretical curve toward the curve for the strong confinement. Electrons and holes in the strong confinement regime interact strongly by Coulomb forces and are localized in the QDs. Nevertheless, one can note that it was assumed that they are not in the form of excitons as for bulk ZnO or ZnO QDs of larger sizes but rather in an unbound state. Obviously, the effect of QC on the optical band-gap also affects excitonic emission of ZnO QDs. Fig. 1.22 shows the room temperature PL of ZnO spherical nanoparticles prepared by chemical methods varying some synthesis parameters. As a reference, PL of a free standing bulk ZnO sample (c) is plotted [74]. Since particle diameters are larger than r_B, here weak confinement condition takes place. Despite, a slight blue shift of the energy band-gap has been measured (0.08 eV) in smaller nanoparticles with size of 5 nm, the peak position of the excitonic emission slightly red shifts and interestingly it broads of an amount inversely proportional to particles diameters. A broadening of the excitonic band can be attributed to the fact that smaller nanoparticles are more affected by QC, thus the FWHM of excitonic PL is sensitive to the broadening of the nanoparticles size distribution: it increases from 0.2 eV of bulk to 0.5 eV for nanoparticles with average size of 5 nm. However, distribution doesn't produce a blue shift of the excitonic peak probably because of the presence of intra-band defect state localized in the surface of nanoparticles wherein the
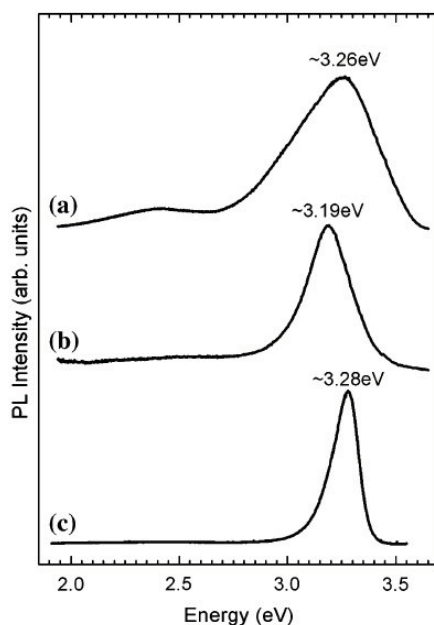
Figure 1.22: Room temperature photoluminescence spectra of ZnO (a) small spherical nanoparticles with ~5 nm in diameter; (b) large spherical nanoparticles with diameter of ~12-14 nm; (c) bulk ZnO [74].

travelling exciton traps. In this way the emission is red shifted compensating the blue shift due to QC. A similar behavior, into a smaller extent, occurs for the nanoparticles with a diameter of 12 nm (1.22 (b)). An excitonic emission dependent on size particle distribution is reported
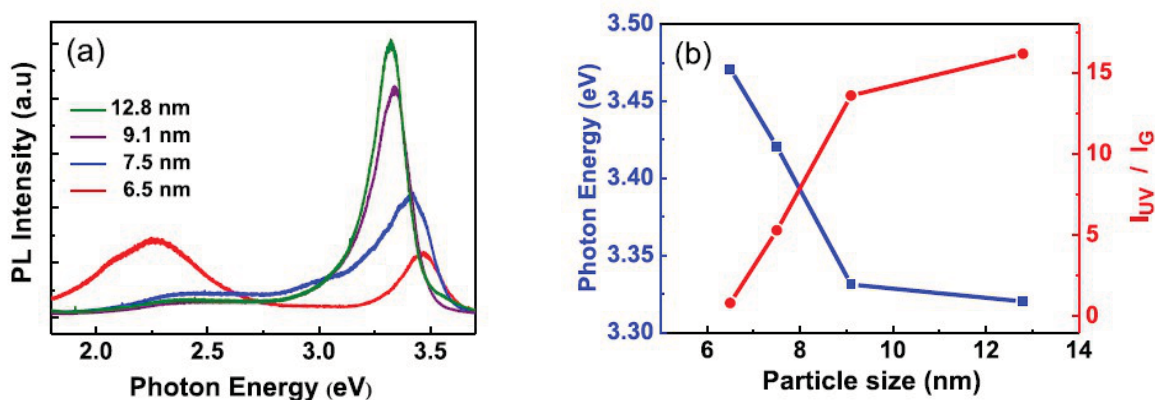
Figure 1.23: (a) PL spectra measured at RT of ZnO nanodots of various average diameters. (b) The blue line represents the PL at RT of ZnO nanoparticles of various average diameters. The red line is the ratio of the steady-state PL intensity ratio of the green (G) vs the UV emissions as a function of the size [75].

in Fig. 1.23 (a) [75]. The ZnO NPs were obtained by a sol-gel methods and shows an excitonic peak position and broadness strongly dependent on nanoparticles size ranging from ~3.3 eV to 3.5 eV with FWHM from 150 to 250 meV varying diameter from 12.8 to 6.5 nm, respectively. In addition, a weak green emission center at 2.26 eV was observed. Previous investigations have

shown that the green luminescence is originating from a free-to-bound recombination between an electron from the conduction band with a hole from a trap level at the particle surface [76]. In addition, this work reports the intensity ratio of the excitonic emission to the green emission decreases with reduced particle size, which implies that the excitonic emission is strong for large particles, whereas the green emission dominates for small particles. According to previous work it can be understood that the increasing surface area to volume ratio for decreasing particle size leads to the predominance of the surface defect-related emission.
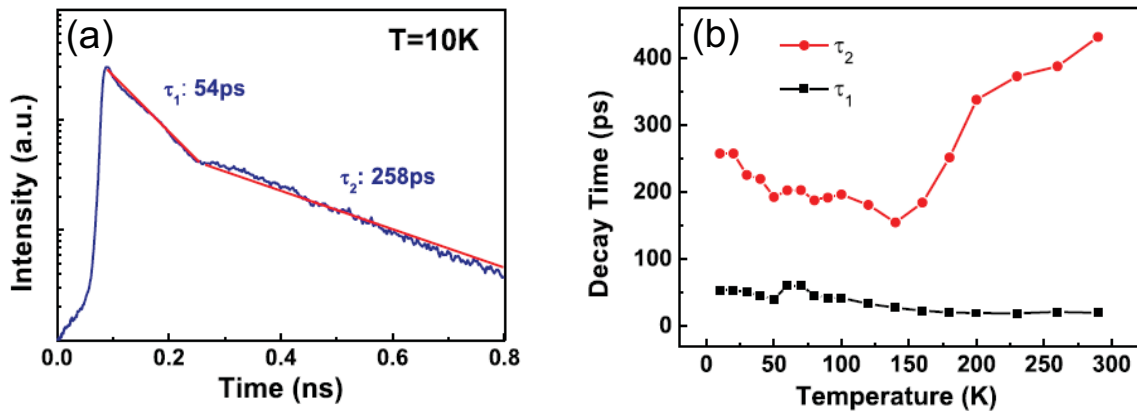
Figure 1.24: (a) Time resolved PL spectra measured at the peak energy. The red curve is the result of fitting using two exponential functions. (b) The two decay times as functions of measured temperature [75].

Free excitons lifetime in defect-free bulk ZnO are characterized by a single exponential decay with a lifetime of the order of nanoseconds [47, 48]. However, many authors have suggested that the exciton lifetime is largely determined by non-radiative recombination due to a high defect density in ZnO nanomaterials [75, 77–80]. Fig. 1.24 (a) displays a typical time evolution of the emission spectrum at 3.371 eV at T=10 K for NPs having d=12.8 nm. The extracted time evolution of the luminescence exhibits a bi-exponential decay with estimated life time τ_1=54 ps and τ_2=258 ps. Both lifetimes are largely shorter than the expected value for bulk ZnO. Many authors have suggested that some of the excitons generated could diffuse and became bound to ionized impurities located at the surfaces of quantum dots which traps the exciton so reducing the luminescence lifetime [75]. The trapping time is expected to depend on the impurity density whereas it is independent of temperature (see Fig. 1.24 (b)), indeed, the fast decay time of about 50 ps is almost independent on the temperature demonstrating that the surface trapping is the predominant decay mechanism. However, the slight increasing of the fast decay time with temperature could be due to an enhanced surface trapping rate related with increasing exciton velocity with temperature. On the other hand, the slow decay should be due to the recombination of confined bound excitons inside the volume of NPs. Above 140 K, the bound excitons at localized ionized states are released as free excitons characterized by a longer lifetime. The enhancement of radiative lifetime on increasing temperature has been also reported for free ex-

citon emission in bulk ZnO [49, 79]. The authors of those works argue that lattice temperature increases the center of mass kinetic energy, therefore changing the Maxwell-Boltzmann distribution of exciton in momentum space. Thereby, the decrease of the electron-hole population which fulfills the momentum conservation requirement for recombination (K=0), and thus the radiative lifetime increases with temperature. It is worth noting that these statements about the exciton dynamics are not conclusively established yet, thus they are currently debated in literature.

1.4   Defect-related Emissions

In addition to UV excitonic emission, ZnO room temperature PL spectra exhibit other emission bands in the visible spectral region which originate from defect emissions [81, 82]. The origin of these emissions has not been conclusively established, and there have been a number of hypotheses proposed for each emission band [81, 82]. However, the present thesis work is focused on a visible emission in the green region (2.2-2.4 eV), which, so far, is the most debated luminescence band [81–83]. Several theoretical studies of defects in ZnO have been reported [84–87] and the calculated energy levels of different defects are summarized in Fig. 1.25. The structure
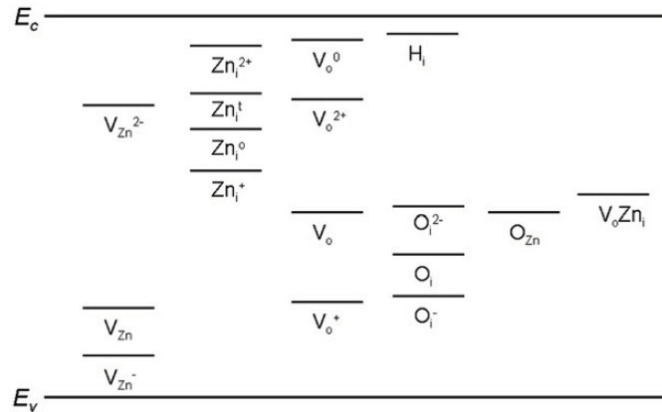
Figure 1.25: Calculated energy levels of different defects in ZnO from different studies in the literature. V_{Zn}, V_{Zn}^- and V_{Zn}^{2-} denote neutral, singly charged, and doubly charged zinc vacancy, respectively. Zn_i^o and Zn_i^t indicate neutral octahedral zinc interstitial and neutral tetrahedral zinc interstitial while Zn_i^+ and Zn_i^{2+} indicate singly charged and doubly charged zinc interstitial. V_O^o and V_O^o denote neutral oxygen vacancy while V_O^+ and V_O^{2+} denote singly charged and doubly charged oxygen vacancy. H_i and O_i represent hydrogen and oxygen interstitial, respectively, while O_{Zn} indicates antisite oxygen and $V_O Zn_i$ denotes a complex of oxygen vacancy and zinc interstitial [75].

of all these defects have been discussed above in the Sec. 1.1.4. It can be clearly observed (see Fig.1.25) that several studies predict different energy levels for the same type of defect, and consequently conclusive identification by a simple comparison of observed peak position and theoretically predicted defect energy level cannot be made. However, a through understanding of the origin of the observed PL bands is mandatory to control the emission capability of ZnO NPs, which is important in view of optoelectronic applications. It is worth noting that the

type of defect formed in ZnO nanomaterials strongly depend on the used synthesis method. If nanomaterials are produced in extreme Zn-rich conditions V_O, Zn_i and Zn_O are present in significant concentrations because of their lowest the formation energy. Instead, V_{Zn}, O_i and O_{Zn} are favored when ZnO NPs are formed under O-rich conditions (see Sec. 1.1.4). Fig. 1.26
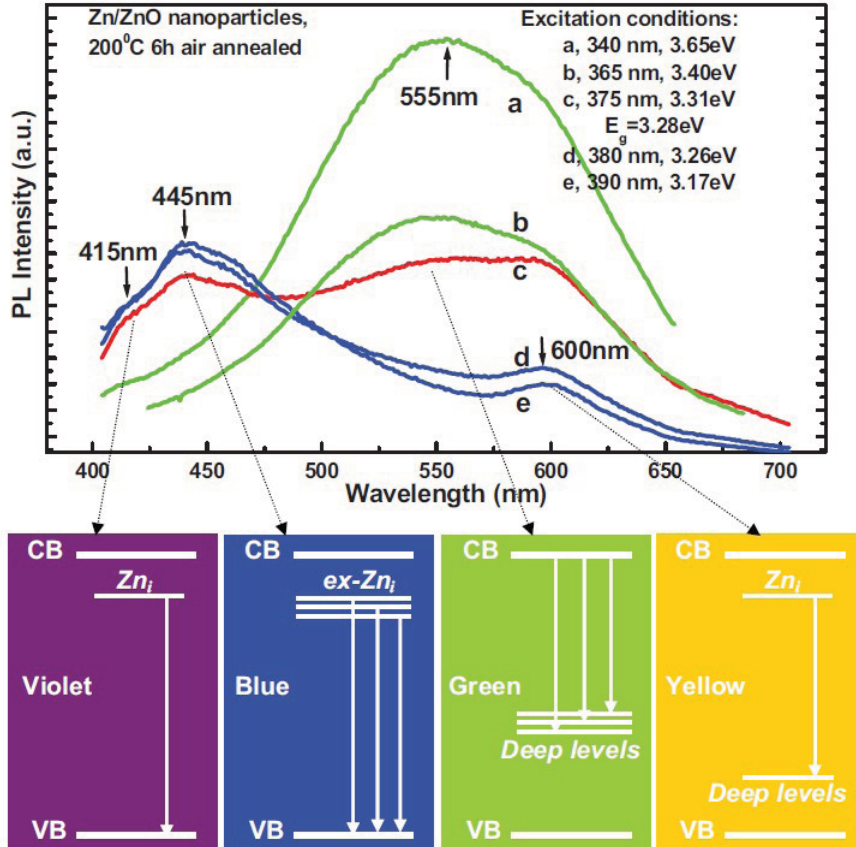
Figure 1.26: Excitation-dependent PL spectra of 200 °C air-annealed nanoparticles, displaying controllable emission of visible emissions. The proposed mechanisms are denoted for violet, blue, green, and yellow emissions, respectively [88].

shows the defect emissions of highly defective ZnO NPs produced by pulsed laser ablation of a zinc plate in water and annealed at 200°C in air. The pictures highlight how the presence of defects formed in highly non-equilibrium conditions has a significant impact on the luminescence of ZnO. Overall, in that work has been shown that the emission features can be varied by changing the excitation wavelength, thus demonstrating the potential application of ZnO NPs in optoelectronic applications and the importance of understand insight the luminescence origin. The most common defect emissions include a yellow-orange band centered at 2.0-2.1 eV, a green emission centered at 2.2-2.4 eV, and a blue PL peaked at 2.7-2.8 eV.

Now, we will discuss about these luminescence band in detail. Among the visible luminescence a broad yellow-orange emission, excited at 3.6-3.8 eV and centered at 2.0-2.1 eV, is commonly observed in samples grown by solution methods [89–93] in O-rich conditions. In contrast with the model of Fig. 1.26, the yellow emission has in general been attributed to defects
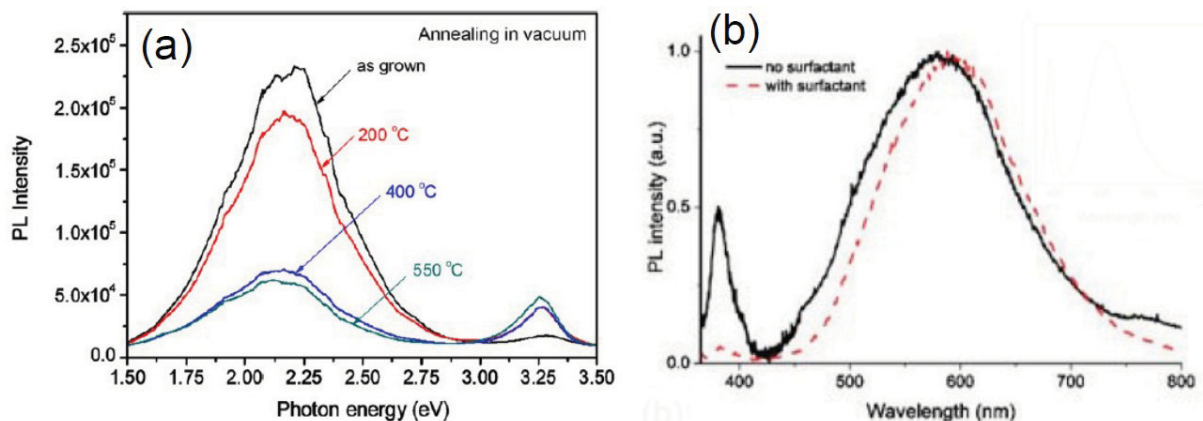
Figure 1.27: (a) The room temperature PL spectra of ZnO nanorod, excited at 3.8 eV, acquired before and after annealing in a vacuum at different temperatures ranging from 200 to 550 °C [89].(b) The comparison of the PL spectra with and without surfactant for ZnO prepared by a chemical method [90].

associated with excess oxygen [89, 90], and presence of hydroxyl groups [92]. The assignment of the emission to interstitial oxygen has been confirmed by the effect induced on it after annealing in a reducing environment. In fact, annealing of hydrothermally grown ZnO nanorods in a vacuum typically results in a reduction of yellow defect emission band, as well as the improvement of UV-to-visible emission ratio [90,92,93] as shown in Fig. 1.27 (a). This effect is expected for O_i defects because, as said before (Sec. 1.1.4), they become mobile above 340 K ($\sim$70 °C) and tend to go out from the NPs exposed to a vacuum. The visible-to-UV intensity ratio is commonly used to evaluate the sample quality for ZnO nanostructures because it depicts the concentration of defects in ZnO. Fig. 1.27 (b) shows the effect of surfactant molecules during the chemical synthesis of ZnO nanoparticles, which prevent the oxygen molecules to enter the NPs.
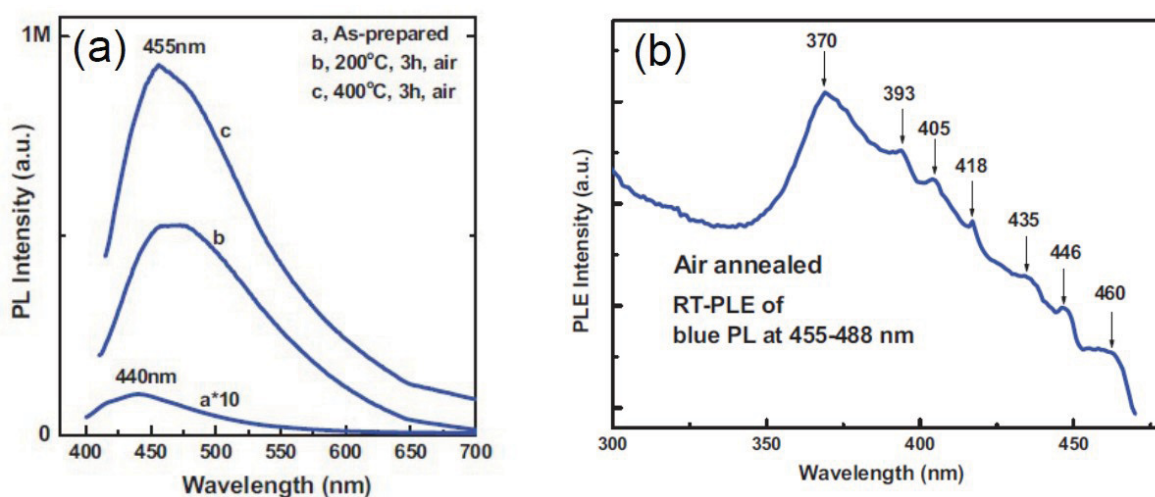
Figure 1.28: (a) Blue emissions of ZnO NPs synthsized by pulsed laser ablation of zinc plate in SDS aqueous solution and changing with annealing in air atmosphere. (b) of the blue emission after air annealing [88].

A Blue band, excited in the range of 2.7-4.0 eV and peaked around 2.8 eV, is commonly observed in ZnO NPs produced by synthesis methods in zinc-rich conditions like pulsed laser ablation (PLAL) of a zinc plate in SDS aqueous solution [37, 88, 94]. Fig. 1.28 (a) presents the typical blue PL of these ZnO NPs and its evolution with annealing in air atmosphere, whereas Fig. 1.28 (b) shows the excitation spectrum of this emission. By the thermal annealing the peak position of the blue emissions slightly redshifts from 440 to 455 nm and its amplitude increases of about 100 times. XRD (X ray diffraction) spectra and HRTEM (high resolution TEM) images observed by Zeng et al. evidence that PLAL produces Zn/ZnO core-shell NPs which after thermal annealing in air become defective ZnO NPs. Basing on EPR (electronic paramagnetic resonance) measurements they suggest that the defect responsible of this blue emission is Zn_i which lies at the interface between a zinc metal core and ZnO shell of ZnO core-shell NPs. According with this assignment, excitation spectrum exhibits a preferential excitation peak at energy near band-gap (3.35 eV) which is slightly smaller than Eg=3.38 eV. Indeed, as discussed in the Sec. 1.1.4, it has been calculated that Zn_i is a shallow donors for ZnO, thus it is expected it creates an energy level near the CB. Besides, small peaks overlapping on the dropping tail could indicate localized Zn_i states. The enhancement of blue band induced by thermal annealing in air has been associated with the oxidation of Zn cores, which quenches the excited states at the metal-semiconductor interfaces [88], however, more research is needed to confirm this attribution.

Green emission is the most commonly observed and also the most controversial visible emission band in ZnO. Many different hypotheses have been proposed to explain its origin, but there is still no consensus [81–83]. It should also be noted that the peak position of green emission is different from one study to another (2.2-2.4 eV) [81]. In some cases, green emission peaks at different positions are assigned to different defects [83]. The proposed hypotheses on the origin of this green emission include zinc vacancies, oxygen antisites, oxygen vacancies and surface defects [10, 81, 88, 95–100]. For example, oxygen antisites were assumed to explain a PL at 2.4 eV in ZnO films based on the rise of the green PL after annealing in O_2 [99].

Zinc vacancies were related to green PL at 2.3 eV in bulk ZnO produced by hydrothermal method comparing the spectra for the samples with different Zn and O implantations [98]. Fig. 1.29 shows the PL spectra from the implanted samples after a thermal annealing at 600 °C in oxygen atmosphere. In order to eliminate the possible effects caused by implantation damage, the PL intensity was normalized to the free exciton PL. Since only the free excitons PL and the green PL appear at room temperature (RT), the relative intensity of the defect related emission provides indication of the defect concentration involved in the defect emission. As shown in Fig. 1.29 (a), the band at 2.3 eV is significantly suppressed after Zn implantations. In contrast with the O implantations having a smaller effect on the green emission, authors infer that during annealing the additional Zn atoms in the samples suppress the emitting defects more effectively that additional O atoms. Therefore, they conclude that V_{Zn} is probably involved in the green emission.

Anyway, the most commonly attribution for the green PL remains the oxygen vacancy based
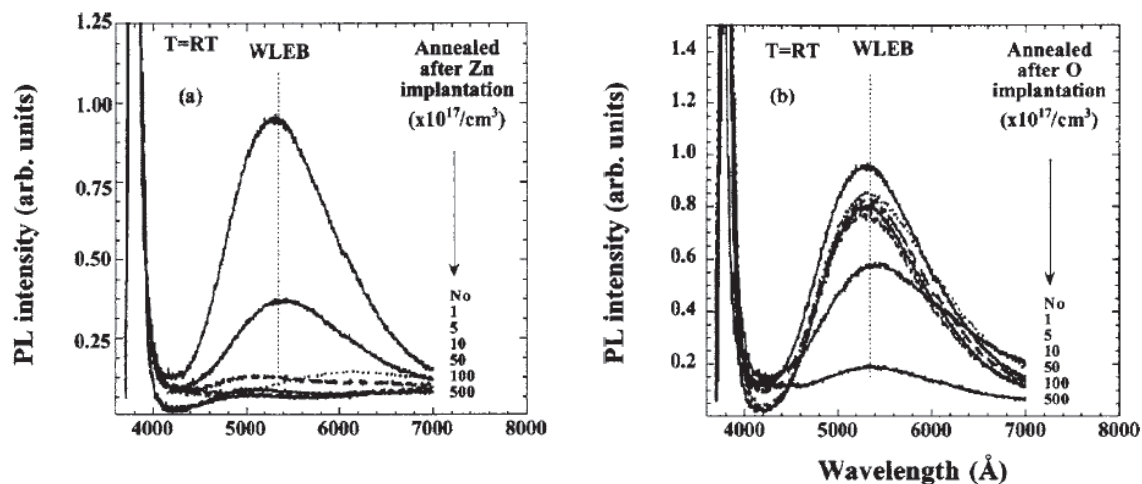
Figure 1.29: PL spectra of the Zn- (a) and O-implanted (b) ZnO samples after thermal annealing in oxygen gas, measured at Room temperature (RT), the excitation energy is 3.54 eV [98].

on its correlation with the structural properties [88, 95–97, 101, 102]. Some works [103, 104] attribute the green band at oxygen vacancies lying at the surface of ZnO NPs. He et al. [104] studied ZnO NPs synthesized by PLAL adding surfactant molecule or changing the pH of water. They investigated structural and emission properties of ZnO NPs using XRD, HRTEM and steady-state luminescence. The absorption and photoluminescence spectra of ZnO produced in the different media are presented in Fig. 1.30. It is possible to observe that the emission
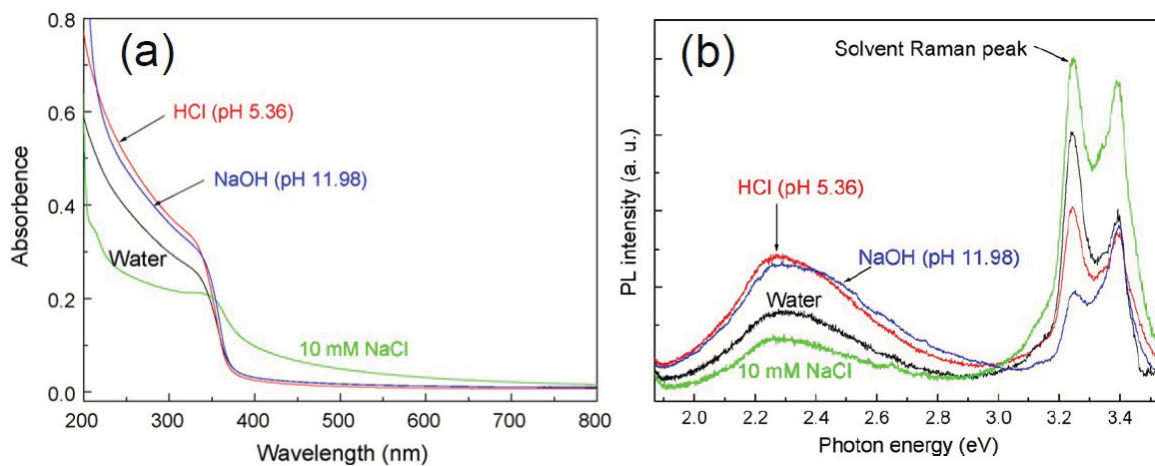
Figure 1.30: Absorption spectra (a) and Photoluminescence spectra (b) of ZnO nanoparticles prepared by PLAL of Zn in deionized water and aqueous solutions. The spectra were excited by an excitation energy of 3.65 eV. The peak at 3.25 eV can be attributed to a solvent Raman peak at 0.40 eV (3240 cm^{-1}, corresponding to an OH-vibration) [104].

band peaked at 2.3 eV, and excited at 3.65 eV, is intense compared to the exciton emission intensity when ZnO is produced in acidic or basic media, while the green emission intensity was somewhat weaker than the exciton emission intensity when ZnO was produced in salt solution or deionized water. They suppose that the green emission at 2.30 eV originated from oxygen

vacancies because nanoparticles prepared by PLAL were grown under insufficient oxidation conditions and infer that oxygen vacancies lying at the surface of ZnO NPs because of the pH effect on the green band intensity. However, this claim contrasts with other experimental data showing a change in the ZnO raman spectrum which can hardly be related to a reduction of the concentration of surface defects, rather than bulk defects. In the Sec. 1.1.2 it has been observed that $A_1(LO)$ at 575 cm^{-1} mode is almost negligible in the spectrum of bulk ZnO materials due to a cancelation between the deformation and Frohlich contributions to the LO phonon scattering cross section. However, oxygen vacancies or zinc interstitials or their complexes are assumed to enhance the $A_1(LO)$ mode [34, 35, 105]. In ZnO films fabricated under different O_2 pressures, the Raman peak at 579 cm^{-1} is reported to decrease with the increase of O_2 pressure [105]. For ZnO single crystals, P ions implantation is reported to increase oxygen vacancies and to enhance the Raman peak at 575 cm^{-1} [34]. In fact, phosphorus is expected to take place to an oxygen site creating a defect similar in an oxygen vacancies in ZnO.
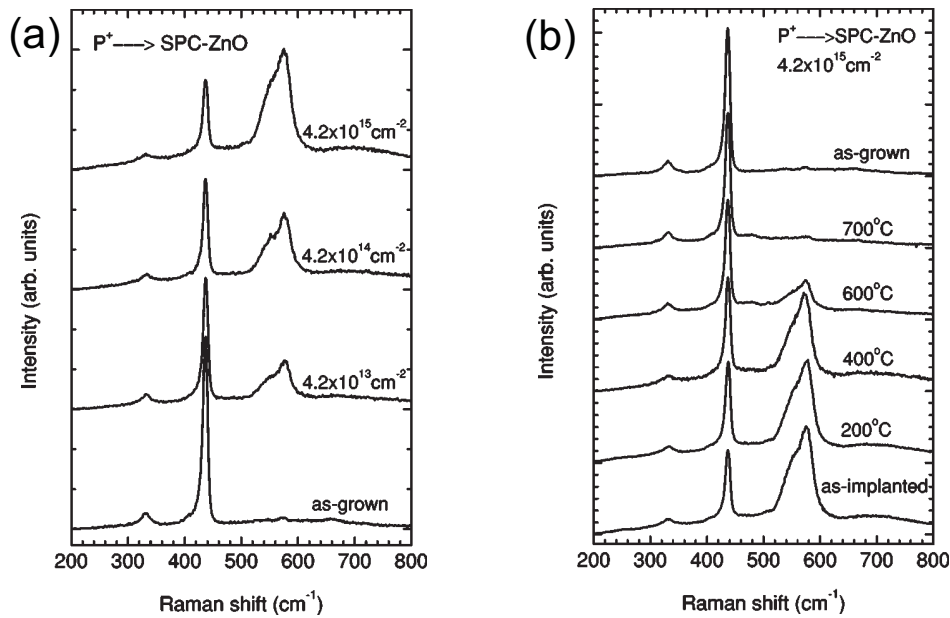
Figure 1.31: (a) Raman scattering spectra measured for ZnO samples before and after P$^+$ implantation. (b) Annealing effect on the Raman spectra measured for the P$^+$ implanted ZnO with dose of 4.23×10^{15} cm^{-2} [34].

Fig. 1.31 (a) shows the Raman spectra for the as-grown and P$^+$ implanted samples. The peak at 575 cm^{-1} increasingly grows with an increasing dose and also becomes significantly broader (500-620 cm^{-1}). Authors precise that this broad peak is not related to the implanted phosphorus impurities because they observed the same peak in the other ion-implanted in ZnO. The broadband around 575 cm^{-1} increases systematically with ion implantation dose and the annealing effect on the Raman scattering, shown in Fig. 1.31 (b), supports the claim that it should be a defect-induced band. In fact, upon annealing at temperatures above 400 °C, the A_1 mode rapidly decreases until it reaches the same level as that of the unimplanted sample at 700 °C, while the E_2 peak gradually recovers.
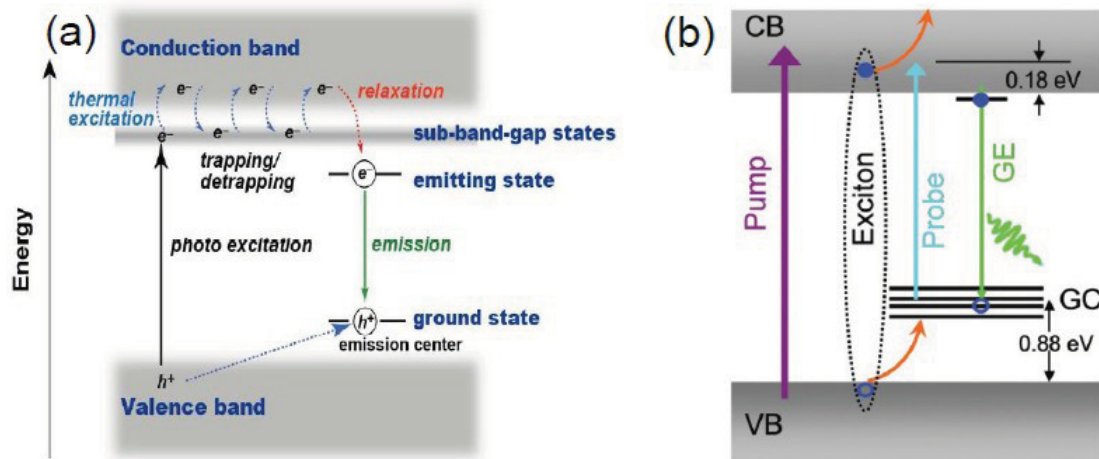
Figure 1.32: (a) A model of the below-band-gap photoexcitation and the subsequent thermal excitation, trapping/detrapping and relaxation processes that are responsible for the green PL emission [106]. (b) A schematic of the proposed excitonic hole trapping and recombination mechanisms at the green emission centers (GC) [36].

Several mechanisms for the ZnO visible emission have been suggested so far. One of this is the recombination of a shallowly trapped electron with a hole in a deep trap [36, 101], and another is the recombination of an electron in singly occupied oxygen vacancies with a photo-generated hole in the valence band [80, 102, 106]. Kodama and Uchino [106] studied the effect of thermal annealing in reducing atmosphere on time resolved luminescence of ZnO nanoparticles having an average size of $\sim$200 nm. They observed a PLE peaked below the optical band-gap, a triple exponential decay law depending both on temperature and on excitation wavelength. By these finding they suggested an emission model in which the photoexcited electrons in the sub-band-gap states (Zn_i) can be transferred to the emitting state via thermally activated trapping/detrapping processes. Instead, Li et al. [36] observed an increase of the green PL after thermal annealing in air at 600 °C on vertical aligned ZnO nanowire. Based on optical spectroscopy analysis they suggest a recombination mechanism involving free electrons in CB with double-defect centres ($V_O + V_{Zn}$) above the VB. When a free exciton meets the V_{Zn}^O, its hole can be captured while its electron is excited to higher energy levels in the CB, taking with it the excess energy (see Fig. 1.32 (b)). These electrons in the higher energy levels subsequently relax back to the CB via phonon emission yielding the green emission. The latter strongly contrast with the previously discussed model as well as the other here not reported. Therefore, we highlight that the defect centers responsible of the green emission remains poorly understood yet, overall, it are not yet consolidated the attributions for each visible emissions to the related native defect.

1.5 Applications for ZnO Nanomaterials

Because of its large variety of chemical and physical properties ZnO is a promising material for technological applications [6, 10–12, 70, 81]. These properties include good transparency, high electron mobility, wide band-gap, strong room-temperature luminescence, high piezoelectric constants, biocompatibility, high thermal conductivity and radiation hardness [67]. Moreover ZnO materials and nanomaterials can be produced by relatively cheaper techniques compared to other semiconductor with similar properties currently used.

1.5.1 Current Applications

To date a large fraction of the ZnO currently produced is used in the rubber and concrete industries [6, 12]. For instance, ZnO is an important additive to the rubber of car tyres. Since it has a high thermal conductivity increases the thermal conductivity of tires, which is crucial to dissipate the heat produced by the deformation when the tyre rolls along the street. Other applications concern medicine or cosmetics, cigarettes filters, pigments, or as an additive to human and animal food. Furthermore, ZnO due to its wide band-gap, is used as an UV-blocker in lotions and as transparent conducting oxide (TCO) in front contacts for solar cells [6, 12].

1.5.2 Forthcoming Applications

Gas Sensors

ZnO nanoparticles due to their high surface volume ratio are of interest for applications in different types of sensors, including gas sensors and biomedical applications where optical sensing [109] and electrical sensing [110] has been reported. Sensing for different gases (oxygen, NO_2, etc.) has been reported [10, 111]. If sensing is based on the change of conductivity upon gas adsorption/desorption they could be composed by FETs or simple two metal contacts across the nanostructure network [111]. Recent experiments have reported that the charge transport in ZnO nanomaterials strongly depends on the environment and in particular on the oxygen content [10]. ZnO gas sensors sensitivity was proposed to be dependent on the concentration of defects such as oxygen vacancies, surface oxygen species and zinc interstitial, which were hypothesized to play a role in NO_2 gas adsorption [111]. Consequently, the control of defects during material synthesis and the related study of the role of native defects in the sensing mechanism and surface adsorption of different molecules is mandatory to obtain a gas sensor with required features.

Optoelectronic Devices

ZnO has a high exciton binding energy of 60 meV, much larger than the thermal energy at room temperature (26 meV). Thus, the exciton in ZnO could be stable even at room temperature, which facilitates efficient excitonic recombination. In comparison with the currently used semiconductors, like GaN, ZnO has a larger exciton binding energy (21 meV for GaN) and can be
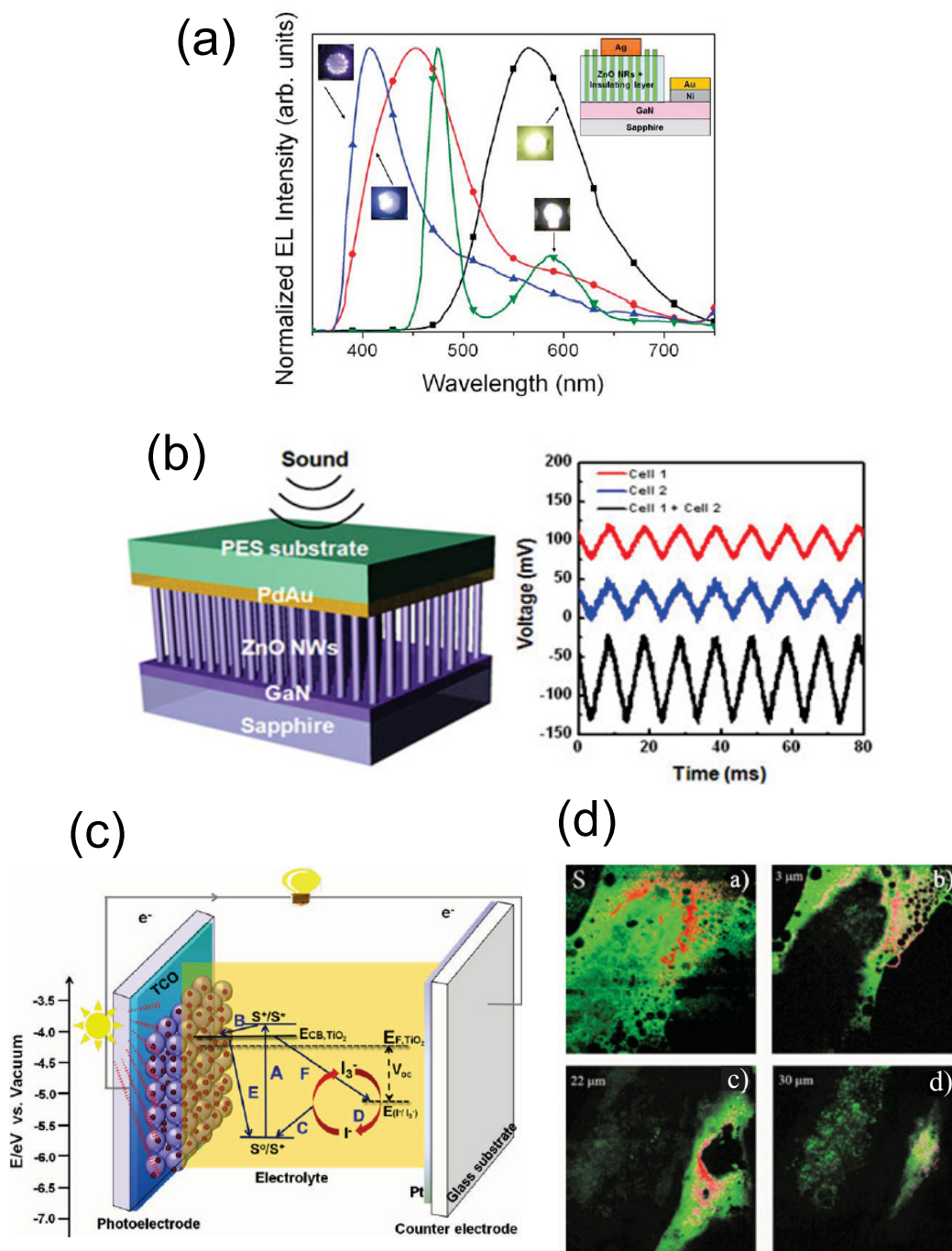
Figure 1.33: (a) Emission spectra and corresponding photos of p-GaN/ZnO NRs LEDs. Violet emission corresponds to p-GaN/Ce:ZnO LEDs, blue and yellow emission comes from p-GaN/ZnO LEDs under reverse bias, and white emission corresponds to p-GaN/ZnO LEDs. The inset shows the device diagram [82].(b) Schematic of a sound-driven piezoelectric nanogenerator based on zinc oxide nanowires and its power-generating performance. (c) The working principle of dye-sensitized solar cell [107]. (d) Illustration of bioimaging application in vivo for ZnO NPs of human skin in vivo (green) and ZnO NPs distribution (red) 4 h after its topical application. En face optical sections of the skin are displayed from (a-d) at depths of 0, 14, 30 and 48 μm from the skin surface designed S, respectively [108].

produced by relatively cheap methods such as evaporation, sputtering and laser ablation in a variety of forms including powder, nanoparticles, nanorods, thin films. For these reasons ZnO have a great potential to replace GaN as the next-generation white or blue light emitting diode material [5, 12]. In recent years, there have been reported numerous ZnO nanostructure-based LEDs both for homojunctions and for heterojunctions with different materials [82]. Since is still a technical challenge to achieve reliable and device quality p-type ZnO materials, so far the most part of device are heterojunctions which make use of other materials as p-type semiconductor. A representative heterojunction device and the examples of different emission spectra peaked at different energy depending on bias and doping is shown in Fig. 1.33 (a). Intense interest in the study of lasing in ZnO nanostructures has started with the report of optically excited room temperature UV lasing from ZnO nanowires [112]. Then, optically pumped lasing has since been reported in a number of different morphologies of ZnO [113]. Nanowire UV lasers and laser arrays could serve as miniaturized light sources for optical interconnections, quantum computing, the microanalysis for biochemical and environmental applications toward the integration of lab-on-a-chip.

Piezoelectric Devices

Its high piezoelectric constant, ZnO is promising for piezoelectric systems [114]. Examples are surface-acoustic wave (SAW) devices and piezoelectric sensors [6, 62, 114]. In an SAW device, a mechanical deformation is induced by electrical contact fingers in a nearly isolating, highly oriented (0001) ZnO films. Emerging field for SAW devices are sensors in automotive applications such as pressure sensors, medical applications, and other industrial applications. Advantages of acoustic wave sensors are low costs, ruggedness, and a high sensitivity, also SAW sensors do not require a power source. Recently, researchers have demonstrated that it is possible to use sound as a power source to drive nanogenerators based on piezoelectric ZnO nanowires. The sound wave was used to vibrate the top contact electrode (see Fig. 1.33 (b)), which generates electric potential through the vertically well-aligned zinc oxide nanowires. When sound with an intensity of $\sim$100 dB was applied to the nanogenerator, an AC output voltage of about 50 mV was obtained from the nanogenerator [114]. Sound power could be used for various novel applications including cellular phones that can be charged during conversations and sound-insulating walls near highways that generate electricity from the sound of passing vehicles.

Photovoltaics

ZnO is a material of considerable interest for applications in low cost photovoltaics, such as dye-sensitized solar cells (DSSC) and hybrid polymer-inorganic nanostructure solar cells. The working principle of a DSSC is shown in Fig. 1.33 (c). Upon sunlight irradiation, the dye molecules become photo-excited and inject the electron into the conduction band of a wide band-gap semiconductor (TiO_2 or ZnO). The oxidized dye is subsequently regenerated by electron transfer from the I^- in the electrolyte and forms I_3^-, while the I^- is regenerated by the

reduction of I_3^- at the Pt counter electrode. The injected electron travels through the semiconductor nanoparticles toward the transparent conductive oxide (TCO) substrate and then to the external circuit. During these processes, electrons from the conduction band of nanoparticles recombine with the oxidized dye or electron acceptor species in the electrolyte solution. The voltage generated under illumination corresponds to the difference between the Fermi level of semiconductor and the redox potential of I^-/I_3^-. ZnO nanomaterials have attracted a large interest in DSSC applications because have higher electron mobility compared to the commonly used TiO_2 [81]. However, to date ZnO DSSCs still have lower efficiencies (3%) with respect to TiO_2 (13%) [107], which can be partly attributed to instability of ZnO in acidic solutions producing the formation of Zn ion-dye complexes [81].

Bioimaging

Semiconductor QDs are among the most promising emerging fluorescent labels for biological imaging. However, the traditional QDs, like CdSe and CdTe, have encountered potential safety concerns in vivo [115]. Luminescent ZnO NPs, due to their special advantages, such as bright emission, low cost, and good biocompatibility, were reported to be a better candidate in biological applications [10]. Despite these advances there are still some obstacle to overcome for using ZnO NPs in bioimaging applications, which are related to their optical properties. First, the luminescent ZnO NPs have a relatively broad emission band, resulting in the overlap of their fluorescence spectra with the biological autofluorescence. Secondly, ZnO have a wide band-gap of 3.37 eV at room temperature, thus locates in the UV region, requiring UV light to excite ZnO luminescence. However, UV light is not suitable for deep tissue imaging in vivo due to the reduced penetration depth (several millimeters in the animal skin), absorption, and scattering of optical signals. In addition, UV light is harmful to cells, tissues, and live animals [116]. To overcome this problems recently has been used multi-photon fluorescence which is characterized by deeper imaging inside tissues and the reduced photo-toxicity of near infrared light. Nevertheless, this technique has not succeeded yet, because an efficient two-photon excited luminescence is correlated with two-photon resonance that is limited to specific wavelengths. For this reasons, a new frontier for ZnO bioimaging applications is based on the (second harmonic generation) SHG technique, which take advantage of noncentrosymmetric structure in ZnO NPs [10]. Thereby, when two photons interact with the asymmetric material in a scattering process produce a single photon at twice the energy which can excite ZnO NPs. Fig. 1.33 (d) shows the in vivo images of human skin treated by the ZnO NPs. The signals from ZnO NPs (red luminescence) can be clearly observed on the skin autofluorescence background, (green luminescence) especially pronounced on the top-most layers of the skin, and the ZnO NPs localization in the skin folds and dermatoglyph (14-30 μm). This result confirmed the potential prospect of ZnO NPs for deep imaging inside tissues by using SHG.

Photocatalysis

Another application of ZnO NPs is photocatalysis. Indeed, ZnO NPs can actually exhibit high photocatalytic efficiency for dye degradation which is comparable with the most studied TiO_2 nanomaterials [116]. However, ZnO is less environmentally stable and it can be susceptible to photocorrosion. Nevertheless, its potentially high efficiency makes it interesting for photocatalytic studies which have been shown photocatalitic efficiency strongly dependent on its morphology and properties.

Chapter 2

Synthesis Methods: Pulsed Laser Ablation in Liquid

The synthesis of nanoparticles (NPs) has received considerable attention in view of the potential for materials with novel properties related to shape, dimensions and composition. In fact, nanoscale materials posses several unique properties such as large surface area, unusual adsorptive properties, surface defects, and fast diffusivities. For these reasons, in order to obtain NPs and nanostructures with specific properties useful in view of specific applications, it is mandatory to improve the control on the synthesis methods. This chapter briefly describes various techniques that are used in the growth of nanostructures, and in particular ZnO NPs. These methods include, sputtering, molecular beam epitaxy and electron beam deposition hydrothermal methods, pulsed laser ablation in liquid and pulsed laser deposition techniques. In particular, we focus our attention on PLAL, which is the technique used to synthesized ZnO NPs in this work. We show the physical processes involved during the synthesis and the effect of parameters on the ablation product.

2.1 Methods for the Growth of Nanostructures

Nanostructured materials are synthesized using a combination of approaches, for example melting and solidification process followed by thermodynamical treatments, or solution/vacuum deposition. There are basically two broad areas of synthesis techniques for nanostructured materials: chemical and physical methods [117–119].

2.1.1 Chemical Methods

The primary advantage of chemical processes with respect to other methods is the good chemical homogeneity, as such synthesis offer mixing at the molecular level. Nevertheless, in some preparations, the chemistry is complex and contamination can also result from the byproducts generated by side reactions in the chemical process. This should be minimized or avoided to

obtain desirable properties in the final product. Moreover, many chemical processes are much expensive thus are not available for an economical production.

Precipitation of a solid from a solution is a common technique for the synthesis of NPs. The general procedure involves reactions in the aqueous or non-aqueous solutions containing the soluble or suspended salts [120]. Once the solution becomes super saturated with the product, due to homogeneous or heterogeneous nucleation the precipitate is formed. If the formation of stable material contains foreign species, it is referred as heterogeneous nucleation; otherwise it is referred as homogeneous nucleation. The growth of the nuclei after formation usually proceeds by diffusion, in which case concentration gradients and reaction temperatures are very important in determining the growth rate of particles. For instance, to produce NPs with a narrow size distribution, all the nuclei must be formed at almost the same time and the subsequent growth must occur without further agglomeration of particles.

The hydrothermal technique is the most used method to obtain nanocrystalline inorganic materials. By this technique it is possible to obtain mono-dispersed and highly homogeneous NPs, but also nano-hybrid and nanocomposite materials. Hydrothermal processing consists of heterogeneous reaction in presence of aqueous solvents under high pressure and temperature conditions to dissolve and recrystallize (recover) materials that are relatively insoluble under ordinary conditions. This synthesis method uses the solubility in water of almost all inorganic substances at elevated temperature and pressures, and subsequent crystallization of the dissolved material from the fluid. Water at elevated temperatures plays an essential role in the precursor material transformation. The pressure, temperature, precursor concentration and time of reaction are the principal parameters in hydrothermal processing.

2.1.2 Physical Methods

Several physical methods are currently in use for the synthesis of NPs and in particular, ZnO NPs. The first and the most widely used technique involves the synthesis of single-phase metals and ceramic oxides by the inert gas evaporation technique [120]. The generation of NPs proceeds by evaporation and subsequent gas condensation from a precursor material, either a single metal or a compound, in a gas maintained at a low pressure, usually below 1 atm. The evaporated atoms or molecules collide with gas atoms or molecules in the vicinity of a cold-powder collection surface, in this way undergo a homogeneous condensation thus forming clusters. Once formed, the clusters must be removed from the region of deposition to prevent further aggregation and coalescence. These clusters are readily removed from the gas condensation chamber either by natural convection of the gas or by forced gas flow.

Sputtering is another technique used to produce NPs as well as thin films [120]. This method involves the ejection of atoms or clusters of designated materials which are subjected to an accelerated and highly focused beam of inert gas such as argon or helium. Sputtering provides films characterized by great adhesion and homogeneity and permits better control of film thickness. During sputtering process occur the creation of gas plasma from an inert gas such as argon by applying voltage between a cathode and anode. The target holder is used as cathode and the

anode is the substrate holder. Source material is subjected to intense bombardment by ions which lead to an ejection of particles from the surface of the target, then they diffuse away depositing a thin film onto the substrate.

Pulsed laser ablation in liquid had been identified as a versatile technique for the preparation of nanostructures, mainly nanorods and quantum dots [37,121–126]. By definition, laser ablation is the ejection of macroscopic amounts of materials from the surface of a solid usually induced by the interaction of short (50 fs to 10 ns), intense (10^6 to 10^{14} W/cm^2) laser pulses with the surface. In laser ablation in liquid the pulsed laser beam is focused on a bulk target immersed in a liquid medium. Since the great advantages on the use of PLAL for the production of NPs we will dedicate to this technique a whole paragraph below.

2.2   Pulsed Laser Ablation in Liquids (PLAL)

PLAL has attracted much attention during the last two decades for the simplicity of the experimental setup, versatility and low cost [121–125]. Moreover, PLAL is a unique approach for the synthesis of a variety of nanomaterials in a variety of liquid solutions [125]. The process proceeds in one step and results in immediate formation of NPs in the liquid in which the target is immersed. The main feature of the process is that ideally the liquid contains only NPs made of the target material and the liquid. There are no counter-ions or residuals of reducing agents left in the solution, and no waste is produced. For this reason PLAL can be considered as a green method of NP synthesis, which is an alternative to chemical methods.

2.2.1   Experimental Setup

The experimental setup for laser ablation of solids in a liquid environment may vary from one research group to another, though their common features are the same. Laser radiation is focused onto a solid target immersed in a liquid which is continuously moved via either a rotator plate or step motor to avoid that the laser beam always hits the same area thus forming craters. Fig. 2.1 (a) shows a generalized experimental setup of laser ablation of solids in a liquid environment. It is assumed that the liquid is transparent at the laser wavelength, otherwise the focalization of the beam would be problematic due to absorption of laser radiation in it. The use of volatile liquids, such as acetone, ethanol, etc., requires a covering of the liquid with a window that is transparent at the laser wavelength. Laser energy per unit area provided to the target during PLAL (called fluence) strongly depends on the focusing of the laser beam that must pass trough a liquid layer. Then, one needs to take into account the change of the focal length of the lens due to refraction or even self-focusing typically for picoseconds (ps) and femtosecond (fs) lasers with high intensity [124, 127, 128]. Considering the refraction of a focused linear beam, the focal length will increase following this

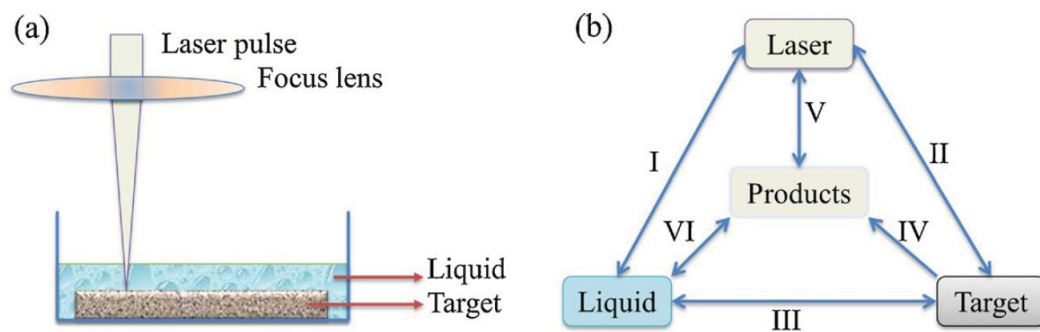$$l\left(1 - \frac{f}{\sqrt{n^2 f^2 + (n^2-1)r^2}}\right), \tag{2.1}$$

Figure 2.1: (a) Schematic diagram of the experimental setup of PLAL. (b) A combinatorial library of constituents and interactions in PLAL: (I) laser–liquid interaction; (II) laser ablation of the target; (III) liquid–hot target interaction; (IV) generation of products from the target; (V) laser–products interaction; (VI) liquid–products interaction [124].

where f is the focal length of the focusing lens in air, l is the liquid thickness, n is the refractive index of the liquid, and r is the radius of unfocused laser beam. For r≪f, the formula can be simplified to

$$\Delta f = l \left(1 - \frac{1}{n} \right) . \tag{2.2}$$

Moving the lens of Δf away from the target surface it is possible to achieve desired focusing, thereby, one can provide the maximum fluence to the target. However, there is a fluence threshold that must not be exceeded in order to avoid nonlinear optical effects like multiphoton absorptions or self focusing from the liquid with consequent reduction of the energy transferred to the target and of the focal length. Self-focusing is also believed to play an important role in white continuum generation by the laser beam propagation [124]; in fact, this is a limiting factor of using a femtosecond laser beam, specially with pulse durations less than 60 fs. This continuum consumes a significant part of laser energy and reduces the efficiency of interaction with target. All non linear effects increase when the accumulation of NPs in the liquid beam path enhances the interaction between laser beam and NPs.

2.2.2   Basic Mechanisms

Laser ablation induces physical modification of matter, due to the fragmentation from bulk into NPs and subsequent chemical modifications due to reactions with the liquid which often produces new compounds and phases. Hence, during PLAL several physical and chemical processes occur. Fig. 2.1 (b) depicts the constituents of laser pulses, liquid media, solid targets and the ablated products may interact with each other. In order to discuss basic mechanisms involved during PLAL it is useful to describe the temporal sequence of the ablation stages (Fig. 2.2). In the following, we set the time t=0 as the instant when the laser pulse hits the target and we assume that the fluence is above the ablation threshold. First of all, the laser pulse must pass through a layer of liquid before reaching the target. To avoid non linear effect, as multiphoton
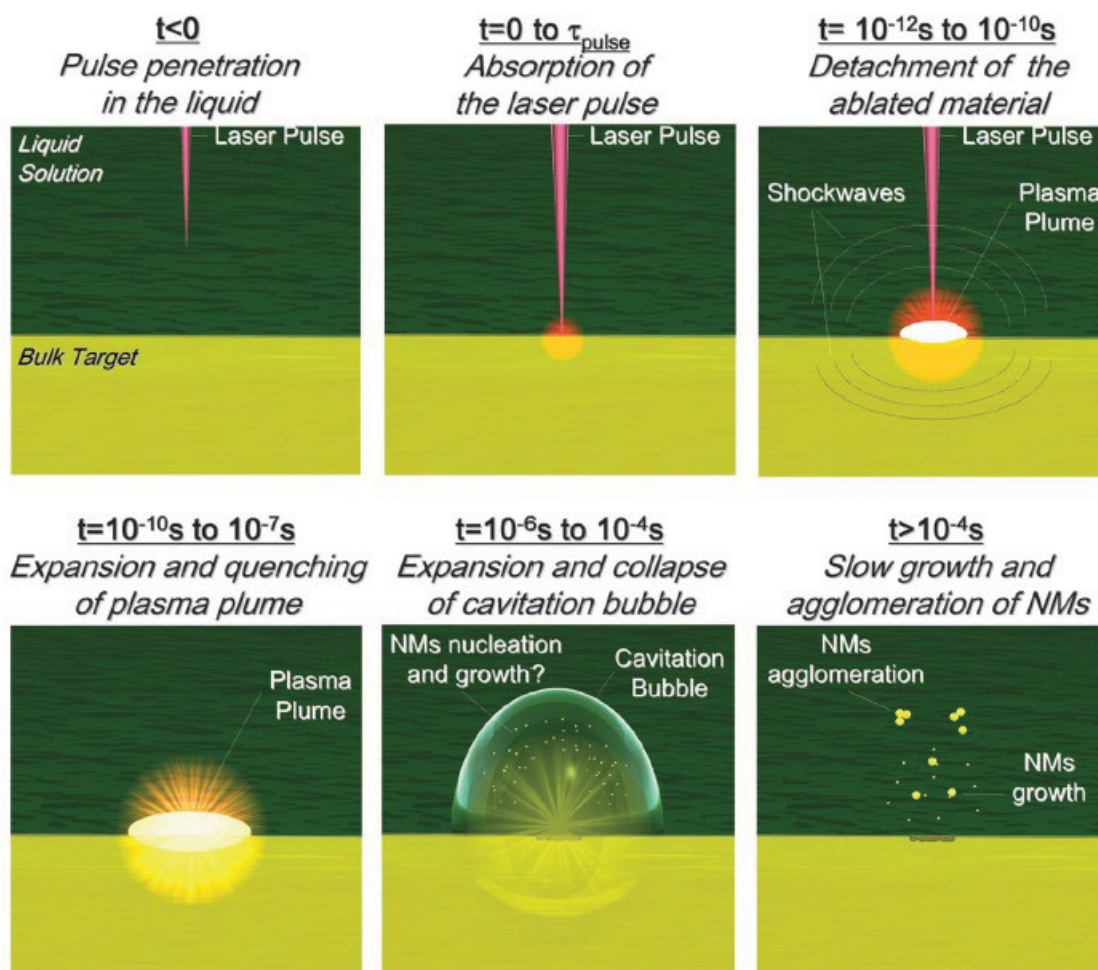
Figure 2.2: Sketch of the timeline of PLAL with ns pulses. Nucleation and growth of NPs are hypothesized in the 10^{-6}-10^{-4} s time range, although precise information is lacking [125].

absorptions and self-focusing, with a pulse duration of picoseconds (ps) or longer the laser is needed to operate in a defocused geometry [129]; whereas with pulse duration of femtoseconds (fs), relevant nonlinear optical effects like self-focusing are observed at fluences required for laser ablation, therefore also the thickness of the liquid layer must be reduced to maintain the defocusing conditions [130].

From t = 0 s to pulse duration, the laser pulse hits the target producing linear and nonlinear absorption processes caused by the high photon density [124, 126, 131]. The thickness of the target in which light is absorbed is of the order of the material skin depth which depends on the value of the absorption constant at the used wavelength [124, 126, 132]. At the fluence used in PLAL, pulses of less than ps lead preferentially to instantaneous multiphoton absorption processes and to localized photoinduced ionization [125, 126]. In the case of an ultrashort laser pulse, the lattice temperature remains unchanged during the absorption of the pulse and the pulse energy is mainly deposited in a thin layer due to photon-electron interaction process. However, for pulse duration longer than 10^{-12} s, due to the electron-lattice thermalization,

the electron kinetic energy can be released to the lattice [132] leading thermal processes like thermionic emission, vaporization, boiling and melting. As a consequence a larger volume than that defined by the spot area and the target skin depth is affected [132]. This effect will be discussed in more detail subsequently.

From 10^{-12} s to 10^{-10} s, consequently to multiphoton absorption and direct photoionization, because of high temperature and high pressure formed in the laser-affected volume, the detachment of matter from the target occurs. Three kinds of thermal processes may lead to material detachment from a laser-irradiated target: vaporization, normal boiling and "explosive boiling" [124, 125, 132]. Explosive boiling occurs when solid matter is rapidly superheated up to the thermodynamic critical temperature, at which the decomposition in vapor and liquid phase in the irradiated material occurs by homogeneous nucleation [131]. When energy is transferred to the target by ps and fs pulses, however, other processes far from thermodynamic equilibrium can occur such as photo-ionization which can induce the "coulombic explosion". In fact, photoionization of the metal target by a monophotonic or biphotonic process, could cause detachment of material from the target by spontaneous fission due to charge repulsion, this detachment can occur in 100 ps [133]. Simultaneously to the ablation process, the recoil pressure of the ablated material drives a shockwave propagating into the target and a second specular shockwave counterpropagating into the liquid solution, with supersonic velocity. A shockwave is a pressure wave travelling in a medium and implies an abrupt discontinuity in density and temperature along its front, thus shockwave propagation heats the liquid and the target and may promote the detachment of matter from the crater [124, 125].

The ablated material contains highly ionized species due to high temperature and direct photoionization, hence it is considered a non-equilibrium "plasma plume". It emits light with an emission spectrum composed of continuous background caused by bremsstrahlung and radiative recombination, and discrete lines typical of the relaxation of excited atomic and molecular species. Plasma temperature is of the order 10^3 K, while pressure and density are about 10^9-10^{10} Pa and 10^{22-23} atoms per cm^3, respectively [132, 134]. After the end of the laser pulse, the plasma plume has a lifetime of the order of tens of ns. Its evolution kinetic abruptly alternates heating by the laser pulse with cooling due to plume expansion and heat exchange with the solvent. If laser pulse duration is more than 10 ps, there is a temporal and spatial overlap between laser pulse and the plasma plume. Thus, plume itself can absorb energy from the laser pulse, so reducing the amount of laser energy directly delivered to the target [135]. This effect, called "plasma shielding", increases the temperature and the lifetime of the plasma plume [131].

From 10^{-10} s to 10^{-7} s, one observes the most important difference between pulsed laser ablation in vacuum and liquid because, unlike in vacuum, the liquid buffer strongly confines the plasma plume around the crater area [126, 136]. The confinement slows down the cooling rate at the interface between the ablated material and the target, because the hot ablated material can provide thermal energy to the underlying target for several ns after the end of the laser pulse. As a final result, the ablation yield in liquid is higher than in gas because a larger portion of the target reaches the energy threshold for detachment. After about 10^{-10} s, the plasma plume

expands and cools in the solution by releasing its energy also to the liquid buffer, therefore the liquid is heated up to temperatures of the plasma plume with consequent degradation ionization and pyrolysis of solution molecules which mix together with target species [125, 134]. It is likely that nucleation and growth processes of NPs starts at this stage, but it is not clear if it takes place before or after mixing of ablated and solution species. For instance, it is not clear if molten material preferentially undergoes solidification or further vaporization and, subsequently, NPs nucleate and grow.

From 10^{-6} s to 10^{-4} s, the energy released by the plasma plume to the surrounding liquid causes the rise of a cavitation bubble which expands up to times of the order of 100 μs (see Fig.2.2). The bubble travels in the liquid up to a maximum radius of the order of millimeters with supersonic speed [135]. During its expansion, temperature decreases and internal pressure drops to a value lower than in the surrounding liquid until the bubble collapses emitting a shockwave. This is the last physical process related to laser ablation of a target in liquid solution [125]. It is worth noting that another open issue about PLAL is when NPs formation occurs, during the expansion of the bubble starts or at the end. This is a relevant point to understand the chemical process leading the formation of NPs because physical parameters such as concentration and temperature of target and solvent species strongly depend on the bubble condition.

For t $>10^{-4}$ s, the system reaches steady state physical and chemical conditions and can undergo minimal modifications due to the condensation of ablated atoms and molecular clusters that still survive in solution. At this stage agglomeration could start yielding precipitation on a timescale longer than minutes for micrometric and nanometric particles. Moreover, depending on the NPs composition, also surface oxidation can occur or prosecute.

2.3 Effect of Ablation Parameters on Produced NPs

Because of several physical-chemical processes involved during PLAL, all the materials and laser parameters affect the final product of the synthesis. Moreover, as discussed above, laser pulses, liquid media, solid targets and the ablated products may interact with each other (see Fig. 2.1 (b)). These interactions occur in the same system and in a short time after the laser pulse, they are strongly coupled and may lead to unique nanostructures that might not be obtained by conventional fabrication techniques. Indeed, by this technique NPs can be tailored by changing laser parameters like pulse energy and photon energy and chemical parameters like solvents which provide a reactive environment that may induce the metal oxidation [137–141]. Indeed, in the second part of this Thesis we'll deal with ZnO NPs produced by PLAL using as target a zinc metal plate and as solvent deionized water [69, 142, 143]. In the following section, we discuss this topic showing the effect of materials and laser parameters on the ablation product. In order to describe the effect of parameters we show some clear example on a variety of materials.

2.3.1   Pulse Wavelength

The skin depth of the target depends on pulse wavelength, and, usually, at shorter wavelengths, the absorption increases thus implying a smaller skin depth. For instance, UV radiation is efficiently and uniformly absorbed by interband transitions in semiconductor or insulant targets producing the regular erosion of all the illuminated area [129]. Also non linear processes such as multiphoton absorption and photoionization processes are favored at short wavelengths, with consequences on temperature, pressure and ionization state of the plasma plume [144]. Conversely, near infrared radiation (NIR) is absorbed preferentially by defects and impurities generating a rugged erosion profile on the spot area [129, 145]. Fig. 2.3 shows experimental results obtained by Intartaglia et al. [137] concerning the production of silicon NPs by PLAL of Si wafer in water using the NIR fundamental (1064 nm) and UV third- harmonic (355 nm) of Nd-YAG 60 ps laser. The results are shown as function of number of laser pulses, i.e., ablation time, for various laser pulse fluence, along with the TEM images of the produced Si NPs. The absorption spectrum in Fig. 2.3 (a) has a broad band between 200 and 800 nm with a shoulder around 500 nm, which is characteristic of Si NPs distribution with mean diameter of tens of nm [137]. Electron microscopy study of the Si NPs obtained after 60 min of NIR PLAL at a fluence of 2.7 Jcm^{-2} confirms a mean diameter of about 40 nm, as shown by the TEM image in Fig. 2.3 (c). Instead, the mean size of Si NPs produced by the third-harmonic already in the first 20000 pulse of ablation is 9 nm, thus, a shorter wavelength for ablation results in much smaller NPs. This result could be tentatively explained considering that shorter wavelength leads to shorter skin depth and so a smaller illuminated volume of the target. Therefore, a minor concentration of ablated material inside plasma plume is obtained, which may reduce NPs coalescence leading a distribution with a smaller average size.

2.3.2   Fragmentation

The overlap of already formed NPs with incoming laser pulses occurs in most PLAL setups, therefore the use of wavelengths that are not absorbed by the NPs is preferred to avoid interaction with the products. On the other end, if NPs absorb laser pulses, they may undergo further modifications, typically a fragmentation, during the synthesis. As a result, the distribution function of particle size shifts to lower dimensions [126, 146, 147]. The physical processes that lead to fragmentation of NPs in the laser beam are still under discussion. The most probable reason leading to reduction of NPs size are the instabilities that develop at the interface of molten NPs with the vapors of surrounding liquid [126]. Indeed, a NPs may absorb enough energy from the laser beam to undergo the phase transition into a liquid state. The temperature of NPs exceeds at this moment the boiling temperature of surrounding liquid, which is therefore vaporized and forms a shell around the NP. The pressure of vapors in this shell is around 10^8 Pa, and its possible asymmetry would result in the break of molten NP inside it into two smaller parts. It is worth noting that fragmentation can take place as long as NPs sufficiently absorb the laser beam. Indeed, plasmonic peak position in metal NPs or the band gap in semiconductor
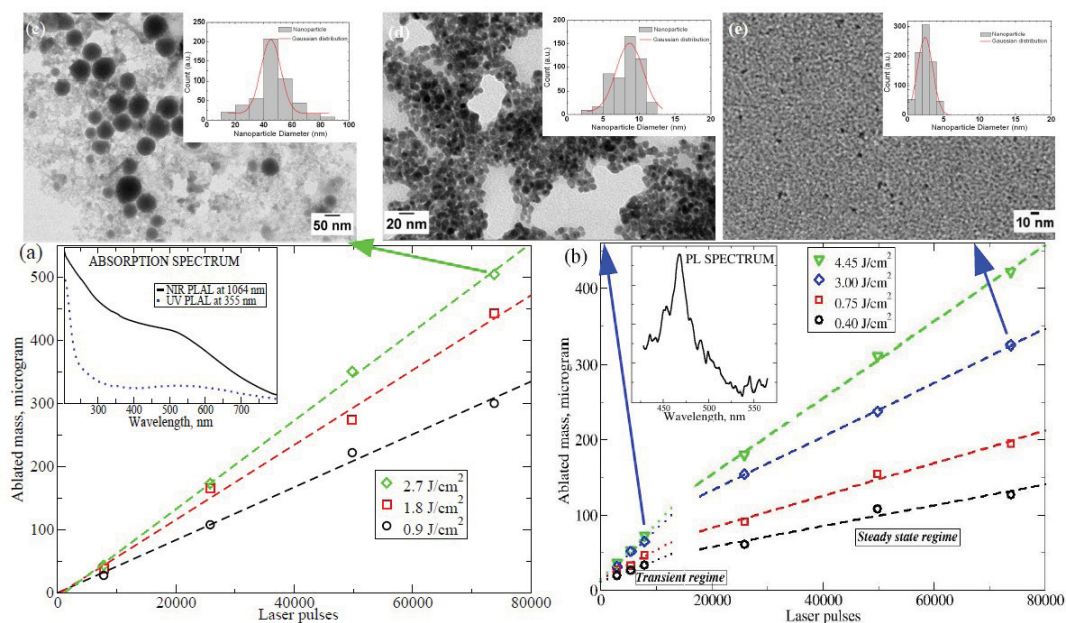
Figure 2.3: Ablated silicon mass as function of the number of laser pulses for NIR (a) and UV (b) PLAL respectively, and TEM images with size distribution of the produced Si NPs. The straight lines over the experimental data points result from the linear fits. The insets in graph (a) and (b) show the measured absorption and photoluminescent spectra of the produced Si NPs respectively. TEM images and size distribution of Si NPs produced by PLAL in water: (c), NIR PLAL at 2.7 J cm^{-2} after 72000 laser pulses; (d) UV PLAL at 3 J cm^{-2} after 6000 laser pulses, (e) UV PLAL at 3 J cm^{-2} after 72000 laser pulses [137].

quantum dots depend on particle size. Hence, the size of NPs decreases upon exposure till NPs become so small that the energy absorbed from the laser pulse is not sufficient for melting and the ensemble of NP acquires its upper limit of NPs size.

Another processes leading to fragmentation is the coulombic explosion. In fact, due to photon or multiphoton absorption the electrons could be ejected by direct photo-ionization or thermionic emission from NPs generating a space charge separation inside the particle. This effect could cause fragmentation of the particle by spontaneous fission due to charge repulsion in the particle [133]. An example of fragmentation depending on laser wavelength of just produced NPs during PLAL is reported in Fig. 2.3. In particular, by NIR PLAL a clear linear increase of the ablated mass as function of ablation time is found for fluences in the range 0.9 to 2.7 Jcm^{-2} (Fig. 2.3 (a)) without any change in the NPs distribution as a function of the time. Instead, in the case of UV PLAL, with fluence in the range 0.4 to 4.4 Jcm^{-2} two very distinct time regimes are observed. As shown in Fig. 2.3 (b), an initial phase (transient regime) is followed by a second phase (steady state regime) with a lower and clearly constant ablation rate. Moreover, the Si NPs produced in the two UV PLAL regimes have different size: 9 nm in the transient regime and 3 nm in the steady state regime, as shown in TEM images of Figs. 2.2 (d) and (e), respectively. The production of ultra small NPs after 60 min of UV PLAL is confirmed by UV-Vis absorption spectroscopy reported in the inset of Fig. 2.3 (a), showing the absorption spectrum

of the colloidal solution obtained with UV PLAL at a fluence of 3 Jcm^{-2}. UV absorption spectrum exhibits a significant increase below 300 nm which is typical of a few nm Si NPs [148]. This experiment shows that as in the case of UV PLAL the ablation process leads first to the production of Si NPs with diameter of about 9 nm in the transient regime (see Fig. 2.3 (b)). Subsequently, these Si NPs diffuse into the solvent, absorb the UV laser pulses, and are therefore photo-fragmented, producing ultra-small Si NPs. Finally, the ultra-small Si NPs having a much lower optical absorption at 355 nm (see inset in Fig. 2.3 (a)), do not interact further with the UV laser, resulting in a steady state regime in which ablation/photo-fragmentation process reaches an equilibrium between the rate of Si NPs produced by ablation and those photo-fragmented by the UV laser pulse. Photo-fragmentation reduces the laser energy reaching the bulk silicon target, and therefore it is responsible for the lower ablation efficiency in the steady state regime.

2.3.3 Pulse Energy

The pulse energy affects the amount of ablated material which enhances almost linearly with the increasing of pulse energy [144]. Because of enhanced fluence provided to the target by laser pulse at higher energy, a larger portion of the target reaches the energy threshold for detachment. Thereby, the larger amount of ablated material implies an higher concentration of target species, like solid and melted fragments, in the plume, which may coalesce thus forming larger NPs. In general, when the pulse energy is increased, broader size distributions with larger average NPs size are observed [129,130,138]; in contrast, some experiments report a decreasing of NPs size with increasing pulse energy [139–141] thus underlining the difficulty of interpretation of complex physical process involved in PLAL. Fig. 2.4 (a) and (b) display the size distribution of Si NPs prepared via femtosecond laser ablation of a silicon wafer in deionized water at two laser pulse energy analyzed by TEM images. It can be seen that histogram obtained with pulse energy=0.4 mJ/pulse shows an average size of 65 nm and a size distribution varying from 10 nm to 120 nm (Fig. 2.4(a)). In contrast, at lower pulse energy (0.15 mJ/pulse), TEM analysis reveals a drastic particle size reduction as reported in Fig. 2.4 (b). The obtained colloidal solution displays a average size of 5.5 nm and a size distribution varying from 1 nm to 8 nm. In Figs. 2.4 (c) and (d) show a blue shift of absorption and photoluminescence spectra with the decreasing on NPs average size. This is related to different quantum confinement regime involving Si NPs: weak regime for larger NPs, strong regime for smaller NPs.

2.3.4 Pulse Duration

Physical processes involved during the absorption of laser pulse are strongly influenced by pulse duration, as discussed in Sec. 2.2.2. For instance, using the same fluence but increasing pulse duration, thermal mechanisms are favored with respect to photoionization mechanisms. Hence, pulse duration is expected to affect NPs size distribution, structure and composition. The observation of the crater left by the laser pulse on the target can be an useful tool which evidences the occurrence of thermal processes during ablation. The crater obtained by fs pulses (Fig. 2.4 (a)),
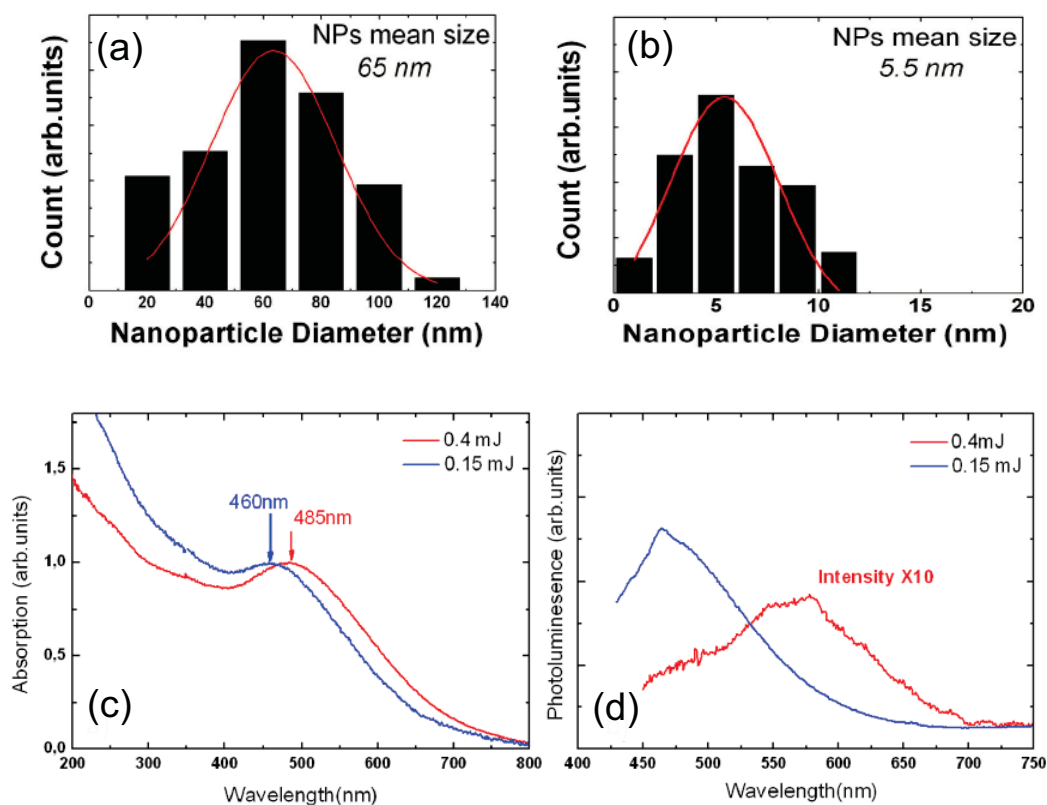
Figure 2.4: Size histogram of silicon NPs colloidal solution prepared via femtosecond laser ablation in deionized water at two laser pulse energy (a) 0.4 mJ/pulse and (b) 0.15 mJ/pulse. Absorption (a) and photoluminescence (b) spectra of the Silicon NPs prepared at 0.4 mJ (red line) and 0.15 mJ (blue line) energy regime [138].

has sharp borders and matches the laser spot, which is typical of ultrafast localized heating and of ablation dominated by direct photoionization processes and electron-ion collisions [144]. The crater obtained by pulses of tens of ps o longer are less sharp (Figs. 2.4 (b) and (c)), which is typical of the thermal ablation processes like vaporization, boiling and ejection of melted material due to the high pressure generated in the crater [129, 144]. In this case, pulse duration is comparable to the electron-lattice thermalization time, thus the conduction of heat outside the laser spot can happen while the source of energy (the laser pulse) is still present [132]. Indeed, Fig. 2.4 (b) shows how the vaporization process generates a recoil pressure and a wavelike structure radiating away from the ablation zone; the structures in the ablation zone arise from the rapid melting and solidification in competition with hydrodynamic instabilities in the melt front. Finally, in the limit of ns pulses, there is a large melt front and a thermal wave is propagated into the material adjacent to the volume where the laser light is being absorbed. The combination of these two effects produces both the corona around the crater (see Fig. 2.4 (c)) and the appearance of the columnar material, which appears to have been "frozen" in the midst of being ejected from the surface. In addition, with ns pulses there is an overlap between laser pulse and plasma plume (plasma shielding). Laser pulse transfers part of the laser energy to the
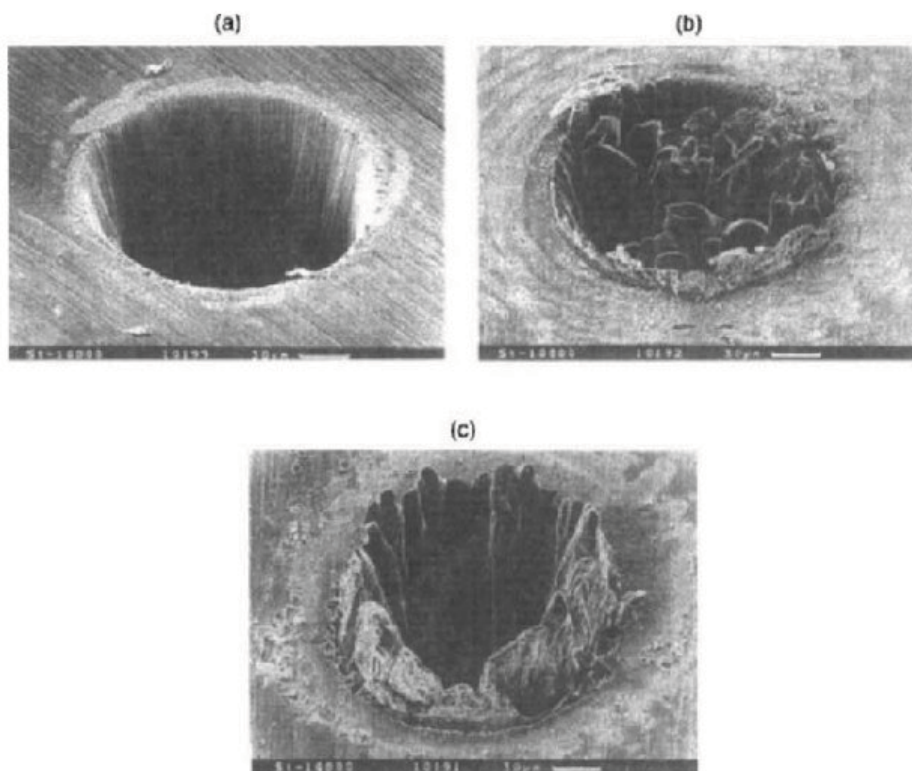
Figure 2.5: Craters on metal targets after laser ablation in gas with 200 fs (A), 80 ps (B) and 3.3 ns (C) pulses, wavelength 780 nm and energy ~ 1 J cm^{-2} [132].

plasma plume leading to an increase of the plume temperature, pressure and lifetime. Under such conditions, the melted drops ejected from the target into the plume have higher chance to be further vaporized. This may lead to sharper size distribution than those obtained with ps and fs pulses due to the improved homogeneity of plasma plume [125]. In contrast, if fragmentation of the melted drops doesn't occurs, due to enhancement of the plume concentration one may observes a broader size distribution, as discussed for increasing pulse energy [138].

2.3.5   Repetition Rate

The repetition rate (RR) defines the number of pulse per second and consequently the time interval between consecutive laser pulses. Since PLAL produces an amount of NPs per pulse, the productivity increases with the repetition rate. However, a linear increase of the number of NPs in solution is observed only for interpulse longer than the lifetime of the cavitation bubble. Since the lifetime is of the order of 100 μs (as discussed in the Sec.2.2.2), a linear increase of the productivity of NPs is observed for repetition rates lower than 1-10 kHz. The cavitation bubble is characterized by a discontinuity of refractive index at the liquid/gas interface, which give rise to scattering of laser light and reduces the amount of energy reaching the target [125]. In addition, many ablation experiments report that increasing repetition rates favor the aggregation and the coalescence of NPs, and also the scattering of incoming laser pulses with NPs, which

causes a decrease in the ablation efficiency [147, 149]. This effects have been explained through an increase of the local concentration of NPs in proximity of the crater due to a reduction of time for NPs to diffuse away from the ablated region, which interact with the laser light. On the other hand, for repetition rates of the order of kHz, the average temperature of the crater is sensibly higher than room temperature. In this way the fraction of matter that reaches the energy threshold for detachment from the target is larger, thus the ablation yield is improved compared to PLAL at room temperature [149]. Sajti et. al [149] have performed an experiment
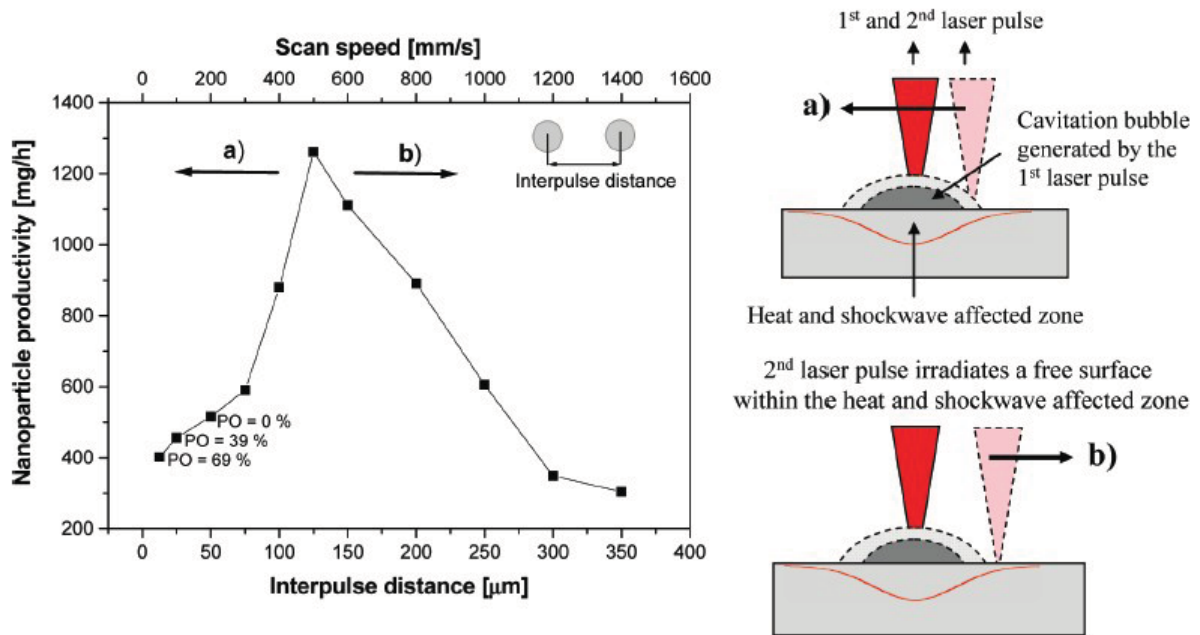

Figure 2.6: (Left) productivity of Al_2O_3 NP as a function of interpulse distance and scan speed using a fixed laser pulse energy of 4.6 mJ at 4 kHz repetition rate and a 4 mm liquid layer. Calculated laser pulse overlaps (PO) are also shown in percentage. (Right) simplified scheme of the processes occurring under laser ablation of a target in liquid, demonstrating the effect of the cavitation bubble and the heat affected zone on subsequent laser irradiation [149].

in which by utilization of the laser scanner allows precise variation and monitoring of pulse overlap during PLAL of Al plate in water. Fig. 2.6 depicts Al_2O_3 NP productivity as a function of scan speed and interpulse distance using a 4 mm liquid layer and 4.6 mJ pulse energy at 4 kHz repetition rate focused on the target (50 μm). As expected, NP productivity, strongly depends on scan speed owing to different pulse overlaps involved. A lower scan speed results in a higher overlap causing the interaction of the laser beam with the previously ablated NPs and the generated cavitation bubble which reduces the PLAL production rate. These absorption and scattering effects decrease with increasing interpulse distance due to the limited size of the cavitation bubble and leads theoretically to a final saturation plateau in the ablation rate [149]. In the figure, it can be observed that the interpulse distance between 75 and 250 μm allows higher particle production rates with a maximum production rate of 1.26 g/h, corresponding to an interpulse distance of 125 μm. This maximum production rate at interpulse of 125 μm has been explain considering that this value corresponds to an irradiated area both out of bubble

region and heated zone by previous laser pulse as well as a shockwave effected zone. These
effects, are likely responsible to the highest PLAL production rate which reaches the order of
gram/hour.

2.3.6 Solvents

The solvent strongly influences the composition and the structure of NPs obtained by PLAL.
The parameters of the solvents, such as viscosity, density and surface tension are relevant for the
dynamics of the cavitation bubble and the confinement of the plasma plume on the crater. In
particular, the increase of solvent viscosity and density improves the confinement of the plasma
plume on the ablated crater, which enhances the ablation efficiency. Besides, solvent molecules
can directly interact with either the ablated species or the growing NPs causing changes in
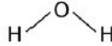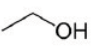the chemical composition and structure with respect to the target. It is worth noting that the
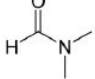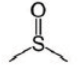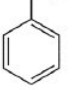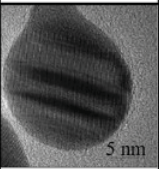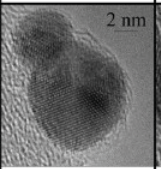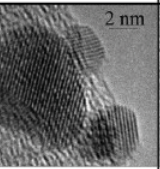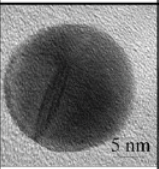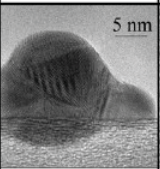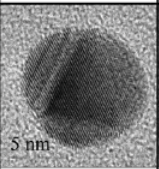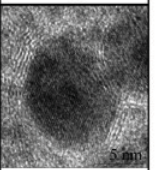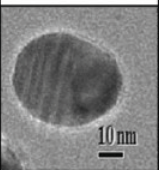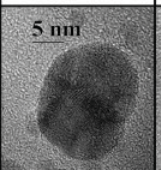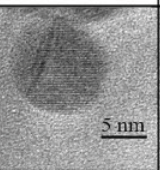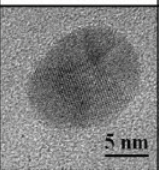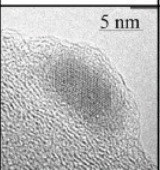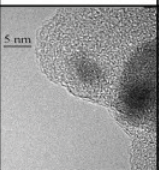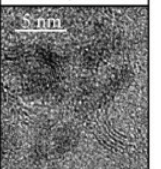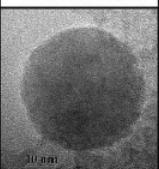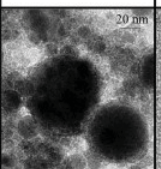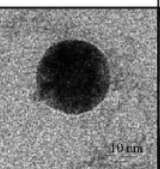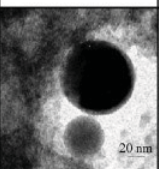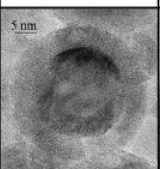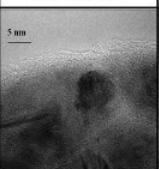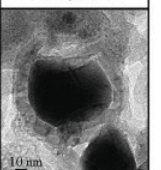
Target / Solvent	Water	Ethanol	Acetonitrile	Dimethyl-formamide	Tetra-hydrofuran	Dimethyl-sulfoxide	Toluene
Au	Metal Au	Metal Au	Metal Au	Metal Au	Metal Au	Metal Au	Metal Au/ Graphite
Ag	Metal Ag/ Oxide AgO	Metal Ag	Metal Ag	Metal Ag	Metal Ag/ Carbon	Metal Ag/ Carbon	Metal Ag/ Graphite
Fe	$Fe_3O_4, Fe_2O_3,$ $Fe(OOH)_2$	$Fe_3O_4,$ FeC_3	$Fe_3O_4,$ Carbon	$Fe_3O_4,$ Carbon	Metal Fe/ Fe_3O_4	Metal Fe/ Carbon	Fe-Carbide/ Graphite

Figure 2.7: Summary of the NPs obtained by laser ablation of Au, Ag and Fe bulk targets in different
solvents with 9 ns pulses at 1064 nm and 10 J cm^{-2}. [125].

purity of a liquid is a relative concept and atmospheric gases like N_2, O_2, H_2O and CO_2, and
traces of other compounds can be found in the solvent. For instance, in water under atmospheric
conditions there is about 9 mg/dm^3 of O_2 and about 14 mg/dm^3 of N_2. In Fig. 2.7 some example

of PLAL of Au, Ag and Fe bulk target in different solvents are reported. One of the most known case of laser ablation in liquids is the PLAL of Au in pure water, which yields gold NPs colloids stable for long time [121]. Their colloidal stability was identified from the presence of Au-O groups at the NPs surface formed by interaction with water molecule. When laser ablation of the gold target is performed in organic solvents, however, the average size of Au NPs is lower and the fraction of nonspherical and aggregated NPs is larger than in water and coagulation and precipitation is observed. The smaller size could be due to the capping effect originated by organic solvents, which hampers nuclei coalescence. The presence of non-spherical Au NPs is compatible with the incomplete coating of the particles surface with capping molecules. Indeed, this causes the growth of NPs only along the portion of the surface which remains uncovered. Similar results have been obtained by PLAL of Ag target in water. Moreover, PLAL in toluene produces smaller NPs because aromatic rings undergo extended pyrolysis when heated at 1000 K at low-oxygen concentration [125], in this conditions graphitic materials are produced. Therefore, coalescence and growth of Ag NPs is stopped in the early stage, when the average size is of a few nm, by the graphitic matrix due to toluene pyrolysis. In a different way PLAL of a Fe target, in general, does not produce Fe NPs. Indeed, due to the reaction between Fe and O, PLAL produces oxide NPs with several compositions and structures such as wustite (FeO), magnetite (Fe_3O_4), maghemite (γ-Fe_2O_3) and hematite (α-Fe_2O_3). The laser ablation of a Fe target in water yields multiphase polycrystalline iron oxide NPs embedded in an amorphous hydroxide matrix [150]. Instead, when the Fe target is ablated in ethanol, two types of NPs are observed: small (below 5 nm) Fe_3O_4 NPs and large (above 10 nm) FeC_3 NPs [151]. Finally, in dimethylsulphoxide, laser ablation of iron gives an amorphous thick matrix embedding metal iron NPs, thus this solvent acts as capping Fe NPs preventing their oxidation [151]. Hence, in the case of Fe target, probably due to stronger interaction with solvent molecules, the chemical composition and structure of the ablation product are heavily affected on the used solvent.

2.3.7 Solutes

Solutes molecules can interact directly with the ablated material or can change the physical-chemical properties of the solvent. For instance, solutes can modify the viscosity, the density and the surface tension of the solvent [151]. The interaction between solutes and ablated material may have different degrees of intensity (Fig. 2.8 (a)). Surfactant molecules can coordinate with the NPs surface by electrostatic interactions and form a molecular layer which limits both NPs coalescence and growth by adsorption of free atoms as well as aggregation and precipitation [146]. At a higher level of interaction there are ligands capable of chemical bonding with the surface of NPs, such as thiolated molecules with Au NPs. In this case, chemical bonds between ligand and NPs produce an irreversible capping effect, thus resulting in a very efficient limitation of NPs growth. When the highest level of interaction between solutes and ablated materials occurs, molecules are able to modify the composition of NPs (Fig. 2.8 (b)). Finally, if solutes undergo activated chemical reactions because the temperature of the just formed NPs is higher than room temperature, NPs can act as nucleation sites, for instance, noble metal salts have been
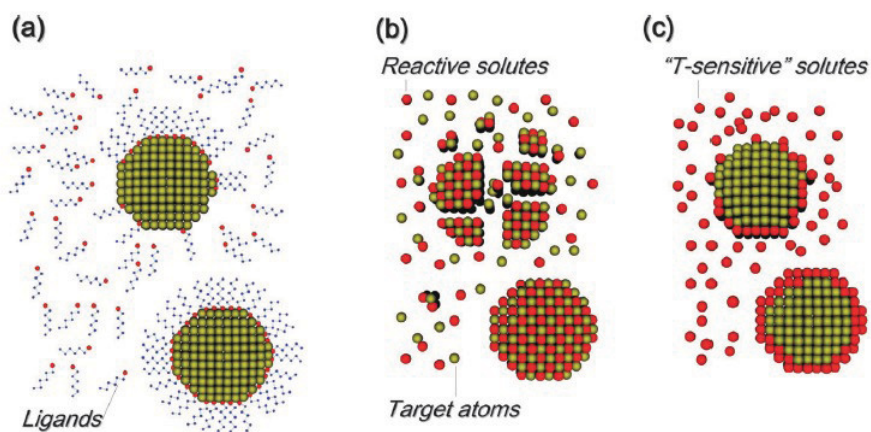
Figure 2.8: Examples of the solute effect: (a) ligands absorb by physical or chemical interactions on the NPs surface (b) solutes react with ablated material to yield a compound different from the bulk target; (c) solutes capable of temperature activated chemical reactions ("T-sensitive" solutes) [146].
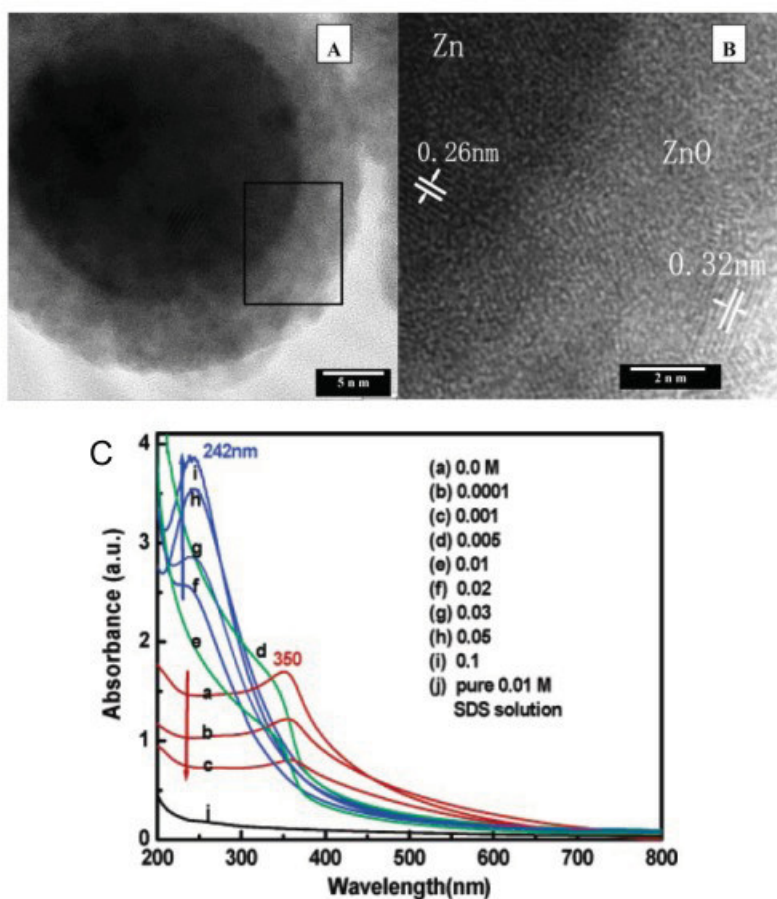
Figure 2.9: HRTEM images of typical NPs produced by PLAL of zinc plate in SDS solutions: 0.01 M (A, B); image B is the local magnified images corresponding to the frame regions marked in image A. (c) Optical absorption spectra of the colloidal solution produced by laser ablation of a zinc plate in aqueous solution with different SDS concentrations [94].

reduced on the surface of oxide or metal NPs yielding a core/shell structure (Fig. 2.8 (c)).

Several experiments have commonly used surfactants molecules as solutes. Among them, sodium dodecyl sulfate (SDS) is characterized by an organosulfate compound with an anionic head-group (sodium salt) and a 12-carbon alcohol tail. Figs. 2.9 (a) and (b) show that PLAL of a zinc plate in aqueous solution with SDS concentration of 0.01 M produces Zn/ZnO core/shell structured particles [94]. The lattice fringes well coincide with metal zinc and zinc oxide, respectively. In addition, Fig. 2.9 (c) shows the UV-vis optical absorption spectra of the colloidal suspension of different samples in aqueous solution with and without SDS. The spectra evidence two absorption peaks at about 350 and 242 nm corresponding to two concentration ranges of SDS, respectively. For the sample prepared in pure water, there is an absorption peak at 350 nm, which decreases with the increase of SDS concentration until it disappears at about 0.03 M, and another peak at 242 nm appears and increases with a further increase of the SDS concentration. Zeng et al. [94] infer that the SDS molecules form a bilayer and even surface micelles on the particle surface which decreases significantly the oxidation rate. This effect produces for NPs large enough, a Zn/ZnO core/shell structure. Moreover, this capping effect, as discussed in the previous section for organic solvent, reduces the average size of the produced NPs.

Chapter 3

Materials and Methods

The purpose of this chapter is the description of the investigated materials, instruments and setups used to perform the experiments that we will present in the next chapters. In particular, we describe the experimental approach based on the use of time-resolved luminescence and also other techniques, such as transmission electron microscopy (TEM), atomic force microscopy (AFM), μRaman, thermal treatments in controlled atmospheres, used to investigate the *ex situ* morphological, structural and optical properties of the samples produced by *in situ* and *ex situ* experiments. Then, we describe our system suitable to perform *in situ* optical absorption (OA) and time resolved photoluminescence (PL) measurements during nanosecond laser ablation of zinc in liquid (PLAL).

3.1   Synthesis of ZnO Nanoparticles

Luminescent ZnO nanoparticles investigated in this thesis were synthesized by PLAL of a zinc plate (Sigma Aldrich 99.99%) with a thickness of 0.5 mm placed at the bottom of a vessel containing the solvent. During the experiments the Zn target was continuously rotated to prevent the laser beam from hitting the same area. Moreover, in this way the colloidal solution was stirred allowing an uniform distribution of NPs in solution. Fig. 3.1 shows the two experimental setups used for sample synthesis. PLAL was performed by a ns Nd:YAG laser and a fs Ti:Sapphire laser with different parameters. Nd:YAG laser ablation was obtained by the first harmonic (λ=1064 nm) at a repetition rate of 5-20 Hz, with a pulse width of 5 ns and 20-90 mJ energy per pulse. The laser was weakly focused by a lens (focal length=10 cm) on the Zn target (spot size~2 mm) immersed either in water or ethanol aqueous solution (10 ml) with a liquid layer of 10 mm above the sample. In order to maintain the same total fluence provided to the target of 25.8 kJ/cm^2, varying other ablation parameters (repetition rate, pulse energy etc...), the irradiation time was ranged from 10 to 50 minutes (600-3000 s). Ti:Sapphire laser ablation was performed by the first harmonic (λ=800 nm) at a repetition rate of 1 kHz, with pulse width ranging from 50 fs to 1.2 ps, and pulse energy of 75-350 μJ per pulse. It was focused by a parabolic mirror (focal length=20.32 cm) on the Zn target (spot size~100 μm) immersed in
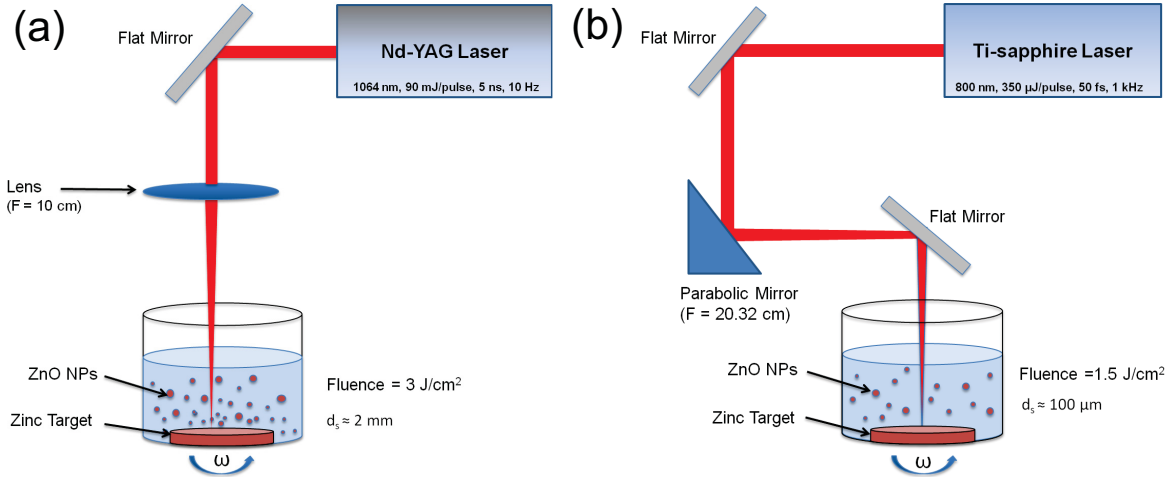
Figure 3.1: Experimental set-up for pulsed laser ablation of zinc plate in a liquid environment by a Nd:YAG laser (a) and a Ti:Sapphire laser (b).

water (2 ml) with a corresponding liquid layer of about 2 mm above the sample. To maintain the same total fluence provided to the target of 855 kJ/cm^2, varying other ablation parameters, the irradiation time ranged from 3 to 15 minutes (180-900 s).

3.1.1   Nd:YAG and Ti:Sapphire Laser

The Q-switched Nd:YAG laser (Quanta System SYL-201) emits pulses of 5 ns duration and wavelength λ_0=1064 nm with a 1-20 Hz repetition rate. The active medium is a yttrium-aluminium-garnet doped with Nd^{3+} ions (Nd:YAG) rod 10 mm long and 7 mm in radius, pumped by a pulsed Xenon discharge lamp via the ∼800 nm Nd^{3+} absorption transition. The Q-switching is triggered by an electro-optic crystal (Pockel cell) placed within the laser cavity. When the pocket cell is not polarized, the cavity Q-factor is low and the population inversion is high without any laser oscillations. When it is activated, the Q-factor suddenly increases and the laser action starts with a strong initial inversion, which generates laser pulse and in a few ns dissipates all the energy stored in the active medium [152–154]. A nonlinear KH$_2$PO$_4$ birefringent crystal is used to perform frequency up-conversion, generating a second harmonic signal at $\lambda_0/2$= 532 nm. A further birefringent crystal (BaB$_2$O$_4$) is used to generate the fourth harmonic at $\lambda_0/4$=266 nm. The nonlinear conversion process critically depends on the relative orientation between the polarization axis and the incident beam and the birefringent crystal axes. The maximum efficiency is obtained when the phase velocities of the frequency-doubled and the fundamental waves are the same within the crystal, this condition is named phase matching [155]. For this reason, the laser is equipped with a system that allows to finely rotate (tune) separately each of the nonlinear crystals in order to maximize the intensity either of the II or of the IV harmonic beams. The maximum laser energies per pulse are 600 mJ, 280 mJ and 65 mJ, for the I, II, IV harmonic beams respectively. The pulse energy can be controlled by varying the voltage applied on the pumping lamp.

The Ti:Sapphire Laser (Solstice) emits pulses of 50 fs, wavelength λ=800 nm with repetition rate up to 5 kHz. The active medium is a Ti-Sapphire rod, pumped by a laser diode emitting light at 532 nm, embedded in the oscillator (resonant cavity) from which comes out a laser beam with diameter 5 nm, pulse energy=7 nJ/Pulse, repetition rate=80 MHz and pulse width = 35 fs, which is amplified by the chirped-pulse amplification principle. Hence, the pulse from the oscillator is first enlarged up to 200 ps by a stretcher, which temporally delays the blue wavelengths within the pulse bandwidth of 35 nm with respect to the red wavelengths by means of a grating pair. Then, the seed pulse is coupled into a regenerative amplifier, where traveling back and forth in the cavity, it pumps another Ti:sapphire crystal. At each passage through the crystal, the trapped seed pulse is amplified until saturation is reached, the maximum repetition rate reduces to 5 kHz. After the amplification stage, the pulse is compressed to 50 fs by temporally synchronizing the blue and red wavelengths within the pulse bandwidth reversing of the "stretching" procedure. The obtained laser beam have a diameter of 7 mm, FWHM=30 nm and a maximum pulse energy of 700 μJ. Because of its very short duration the laser pulse at 800 nm is transform-limited due to energy-time Heisenberg uncertainty principle, it fixes the lowest limit of the bandwidth to be 30 nm. The pulse duration can be controlled by acting on the compressor parameters. In this way, one can tune pulse duration from 50 fs up to 10 ps.

3.2 Ex situ Measurements

3.2.1 Optical UV-Visible Absorption

Ex situ absorption measurements were carried out by a JASCO V-570 double beam spectrophotometer. It is equipped with two different light sources: a tungsten iodine lamp operating in the range 340÷2500 nm and a deuterium discharge tube operating in the range 190÷340 nm. The light emitted by the lamp is resolved by a monochromator based on a Czerny-Turner mount, with a 1200grooves/mm grating, the bandwidth, $\triangle\lambda_{exc}$, being regulated by a slit. The monochromatic excitation light is then divided into two beams by a beam splitter: a portion enters the sample and the other is used as a reference. A photomultiplier tube alternatively measures the intensity of the reference signal, $I_0(\lambda_{exc})$, and that of the light transmitted by the sample, $I_t(\lambda_{exc})$. As a result, it outputs the optical density:

$$O.D. = \log_{10}\frac{I_0(\lambda_{exc})}{I_t(\lambda_{exc})} , \tag{3.1}$$

in this way the temporal fluctuations of the source intensity are compensated by the reference signal. The absorption coefficient can be obtained taking into account the Lambert-Beer law, by using the following relation:

$$\alpha(\lambda_{exc}) = 2.303\frac{OD}{d} , \tag{3.2}$$

where d is the sample thickness. All the measurements have been recorded in the range 190-900 nm (1.38-6.5 eV) using steps of 0.5 nm, a spectral bandwidth of 2 nm, a scan speed of 100 nm/min and averaging the data for 1 s at each point.

Tauc Plot

In order to estimate the optical band-gap of semiconductors and insulators the Tauc Plot was used. Tauc et al. [156] proposed this method using optical absorbance data plotted appropriately with respect to energy. This was further developed by Davis and Mott's in a work on amorphous semiconductors [157, 158]. They showed that the optical absorption depends on the difference between the photon energy and the band gap as follows:

$$(\alpha h\nu)^{1/n} = A(h\nu - E_g),\tag{3.3}$$

where h is the Planck's constant, ν is the photon's frequency, α is the absorption coefficient, E_g is the band gap, and A is a proportionality constant. The value of the exponent denotes the nature of the electronic transition, whether allowed or forbidden as well as direct or indirect:

- for direct allowed transitions: n=1/2,

- for direct forbidden transitions: n=3/2,

- for indirect allowed transitions: n=2,

- for indirect forbidden transitions: n=3.

The typical procedure for a Tauc analysis consists in the acquition of the optical absorbance data for the sample spanning a range of energies from below the band-gap transition to above it. Plotting the $(\alpha h\nu)^{1/n}$ versus $(h\nu)$ one judges which value between of n provides the better fit and thus identifies the correct transition type. The power law with n=2 is in general used for zinc oxide which is well known to have a direct allowed transition (Chapter 1). Fig. 3.2 shown example of Tauc plot for ZnO where the absorption coefficient times the photon energy to the second power is plotted versus the incident photon energy [158]. At low photon energies the material is transparent; near the band-gap value the absorption rises and shows a region of linearity in this squared-exponent plot. This linear region is used to extrapolate the x-axis intercept, that is the band-gap value (here 3.27 eV). At even higher energies, the absorption processes saturate and the curve again deviates from the linear trend. This deviation near the band-gap region can be associated either to defect absorption states or to "Urbach Tail", which consists in states usually described by an exponential function, as previously argued in the Sec.1.1.3.

3.2.2 Steady State Photoluminescence

Steady state PL and PL excitation spectra (PLE) were performed using a JASCO FP-6500 spectrofluorometer. The excitation light is emitted by a 150 W discharge Xenon lamp; its
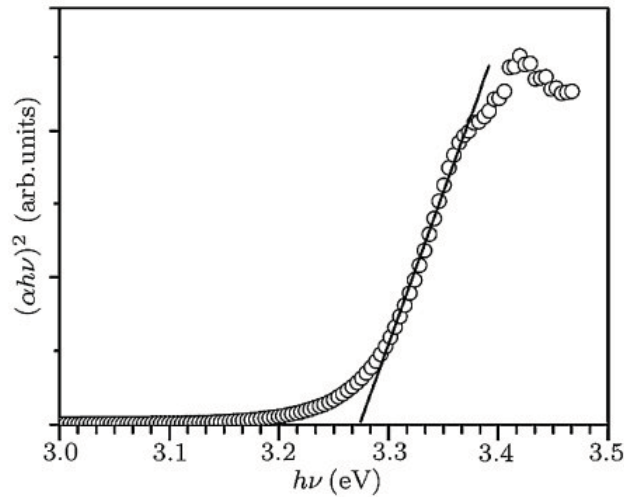
Figure 3.2: Example Tauc plot from UV-Vis analysis of a ZnO thin film that illustrates the method of fitting the linear region to evaluate the band-gap at the x-axis intercept [158].

wavelength, λ_{exc}, is selected by a monochromator using a holographic concave grating with 1800 lines/mm; its bandwidth, $\triangle\lambda_{exc}$, is regulated by the monochromator slit. The monochromatized excitation light is directed to a beam splitter that divides it into two beams: the one enters a photomultiplier (PMT1) and the other hits the sample, positioned in a standard 45° backscattering geometrical configuration. The emitted luminescence light is analyzed by another monochromator, based on a holographic concave grating with a 1800 lines/mm grating, which selects the emission wavelength, λ_{em}, in a range from 220 to 750 nm with a bandwidth from 1 to 20 nm, $\triangle\lambda_{em}$. Finally, the luminescence signal is detected by a second photomultiplier (PMT2). The output signal is the ratio between the intensities measured by PMT2 and PMT1, so that the luminescence spectra are corrected for the temporal fluctuations of the source intensity. The signal to noise ratio of the luminescence spectra depends on the choice of the bandwidth and of the scan speed of the monochromator and by the gain and the time response of the photomultiplier. In this thesis the emission spectra was acquired by time resolved PL setup, while JASCO FP-6500 spectrofluorometer was mainly used to obtain excitation spectra and the PL quantum yield (QY). PLE spectra were acquired fixing the emission wavelength and changing the excitation wavelength. In this way we detect the emission process efficiency as a function of the excitation wavelength. The PLE spectra were corrected for the intensity distribution of the excitation xenon lamp. For this purpose a sample of Rhodamine B (in glycerol) was used, which absorbs all incident light from 220 nm to 600 nm and emits at 640 nm with a constant (near to 1) quantum yield [159]. Thereby, we obtain an absolute measurements of the lamp intensity as a function of wavelength. The PLE spectra divided for the lamp response allow us to obtain the corrected PLE spectra. Hence, the intensity values are affected by an uncertainty of about 10% mainly due to the lamp intensity fluctuations. The PL QY were obtained by comparing the PL intensity of the sample emission with that obtained from an aqueous solution (pH=13) of fluorescein excited at 470 nm, used as a reference of known $QY_R=0.95$. To this aim, the

fluorescence from the sample and the reference were measured in exactly the same conditions and geometry. Indeed, quantum yield values can be calculated according the following equation

$$QY_S = QY_R \frac{\int I_S dE}{\int I_R dE} \frac{1 - 10^{-OD_R(E_{ex_1})}}{1 - 10^{-OD_S(E_{ex_2})}} \frac{I_L(E_{ex_1})}{I_L(E_{ex_2})} \frac{n_S^2}{n_R^2}, \tag{3.4}$$

where $I_S, OD_S(E_{ex_1})$, $I_L(E_{ex_1})$ and $I_R, OD_R(E_{ex_2})$, $I_L(E_{ex_2})$ are the PL intensity, optical density at E_{ex_1} and the intensity of the excitation source for the sample and the fluorescein standard, respectively; n_S and n_R are the refractive index of sample and fluorescein. This expression is mostly intuitive, except for the use of the ratio of refractive indices of the sample (n_S) and reference (n_R). This ratio has its origin in consideration of the intensity observed from a point source in a medium of refractive index n_i, by a detector in a medium of refractive index n_0. The observed intensity is modified by the ratio (n_S^2/n_R^2), therefore this ratio of (3.4) comes from the Snell law's in the two different liquid media containing the sample and reference (fluorescein) [159]. Since the analyzed samples and reference were very dilute aqueous solutions $n_S/n_R \approx 1$.

3.2.3 Time Resolved Photoluminescence Technique

To explain the time-resolved technique, we consider a two-level system of energies E_0 and E_1, respectively, with $E_1 > E_0$. We indicate with N_0 and N_1 the number of atoms per unit volume in each state, that is, the populations of each level. We suppose that the system interacts with e.m. radiation of photon energy $E_{exc} = E_1 - E_0$ so that, due to the interaction with the radiation, $N_1(t) > 0$. Considering a continuum source excitation the equation that describes the variation of N_1 with time can be written as:

$$\frac{dN_1}{dt} = I_0(E_{exc}) \left(1 - e^{-\alpha(E_{exc}d)}\right) - (K_r + K_{nr})N_1(E_{exc}, T), \tag{3.5}$$

where the first term in agreement with the Lambert-Beer law represents the absorbed photons in a sample with thickness d and absorption coefficient α. While the second term leads a decrease of N_1 by radiative and non-radiative processes. Radiative processes give rise to emission of photons with energy equal to $E_1 - E_0$, and thus are responsible for the luminescence, the rate K_r being the spontaneous Einstein coefficient and it is usually independent of the temperature [160]. Non-radiative processes are assisted by phonons with a rate K_{nr} depending on the temperature in accordance to the Arrhenius equation [161]:

$$K_{nr}(T) = Ae^{-\Delta E/kT}, \tag{3.6}$$

where A is a pre-exponential factor and ΔE is the activation energy of the non-radiative processes. The luminescence intensity, i.e. the number of photons emitted per unit time, is given

by

$$I(E_{em}, E_{exc}) = K_r N_1(E_{exc}) I(E_{em}) \,, \tag{3.7}$$

where $I(E_{em})$ is the emission line-shape determined both by homogeneous and inhomogeneous contributions. Steady state luminescence experiments are performed when the system undergoes a continuous excitation; in this case $dN_1/dt=0$ and combining Eq. (3.7) and (3.5) we get:

$$I(E_{em}, E_{exc}, T) = \frac{K_r}{K_r + K_{nr}} I_0(E_{exc}) \left(1 - e^{-\alpha(E_{exc})d}\right) I(E_{em}) \,, \tag{3.8}$$

where $k_r/(k_r+k_{nr})=\eta$, is the quantum yield that is the ratio between the number of emitted and absorbed photons. From Eq. (3.8) we can define two types of luminescence spectra:

- (i) the emission spectrum (PL spectrum) in which the intensity is measured as a function of E_{em} for fixed E_{exc}. This type of spectrum measures the shape and intensity of the band emitted by the sample;

- (ii) the excitation spectrum (PLE spectrum) measures the luminescence intensity, monitored at a fixed E_{em}, as a function of E_{exc} and represents the excitation efficiency of the luminescence spectrum.

If after a short time we switched off ($I_0 = 0$) the light source, the Eq. (3.5) can be solved without the first term, in this case we get

$$N_1(T) = N_1(0) e^{-t/\tau(T)} \,, \tag{3.9}$$

where τ is

$$\tau(T) = \frac{1}{K_r + K_{nr}(T)} \,, \tag{3.10}$$

τ is the mean lifetime of the population in the excited state and it indicates the time necessary to reduce N_2 of a factor of e. The time dependence of luminescence spectra is studied by using a pulsed excitation. After the excitation of defect by a narrow pulsed laser, which produces the population of $N_1(0)$ electrons in the excited state, the light source is switched off and $N_1(t)$ decays according to Eq. (3.9). Then, putting together Eq. (3.5) and Eq. (3.9) we obtain:

$$I(E_{em}, E_{exc}, t) = -\frac{dN_1}{dt} = (N_1(0)/\tau) e^{-t/\tau} = K_r I(E_{em}, E_{exc}) N_1(0) e^{-t/\tau} \,, \tag{3.11}$$

This equation defines the time resolved luminescence for a defect center screened from its environment, that can be experimentally tested by detecting PL spectra at varying the time delays from the excitation pulse at fixed acquisition time window. In general, radiative lifetime ranging from a few of ns up to ms for dipole allowed and forbidden transition, respectively. Non radiative lifetimes can be shorter than ps, thus, luminescence lifetime span a wide range of times. Con-

sidering a semiconductor, a possible recombination process involve a free light-excited electron with a free hole. In intrinsic semiconductors light intensity with energy larger than the optical band-gap generates n free electrons and n free holes in the crystal. Then, intensity would be given by an expression of type:

$$I(t) = -\frac{dN_1}{dt} = \gamma n^2 \,. \tag{3.12}$$

Such process is called bimolecular recombination, in contrast with monomolecular precess described by the Eq. (3.11). From (3.12) one finds

$$I(t) = \frac{\gamma n(0)^2}{(n(0)\gamma t + 1)^2} \,, \tag{3.13}$$

where γ represents the probability that a free electron meets with a free hole in the crystal. For large value of time, the intensity decays as t^{-2}. Several variation of this mechanism may be found in the literature involving trapping of the released electron.

3.2.4   Time Resolved Photoluminescence: Experimental Apparatus

The experimental apparatus to perform time-resolved photoluminescence measurements is composed by: a pulsed excitation system (tunable pulsed laser), a dispersion system (spectrograph) and a detector (Intensified CCD camera). An accurate description of these components is treated elsewhere [154, 162]. Here, we give only a general overview, functional to the understanding of the results reported in the next chapters.

The **Tunable Laser** (VIBRANT OPOTEK) is an integrated system, in which the third harmonic of a Nd:YAG laser is used to pump an Optical Parametric Oscillator (OPO) that converts it into a tunable output. The main components are a Q-switched Nd:YAG laser, harmonic modules, the OPO and the UV conversion modules. The Q-switched Nd:YAG laser (QUANTEL) emits pulses of 5 ns duration and wavelength λ_0=1064 nm with a maximum repetition rate of 10 Hz. Its principle of operation is the same discussed in Sec. 3.1.1. The beam at 1064nm (fundamental harmonic) produced by the Nd:YAG laser is directed into the Second Harmonic Generator (SHG), where the wavelength is converted to $\lambda_0/2$=532 nm, and then into the Third Harmonic Generator (THG), where it is converted to $\lambda_0/3$=355 nm. By dichroic mirrors the THG beam reaches the OPO, which is a non-linear optical device made by a birefringent non-linear BBO (β-BaB2O4) crystal placed within an optical cavity. The OPO splits the laser light into two beams, signal and idler, with frequencies ω_s and ω_i, respectively. Because of energy conservation, the frequencies are related to that of the pump:

$$\omega_p = \omega_s + \omega_i \,, \tag{3.14}$$

In order to achieve the phase matching condition within the OPO, the conservation of momentum

has to be fulfilled:

$$\overrightarrow{k}_p = \overrightarrow{k}_s + \overrightarrow{k}_i \,. \tag{3.15}$$

The previous equation can be written in the form:

$$n_p\omega_p = n_s\omega_s + n_i\omega_i \,, \tag{3.16}$$

where n_p, n_s and n_i are the refraction index of the non-linear crystals at the frequencies ω_p, ω_s and ω_i. The OPO output can be continuously tuned over a wide spectral range taking advantage of the fact that the refractive index depends on the polarization of the light and its orientation with respect to the optical axis of the non-linear crystal. In fact, by using an incorporated stepping motor controlled via software we can vary the angle between the optical axis of the crystal and the beams' direction, thereby, the λ_s can be varied from 410 nm to 710 nm, the λ_i from 710 nm to 2400 nm. Finally, it is also possible to generate a beam of shorter wavelengths by halving the wavelength of the OPO beam. This is performed by three UV modules composed by non-linear crystals mounted on another stepping motor, each of them is used for a particular range:

- UV-1 in the range (210-245) nm

- UV-2 in the range (245-355) nm

- UV-3 in the range (355-410) nm

The excitation beam with a spot size of $\sim$5 mm^2 hits the sample (colloidal solution in a quartz cell). The emitted light is collected by a lens and then arrives at the detection system. The energy of the laser pulses is measured with a pyroelectric detector positioned before the sample holder to measure the intensity of incident laser radiation. The accuracy of pulse energy measures, taking into account the laser fluctuations, is $\sim$10%. The light emitted from the sample is spectrally resolved by a **Spectrograph** (SpectraPro 2300i, PI Acton, 300 mm focal length) equipped with three gratings differing on the blaze wavelength, λ_{blaze}, and in the number of grooves per mm:

- Grating-1: λ_{blaze}=300 nm and 150 grooves mm^{-1}

- Grating-2: λ_{blaze}=300 nm and 1200 grooves mm^{-1}

- Grating-3: λ_{blaze}=500 nm and 300 grooves mm^{-1}

The spectral resolution with each grating is 21.6 nm$\cdot$mm^{-1} for the Grating-1, 2.7 nm$\cdot$mm^{-1} for the Grating-2 and 10.8 nm$\cdot$mm^{-1} for the Grating-3.

The luminescence signal resolved by the spectrograph is detected by the **Intensified CCD Camera** (PI-MAX Princeton Instruments). Incoming light hits the photocathode which releases electrons that are accelerated into the Micro-Channel Plate (MCP). The MPC is an image

intensifier consisting of a thin semiconductive glass plate (0.5÷1.5 mm), that is perforated by more than 10^6 small holes (channels) with a diameter in the range 10÷25 μm. Since the inner surface of the channels has a high secondary emission coefficient, the electrons that hit the channel walls generate additional electrons with a gain depending on the voltage at the MCP output. The electrons are further accelerated by a high voltage (5÷8 kV) and strike the phosphor coating on the fluorescent screen causing it to release photons. These photons are transferred to the surface of CCD, with 1024×256 pixels by optical fibers producing charges at the pixels proportional to the number of incident photons. These charges are converted to an analog voltage and then digitally encoded by a A/D converter and transmitted to the interface of the computer. The possibility of varying the photocathode voltage allows to enable or to disable the
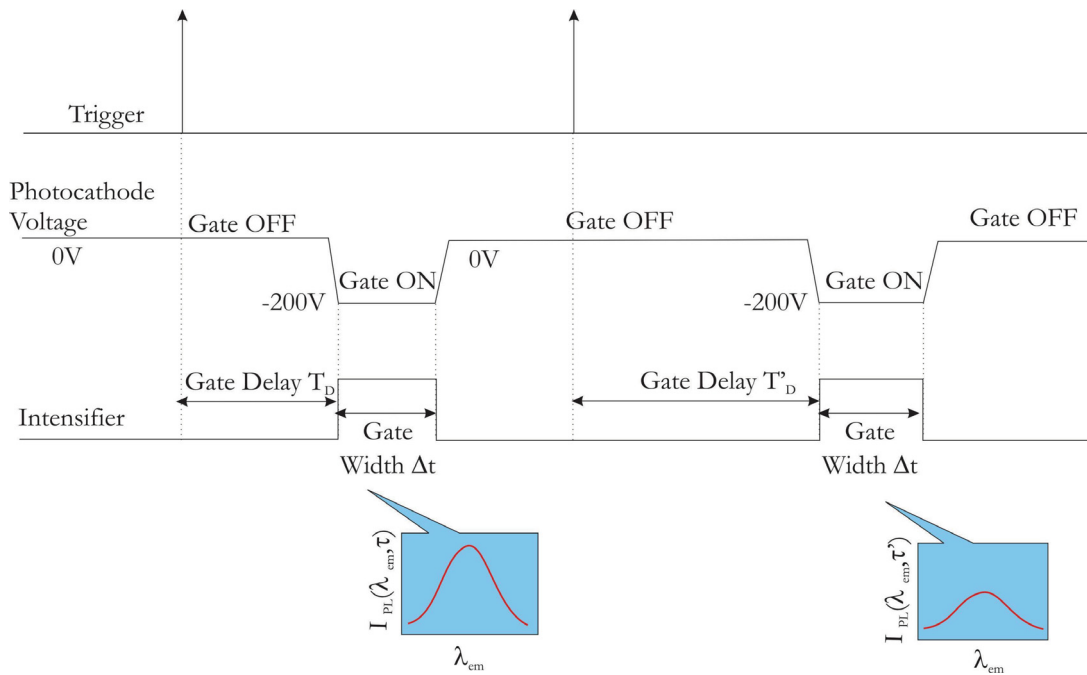
Figure 3.3: Diagram of the CCD timing: GATE ON and GATE OFF modes. Figure taken from L. Vaccaro Ph.D thesis [162].

CCD: in the GATE ON mode the photocathode voltage is -200 V and the CCD sees the light, in the GATE OFF mode the photocathode voltage is 0 and the CCD does not see the light. This peculiarity permits the detection of time resolved luminescence spectra synchronized with the laser excitation pulses. In fact, the CCD is triggered by an electronic synchronization signal produced by the laser 60 ns before the Q-switching. The main instrumental parameters of the CCD are:

- The Gate Delay, T_D, and Gate Width, Δt, fixed by a delay generator regulating the acquisition times. The Gate Delay regulates the temporal shift of the acquisition window with respect to the trigger signal (see the diagram of Fig. 3.3); Instead, Gate Width determines the amplitude of the time window during which the CCD is enabled to reveal the luminescence light (GATE ON mode).

- CCD Accumulation and Software Accumulation that determine the number of acquisitions to which the CCD is exposed before discharging and the number of acquisitions summed by the software, respectively. Both parameters increase the signal-to-noise ratio, however the CCD Accumulation has an upper limit due to saturation of the CCD.

3.2.5 Atomic Force Microscopy

Atomic force microscopy (AFM) takes advantage of the interaction between a probe fixed at the free end of a cantilever and the surface of the sample. The AFM is based on the feedback loop which keeps at a constant value an interaction parameter while the probe is scanned across the sample surface. This technique allows to obtain the morphology of a surface through point by point (x,y) measurements of surface height (z), which can be used to form images. Normally, the probe is a sharp tip, which is a 3-6 μm tall pyramid with 15-40 nm end radius. Though the low lateral resolution, depending on the tip dimension of about 30 nm, the typical vertical resolution can be up to 0.1 nm. In the typical configuration the cantilever moves across the sample surface, mounted on the sample stage, while a laser beam is pointed on its free end. The reflected laser beam strikes a position-sensitive photo-detector consisting of four-segment photo-detector. When the tip interacts with the surface of the sample the photodiode measures the differences between its segments signals, which indicate the position of the laser spot, and thus the vertical and lateral deflections of the cantilever. The most used modes for AFM measurements are: contact mode and tapping mode. In the first, the parameter kept constant during the scanning on the surface is the cantilever deflection due to interaction between the tip and sample surface. When AFM operates in tapping mode the cantilever is driven to oscillate up and down near its resonance frequency by a small piezo element in the cantilever holder. The combined effects of several kind of forces acting on the cantilever when the tip comes close to the surface, Van der Waals forces, dipole-dipole interactions, electrostatic forces, etc..., cause the amplitude of the cantilever's oscillation to change as the tip gets closer to the sample. Such an amplitude is used as the parameter that goes into the electronic servo that controls the height of the cantilever above the sample. The servo adjusts the height to maintain a set cantilever oscillation amplitude as the cantilever is scanned over the sample. Tapping mode allows to reduce damage the sample surface because of the short duration of the applied force, and because the lateral forces between tip and sample are significantly lower. In fact, tapping mode imaging is used to acquire image of NPs deposited onto a ultra flat substrate (for example Mica) and even for the visualization of supported lipid bilayers or adsorbed single polymer molecules under liquid medium.

AFM measurements were done in air by two different instruments: a Bruker FAST-SCAN microscope working in the soft tapping mode and using a FAST-SCAN-A probe with an apical radius of about 5 nm, and a multimode V (Veeco Metrology) scanning microscope working in the tapping mode and using a commercial silicon probe having a tip radius of 10 nm. All images were acquired on a dried droplet of the colloidal solution containing nanoparticles deposited onto a mica substrate.

3.2.6 Raman Microscopy

Phenomenology

Raman effect is a anelastic scattering phenomenon of light upon interaction with matter. The light diffused by the sample contains two contributions: the first and most intense, called Rayleigh scattering, has the same frequency (ν_0) of the incoming light, the second, called Raman scattering, has frequencies $\nu_0 \pm \nu_m$; where ν_m indicates the vibrational frequency of the molecule [163]. Signal having $\nu_0 - \nu_m$ frequencies is called Stokes, whereas signal with $\nu_0 + \nu_m$ is called anti-Stokes. Thus, by Raman spectroscopy, it is possible to measure the vibrational frequency, ν_m, as the shift from the incident beam frequency (ν_0). Hence, a Raman spectrum consists of a plot of the scattered intensity as a function of frequency. This spectroscopy allows to probe the vibrational modes of a molecule or a crystal, sometimes bearing some advantages with respect to common IR spectroscopy. Indeed, Raman effect occurs when the polarizability if the sample is coupled with its vibrational mode, thus is a function of the vibrational displacement. Instead, IR is an absorption effect which occur when the dipole moment is coupled with vibrational mode. As a result, depending on molecular symmetry, it can happen that a vibrational mode is Raman-active but non IR-active, or vice versa [163]. In this Thesis we are going to report Raman measurements to detect the vibration modes of the produced NPs aimed to identify their structure. Phonon-modes frequencies, broadening parameters and the relative intensity ratio, also provide information about crystal quality and allow us to investigate about the presence of defects inside nanocrystals. Moreover, it is known that a shift of the phonon-mode frequencies can be related to the effect of quantum confinement in quantum dot. Hence, a Raman study could clarify important aspects on quantum confinement effects of ZnO NPs.

Instrument

Raman spectra were acquired by a confocal Raman microscopy, Bruker SENTERRA spectrometer (λ=532 nm, power 20 mW), supplied with a CCD camera and a microtranslation stage, which is equipped with a confocal microscope. The apparatus is connected to a computer able to acquire both the visual images of the sample and the Raman spectra, obtainable at low and high spectral resolution. The laser beam runs through the microscope objective, and is focused on the sample. The light is back from the sample in the opposite direction to the incident direction and is collected with the same objective and focused on the entrance slit of the monochromator. Since Rayleigh radiation is usually much more intense than Raman scattering, a notch filter is introduced to drastically reduce the intensity at the laser radiation frequency. In this instrument the notch filter leaves unchanged the intensity of light with Stokes-shift exceeding 150 cm^{-1}. The instrument is equipped with two gratings (400 and 1200 lines/mm), from which it is possible to vary the resolution and spectral range. For high resolution, 3-5 cm^{-1}, it has a range of 53-3700 cm^{-1}; while in the case of low resolution measurements, 9-15 cm^{-1}, the investigated range is 50-4478 cm^{-1}. The detector is constituted by a CCD (1024x256) cooled by a Peltier cell to -55 °C. The sample is placed on a mobile support with a motorized movement controlled

by software to focus on the laser beam optimating the Raman signal. To carry out Raman measurement a droplet of the colloidal solution containing nanoparticles was dried onto a steel substrate, known to yield no Raman signal in itself.

3.2.7 Transmission Electron Microscopy

The structure of the produced nanoparticles was characterized as well by high resolution transmission electron microscopy (TEM) high resolution TEM (HR-TEM) and selected-area electron diffraction (SAED). HRTEM measurements were performed in Germany at the Karlsruhe Institute of Technology (KIT) using an aberration-corrected FEI Titan 380-300 microscope at 300 kV acceleration tension. The specimens were prepared by dropping the ablated solution over a holey carbon-film copper-grid at room temperature in air. TEM is a microscopy technique in which a beam of electrons is transmitted through an ultra-thin specimen [164]. An image is formed from the interaction of the electrons transmitted through the specimen; it is magnified and focused onto an imaging device such as a fluorescent screen, or detected by a sensor such as a CCD camera. The image can be obtained either in the bright field (BF) or dark field (DF) mode. In the BF mode, an aperture is placed in the back focal plane of the objective lens which allows only the direct beam to pass. In this case, the image results from a weakening of the direct beam due to the interaction with the sample. Hence, sample thickness and diffraction contrast contribute to the image formation which appears with dark contrast in the crystalline areas in presence of heavy atoms. In the DF mode, the direct beam is blocked by the aperture while one or more diffracted beams pass the objective aperture. Since diffracted beams have strongly interacted with the specimen, DF images contains very useful information, such as the presence of planar defects, stacking faults or particle size.

HRTEM

High-resolution transmission electron microscopy (HRTEM) is an imaging mode of the TEM microscope that allows for direct imaging of the atomic structure of the sample [165]. In contrast to TEM imaging mode (DF and BF), in HRTEM measurements to obtain lattice images, a large objective aperture is selected which allows many beams including the direct beam to pass. HRTEM is a powerful tool to study properties of materials on the atomic scale, such as semiconductors, metals and nanoparticles. The main difficulty in HRTEM is that image formation relies on phase contrast which is not intuitively interpretable, besides, the image is influenced by aberrations of the imaging lenses in the microscope that reduce image quality. The contrast of a HRTEM image arises from the interference in the image plane of the electron diffracted beam with the direct beam. The most part of the structural information of the sample is contained in the phase of the diffracted electron wave. However, only the amplitude of the electron wave in the image plane is possible to record. To this aim the aberrations of the microscope (like defocus) have to be tuned in a way that converts the phase of the wave at the specimen exit plane into amplitudes in the image plane. The electron wave, resulting from the

interaction with a crystalline sample, as a function of the spatial coordinate x is a superposition of a plane wave and a series of diffracted beams with different in plane spatial frequencies u corresponding to scattering angles. Then, electron wave passes through the imaging system of the microscope where suffers further phase change and interferes as the image wave in the imaging plane (CCD camera). It is worth noting that high intensity in the HRTEM images might or might not indicate the positions of projected atom columns in that precise location. Therefore, the recorded image is not a direct representation of the samples crystallographic structure.

SAED

Selected area electron diffraction (SAED) is a crystallographic experimental technique that can be performed inside a TEM microscope. In order to obtain a diffraction pattern, TEM microscope operates in diffraction mode in which a diffracted electron beam image is focused at the back focal plane of the objective lens and projected onto the screen by the imaging lens system. During TEM measurements a fraction of electrons will be scattered to particular angles, determined by the crystal structure of the sample, while others pass through the sample without any deflection. As a result, the image on the screen will be a series of spots constituting the selected area diffraction pattern, whereby each spot corresponds to a satisfied diffraction condition of the sample's crystal structure [164]. If the sample is tilted, the same crystal will stay under illumination but different diffraction conditions will be activated and different diffraction spots will appear. In any case, it is possible to extract by anti-Fourier transformation the crystalline plane of the structure. SAED is referred to as "selected area" because the user by an aperture, typically located in the first image plane below the specimen, can easily choose from which part of the sample to obtain the diffraction of pattern.
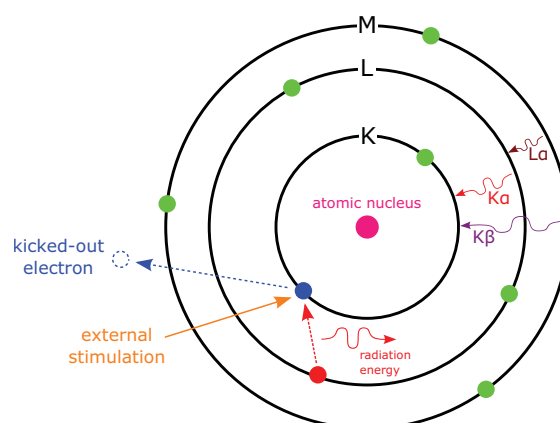
Figure 3.4: EDX scheme.

EDXS

Energy-dispersive X-ray spectroscopy (EDX) is an analytical technique used to identify the elemental composition of materials based on the interaction between an high-energy electron beam and the sample. Its characterization capabilities are due to the fundamental principle that each element has a unique atomic structure allowing an unique set of peaks on its X-ray emission spectrum [166]. To obtain the characteristic X-rays emission, a high-energy beam of charged particles, such as electrons, is focused into the sample being studied. An atom within the sample contains ground state electrons in discrete energy levels or electron shells bound to the nucleus. The incident beam may excite an electron in an inner shell, ejecting it from the shell thus creating a vacancy, subsequently an electron can "fall" from an outer orbit (higher-energy shell) filling the hole. In this way, the difference in energy between the two shells may be released in the form of an X-ray (see Fig. 3.4). The number and energy of the X-photons emitted from a specimen can be measured by an energy-dispersive spectrometer, energies of interest in electron probe analysis are mostly in the range 1-10 keV. Since the energies of the X-rays correspond to the difference in energy between the two shells (K, L, M) of the atomic structure of the emitting element, EDX spectrum displays the corresponding sample X-ray lines (K_α, L_α, K_β). By the comparison between the lines positions with reference tables of energies, graphs or computer database, EDX allows the elemental composition of the "unknown" sample to be measured [166]. The quantitative EDX analysis is based on the fact that the relative intensity of an X-ray line is approximately proportional to the mass concentration of the element concerned. The true concentration (C') of elements in the sample can be estimated by

$$C' = \left(\frac{I_{sp}}{I_{st}}\right) C_{st} \tag{3.17}$$

where I_{sp} and I_{st} are the intensities measured for specimen and standard, respectively, and C_{st} is the concentration of the element concerned in the standard. To obtain the true concentration are required several corrections among which background and absorption correction are the most important. The latter is due to attenuation of the X-rays as they emerge from a finite depth in the sample thus depending on the angle between the surface of the specimen and the X-ray path to the spectrometer.

3.3 In situ Measurements

3.3.1 Experimental Setup

To directly probe the evolving nanomaterials during the PLAL experiments and to monitor in real time the undergoing NPs synthesis and reactions, we performed online UV-VIS optical absorption (OA) and photoluminescence (PL) measurements; Fig. 3.5 depicts the experimental setup. During Nd:YAG laser ablation, the liquid containing the ablated material was continuously pumped by a peristaltic pump (flow=11.5 ml/s) in a closed circuit traversing two quartz
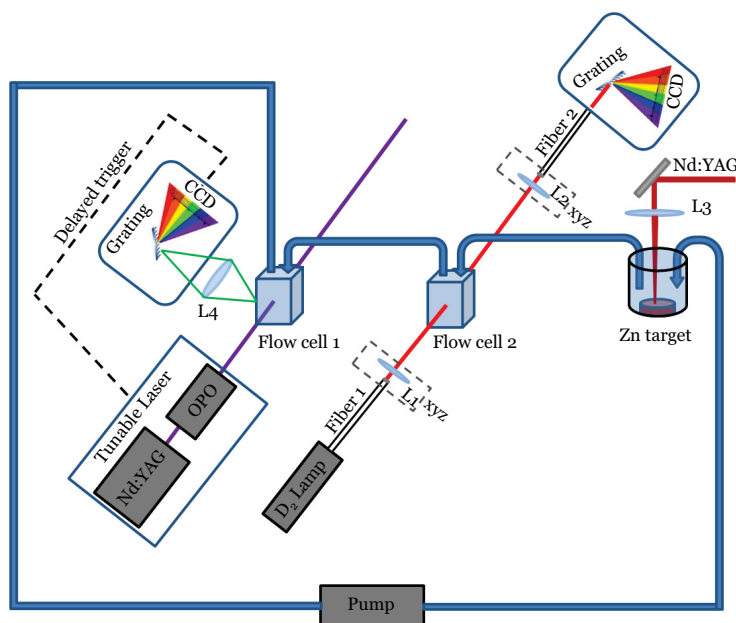
Figure 3.5: Experimental setup for in situ OA and PL measurement during laser ablation of a zinc plate in liquid environment.

flow cells (optical path=10 mm). The first flow cell was used to acquire the OA spectra by an optical fiber spectrophotometer (AVANTES 2000), equipped with a D_2 lamp and a grating which disperses the transmitted light into a CCD camera. The second flow cell was used to measure time resolved PL spectra by a tunable laser and the experimental apparatus described above for *ex situ* PL measurements. OA and PL spectra are averaged over 1 s and 10 s, respectively, to enhance the signal to noise ratio.

3.3.2   The Optical Fiber Spectrophotometer

Optical absorption spectra for *in situ* measurements are performed with an optical fiber AVANTES S2000 spectrophotometer working in the range 190-470 nm. The optical source is a deuterium lamp that injects light into the optical fiber consisting of pure silica core/F2-doped silica cladding with diameter of 200 μm. They are loaded with H_2 to better resist to the prolonged exposure to UV light without being deteriorated. The light carried by the optical fiber is used as the probe beam (PB), which is collimated by a lens (L1) so as to have a 3 mm diameter. Then, it passes trough the flow cell 1 containing the ablated material in colloidal solution. The transmitted portion of the PB is collected from a second lens (L2) coupled to another fiber that brings it to the detector. The two lenses are mounted on independent micrometric positioning controls (xyz), which permit to control the alignment of the PB to the sample thus optimizing the collection efficiency. The detector consists of a 1200 lines/mm gratings with blaze at 300 nm each for any channel, dispersing on a 2048 channels Charge Coupled Device (CCD) array. The latter is coated with a fluorescent compound to enhance its sensitivity in the UV.

   In order to perform time dependent in situ absorbtion measurements during and after the

end of a laser irradiation we adopt the following procedure. First, the D_2 lamp is disconnected from the fibers and it is acquired a dark reference signal on the Master channel $I_D(\lambda)$. Then, the lamp is connected again and the pump starts to flowing the liquid in the closed circuit. At a time t_0 before the irradiation begins, a reference signal, $I(\lambda, t_0)$, is acquired. Finally, the Nd:YAG laser is turned on and the laser ablation begins. Since the OA measurements are carried out in flow cell 1, which is a separate location from where ablation takes place (vessel), no scattered light from the Nd:YAG laser is detected by the CCD. Defining $I(\lambda, t)$ the signal acquired at time t by the detector, the difference absorption due to the evolution of the sample during PLAL after t is calculated as:

$$\triangle OD(t) = \log_{10}\left(\frac{I(\lambda, t_0) - I_D(\lambda)}{I(\lambda, t) - I_D(\lambda)}\right) , \tag{3.18}$$

this equation is valid in the approximation in which the dark signal does not depend on time. If one observes a temporal drift of the lamp and/or the detector, it is mandatory the subtraction of a second term at the Eq. (3.18), which is formally identical to the first one apart from being estimated from another channel (slave) wherein the light does not traverse the sample. The correction could be necessary since this is a single beam system in which the acquisition of the reference is performed only once, at the time t_0. However, after an instruments warm up, we have monitored the reference in the flow cell with water before the beginning of PLAL for each experiment. We observed that there are no changes in the reference spectrum for at least one hour, which is the typical duration of our experiments.

Chapter 4

ZnO NPs Synthesized by ns Pulsed Laser Ablation in Water

In this chapter we investigate ZnO NPs produced by pulsed laser ablation (PLAL) of a zinc plate in water by the experimental approach described in Chapter 3, based on the use of time-resolved luminescence and complementary techniques which allow to obtain the morphological and structural properties. This investigation clarifies important aspects of the photophysics of ZnO NPs and indicates that ZnO emission can be controlled by thermal annealing, which is important in view of optoelectronic applications.

4.1   Introduction

As discussed in detail in Chapter 1, Zinc oxide is a wide band gap semiconductor with great potential for a large variety of practical applications, such as piezoelectric transducers, photo-voltaics, transparent electrodes, gas sensors, bioimaging probes, drug delivery, light emitters and photocatalysis [2, 5, 10, 11, 69, 70]. Its direct band-gap of 3.37 eV (in bulk form) and the large exciton-binding energy of 60 meV [6,13] make ZnO especially promising for photonic applications in the UV or blue spectral range even at room temperature.

Several techniques have been used to synthesize ZnO NPs (see Chapter 2), they may confer specific properties related to dimension and composition of NPs [117–119]. Among them, some studies have demonstrated that it is possible to produce ZnO NPs by PLAL, and in particular, ablating a zinc metal plate in water [69, 142, 143]. Synthesis may take place by various mechanisms like nucleation and growth or ejection of hot drops from the metal target interacting with the solvent which provides a reactive environment that induces the zinc oxidation. Moreover, as shown in Chapter 2, the ablation product strongly depends on the other ablation parameters such as laser photon energy, fluence, repetition rate (RR), pulse duration, wavelength [137, 139–141].

In addition to the near-UV excitonic emission peak (3.3 eV), ZnO nanomaterials exhibit visible luminescence which strongly depend on the physical and chemical conditions occurring during their synthesis. One of the most debated luminescence is a green emission centered at 2.2-

2.4 eV, the origin of which is still matter of debate [81–83]. Proposed hypotheses on the origin of this green emission include zinc vacancies, oxygen antisites, oxygen vacancies and surface defects [10, 81, 88, 95–100]. For example, Zinc vacancies were related to green PL at 2.3 eV in bulk ZnO comparing the PL spectra for the samples with different Zn and O implantations [98], instead, oxygen antisites were assumed to explain a PL at 2.4 eV in ZnO films based on the rise of the green PL caused by annealing in O_2 [99]. Besides, as discussed in Sec. 1.4, a variety of mechanisms have been suggested to explain the recombination mechanisms producing the green emission. These range from recombination involving trapped electrons or holes in ionized oxygen vacancies (V_O) [36, 101, 102] to recombination mediated from sub-band-state of Zn_i [106] as well as double centres defects like ($V_O + V_{Zn}$) above the valence band [36].

All experiments reported so far to study the optical properties of ZnO NPs lack of a complete characterization with time-resolved PL measurements, which is mandatory to obtain a comprehensive view of the photophysics of luminescent defects or excitons and, in particular, of the emission mechanism responsible of the green PL. To this aim, one needs to obtain a thorough picture of the structural, morphological and optical properties of the produced ZnO NPs, a task which can only be achieved combining several experimental techniques. Moreover, thermal treatments in controlled atmosphere can be used as an additional method to give more information.

In this chapter we investigate ZnO NPs produced by PLAL of a zinc plate in water by the experimental approach, described in Chapter 3, based on the use of time-resolved luminescence and complementary techniques, that is Transmission Electron Microscopy (TEM), Atomic Force Microscopy (AFM), μRaman, ex situ treatments, used to probe the morphological and structural properties, thus providing a solid support to discuss the origin of the observed PL bands. A deep understand on the origin of the green emission is needed to control the emission capabilities of ZnO NPs. In addition, the defects responsible of the green emission could influence also the electrical properties, carrier lifetime [52, 53]. The control of defects concentration and their effect on the NPs properties is therefore essential to its successful application in gas sensors and optoelectronic devices.

4.2 Morphological Properties

The synthesis of ZnO NPs was carried out by ns PLAL of a Zinc plate placed at the bottom of a vessel containing 10 ml of deionized water. The first harmonic (λ=1064 nm) of a pulsed Nd:YAG laser operating at a repetition rate of 10 Hz and with an energy per pulse of 20-50-90 mJ, focused by a lens on the Zn target (spot size~2 mm). In order to maintain the same total fluence of 25.8 kJ/cm^2, the irradiation times of 67, 27, 15 minutes, respectively, were used in the three ablation experiments. During the PLAL experiments it is observed that the colorless liquid changed to a coloured suspension, indicating the production of NPs. At the end of PLAL, we obtained a brownish colloidal solution, which gradually changes to pale yellow in tens of minutes. The results here reported have been obtained on the stable colloidal solution.
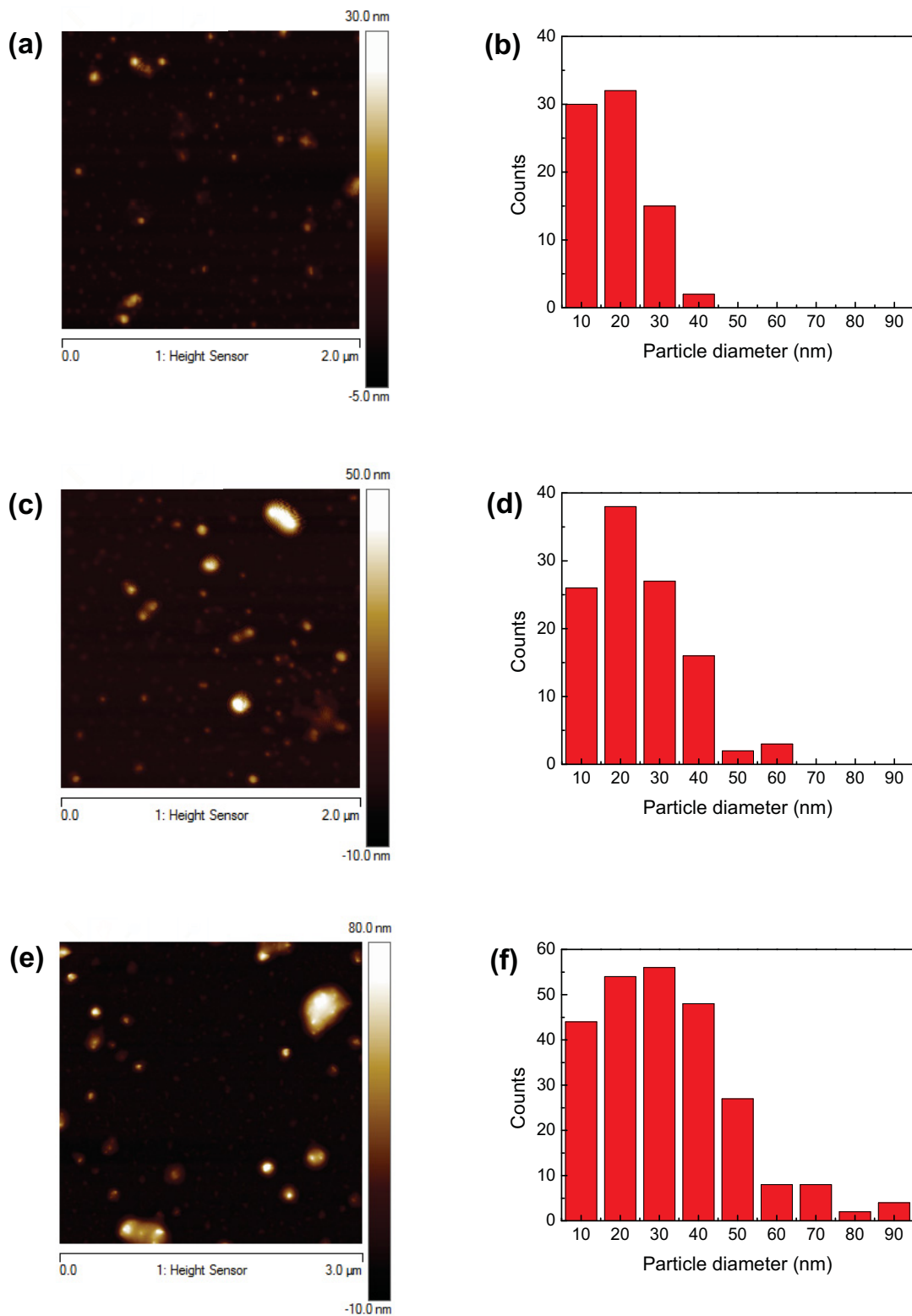
Figure 4.1: (a),(c),(e) AFM image 2×2 μm^2 of the dried colloidal solution of ZnO NPs produced by PLAL with energy per pulse of 20, 50 and 90 mJ, respectively; (b),(d),(f) Size distribution calculated from AFM image (a), (c), (e), respectively. The image is partly taken from [167]

The AFM images and particle size distributions of NPs are shown in Fig. 4.1. They reveal that the ablation products consist in broad distributions of spherical-like nanoparticles with sizes of the order of tens nanometers which are dependent on pulse energy provided during PLAL. In particular, we obtained a larger size distribution and a larger average NPs size on increasing the pulse energy. Indeed, the average size was about 18, 23, 30 nm for E_p=20, 50, 90 mJ, respectively. This dependence of the size distribution with pulse energy agrees with other results reported in the literature [129, 130, 138].

4.3   Structural Properties

In order to obtain the structure and chemical composition of the produced nanoparticles we performed HRTEM and EDX measurements dropping the colloidal solution over a holey carbon-film copper-grid at room temperature in air. Figs. 4.2 (a),(b) and (c) display the typical HRTEM images of three nanoparticles with d=30 nm, d=40 nm, and d=50 nm respectively, which highlight the formation of crystalline NPs. The magnified square regions of the nanoparticles evidence that the distances between adjacent lattice planes are 0.259±0.001 nm, 0.1630±0.0006 nm, 0.289±0.001 nm and 0.248±0.002 nm, which are consistent with the (002), (110), (100) and (101) crystalline plane distances of ZnO in wurtzite structure, respectively. Table 4.1 summarizes the lattice distance values obtained by HRTEM images and related crystalline planes as compared to the reported values by Kihara et al. [1]. It is worth noting that the (100) distance, 0.289 nm

(h k l)	(0 0 2)	(1 1 0)	(1 0 0)	(1 0 1)
Measured d(nm)	0.259±0.001	0.1630±0.0006	0.289±0.001	0.248±0.002
COD d(nm)	0.2602	0.1625	0.2814	0.2476

Table 4.1: Lattice distance values obtained from HRTEM images and corresponding crystalline planes compared to the values reported in ref. [1].

in our case, is slightly larger than the measured value for bulk ZnO (0.281 nm) [1]. Since the (002) distance of 0.259±0.001 nm agrees with the reported lattice parameter c=0.5206 nm, this finding can be attributed to slightly distorted lattice parameter a. Using the following crystal geometric equation for hexagonal lattices, we can calculate the lattice parameter a:

$$\frac{1}{d^2} = \frac{4}{3}\left(\frac{h^2 + hk + k^2}{a^2}\right) + \frac{l^2}{c^2}, \tag{4.1}$$

where (h,k,l) are the Miller index of the crystalline plane and a, c are the lattice parameters. By Eq. (4.1) we obtained the lattice parameter a= 0.334±0.001 nm, which is larger as compared to the expected value of 0.3249 nm. It is known that in highly defective nano-materials the lattice constants can be slightly different with respect to the bulk material [168]; for example, Zeng and co-workers showed a deviation of ZnO (100) lattice distance from the normal value in highly defective ZnO NPs produced by PLAL [88]. Further information about NPs can be derived by
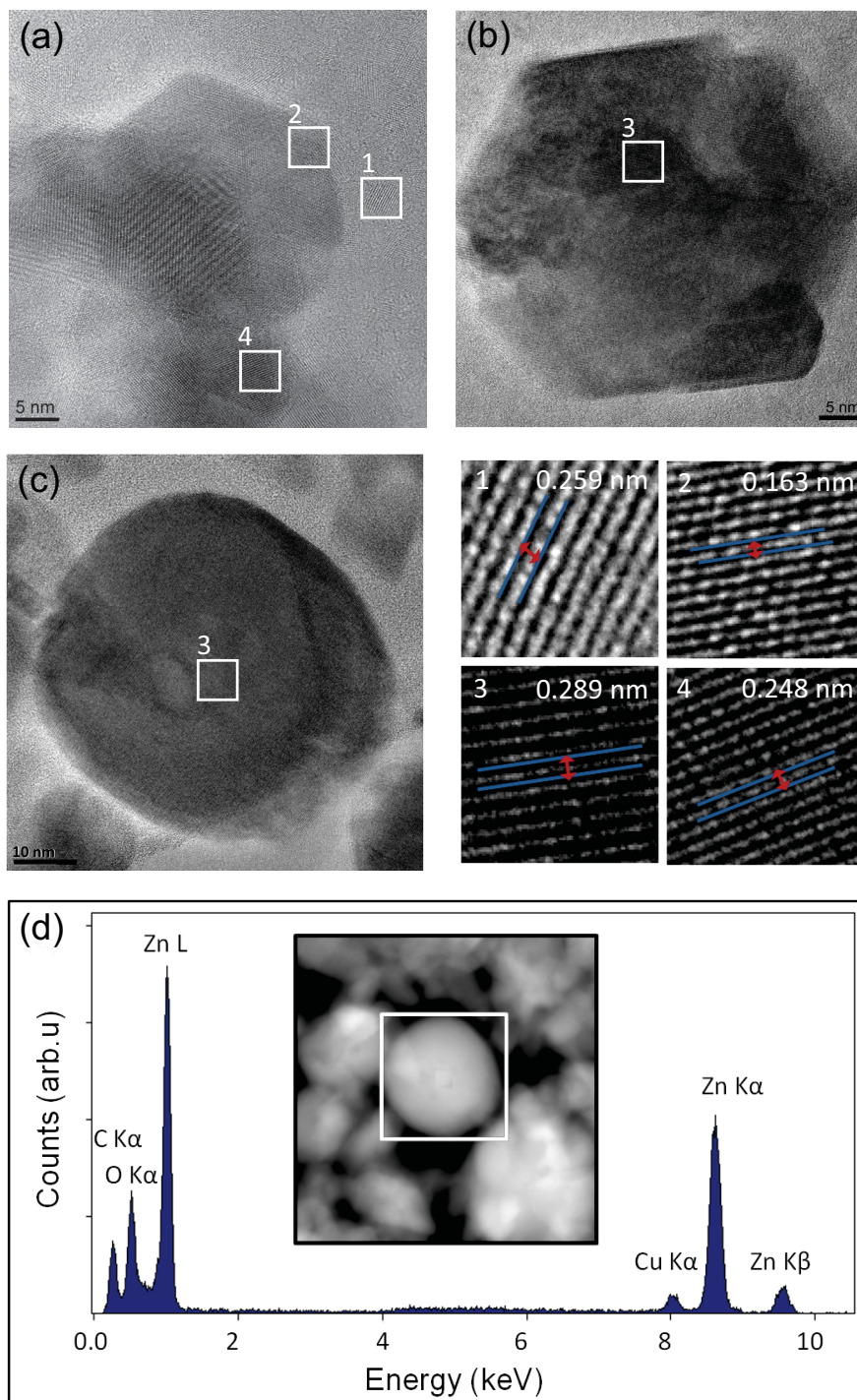
Figure 4.2: (a),(b) and (c) HRTEM images of three typical ZnO NPs with $d = 30$ nm, 40 nm and 50 nm, respectively; and related magnified images of selected regions which show the crystalline planes of the nanoparticle; (d) HAADF image of the NPs highlighting the area used for the EDXS analysis (square region) and the corresponding area-EDX spectrum. Figure partly modified from [167].

using high-angle annular dark-field imaging (HAADF) TEM combined with Energy-dispersive X-ray spectroscopy (EDXS). The Zn and O content within a single large nanoparticle is determined from EDXS line analysis, by scanning a square region within single NPs. Fig. 4.2 (d) shows

the HAADF image of a nanoparticle with d= 50 nm within the same square region. The EDX spectrum reported in Fig. 4.2 (c) reveals the characteristic X-ray lines of Zn-K, Zn-L and O-K series, besides the lines of Cu-K series from the grid and C-K from the amorphous substrate. The quantification of Zn and O content has been obtained by a fitting procedure and results in an average chemical composition of $Zn_{0.47-0.43}O_{0.53-0.57}$ for the NPs, which is consistent with the chemical composition of ZnO [169]. The small increase of the O content within nanoparticle as compared to that of ZnO, could be attributed to H_2O and O_2 molecules trapped inside the ZnO NPs during the formation processes involved in PLAL. However, a minor contribution due to the presence of oxygen on the amorphous substrate cannot be excluded.

4.4 Optical Properties

The purpose of this section is to describe our studies on the optical properties of the as-grown materials. To this aim, we acquired optical absorption (OA) and photoluminescence (PL) spectra, the latter were acquired by both steady-state and time resolved technique. Steady-state PL was mainly used to obtain excitation spectra by finely varying the excitation wavelength and to estimate the emission quantum yield (QY). Time resolved PL was used to investigate the PL dynamics which are responsible to the UV and visible emission of ZnO NPs. The OA, steady state PL and PLE spectra of ZnO NPs dispersed in water are shown in Fig. 4.3. The absorption spectra of Fig. 4.3 (a) show the typical sharp edge of wurtzite ZnO and are located at the same spectral position for the three samples. Figs. 4.3 (b) and (d) display two emission spectra of the nanoparticles obtained at 20, 50 and 90 mJ per pulse and excited upon UV excitation (4.66 eV) and acquired at two different spectral regions 2.8-3.7 eV and 1.6-3.0 eV, respectively. All PL spectra are normalized for the optical density at the excitation energy so that the PL signals are normalized to the ZnO content in the solutions. The first is a narrow UV emission peaked at ∼3.32 eV and with a FWHM of about 0.2 eV; the second is a broad green band centered at ∼2.25 eV with a FHWM of 0.6 eV. In agreement with the literature results reported in Chapter 1, these emission bands could be assigned to excitonic emission and the green defect emission of ZnO. We note the presence of a peak around 3 eV in the PL spectra of Fig. 4.3 (b) which makes asymmetric the curve at 3.32 eV and its intensity is independent of sample. This contribution was also observed placing the quartz cell in the sample chamber with only deionized water, thus we suppose that it is due either to an unexpected contribution of quartz cell or to an instrumental artifact. In the inset we report the defect/exciton intensity ratio as a function of the pulse energy used during PLAL. This ratio can be used to evaluate the sample quality of ZnO nanostructures because it depicts the concentration of defects with respect the amount of ZnO [90, 92, 93]. One can note that the defect concentration does not show a trend with increasing the pulse energy, thus revealing that the samples "quality" does not depend on the pulse energy. By comparing the PL intensity of the sample emission with that obtained from an aqueous solution (pH=13) of fluorescein excited at 470 nm, used as a reference of known QY_R=0.95, it is possible to estimate the quantum yield of the green luminescence. To this aim,

the fluorescence from the sample and the reference were measured under the same conditions and geometry. Using (3.4) we have obtained the quantum yield of both green and excitonic PL to be around 0.2% and 0.1%, respectively.
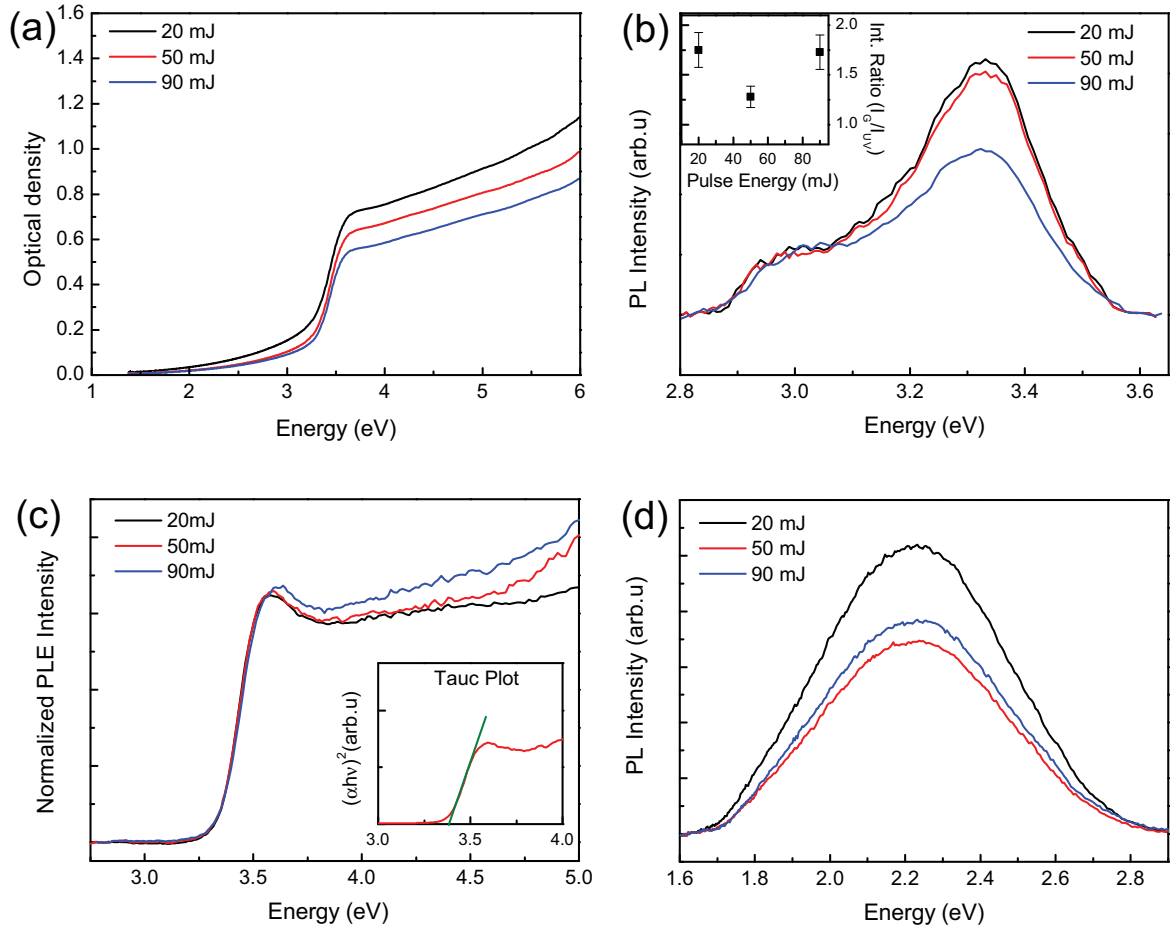
Figure 4.3: (a) UV-Vis optical absorption of the colloidal solution prepared with laser energies of 20 mJ, 50 mJ and 90 mJ per pulse; (b) ZnO exciton- and (d) defect-related steady state PL excited at 4.66 eV, inset in panel (b) shows the defect/exciton intensity ratio as a function of the used pulse energy. (c) Excitation spectra of the three samples obtained monitoring the defect emission intensity at 2.25 eV [167], inset shows the Tauc plot of the excitation spectrum obtained at 50 mJ in the hypothesis of direct band-gap.

Monitoring the emission peak of the green band (2.25 eV) we obtained its excitation spectrum (PLE) which exhibits a sharp threshold at ∼3.5 eV and appears almost flat at higher energies (see Fig.4.3 (c)). The shapes are identical in all samples and indicate that the green band is excited only by photon energies larger than the band-gap, thus suggesting the excitation initially involves a band-to-band transition producing a free electron-hole pair [167]. In fact, as already discussed in Chapter 3, plotting the squared product of OA and photon energy as a function of photon energy it is possible to extrapolate a linear region which intersects the energy axis at the band-gap (see the green straight line in the inset of Fig.4.3 (c)), as expected for direct allowed transitions. In this way, we estimated a value of E_g=3.38±0.01 eV, which is consistent with the

band-gap of wurtzite ZnO in bulk form [6,12,13]. We don't report the PLE spectrum of excitonic emission because, when the excitation energy falls in the edge region, the emission peak is too close to excitation and the excitonic lifetime is of the order of excitation pulse rise time (as we show below), thus is not possible single out the exciton contribution to the scattered excitation pulse. However, we are able to verify that its PLE spectrum follows the absorption curve keeping flat at photon energy larger than 4 eV. It is worth noting that, despite nanoparticles size distributions of the three samples are different, all samples show the same optical band-gap. Moreover, there is no any effect on the excitonic PL spectrum which is peaked at 3.32 eV, that is 60 meV below the optical band-gap obtained from the PLE spectrum, matching the value of the exciton binding energy E_b in bulk wurtzite ZnO. This can be attributed to the fact that since almost all NPs are larger than excitonic Bohr radius (2.23 nm) [2], thus they have optical properties similar to the bulk material.

In order to complete the optical characterization we also performed time resolved PL on the ZnO NPs. Fig. 4.4 (a) reports the excitonic emission of the sample produced with 90 mJ per pulse, acquired by time resolved spectra, excited at 4.66 eV and detected with a time window T_W=10 ns and a time delay T_D=0 ns respect to the arrival of laser pulses. By using time resolved technique we were able to eliminate the signal around 3 eV, in this way, a symmetric and cleaner shape of the PL curve was obtained. It evidences a Lorentzian shape with a FWHM of 0.20 eV and peaked at 3.32±0.01 eV confirming the attribution of this PL signal to the excitonic emission. In particular, based on Tokoyozawa theory, this shape reveals that the mobile nature of the exciton prevails with respect the tendency to be momentarily localized in the lattice due to interaction with phonons [45, 46]. As discussed in the Sec.1.1.3, Lorentzian width (FWHM) is determined by energy-time uncertainly principle, because the exciton remains a finite time in the K=0 state due to phonon-induced scattering toward K≠0 levels. Hence, considering the measured value of FWHM=0.2 eV and using the energy-time uncertainty principle, we can obtain the minimum life time wherein the exciton remains in the state with K=0: $\Delta t \geq \hbar/FWHM \sim 5 \times 10^{-15}s$. This PL band is characterized by a sub nanosecond lifetime, hence, in order to estimate the exciton lifetime it is mandatory to take into account the instrument response using a fitting function which consists of the convolution between a single exponential decay function, $exp(-t/\tau)$, and a Gaussian curve accounting for the laser profile. Based on this procedure, Fig. 4.4 (b) shows the time decay curve of the PL band and the best fit function from which we obtain the lifetime of the excitonic PL, τ=800±100 ps. This value is much smaller than the reported value in high quality bulk ZnO materials which reaches several nanoseconds [47, 48], it substantially agrees with the lifetime in the range of hundreds of picoseconds found in ZnO nanostructures [75, 77–79]. As argued in Sec. 1.3, in these works the authors suggested that the exciton lifetime is largely determined by non-radiative recombination due to a high defect density, although no obvious correlation was found between the excitonic PL decay times and defect emission intensities [77].

The PL spectrum of Fig. 4.4 (c), excited at 4.66 eV and detected with T_W=10 ms and T_D=20 ns, shows the broad green emission centered at 2.2 eV, while Fig. 4.4 (d) reports the
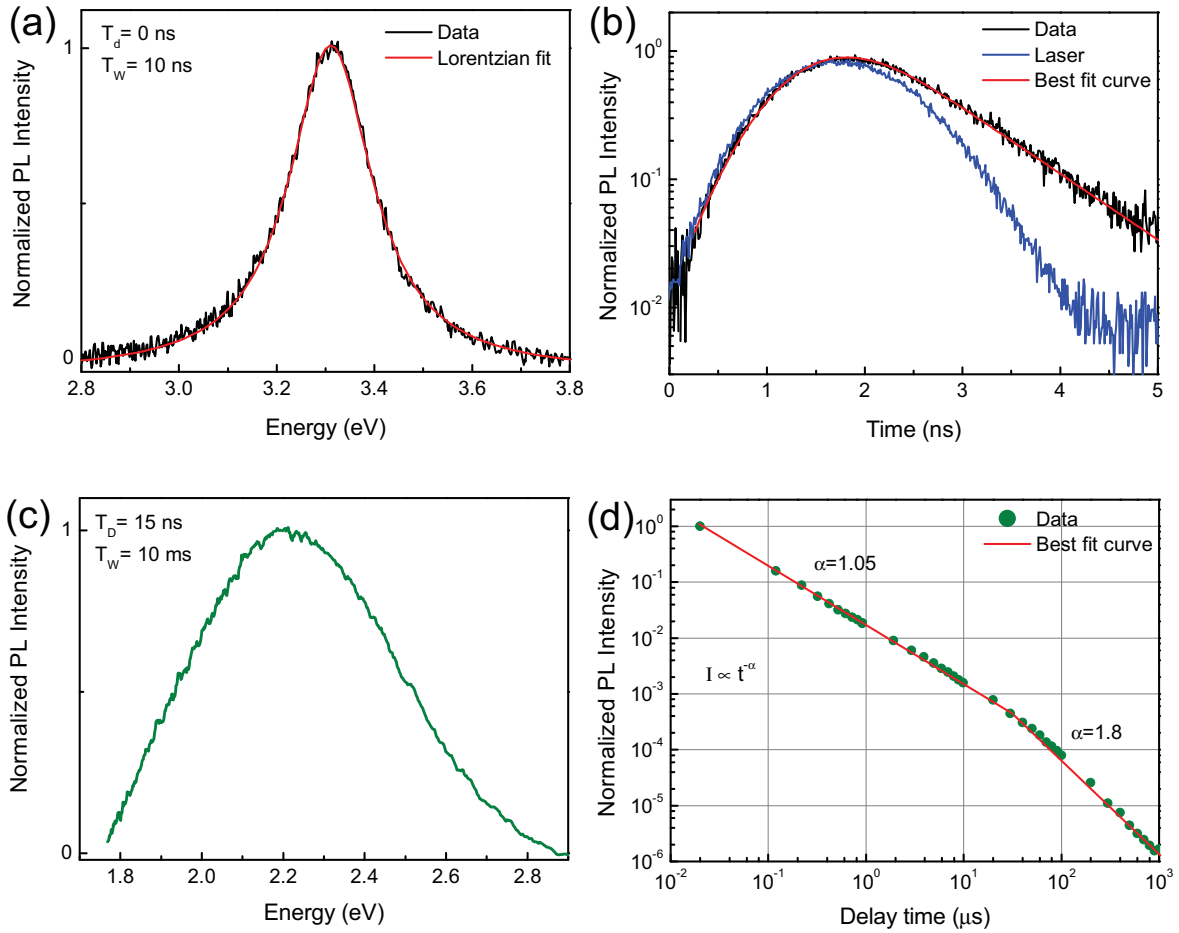
Figure 4.4: ZnO exciton-(a) and defect-related (c) time resolved luminescence PL excited at 4.66 eV. The excitonic luminescence was fitted by a Lorentzian curve (red solid line); (b) Time decay curve of the exciton PL;the smooth solid line represents the best fit to the PL decay using a convolution function between a single exponential and the instrument response function (blue line).(d) Time decay curve of the defect related PL; the smooth solid line represents the best fit linear curve. Figures are taken from [167].

time decay curve of the PL band in a log/log scale. Data follow two different linear trends consistent with a power law time dependence $I \propto t^{-\alpha}$ across 5 decades of time; the first one in region from 20 ns to 40 μs and the second one from 40 μs up to 1 ms. By a fitting procedure we get α=1.05$\pm$0.05 and α=1.8$\pm$0.1 for the two ranges of time. A power law decay kinetics of the PL intensity with $\alpha \approx 1$ has been observed for self-trapped excitons in irradiated single crystals of anatase TiO_2 and attributed to tunneling recombination of trapped electrons and holes [170]. In a recent work Huntley [171] has shown that a power law of the PL decay with $\alpha = 1 - 1.5$ can result from the tunnelling of trapped electrons to recombination centres which are randomly distributed in space. Instead, the power law decay for t>40 μs nearly matches the hyperbolic t^{-2} time dependence typical of bimolecular recombination for a balanced donor-acceptor system [68, 172]. Such behavior suggests that the defect PL decay in the first three decades of time is driven by tunneling of trapped carriers to recombination centres (α=1.05). However, for sufficiently larger time (t>40 μs) most of the electrons or holes come out from their

trap, thus the recombination takes place by the electro-hole diffusion and the main mechanism becomes a bimolecular recombination (α=1.8). We observe that, in contrast with previous works [101, 106], the decay kinetic does not change varying the excitation energy in the whole range of the excitation spectrum (from 3.3 to 5 eV). This fact indicates that exciting over the band-gap (E>E_g) the surplus energy provided to the created electron-hole pair as kinetics energy does not influence the recombination mechanism that produces the green luminescence.

As above reported many point defects have been suggested for the green emission [10,81,100], the most accepted being the oxygen vacancy [88, 95, 96]. Since ZnO NPs were synthesized by PLAL in water of a Zn plate, they are formed under Zn-rich conditions, thus the most likely defect types are oxygen vacancies and Zinc interstitial, having the lowest formation energy (see Sec.1.1.4). However, PL and PLE are in contrast with the expected results for Zinc interstitial in ZnO NPs. In fact, Zeng and co-workers have reported a PL band, attributed to Zinc interstitial, peaked at 2.8 eV in ZnO NPs produced by PLAL in water of a Zn plate [88, 94], which is at larger energy compared to the 2.2 eV PL band showed in this work. Besides, the PLE spectrum of this blue PL reveals a peak at energy close to band-gap (3.2 eV) and also a slowly dropping tail, which continues into the violet region, very different with respect to the sharp-edged green PLE in the UV region described above [88].

4.5 Ex-situ Treatments

In this section we will deal with the effects of ex-situ treatments on the as-grown sample obtained with E=90 mJ per pulse, and in particular, we performed surface treatments and thermal treatments. The first was performed with the main purpose to localize the defects in ZnO NPs, therefore if defects lie at the surface or inside NPs, the second to obtain more information on the defect type and luminescence mechanism responsible of the green emission origin.

4.5.1 Surface Treatments

As early discussed (Sec.1.4), surface states have been argued by He and coworkers [104] to generate the green emission at 2.2 eV. Their statement is based on the effect on the steady state luminescence of the water pH and of surfactant molecule (LDA) added to the colloidal solution containing ZnO NPs. In order to verify this assignment we have studied the defect-related luminescence as a function of pH of the solution. Fig. 4.5 reports the emission curves of the colloidal solution, acquired with the same temporal parameters of Fig. 4.4, at various pH values, ranging from 3.5 to 10, and with surfactant SDS molecules. This molecule is characterized by an anionic head group which surrounding the NPs can potentially interact with defected located at their surface. We note a cut peak at 3.1 eV on the left of excitonic emission (see Fig. 4.5). Since it was also detected using a quartz cell containing only deionized water, we suggest that it could be an impurity of the Nd:YAG laser used for exciting the samples. Inset shows the corresponding OA curves where we note that the line shapes are substantially independent of the environment surrounding NPs. All PL spectra are normalized for the optical density at the excitation energy

(4.66 eV) so that the PL signals are normalized to the ZnO content in the solutions. Fig. 4.5 (b) clearly shows that varying the pH from 3.5 up to 10 and adding SDS molecules, even with concentration (0.1 M) over the critical micelle concentration (0.008 M), the intensity of the green emission does not change. The fact that the extreme alteration of the chemical conditions does not produce any effect on the defect-related PL can be understood as the lack of interaction between defects in the grown ZnO NPs with solvent molecules. This suggests that the formation of defects occurs inside the NPs rather than at the surface. Furthermore, the excitonic emission reported in Fig. 4.5 (a) surprisingly show an enhancement of the peak with decreasing on pH, while it remains stable upon adding SDS molecules compared to the sample in water with pH=7. This behavior can be related to the passivation of surface defects, which are different from those producing the green band, due to interaction with H_3O^+ ions. Indeed, excitons could bind to defects which act as recombination centers, thus their dynamics and related luminescence are strongly influenced by defects. Thereby, an increasing number of H_3O^+ ions causes a decreasing of defects and so an enhanced excitonic luminescence up to a factor of three compared to the intensity in neutral water. This behavior has been also observed in other semiconductor in nanometric form, such as silicon NPs [173].

4.5.2 Thermal Treatments

In the previous section we have demonstrated that defects emitting the green emission at 2.2 eV lie inside ZnO NPs rather than at the surface. In order to better identify their nature thermal treatments in controlled atmosphere are a powerful investigation tool. In fact, studying the effect of thermal annealing on the structural properties and green emission we can verify if the point defects responsible of the green emission are oxygen vacancies. For these reasons we performed thermal treatments on the powder of ZnO NPs ($W_T \sim 6$ mg) obtained by the dried colloidal solution produced by ablation. These experiments were done in a Parr Reactor equipped with a temperature control system. Sample was put inside the vessel and the heater is switched on after that the vessel was filled with the desired gas. Treatment was performed at 300 °C (573 K) in 100 bar of oxygen or inert helium atmosphere for 3 hours, corresponding to a number of oxygen molecules in the reactor volume ($\sim 10^{-3}$m^3) of n_{O_2}=10^{24}. At the end of thermal treatment, the heater is switched off and the samples are cooled in the treatment atmosphere. Heating and cooling times are about 2 hours, respectively. Taking into account the density of ZnO (δ_{ZnO}=5.6 g/cm^3), the main radius of 15 nm (R) and considering the spherical shapes of NPs, the weight of a single NP can be estimated by

$$W_{1NP} = \frac{4}{3}\pi R^3 \cdot \delta_{ZnO} \sim 10^{-17}g. \tag{4.2}$$

Then, we obtain the total number of NP in the sample $N_{NP} = W_T/W_{1NP} \sim 10^{14}$ and, being the molecular weight of ZnO 81.37 g/mol, we can calculate the total number of ZnO molecule which constitute NPs, $n_{ZnO} = N_A W_{1NP}/W_{mol} \sim 10^5$. Thereby, we can infer that in this thermodynamic conditions there are $\sim 10^{10}$ O_2 molecules per NP, which being more than ZnO
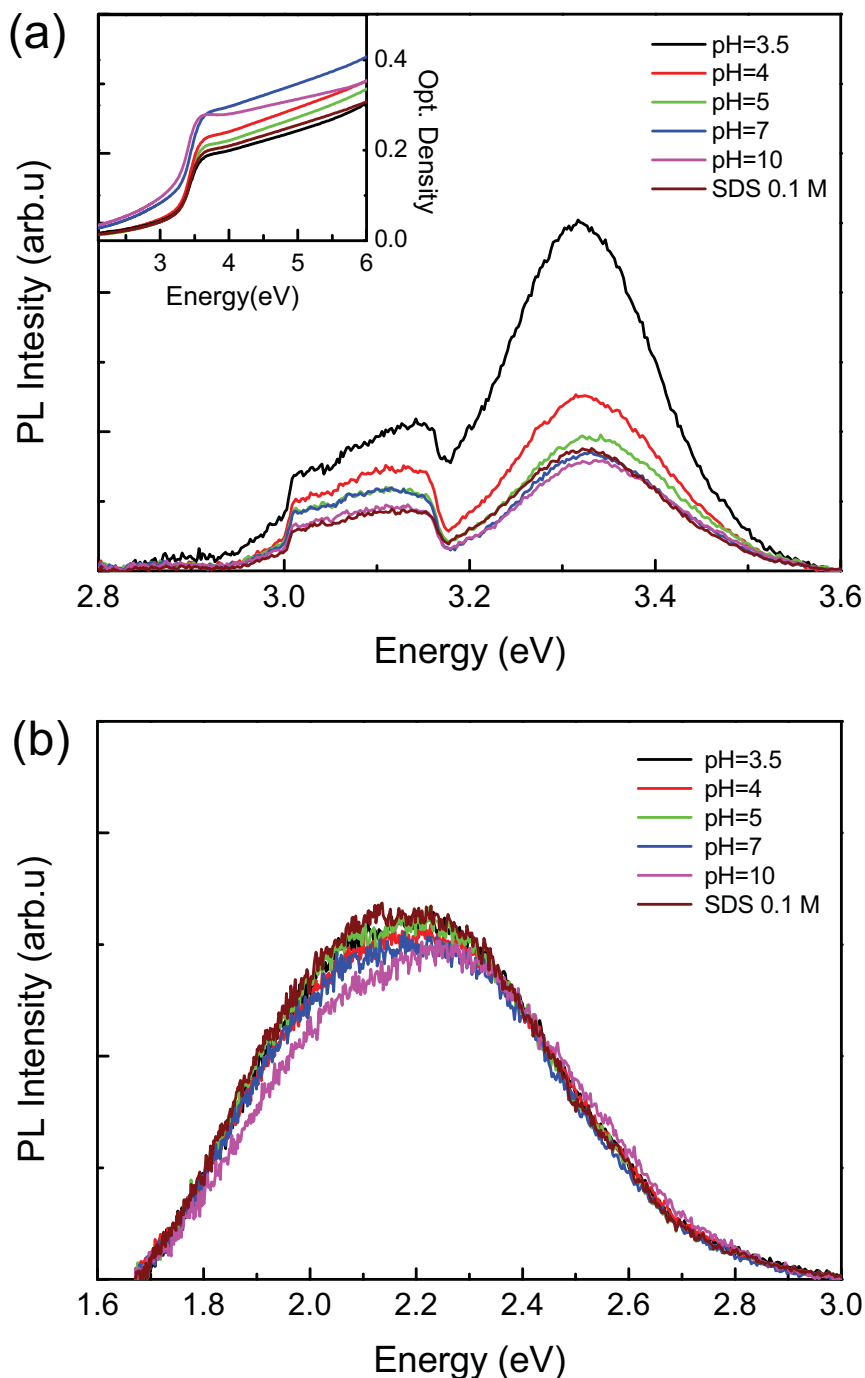
Figure 4.5: ZnO exciton-(a) and defect-related (b) time resolved luminescence PL excited at 4.66 eV acquired upon changing the pH of water or added SDS 0.1 M added in solution. Inset in panel (a) shows the OA spectra of the samples at various pH and with SDS 0.1 M added in solution. Figure (b) is taken from [174].

molecules per NP ($\sim 10^5$) might significantly affect the NPs stoichiometry reducing oxygen vacancies. Taking into account the diffusion constant in defective ZnO nanostructures for O_2 reported in literature $\varrho = 10^{-14} - 10^{-15}$ cm^2/s at 600 K [175], during thermal annealing, oxygen molecules present in atmosphere can diffuse through the nanoparticles in a time obtained by

$t = R_{NP}^2/6\varrho = 10^2 - 10^3$ s. In any case, this value is much shorter than the treatment time, thus O_2 molecules can easily cross the ZnO NPs.
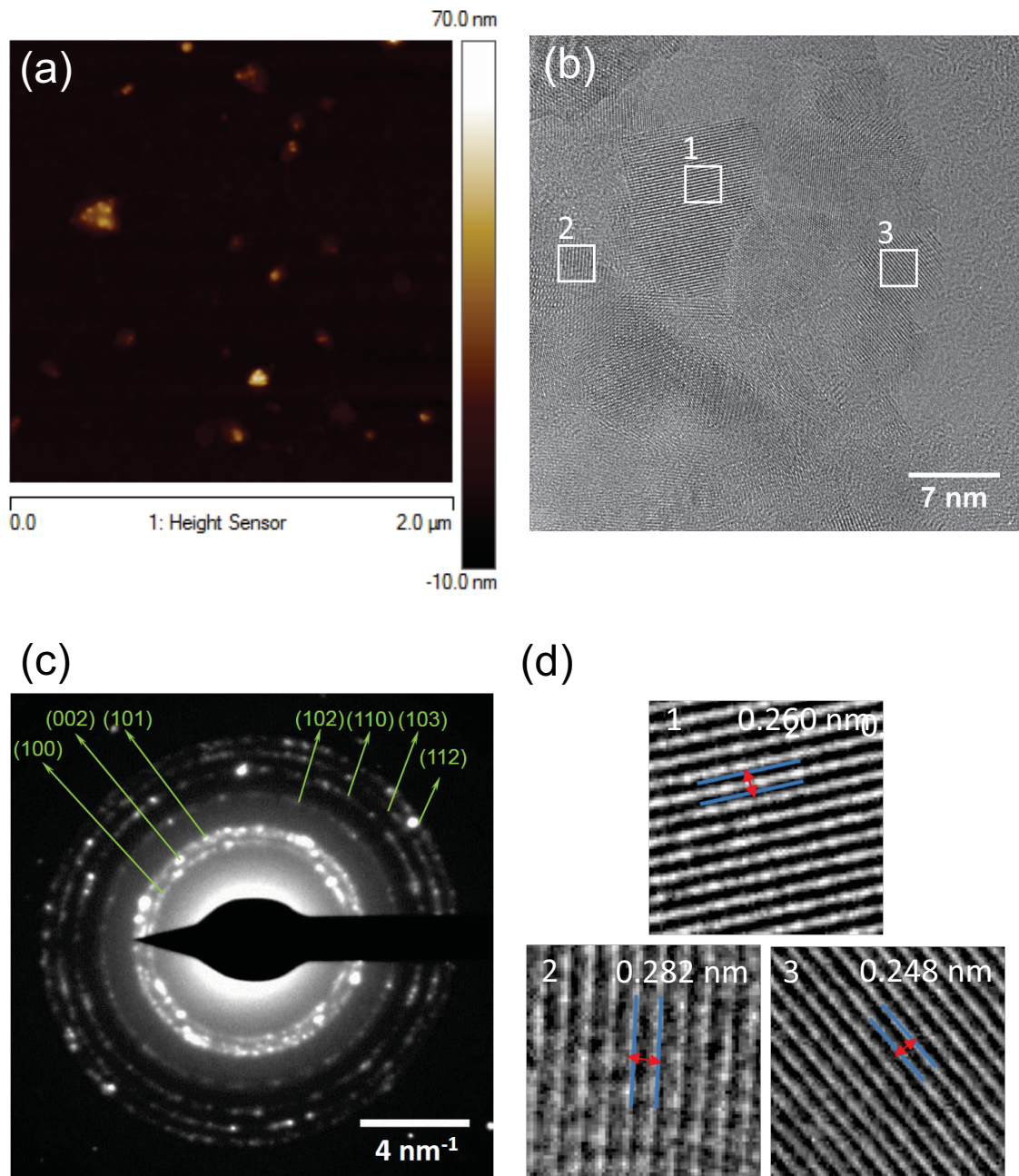
Figure 4.6: (a) AFM image $2 \times 2 \ \mu m^2$ of ZnO NPs taken after the thermal treatments at 300 °C in 100 bar of oxygen atmosphere. (b) SAED pattern obtained from a selected area of a HRTEM image containing several ZnO NPs, arrows indicate the lattice planes of ZnO in wurtzite structure. Figure taken from [167]

Morphological and structural properties of the treated ZnO NPs powder in O_2 atmosphere are reported in Fig. 4.6. The AFM image (Fig. 4.6 (a)) shows that NPs maintain size of tens of nanometers as for the untreated sample. HRTEM image (Fig. 4.2 (b)) displays three of the

crystalline plane of ZnO NPs; the magnified square regions ((Fig. 4.2 (d))) of the nanoparticles evidence that the distances between adjacent lattice planes are 0.260±0.001 nm, 0.282±0.001 nm and 0.248±0.002 nm, which are consistent with the (002), (100) and (101) crystalline planes distances of ZnO in wurtzite structure, as for the untreated sample. We highlight that the distance between lattice plane (100), 0.282±0.001 nm, is consistent with the expected value (0.281 nm). Moreover, SAED pattern (Fig. 4.6 (c)) demonstrates that ZnO NPs are crystalline and all observed Debye-Scherrer rings can be attributed to the hexagonal ZnO with lattice parameters a= 0.325 nm and c=0.521 nm. Thus, NPs after thermal treatments preserve their crystalline structure. In addition the lattice parameter a= 0.334±0.001 nm obtained in the untreated sample reduces down to the reported value for defect free ZnO (0.3249 nm) suggesting a reduction of defects inside NPs. This results demonstrate that treatment does not produce a significant variations on the structure and particle sizes. The same results have been obtained for ZnO NPs treated in He atmosphere.

Fig. 4.7 reports the excitonic- and green- related PL bands of the ZnO powder acquired before and after thermal treatment in oxygen and in helium atmosphere. We note that the excitonic PL is not detected in the powder form of the sample: we suggest that it is quenched by aggregation of NPs. Thus, to acquire the excitonic PL we dissolved the powder of ZnO NPs (treated and untreated) in deionized water. The PL measurements of the two signals were performed with the same time parameters of Fig. 4.4. It is evident that the intensity of the green band after thermal annealing in oxygen atmosphere decreases of about seven times compared to the as grown powder. In addition, we observe a concurrent increase of a factor of three of the excitonic luminescence. In general, competition of the green- and the excitonic- PL emissions is found in ZnO: when the green band is strong, the excitonic band tends to be small or absent and conversely [75, 95, 176, 177]. Indeed, as previously discussed, the ratio of the visible defect-to-UV emission can be used to evaluate the sample quality because it depicts the concentration of defects in ZnO.

Studying the effect of thermal annealing on Raman spectrum it is possible to gain information about changes in the structure of ZnO NPs. The μRaman spectra of the ZnO NPs acquired before and after thermal treatments are reported in Fig. 4.8. As already reported (Sec. 1.1.2) Raman peaks at 334 cm^{-1}, 438 cm^{-1}, 565 cm^{-1} correspond to $E_2^{(2)}$, $E_2^{(2)} - E_2^{(1)}$ and $A_1(LO)$ modes of ZnO in wurtzite structure [32]. The most evident change of the Raman spectra induced by the thermal annealing involves the intensity of the peak at 565 cm^{-1} accompanied by a blue shift up to 573 cm^{-1} that is the expected value for ZnO Bulk. This peak, which dominates the spectrum of untreated ZnO NPs, reduces of a factor of six after thermal treatment. It is worth noting that this mode is almost negligible in bulk ZnO, which is due to a cancelation between the deformation and Fröhlich contributions to the LO phonon scattering cross section [33]. However, the presence of defects such as oxygen vacancies or zinc interstitials can strain the structure inducing an enhancement of A$_1$(LO) phonon mode [34, 35, 105, 177, 178]. Indeed, being our ZnO NPs rich of defects, as usual in most ZnO nanostructured materials, this peak is prominent compared to the $E_2^{(2)}$ mode [32]. As previously discussed in the Sec. 1.4, in ZnO films fabricated
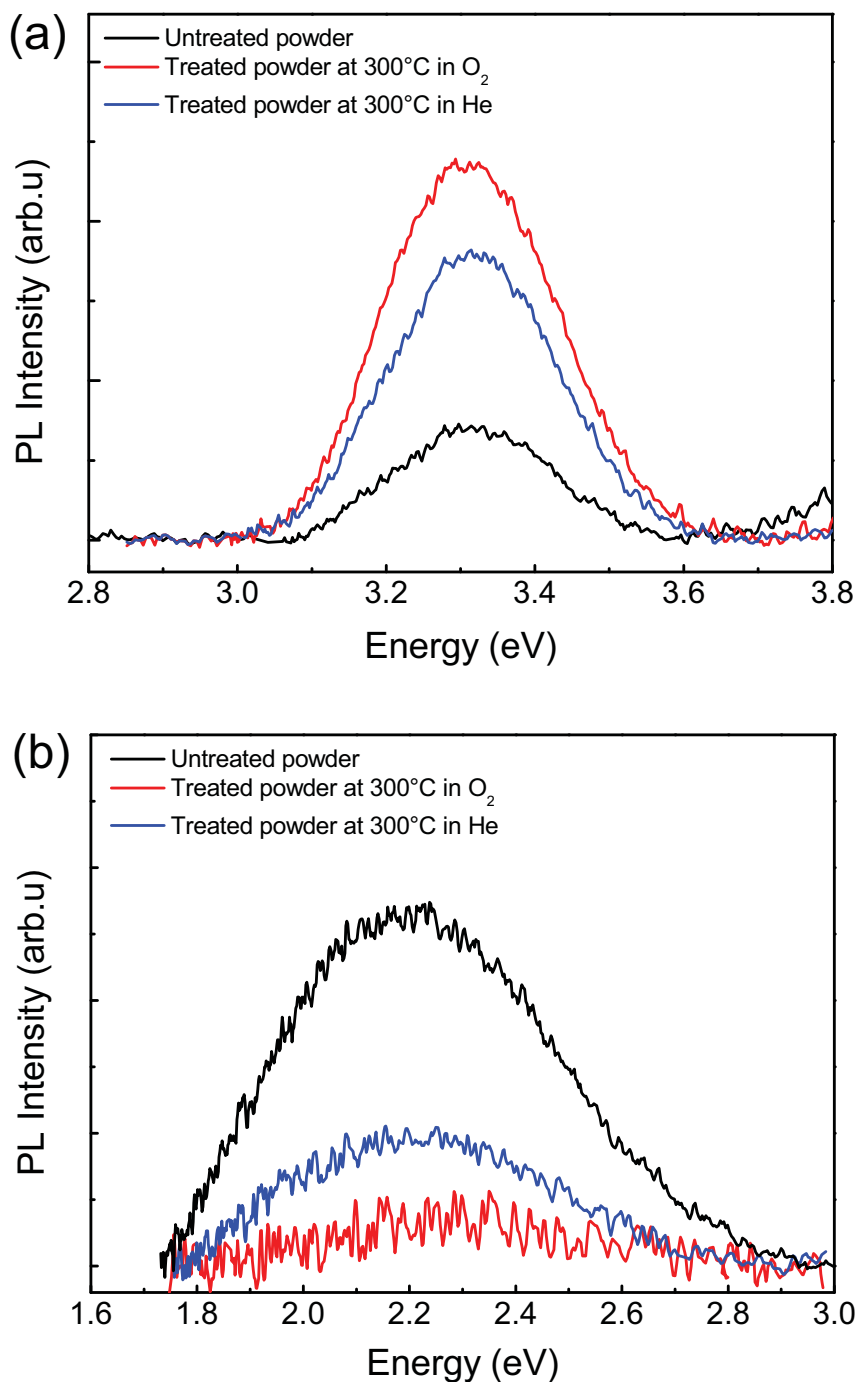
Figure 4.7: Excitonic- (a) defect- (b) related PL , excited at 4.66 eV, of the ZnO NPs powder produced by PLAL acquired before and after thermal treatment at 300 °C in 100 bar of oxygen (red line) and helium (blue line) atmosphere. Figure modified from [167]

under different O_2 pressures, the Raman peak at 579 cm^{-1} is reported to decrease with the increase of O_2 pressure [105]. This finding is ascribed to the reduction of defect states. For ZnO single crystals, P ions implantation is reported to increase oxygen vacancies and to enhance the Raman peak at 575 cm^{-1} [34]. Overall, the decrease of the A_1(LO) peak (Fig. 4.8), the reduction of defect PL (Fig. 4.7 (b)) and the increase of the excitonic PL (Fig. 4.7 (a)), observed
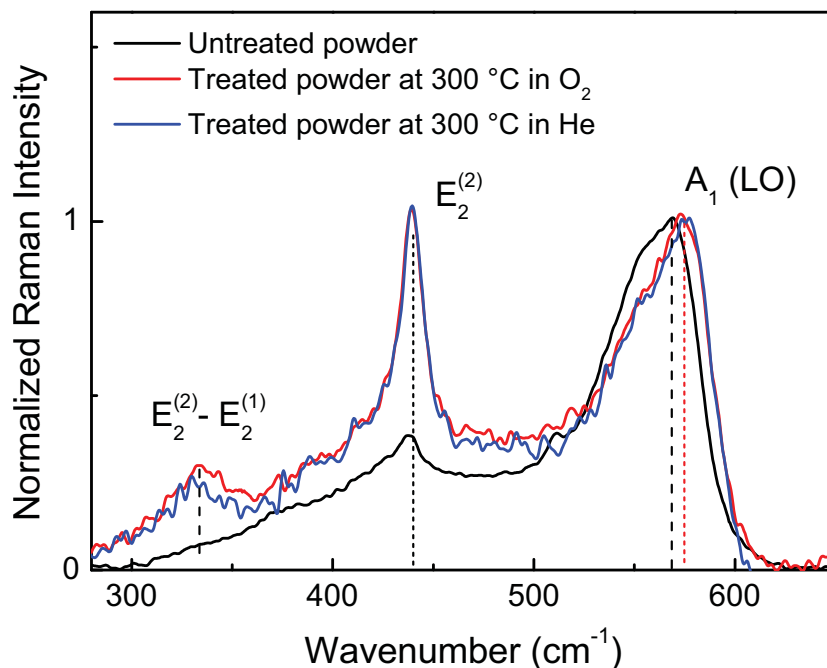
Figure 4.8: μRaman spectrum of the ZnO NPs produced by PLAL acquired before and after thermal treatment at 300 °C in 100 bar of oxygen (red line) and helium (blue line) atmosphere. Raman intensity are normalized to the difference between the intensities of the $A_1(LO)$ raman peak and background. Figure taken from [167]

here upon treatment in O_2, can be explained as an effect of the reduction of oxygen vacancies. O_2 molecules react with oxygen vacancies and, being in sufficient numbers, they complete the oxidation process of ZnO NPs which are slightly substoichiometric. In this way, O_2 molecules reduce the concentration of defects in ZnO NPs. Rather unexpectedly, we found that thermal treatments in He atmosphere also cause the same reduction of the $A_1(LO)$ peak (see Fig. 4.8), but they produce a different quantitative effect on the optical properties of the ZnO NPs. In particular, we obtained an intermediate reduction of the green PL (a factor of three) with respect to the oxygen atmosphere (a factor of seven) and a weaker increase of the excitonic PL (as from Fig. 4.7). This annealing effect in He atmosphere can be explained considering that H_2O or O_2 could already be present and trapped inside the ZnO NPs left by their formation processes involved during and after PLAL. Consistently, EDX spectrum shown in Fig. 4.2 (d) reveals an excess in oxygen content for the ZnO NPs. These molecules, left by the oxidation processes involved during PLAL, during the annealing can diffuse through the NPs. In this way, complete the oxidation process reducing the number of oxygen vacancies inside ZnO NPs. This leads to the decrease of both green PL and $A_1(LO)$ mode and to the rise of the exciton PL. In the case of the thermal annealing in oxygen atmosphere we added oxygen molecules which enter in the NPs; this process induces a further oxidation and consequently a further reduction of the oxygen vacancies. Consistently, we observe a further decrease of the green PL and a concurrent further increase of the excitonic PL. Summarizing, these results suggest the attribution to oxygen vacancies as defect responsible of the green emission at 2.2 eV. In the next chapter, we'll discuss

further arguments through the analysis of results obtained by *in situ* optical measurement which strongly support this assignment.

4.6   PL Model
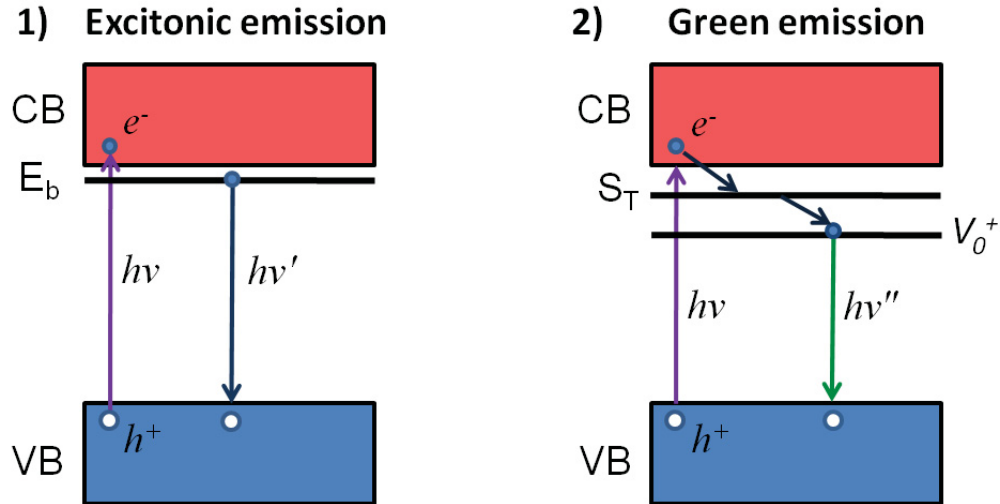
Figure 4.9: Photoluminescent processes suggested for ZnO NPs: 1) typical exciton emission; 2) recombination of a shallowly trapped hole with a deeply trapped electron into singly ionized oxygen vacancies. Figure taken from [167]

On the basis of our experimental results we propose two mechanisms leading to the PL emissions (illustrated in Fig. 4.9): one is the typical exciton emission or near-band-edge emission, *i.e.*, photo-generated electrons recombine with holes in the valence band or in traps near VB, producing the PL band peaked at 3.32 eV with a lifetime of about 800 ps. As for the visible emission at 2.2 eV related to the oxygen vacancies, we propose that the recombination occurs between a hole in the VB and an electron deeply trapped in a singly ionized oxygen vacancy. The energy level of this oxidation state of the oxygen vacancies has been determined by Janotti and co-workers by density-functional calculations to be about 1 eV below the CB [5], which is consistent with the peak position of the green PL. Finally, in order to take into account the power law decay discussed above, we propose the electron to be temporarily trapped in an unknown trap state (S_T in Fig. 4.9). From this state, the electron tunnels into a double ionized oxygen vacancy (V_O^{2+}) which become a singly ionized oxygen vacancy defect (V_O^{+}). As a consequence of the reduced number of oxygen vacancies by thermal annealing, we suggest that the competition between the green- and the excitonic- PL emissions is due to a more favorite excitonic radiative channel than the defect mediated recombination. Our data partly agree with the statements argued in the Sec. 4.4, indeed, using the quantum yield value (QY=0.001) we can obtain the K_r=QY/τ= 1.25x10^6/s and K_{nr}=(1-QY)/τ=1.25x10^9/s, that is, $K_{nr} \gg K_r$. Therefore, excitons life time is governed by non-radiative recombination rate K_{nr} due to the presence of oxygen vacancies inside ZnO NPs. However, according to our model K_{nr} includes an

charge transfer of the electrons, K_{ET}, from the CB to the trap states ST from which subsequently the tunneling towards the recombination centers (oxygen vacancies) occurs.

We observe that the mechanism for the green band at 2.2 eV is different from latest proposed models consisting of a recombination involving free electrons in CB with double-defect centers V_{ZnO} (oxygen vacancy + zinc vacancy) above the VB [36], or oxygen vacancies indirectly assisted by zinc interstitial [80]. In the first case, Li et al. [36] based only on the optical spectroscopy analysis, to explain an increase of Green PL after thermal annealing in air at 600 °C on vertical aligned ZnO nanowires, tentatively attributed the green band to V_{ZnO} at the surface of the nanowires. Hence, their claim as a consequence of an opposite effect of thermal annealing on the green PL. In the latter case, Kodama et al. [80], explored the temperature dependence of the steady-state PL and PLE characteristics of the green emission band in undoped ZnO bulk crystals. However, He et al. did not show any evidence of the presence of Zn_i in ZnO crystals and also here any PL features (PL emission at 2.8 eV) related to this defect are observed. Furthermore, their model takes into account the influence of the excitation energy on the exponential decay kinetics of the green band. In contrast, we have observed above a power law decay kinetics which does not changes varying the excitation energy in the whole range of the PLE spectrum. Finally, being our emission mechanism based on results obtained by a complete investigation of the structural and optical properties of ZnO NPs and their response to the ex-situ treatments, it is more detailed than previous existing ones involving electron or holes trapped in ionized oxygen vacancies. In this sense, time-resolved studies have allowed us to carry out new pieces of information not previously available in the literature.

4.7   Conclusions

ZnO NPs with an average size of 30 nm were synthesized by PLAL of a zinc plate in deionized water and characterized by time-resolved luminescence and complementary techniques (TEM, AFM, μRaman). HRTEM images show crystalline ZnO NPs in wurtzite structure with a change in the nanocrystal lattice parameter a as indicated by a larger distance between (100) lattice planes. Consistently, optical absorption and time resolved PL spectra show the typical absorption edge of the wurtzite ZnO (E_g=3.38 eV) and the relative excitonic fast PL peaked at 3.32 eV with a single exponential life time of about 800 ps. In addition, we observed a visible PL at 2.2 eV due to the presence of defects in ZnO NPs with a sharp edged excitation spectrum and a power law decay time. These findings indicate a recombination processes, not mentioned in the existing literature, driven by tunnelling of trapped electrons to centres randomly distributed in space. Extreme changes in pH of water do not produce any effect on the defect-related PL revealing the lack of interaction between defects and solvent molecules and suggesting that defects lie inside the NPs. Our finding disagrees with results shown in other works [104] and discussed in Sec. 1.4, which indicate that defects responsible to the green PL are located at the surface. Thermal annealing at 300 °C in O_2 atmosphere, and to a smaller extent, even in He atmosphere, produces a reduction of A_1(LO) mode at 565 cm^{-1} which is related to oxygen vacancies, more-

over, thermal treatments lead to a decrease of the green PL while the excitonic luminescence at 3.32 eV is enhanced. Hence, our structural-optical combined study allow us to demonstrate the relation between oxygen vacancies and the green PL in ZnO NPs, which until now it was a debated issue. Based on our experimental results we propose a recombination mechanism responsible of the green PL involving a hole in the VB recombining with a deeply trapped electron in singly ionized oxygen vacancies. The electron is previously trapped in an unknown trap state and then tunnels toward the recombination center (oxygen vacancies). These results underscore the possibility of controlling the intensity of the PL bands of ZnO NPs by thermal annealing procedures. Overall, we have gained additional information on the origin and mechanism of the green PL providing a significative advance to the research useful also in view on the use of ZnO NPs in optoelectronic applications.

Chapter 5

Growth Processes of ZnO NPs During Pulsed Laser Ablation in Liquid

This chapter concerns the study of the formation of ZnO NPs during pulsed laser ablation of a zinc plate in aqueous solution. We use *in situ* optical spectroscopies to investigate the oxidation kinetics and to understand the generation mechanism of the oxygen vacancies so as to control their concentration inside nanoparticles.

5.1 Introduction

The experimental results presented in the previous chapter have shown the morphological, structural and optical properties of ZnO NPs produced by PLAL in water. Our results point out that oxygen vacancies are responsible of the green emission and allow us to propose a model accounting for the electron-hole recombination mechanism producing PL emission of ZnO NPs. However, many questions remained open such as the sequence of events eventually leading to the formation of oxidized ZnO NPs from the Zn metal target and the generation processes of oxygen vacancies. These problems are supported by the fact that the synthesis produces a brownish colloidal solution, which gradually changed to pale yellow in tens of minutes indicating chemical reactions which continues even after the end of PLAL. Indeed, all PLAL experiments reported so far have only used ex-situ methods to study the endproduct of the synthesis when the stable metal oxide NPs have already grown [69, 81, 88, 95, 96, 98, 100, 142, 143, 167]. To overcome this problem, it is mandatory to directly probe the evolving nanomaterials during the PLAL experiments, in order to monitor in real time the undergoing NP synthesis and reactions.

In this chapter, we report online UV-VIS optical absorption (OA) and photoluminescence (PL) measurements carried out during Nd:YAG laser ablation of a zinc metal plate with different laser repetition rates (RRs) in aqueous solution or mixed aqueous/alcohol solutions. In particular, we are going to show the oxidation processes involved during laser ablation providing useful information to control the oxidation kinetics as a function of PLAL parameters.

5.2   In situ Optical Spectroscopy

5.2.1   Optical Absorption

One of the main techniques employed in this work to investigate the oxidation processes during PLAL in aqueous solution is *in situ* optical absorption spectroscopy, carried out by the experimental apparatus described in detail in Chapter 3. Briefly, during the ablation the liquid containing the ablated material was continuously pumped (flow=11.5 ml/s) in a closed circuit traversing two quartz flow cells. One of the flow cell was used to detect OA spectra by an optical fiber spectrophotometer, equipped with a D_2 lamp and a grating which disperses the transmitted light into a CCD camera.

Fig. 5.1 shows the difference OA spectra acquired at several times during and after laser ablation. During the course of PLAL (panel (a)), the colloidal solution displays a growing OA spectrum where two contributions specific of different nanostructures can be recognized. The first is a broad peak around 5 eV which is attributed to the surface plasmon resonance (SPR) of metallic Zn nanoparticles [69, 94]. The second is a shoulder at 3.5-3.7 eV, consistent with the absorption edge of zinc oxide shown in the previous chapter. The coexistence of metal and oxide NPs during PLAL demonstrates that the Zn oxidation does not occur "instantaneously" within the high-temperature and high-pressure plasma plume formed by ablation, but it is rather due to later reactions with the solvent. A similar behavior had been previously proposed for other ablated metals, however based on ex situ measurements [151]. Inset in panel (a) shows the normalized OA spectra during PLAL and evidences that in the first seconds there is a prominent contribution of the SPR peak, with a negligible contribution of the ZnO edge. Moreover, the figure shows that the SPR peak quickly broadens and shifts to higher energies, from 4 eV up to 5 eV, mostly within 120 s from the beginning of PLAL. Being the spectral position of the SRS peak sensitive to the NP size [179], these data indicate a time-dependent size distribution of metal Zn NPs during the earliest phase of PLAL. Indeed, a blue shift of the SPR peak can be attributed to an earliest superficial oxidation experienced by Zn NPs, which produces Zn/ZnO coreshell NPs, thus reducing the size of the metallic Zn core. It is worth noting that the OA spectrum keeps evolving even after the end of ablation, as shown in Fig. 5.1 (b). Indeed, it is evident that the plasmonic peak decreases from the end of PLAL, while the ZnO absorption edge becomes progressively sharper. The inset in panel (b) shows the OA kinetics at the fixed energy (5 eV) corresponding to the SPR peak position. One can clearly see an abrupt change of slope at the end of PLAL, after which the absorption decreases mostly in about 300 s due to the decay of the SPR peak. The kinetics in Fig. 5.1 (b) implies a decrease of the amount of metallic Zn species in favor of ZnO NPs. Only after t~1200 s from the end of PLAL, we observe the typical absorption spectrum of ZnO, due to the complete zinc oxidation in the colloidal solution. The arrow in Fig. 5.1 (b) highlights a small red shift of the plasmonic absorption peak during its decay, which can be attributed to a variation of the size distribution of Zn cores during oxidation. In particular, we infer that the smallest Zn particles (whose SPR resonance appears at larger photon energies) are the first to be oxidized.
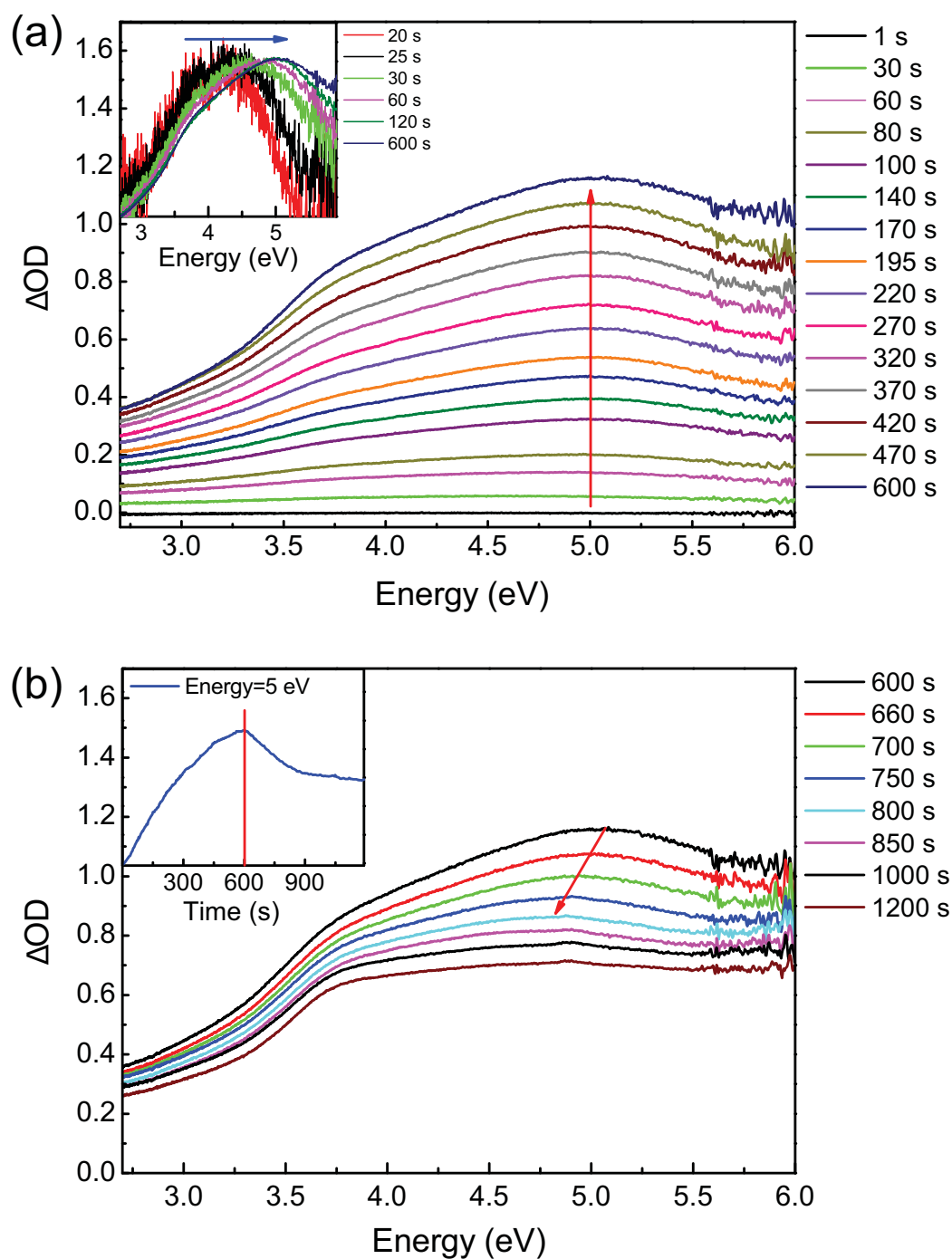
Figure 5.1: UV-Vis difference OA of the colloidal solution acquired at several times during (a) and after (b) laser ablation (integration time 1 s), as calculated with respect to a OA spectrum acquired before the beginning of PLAL; inset in (a) shows the shift of the normalized spectra; inset in (b) shows the OA kinetics at fixed energy E=5 eV. The arrows indicate the SRS peak position at different times. Figure taken from [97].

Data in Fig. 5.1 support the model proposed by Zeng and co-workers, based on ex-situ measurements on a sample produced by PLAL of Zn in an aqueous solution of sodium dodecyl-sulfate (SDS) [94]. According to this work, Zn NPs formed within the plume react with solvent

molecules and undergo an initial, very fast surface oxidation yielding Zn/ZnO core-shell NPs. When SDS concentration exceeds the critical micelle concentration (0.008 M), these Zn/ZnO core-shell NPs remain stable because of the capping effect provided by SDS around each NP, which prevents the NPs from being further oxidized. In our case, no surfactant molecules are used and the oxidation proceeds all the way to the core, being almost completed in about 600 s after the end of ablation. Therefore, OA data suggest the initially produced Zn NPs to be oxidized in two phases: an earliest and superficial oxidation (first 120 s of PLAL) which causes a shrinking of the Zn cores, and a later and slower oxidation, completed only well after the end of ablation and eventually leading to the complete disappearance of the metal.

5.2.2   Morphology of the Produced NPs

The AFM image of stabilized NPs produced at RR=10 Hz is displayed in Fig. 5.2 (a) and reveals that the ablation product consists in a broad distribution of spherical-like NPs. In detail, distribution in Fig. 5.2 (b) shows that the sizes range from about 10 nm to 70 nm with an average value of about 30 nm. Because the spectral position of the SPR peak is sensitive to the NP size [179], it is possible to infer that Zn cores have a 20 nm average size [69,94]. Thus, we can conclude that at the end of PLAL the faster oxidation in the sample at RR=10 Hz produces Zn/ZnO core shell NPs with an average core size of 20 nm and a shell size of 10 nm.

We note that despite the synthesis conditions are different, we obtain the same morphology of ZnO NPs of the ablation experiment reported in Chapter 4. In fact, during in situ experiment the liquid is continuously flowing in a closed circuit transported away from the volume where ablation takes place. Based on our typical flow rate of 11 ml/s, we can calculate the portion of liquid as large as the laser illuminated volume ($V_0 \approx 0.1$ ml) which is removed in about 10 ms. This time is much shorter than 100 ms interpulse (10 Hz), thus any disturbance by adjacent pulses on the formed product is avoided. Besides, once it leaves the laser-illuminated volume, it is quite unlikely that a Zn nanoparticle will cross it again, because V_0 is much smaller than the overall volume flowing in the whole circuit (about 50 ml). The fact that in ablation experiment performed without fluxing the ablated solution we produce the same NPs morphology can be understood considering that the used wavelength (1064 nm) is far from the SPR absorption peak at 245 nm and from the ZnO edge at about 350 nm, which reduces any energy transfer from the laser to the NPs. Therefore, only the target Zn material has a strong absorption at the laser wavelength, and secondary effects such as fragmentation are avoided.

5.2.3   Photoluminescence

To obtain further detail on the oxidation kinetics we also performed PL measurements on the colloidal solution during and after the end of PLAL by the same experimental setup used to acquire OA spectra. Time resolved PL spectra were acquired using the second flow cell, they were excited by a tunable laser consisting of an optical parametric oscillator pumped by the third harmonic of a Nd:YAG laser (pulse width 5 ns, RR 10 Hz). The emitted light was
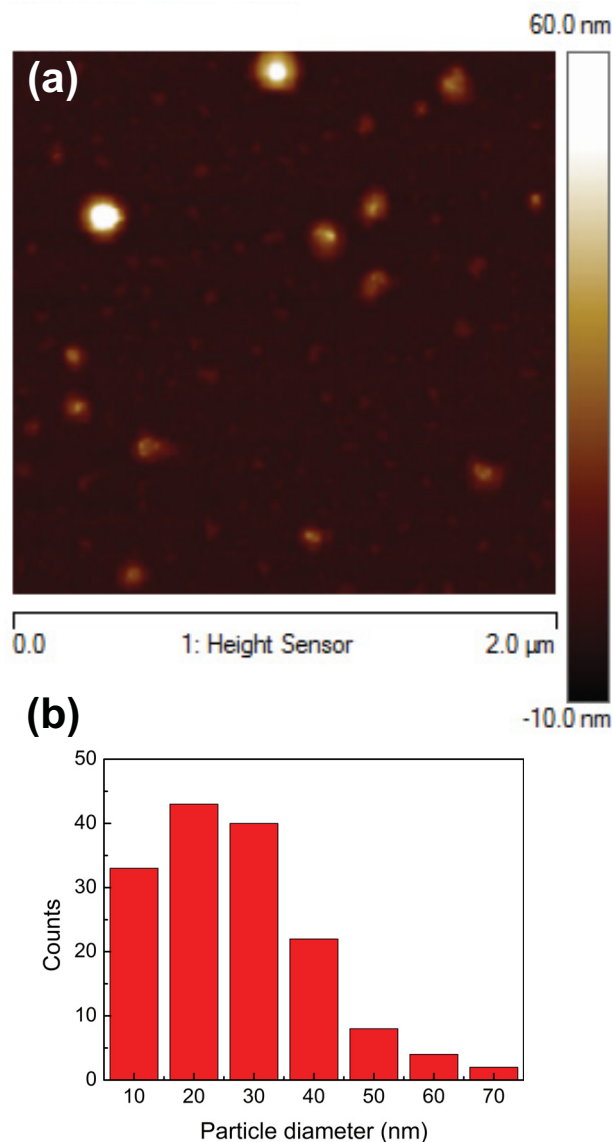
Figure 5.2: (a) AFM image 2×2 μm^2 of the dried colloidal solution of ZnO NPs produced by PLAL at RR=10 Hz; (b) Size distribution calculated from AFM image. Figure taken from [97].

spectrally resolved by a grating and then acquired by an intensified CCD camera. Indeed Zn metal is not luminescent, thus the exciton related emission singles out the ZnO contribution to the OA spectra. Instead, the defect emission in the green region can be used to detect defects concentration in the oxidized portion of the material. On these grounds, Fig. 5.3 shows the PL bands peaked at 2.25 eV (defect emission) and at 3.32 eV (excitonic emission) as observed during and after PLAL; whereas Fig. 5.4 reports the intensity of the two signals as a function of time. Both PL signals grow with ablation time, and most importantly, they continue to grow spontaneously for ~600 s even after the end of PLAL, consistently with OA data showing an oxidation process that continues after the end of laser ablation. The inset in Fig. 5.4 shows the PL and OA kinetics during the first 200 s of PLAL, normalized at t=200 s. We highlight that the SPR absorption signal of Zn starts to grow immediately after the beginning of PLAL (t=0),
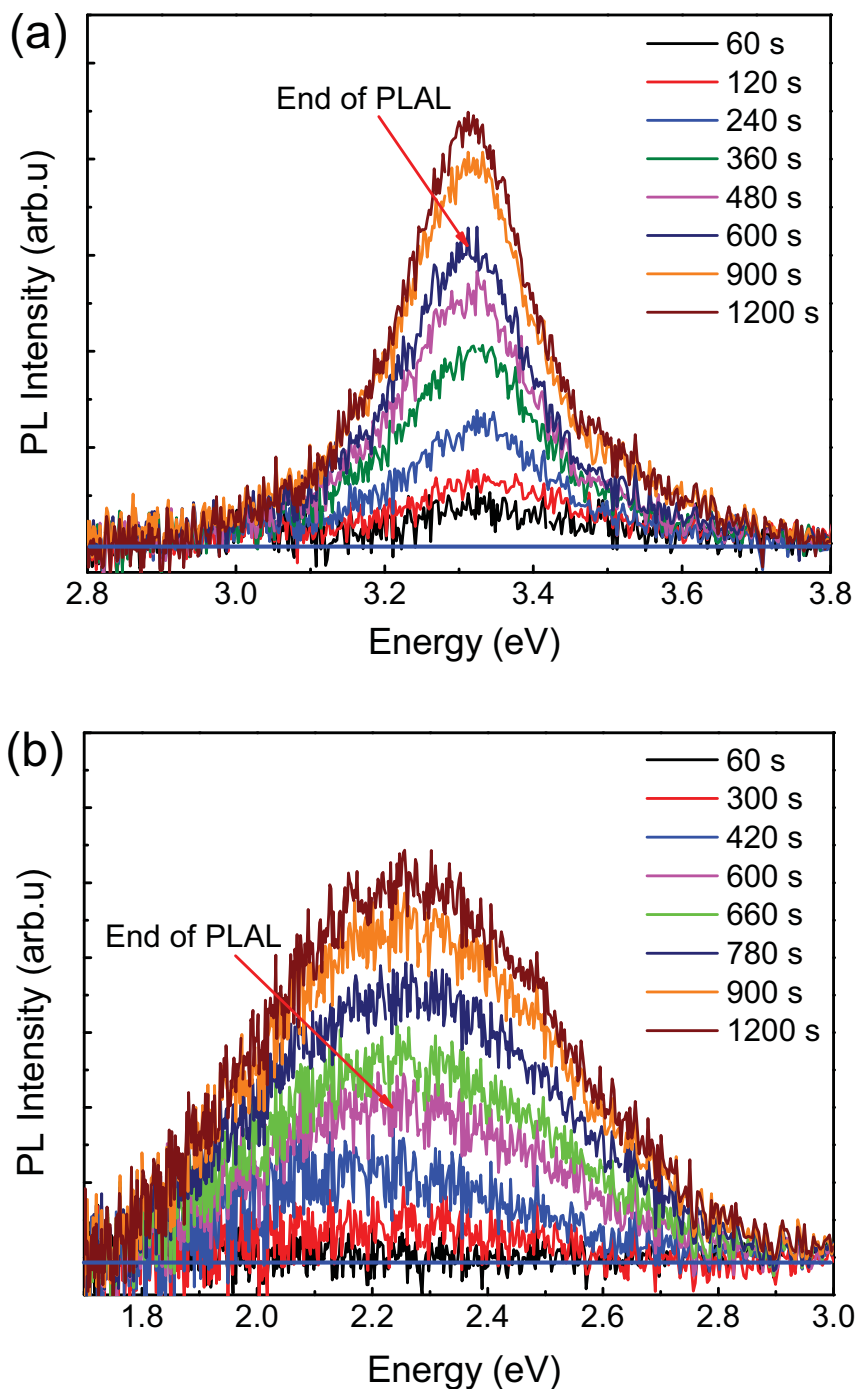
Figure 5.3: PL spectra of the colloidal solution acquired at several times during and after laser ablation. (a) Exciton- (b) defect-related PL of ZnO excited at 4.96 eV and 3.54 eV, respectively. Figure taken from [97].

whereas the rise of both PL signals is delayed. This difference implies that the formation of ZnO, as monitored by exciton PL, is slightly delayed from the generation of Zn NPs. Moreover, we infer that the earliest superficial oxidation of Zn essentially produces a defect-free ZnO, because the defect-related PL remains negligible for the first 100 s and fully begins to rise with maximum
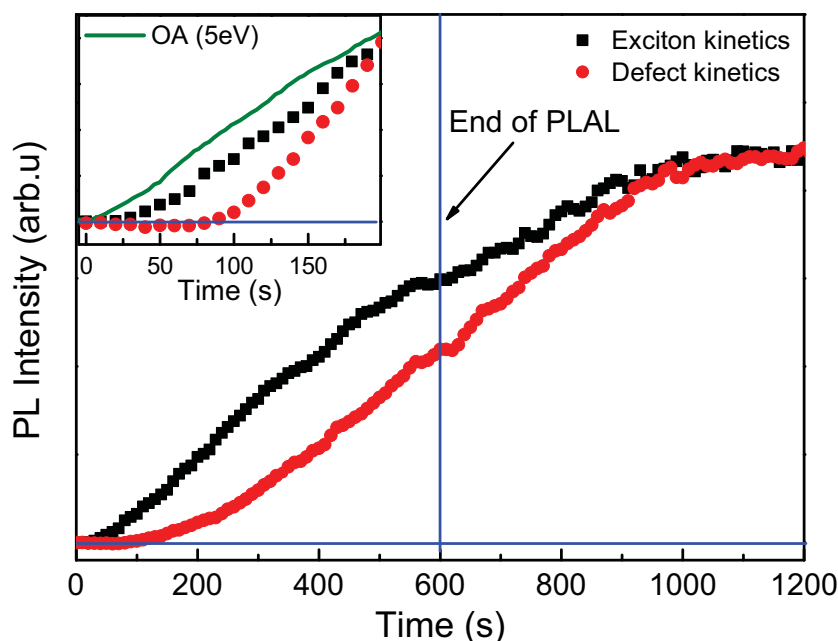
Figure 5.4: Intensity of the two PL bands as a function of time, normalized at 1200 s. Inset shows the 5 eV OA and PL kinetics during the first 200 s of PLAL, whereby the curves are normalized to the maximum value. Figure adapted from [97].

slope only 200 s after PLAL starts (see main panel). Only later, excitonic and defect related PL grow together, highlighting that the further and slower oxidation leaves behind a defective ZnO material.

5.3 In situ Experiment Varying the Repetition Rate

In order to complete the information taken from *in situ* experiments we performed PLAL of a zinc plate in water varying the used repetition rate (RR), 5 Hz, 10 Hz, 20 Hz, maintaining constant the total fluence which was fixed to 9.5×10^3 J/cm^2. Since the amount of produced materials is proportional to the pulse number hitting the zinc target, in this way, we obtain the same concentration of the samples at the end of PLAL. A plot of the absorption spectra (Fig. 5.5) of the colloidal solution, acquired at several times during and after the end of laser ablation, evidences that the curves keep evolving even after the end of ablation for about 1200 s. Interestingly, the absorption spectra exhibit a different shape and their temporal evolution depends on the used RR. In fact, those obtained by PLAL at 10 Hz and 20 Hz have a similar shape with the SPR peak at 5 eV of metallic Zn NPs, which decreases after the end of PLAL until it disappears after 900 s and 400 s, respectively. Instead, SPR is negligible in the sample prepared at 5 Hz, where the OA shape almost does not change during PLAL and remains stable after the end of PLAL. Figs. 5.6 (a) and (b) show the comparison of the OA profiles at different RRs recorded at the end of PLAL, and after 1200 s from the end of PLAL, respectively. Fig. 5.6 (a) highlights different relative ratios between the two contributions in the absorption spectra obtained at various RRs: in agreement with Fig. 5.5 we note that in the sample produced
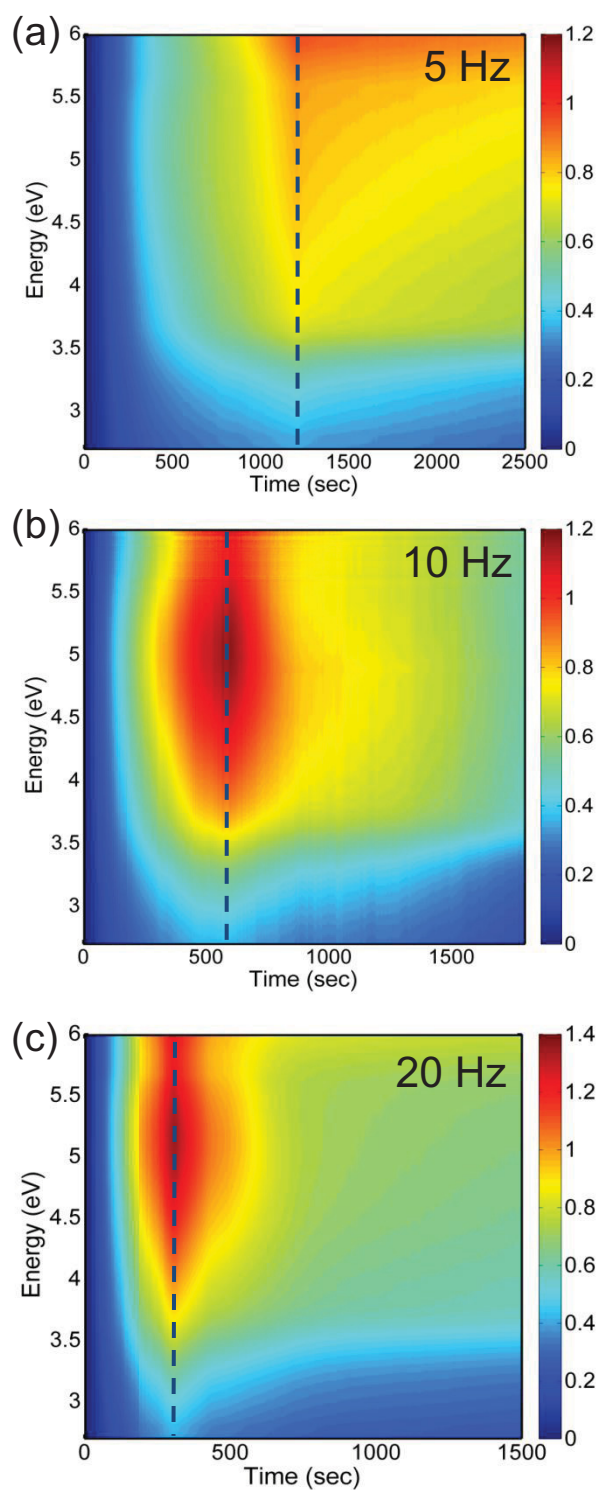
Figure 5.5: Time-energy 2D-plot of the absorption of a colloidal solution prepared by PLAL, as recorded at several times (each measurement requires 1 s) during and after laser ablation carried out with pulse RRs: (a) 5 Hz, (b) 10 Hz, (c) 20 Hz. Color scales indicate the UV-Vis difference OA of the colloidal solutions calculated with respect to the OA spectra acquired before the beginning of PLAL. The dashed blue lines indicate the end of PLAL. Figure taken from [180].
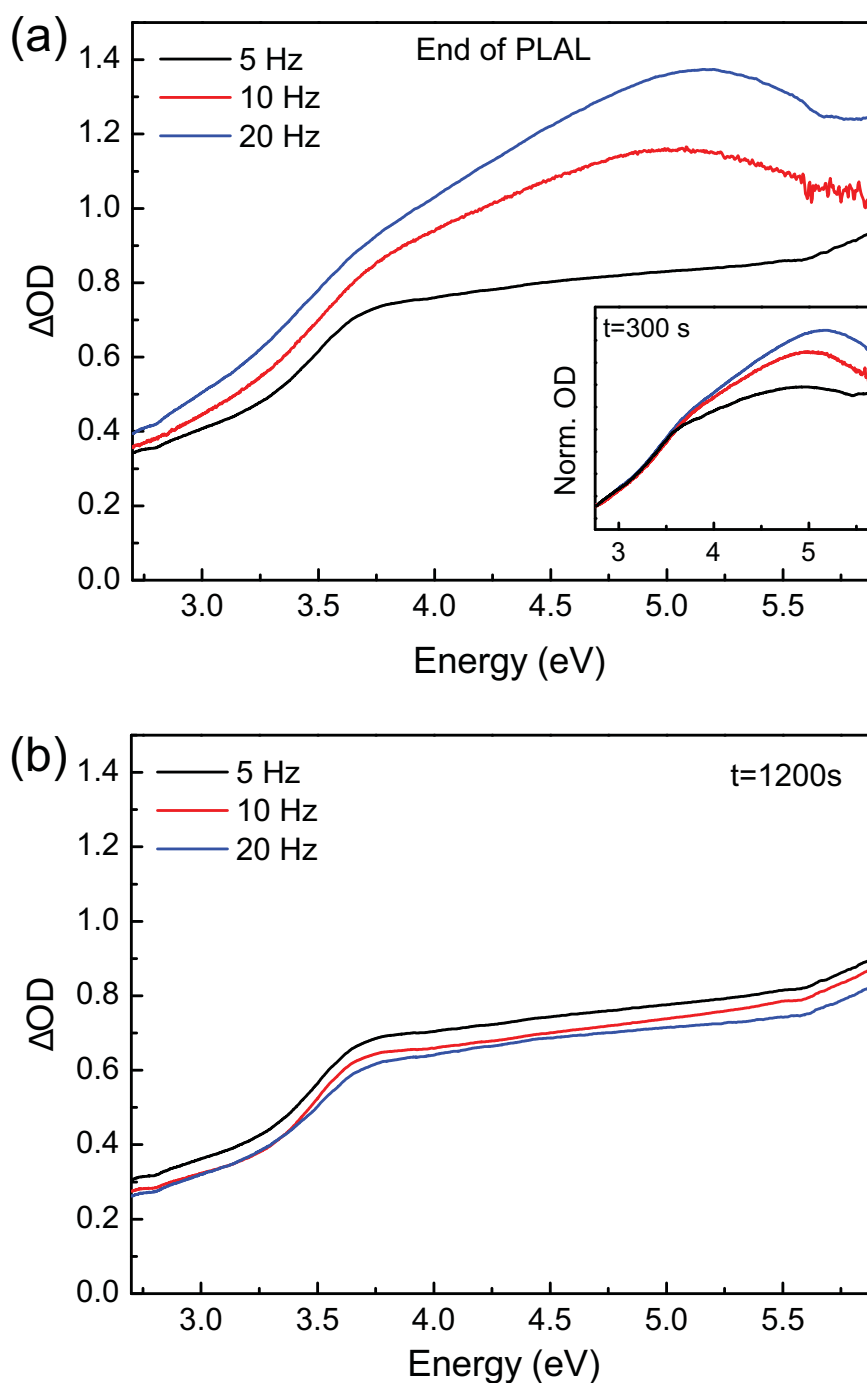
Figure 5.6: UV-Vis difference OA of the colloidal solution, obtained by using different pulse RRs, acquired at (a) and after 1200 s (b) from the end of laser ablation. They are calculated with respect to a OA spectrum acquired before the beginning of PLAL. Inset in the panel a shows the OA spectra normalized at the edge plateau (3.6 eV) acquired after 300 s from the beginning of ablation. Figure taken from [180].

at 20 Hz the SPR contribution is higher than that measured in the sample produced at 10 Hz; moreover it completely disappears at 5 Hz. Finally, Fig. 5.6 (b) shows the OA spectra acquired after 1200 s from the end of PLAL, when the colloidal solution is stable after the completion of

all post-irradiation kinetics due to oxidation. Consistently with the OA spectra shown in the first section, in this case we observe the same absorption spectrum for the three samples, all exhibiting the typical absorption edge of ZnO in wurtzite structure.

The different weights of the SPR peak contribution in OA spectra, depending on RR, can be explained considering that the slower oxidation step discussed above is sensitive to RR. In particular, a longer temporal separation between successive pulses (that is, a lower RR) allows this oxidation to proceed together with the production rate of Zn NPs performed by PLAL thus leading to the prominence of ZnO absorption edge. In contrast, at higher RR there is a prominence of SPR peak because the oxidation fails to follow the zinc production rate. In this second case, however, oxidation proceeds after the end of PLAL ultimately yielding the same, highly oxidized, nanomaterial in a longer times (Fig. 5.6 (b)) independently of the RR. The complete absence of the SPR peak of metallic Zn NPs from the OA spectra at the end of ablation with 5 Hz could be just due to the longer duration of the ablation experiment leading to the NPs to interact with water longer than those produced with higher RR. In order to rule out this possible artifact we also compared in the inset of Fig.5.6 (a) the absorption spectra acquired at the same delay time (300 s) from the beginning of PLAL normalized at the ZnO edge plateau (3.6 eV) contribution to highlight the different shapes. This graph confirms the trend observed in the main panel of Fig. 5.6 (a), and in particular, it shows an almost negligible contribution of the SPR peak in the sample obtained with 5 Hz. These results demonstrate that RR directly influences the oxidation of Zn NPs thus supporting our previous claim that at lower RR the oxidation proceeds together with the production rate of Zn NPs performed by PLAL.

Since in situ experiments were performed by fluxing the colloidal solution any disturbance by adjacent pulses on the formed product is avoided, as already evidenced in the Sec. 5.2.2. Indeed, the morphology of ZnO NPs produced at 5 Hz and 20 Hz show the same result obtained at 10 Hz (Fig. 5.1) with sizes range from about 10 nm to 70 nm and an average value of about 30 nm. Taking into account that the spectral position of SPR peak in the sample at 10 Hz and the average size estimated by AFM image, we earlier concluded that at the end of PLAL the oxidation produces Zn/ZnO core shell nanoparticles having Zn cores with size of 20 nm and a shell size of 10 nm. One can note that the SPR peak position of the sample at 20 Hz is slightly blue-shifted (5.1 eV) with respect to 10 Hz sample (5.0 eV) which might indicate a slightly bigger Zn core at the end of PLAL. Instead, as indicated by OA data, the zinc core completely disappears at 5 Hz.

To obtain further detail on the oxidation kinetics we also performed PL measurements on the colloidal solution during and after the end of PLAL. Fig. 5.7 (a) and (b) show the intensity of the two PL signals during and after PLAL, normalized at t=600 s from the end of PLAL. Since PLAL was performed in such a way to provide the same total fluence in the three ablation experiments, the PL kinetics are reported as a function of pulse number until the end of PLAL, and as a function of time after the end of PLAL. In agreement with the results of OA measurements, the PL signals grow with ablation time, and most importantly, both PL bands of the samples obtained at 10 Hz and 20 Hz continue to grow spontaneously even after the end of PLAL,
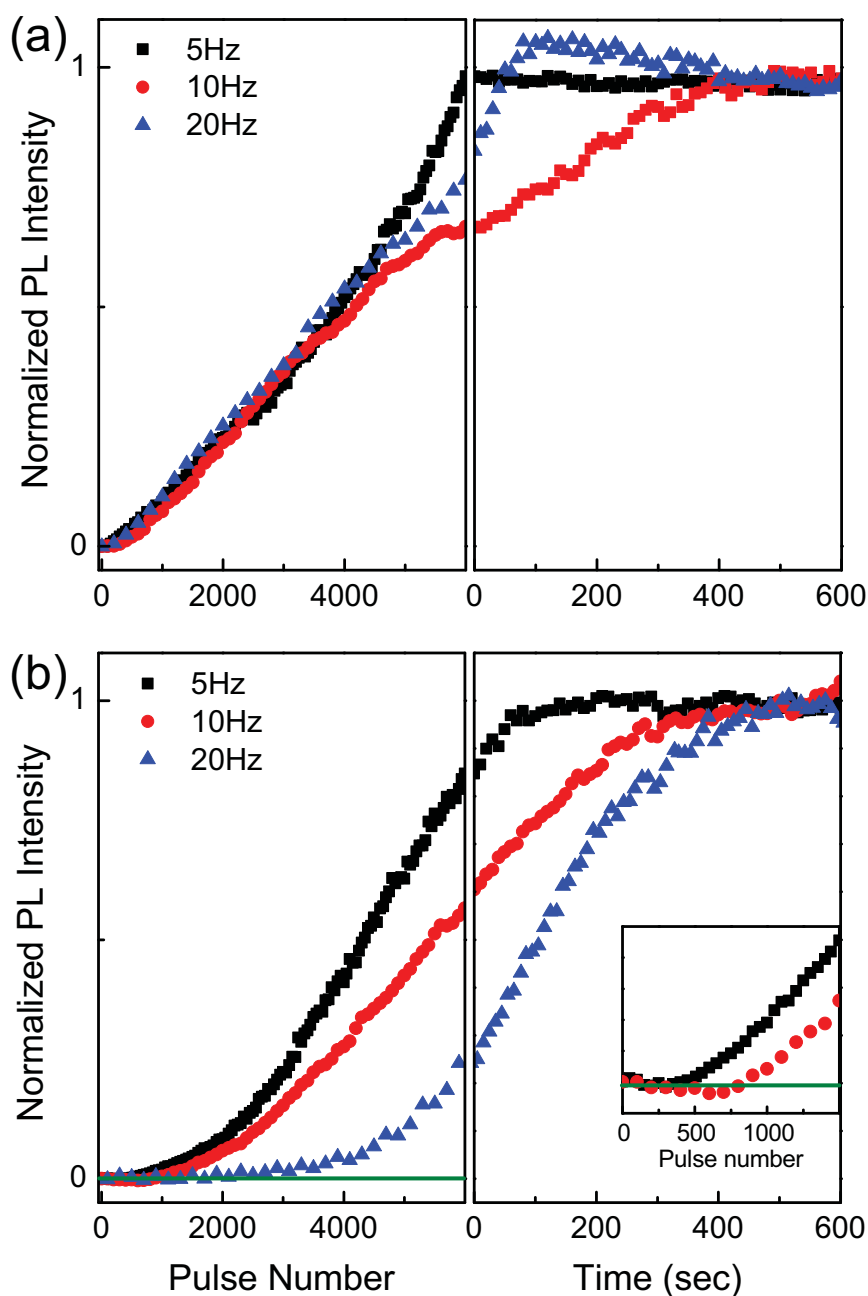
Figure 5.7: Intensity of the excitonic related PL bands (a) and of the defect related PL bands (b) as a function of time at the different RRs, normalized at 600 s after the end of laser ablation; inset shows the defect-related PL kinetics at 5 Hz and 10 Hz during the first 1500 pulse of PLAL. Figure adapted from [180].

whereas the sample at 5 Hz remains almost stable. In more detail, the comparison of excitonic PL kinetics as a function of the fluence provided during PLAL, reveals that PL curves start to grow from the beginning of the ablation and increase together for 4000 pulses, then they gradually split until the end of ablation. Since the excitonic PL is directly proportional to the concentration of ZnO in the sample, this result confirms our claim based on the OA and PL data obtained from the experiment at 10 Hz, that the oxidation occurs in two step: a fast and

a slower oxidation. Indeed, a fast oxidation (much faster than the interpulse time) dominating the initial production of ZnO species from Zn NPs cannot be affected by the different used RRs. Instead, the slower oxidation becomes relevant after 4000 pulses and fails to keep up with the zinc production rate which is proportional to RR, leading to the split of the excitonic kinetics until the end of PLAL. In agreement with this, Fig. 5.7 (b) shows that the rise of defect bands is always delayed from the beginning of PLAL. The inset on the left of Fig. 5.7 (b) shows the defect-related PL kinetics at 5 Hz and 10 Hz during the first 1500 pulse of PLAL. We can see that the defect emission starts to grow after ∼600, 1000 and 3000 pulses on increasing RR, respectively, with respect to the rise of excitonic emissions, corresponding to the almost constant time delay (120, 100 and 150 s respectively) needed for the slower oxidation reaction to proceed. Hence, these results demonstrate that the green emission is mostly due to the slower oxidation step, which becomes relevant, independently of the used RR, after ∼100 s from the beginning of PLAL.

5.4   In situ Experiment Varying the Solvent

In order to control the oxidation rate of Zn NPs, we performed PLAL of the zinc plate in a mixture of ethanol and water at fixed RR=10 Hz, while keeping constant the other experimental parameters. Figs. 5.8 (a) and (b) show the AFM image and particle size distribution of NPs synthesized by PLAL in pure ethanol. Also in this case PLAL produces spherical-like NPs, with sizes ranging from about 5 nm to 60 nm with an average value of about 20 nm. Figs. 5.9 (a) and (b) show the OA spectra acquired at the end of PLAL and after 3600 s, respectively. The OA profile of the sample produced in pure ethanol (100% EtOH) exhibits only the SPR peak contribution at 5 eV, which is consistent with the average size obtained by AFM measurements of 20 nm, whereas there is no evidence of the ZnO edge. Moreover, OA spectrum does not show any change within 3600 s from the ablation end (Fig. 5.9 (b)) nor during the next seven days, where it appears slightly reduced in intensity probably due to precipitation of Zn NPs. Thus, Zn NPs in ethanol remain stable without suffering oxidation and indefinitely maintaining their metallic core after synthesis. Instead, OA spectra obtained by the colloidal solution produced with 20% and 30% of ethanol in aqueous solution show the formation of the same two contributions present in pure water but with different weights. In particular, they show that an increase of the ethanol concentration implies a more prominent contribution of the SPR peak of Zn NPs with respect to ZnO edge, when measured at the end of PLAL (Fig. 5.9 (a)). Moreover, the OA spectra keep evolving for 2200 s (ethanol 20%) and 3000 s (ethanol 30%) after the end of PLAL and, once the oxidation has been completed, they show the typical absorption edge of ZnO revealing that we obtained the same final product as for PLAL in pure water. This experiment demonstrates that by mixing the two solvents characterized by different oxidation rates it is possible to tune the oxidation degree of the just produced Zn NPs from zero (pure ethanol) to complete oxidation within 900 s (pure water).
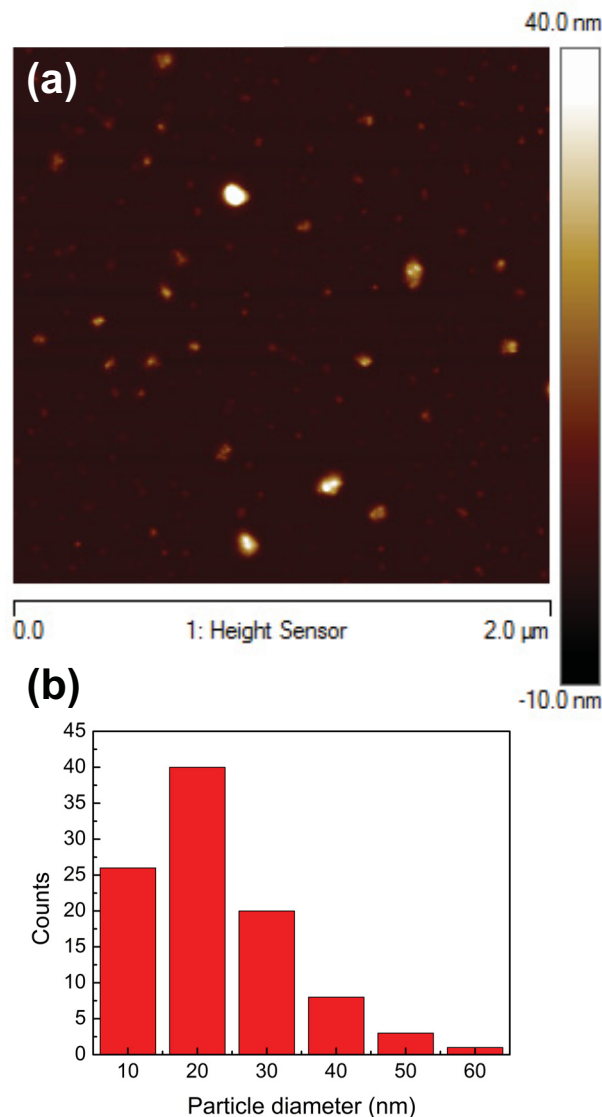
Figure 5.8: (a) AFM image $2 \times 2 \ \mu m^2$ of the dried colloidal solution of ZnO NPs produced by PLAL in pure ethanol at RR=10 Hz; (b) Size distribution calculated from AFM image. Figure taken from [180].

5.5   Oxidation Model

Based on our experimental results, the formation of ZnO NPs can be understood as a sequence of four steps, illustrated in Fig. 5.10 (I) A high-temperature and high-pressure Zn plasma plume is produced quickly after the interaction between the pulsed laser and the metal target. The subsequent ultrasonic and adiabatic expansion of such plasma leads to cooling and hence to the formation of Zn NPs. During this initial phase (in the first seconds of PLAL), we observe the linear growth of the OA plasmonic peak with time in the absence of ZnO absorption edge and of the excitonic peak (see Fig. 5.1). (II) Due to the reaction of the Zn NPs with water molecules, the surface is oxidized and a defect-free ZnO shell is formed. The reaction responsible for this
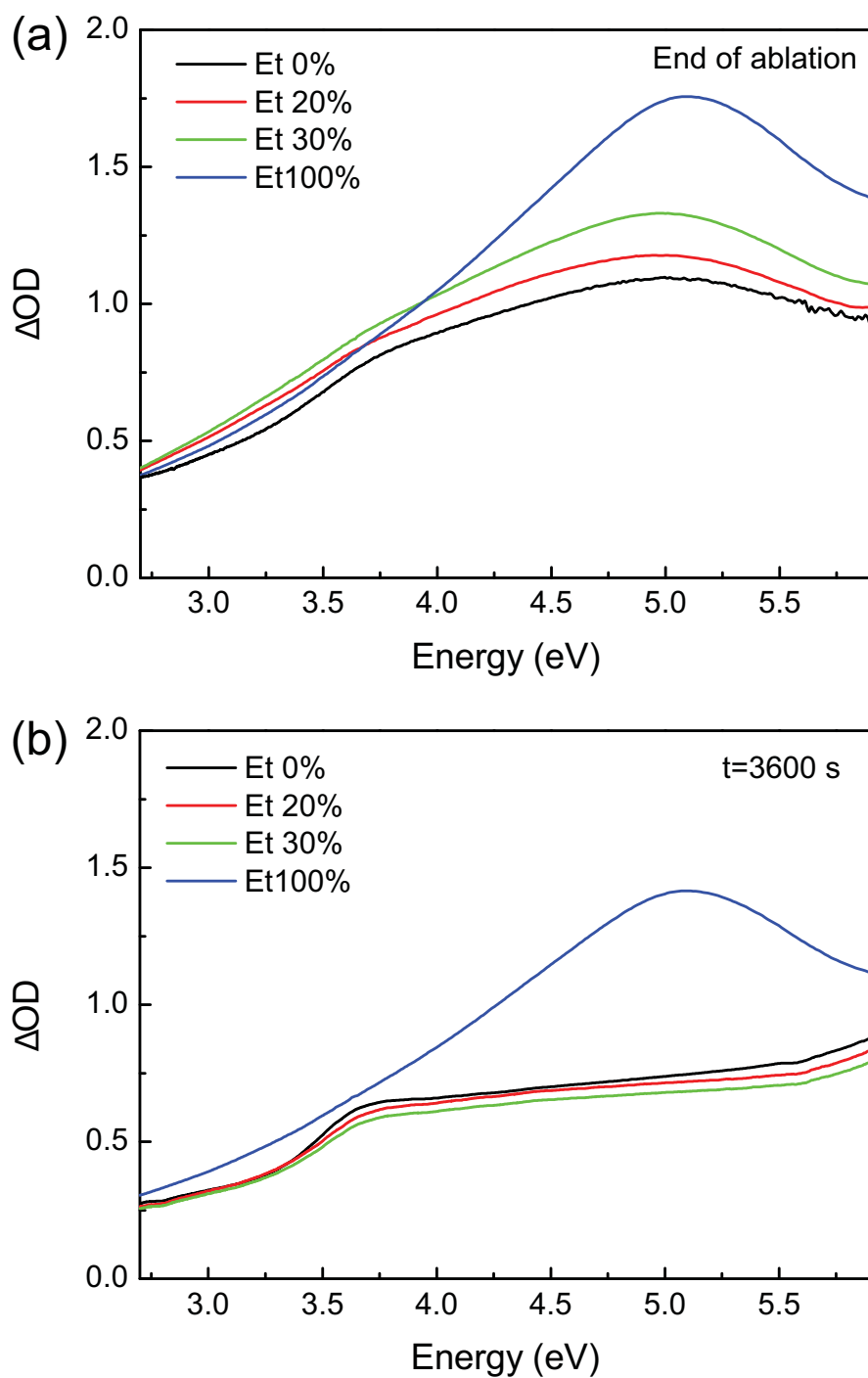
Figure 5.9: UV-Vis difference OA of the colloidal solution, obtained by using different mixtures of water and ethanol at fixed RR=10 Hz, acquired at (a) and after 3600 s (b) from the end of laser ablation. Figure taken from [180].

step could be the following:

$$Zn + H_2O \rightarrow ZnO + H_2 \,, \tag{5.1}$$
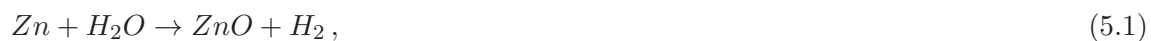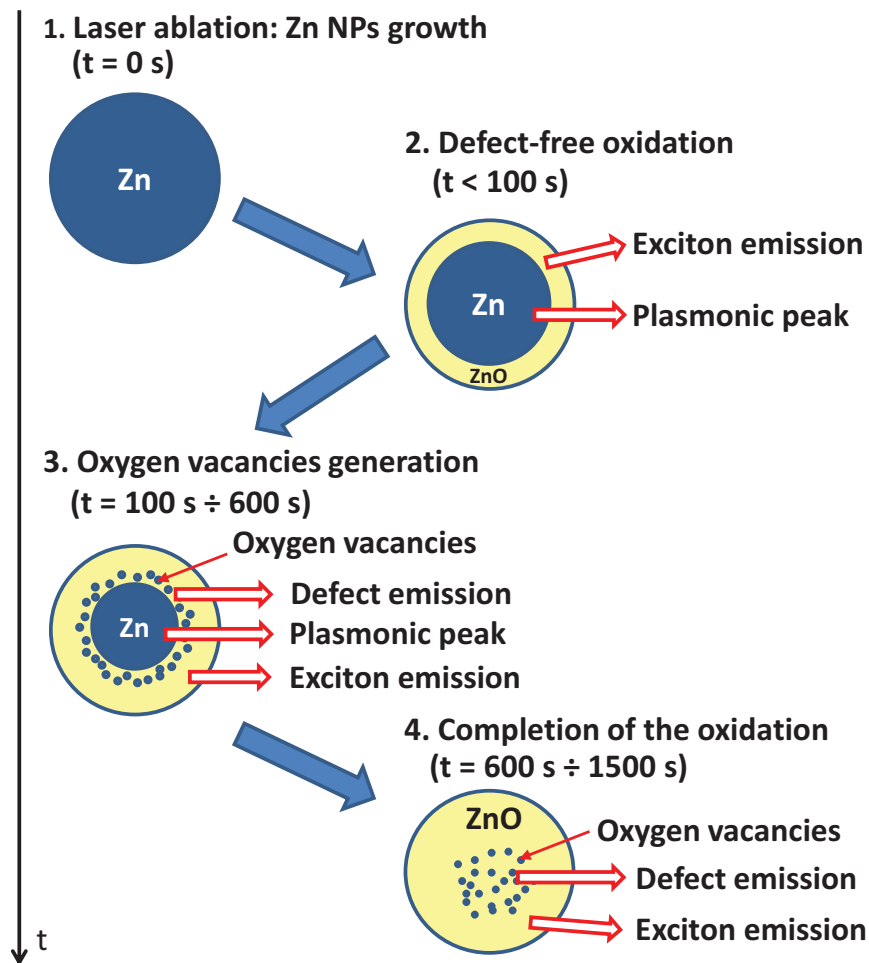
Figure 5.10: Illustrations of a formation model for ZnO NPs in four steps. Figure taken from [97].

This process leads to the growth of the exciton PL signal and of a hint of ZnO edge absorption, while no defect-related PL is observed yet (t<100 s). (III) Oxidation continues until all the Zn NPs become ZnO. However, water molecules must now pass through a shell of ZnO before reaching the Zn core. Hence, the oxidation is somewhat hindered, becomes slower and leaves behind defects. Indeed, during this phase (100-600 s) we see the growth of defect-related PL which is attributed to oxygen vacancies. (IV) After the end of ablation (600-1500 s), the oxidation proceeds further, eventually leading to a population of ZnO NPs which have completely lost their metallic cores, but remain slightly sub-stoichiometric in that they host sizeable concentrations of oxygen vacancy defects. Indeed, at this stage we see a further growth of both PL bands while the SRS peak in the OA spectrum decreases and finally disappears.
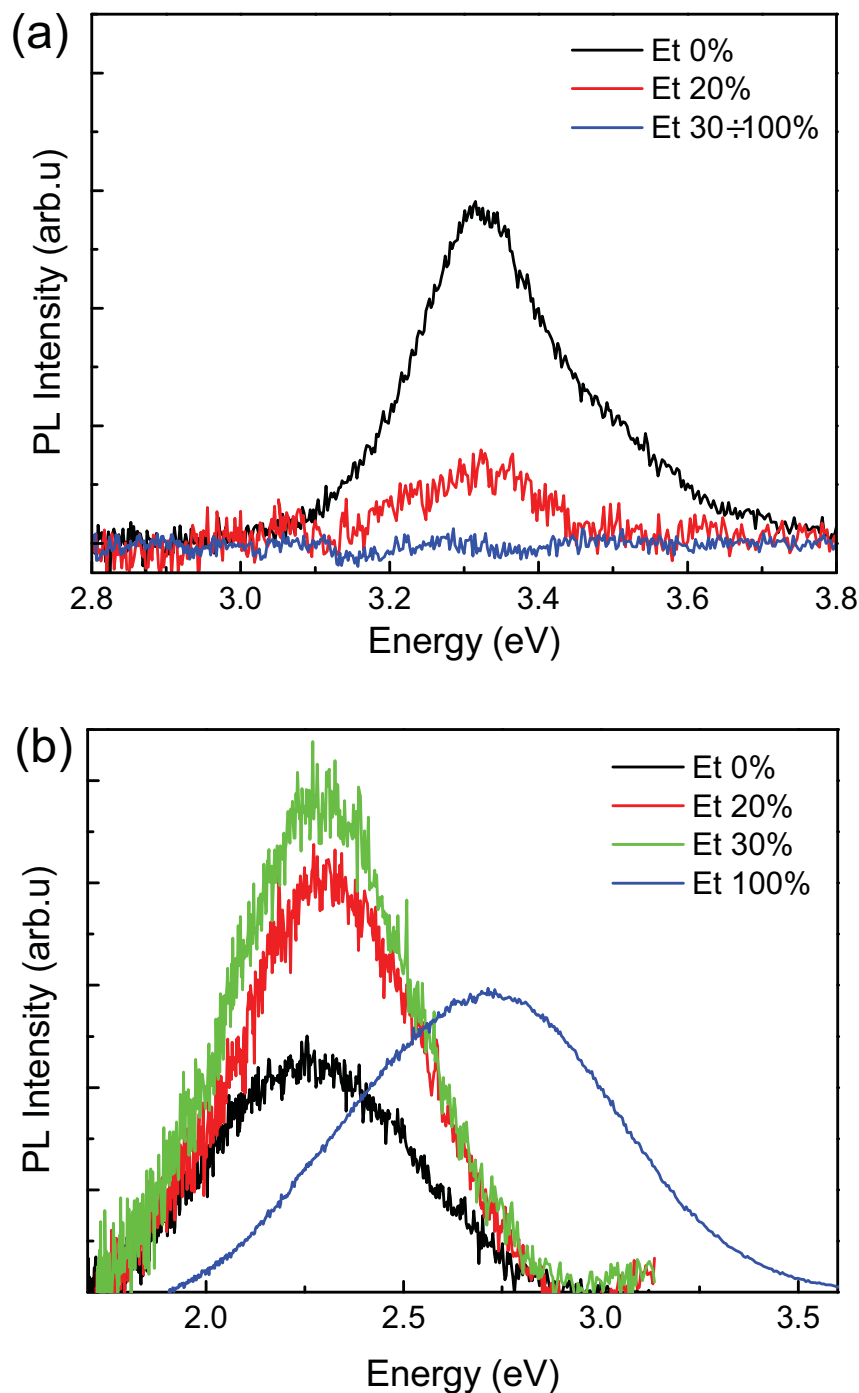
Figure 5.11: (a) Excitonic PL and (b) Defect related PL of the colloidal solution produced in pure water and in various mixtures of water and ethanol. Figure taken from [180].

5.6   Ex situ Effect of Ethanol

To better investigate the optical properties of the produced ZnO NPs we studied the effect of ethanol on the luminescence properties. Figs. 5.11 (a) and (b) report the excitonic- and defect-related PL bands of the colloidal solution produced in pure water and in various mixtures

of water and ethanol ranging from 0 to 100% of Ethanol. All PL measurements of the two signals were performed with the same parameters as in Fig. 5.6 and are normalized for the optical density at the excitation energy 4.66 eV. Fig. 5.11 (a) highlights that the intensity of the excitonic luminescence drops of a factor of seven when we perform PLAL in a mixture of water and ethanol (20%) and it is not detected in the samples prepared at larger ethanol concentration, thus suggesting that the excitonic PL is quenched by ethanol molecules present in solution. In fact, in the previous chapter we have shown the effect of pH on the excitonic PL intensity, so evidencing that it is strongly sensitive to the NPs surface. Moreover, we have also observed that the excitonic bands disappears when we dry the colloidal solution obtaining ZnO powder. Fig. 5.11 (b) shows an opposite trend for the defect emission as a function of ethanol
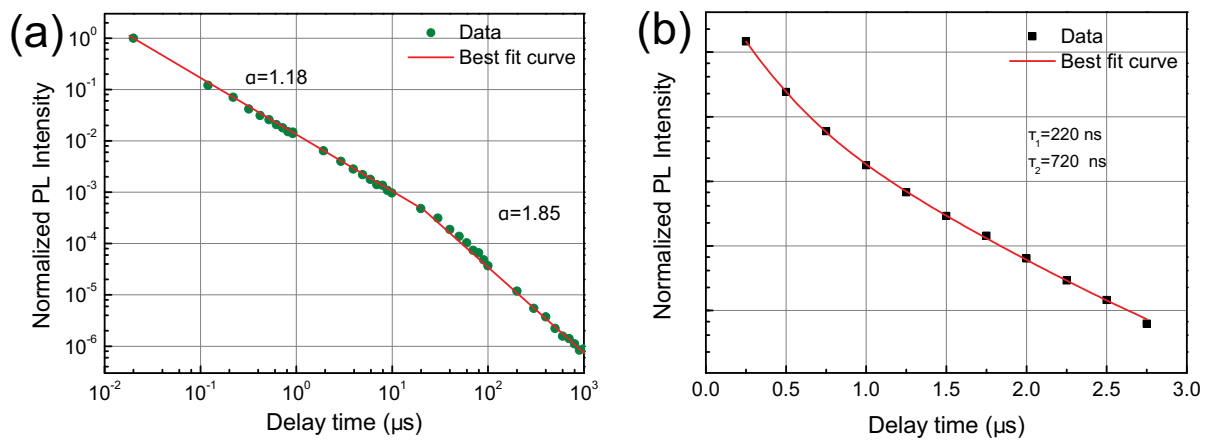
Figure 5.12: (a) Time decay curve of the green PL of the colloidal solution produced in a mixture with water and 30% ethanol. (b) Time decay curve of the blue PL of the colloidal solution produced in pure ethanol. The smooth solid lines represent the best fit curves.

concentration up to 30% leading to an enhancement of the defect band of a factor of about 2.5, whereas the PLAL in pure ethanol, which produces metal Zn NPs, exhibits a PL emission in the blue region with different features as compared to the green band: it is centered at 2.8 eV with a FWHM=0.8 eV. Moreover, Fig. 5.12 (b) shows that the blue band is characterized by a two exponential decay law with τ_1=220±30 ns and τ_1=720±70 ns, thus it doesn't exhibit the power law decay time which was observed for the green emission (Fig. 5.12 (a)). This blue band is probably related to surface states forming outside Zn NPs due to a capping effect of ethanol molecules, nevertheless, this attribution needs to be further verified. The enhancement of the green band intensity is accompanied by a increase of the initial decay slope α=1.18 with respect to the sample obtained in pure water α=1.05, shown in Chapter 4. This fact can be explained using the tunneling theory reported by Huntley [171], in agreement with this, the exponents of power law describing the decay curve of green band become more and more negative on increasing the concentration of the recombination centers (oxygen vacancies) in the sample.

The competition of the green and the excitonic- PL emissions has been shown in the previous chapter as a consequence of thermal annealing in controlled atmosphere (Sec. 4.5.2). In that experiment we highlight a relationship between emission properties and structural prop-

erties evidenced by Raman spectrum which is due to the reduced number of oxygen vacancies. Fig. 5.13 displays μRaman spectra acquired in the samples synthesized in pure water, ethanol
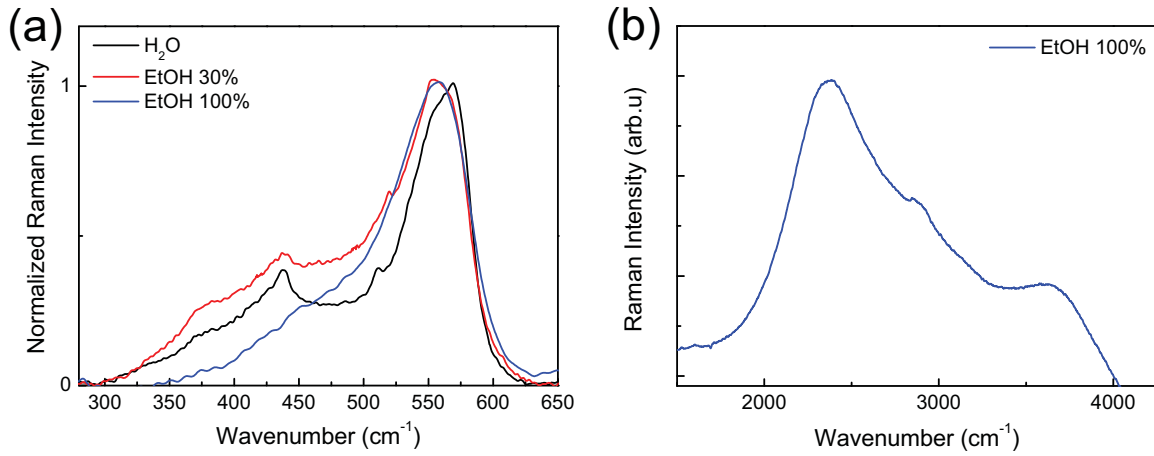
Figure 5.13: (a) μRaman spectrum of the ZnO NPs produced by PLAL in water, 30% ethanol and 100% ethanol. Raman intensity are normalized to the difference between the intensities of the $A_1(LO)$ Raman peak and background. (b) μRaman spectrum of the sample with 100% acquired from 1000 cm^{-1} to 4500 cm^{-1}.

30% and 100% and normalized to the difference between the intensities of the $A_1(LO)$ raman peak (565 cm^{-1}) and background. Raman spectra reveal an opposite trend than shown previously. In this case, we observe an enhancement of the $A_1(LO)$ mode, related to defects, with respect to $E_2^{(2)}$ accompanied to a red shift from 565 cm^{-1} to 554 cm^{-1}. Then, Raman spectra evidence that the sample prepared with 30% ethanol is ZnO in wurtzite structure characterized by a major number of oxygen vacancies, consistently with the increased green band. A further Raman peak at about 375 cm^{-1}, present in the sample with 30% ethanol, can be attributed to residual Zn(OH)$_2$ due to an incomplete oxidation hampered by ethanol molecules. Instead, the sample prepared in pure ethanol shows the $A_1(LO)$ mode whereas the most important mode for the wurtzite structure, $E_2^{(2)}$ mode, is not present. The presence of the $A_1(LO)$ mode could be related to a partial and disordered oxidation of the Zn NPs powder which were exposed to a focused laser source (532 nm) in air to obtain Raman measurements. Besides, this sample is characterized by three very broad Raman peaks in the range 2000-4000 cm^{-1} which can be attributed to stretching mode of O=C=O (2363 cm^{-1}), -CH$_2$ and -CH$_3$ (2880 cm^{-1}), as well as CO-H (3400-4000 cm^{-1}) placed at the NPs surface responsible of the blue emission.

We can conclude that the behavior of PL and Raman spectrum in the presence of Ethanol might be a consequence of the enhanced number of oxygen vacancies due to a more incomplete oxidation in ethanol mixture, then a defect-mediated recombination is enhanced as compared to excitonic emission. Finally, in addition to control the oxidation kinetics of Zn NPs, PL measurements reveal that by PLAL in a mixture of water and ethanol it is possible to change the concentration of oxygen vacancies in ZnO NPs.

5.7   Conclusions

Online UV-Vis OA and PL measurements during PLAL are used to probe the oxidation processes of Zn NPs during PLAL of a zinc plate in aqueous solution. Online spectra at fixed RR=10 Hz show a delayed growth of exciton PL signal from the beginning of PLAL demonstrating that the oxidation of the ablated Zn mainly occurs out of the plume region, due to the reaction of Zn NPs with water molecules. Consistently, OA spectra reveal transient Zn/ZnO core-shell NPs, which are fully oxidized and lose their metallic core only hundreds of seconds after the end of PLAL. Defect-related PL signal arises with a further delay time (100 s) compared to exciton PL, indicating that the earliest oxidation of Zn essentially produces defect-free ZnO. OA spectra of the samples obtained at laser RR of 5 Hz, 10 Hz and 20 Hz exhibit a different post-ablation shape and temporal evolution. In particular, as evidenced by SPR peak at ∼5 eV, the Zn/ZnO ratio at the end of PLAL decreases at lower laser RR. Luminescence measurements show that excitonic kinetics is almost independent of the RR, being only a function of the number of pulses. Moreover, we observe a defect emission a 2.2 eV attributed to oxygen vacancies, which starts to grow after a number of pulses proportional to the used RR, corresponding to the almost constant time delay of ∼100 s. OA and PL spectra acquired on the stable colloidal solution show the typical absorption edge of the wurtzite ZnO (Eg=3.38 eV) and related excitonic PL peaked at 3.32 eV. These findings can be explained considering that the initially produced Zn NPs are oxidized in two phases. An earliest and superficial oxidation and a later and slower oxidation, which is sensitive to the RR and it is completed only well after the end of ablation leading to the complete disappearance of the metal species. OA kinetics during and after PLAL in a mixture of water and ethanol from 0 to 100%, we have demonstrated that it is possible to control the oxidation rate of the just produced Zn NPs, which is from 900 s in pure water to at least one week in pure ethanol. On the basis of the experimental results, we have proposed a simple model that explains the growth of defective ZnO NPs as a result of aqueous oxidation of Zn NPs slowed down and hindered by water diffusion through the ZnO shell. Therefore, *in situ* measurements allow us to deep understand how PLAL of a zinc plate in both water and ethanol solution produces ZnO NPs, then we provide a significative advance to the knowledge of oxidation processes of Zn NPs. Finally, *ex situ* measurements show an enhancement of the green to exciton intensity ratio accompanied by an increase of the $A_1(LO)$ mode, related to oxygen vacancies, on increasing ethanol concentration. These findings agree with that show in the previous chapter as a consequence of thermal annealing, thus they endorse our attribution to oxygen vacancies as defect from which originate the green PL. Moreover, they suggest that the ethanol/water ratio also controls the concentration of oxygen vacancies inside ZnO NPs.

Chapter 6

ZnO NPs Synthesized by fs Pulsed Laser Ablation in Water

In this chapter we investigate ZnO NPs produced by pulsed laser ablation (PLAL) of a zinc plate in water using a fs pulsed Laser. The experimental approach was based on *ex situ* measurements using time-resolved luminescence and complementary techniques. We'll deal with the properties of NPs produced by varying pulse energy and we'll compare their properties with those of ZnO NPs generated by nanosecond laser pulse discussed in the previous chapters. Nevertheless, we point out that this investigation is still in progress and needs to be studied in further detail.

6.1 Introduction

The experimental results reported in the previous chapters have shown that nanosecond PLAL of zinc in water produces luminescent ZnO NPs in wurtzite structure. Furthermore, we have evidenced the possibility to control the defect concentration responsible of the green emission at 2.2 eV by mixing ethanol to deionized water. In Chapter 2, we have argued that NPs formation may take place by growth of ejected hot drops and solids from the target which interact with the solvent, which provides a reactive environment thus inducing, for instance, metal oxidation. In addition to the solvent, other ablation parameters play a crucial role in controlling the properties of the produced NPs. Indeed, physical processes involved in PLAL are strongly affected by pulse duration, in particular, using fs pulses ultrafast localized heating is observed; thus, ablation is dominated by direct photoionization processes and electron-ion collisions [144] rather than thermal processes such us evaporation and boiling.

Despite of this, no ablation experiment, using fs laser pulses on a Zn target was already done to our knowledge. Hence, it is not known if ZnO NPs are induced and, most important, if they are characterized by similar properties compared to those obtained by ns pulses. In the previous chapter we have shown that on increasing the energy of ns pulses (from 20 to 90 mJ) it is obtained a more and more large sized distribution of ZnO NPs with average sizes from 18 to 30 nm. Since the studied NPs have sizes bigger than the exciton Bohr radius no effect of

quantum confinement is observed. Therefore, by PLAL with ns pulses we were unable to obtain a controlled distribution of ZnO NPs which is mandatory to modulate their optical properties.

In this chapter we investigate ZnO NPs produced by PLAL of a zinc plate in water by using fs laser pulses (50 fs) at various pulse energies (75-350 μJ). Our experimental approach was based on the use of time-resolved luminescence and Atomic Force Microscopy (AFM) which allow us to investigate the morphology and to obtain a complete optical characterization of the produced NPs.

6.2   Morphological Properties

ZnO NPs were synthesized by PLAL using a Ti-sapphire pulsed laser, with pulse width of 50 fs, focused on a Zinc target placed at the bottom of a vessel containing 2 ml of deionized water. The Ti-sapphire laser wavelength is λ=800 nm and the repetition rate was selected at 1 kHz to avoid the spatial overlap between laser pulse and the previously created cavitation bubble (bubble lifetime$\sim$100 μs). In this way we reduced the scattering of incoming laser pulses with NPs and cavitation bubble optimizing the ablation efficiency (see Sec. 2.3.5). We also note that the ablation efficiency strongly depends on the used solvent amount, in particular, the efficiency drops to zero when water volume exceeds 2 ml. Since the fs laser beam must pass trough a liquid layer, this behavior can be attributed to self-focusing or to the generation of a white continuum which consumes laser energy and reduces the efficiency of interaction with target [124]. The laser beam was focused by a parabolic lens (the spot size on the Zn target was $\sim$100 μm); the energy per pulse was chosen to be 75, 150 and 350 μJ which correspond to the fluence on the target of 0.75, 1.5, 3.5 μJ/cm^2. In order to maintain the same total fluence of 855 kJ/cm^2, we used irradiation times of 900 s, 450 s and 180 s, respectively. At the end of PLAL, we obtained a stable pale yellow colloidal solution.

The AFM images and particle size distributions of NPs are shown in Fig. 6.1. They reveal that the ablation products consist in distributions of spherical-like nanoparticles with sizes of the order of nanometers which are dependent on laser pulse energy. In particular, larger size distribution (from 5 to 20 nm) and larger average NPs size (10.5$\pm$0.2 nm) were obtained with larger pulse energy (350 μJ), whereas we obtained a sharper distribution ranging from 2 to 17 nm and average size of 7.40$\pm$0.14 nm with 75 μJ, and the sharpest distribution ranging from 1.5 to 10 nm with average size of 5.20$\pm$0.08 nm with 150 μJ. Hence, we didn't find a clear dependence of the size distribution on pulse energy as for the results obtained with ns pulse energy; this finding points out the difference of physical process involved in fs PLAL. Nevertheless, in this case we synthesized smaller NPs characterized by a more regular spherical-like shape with average radii (2.6, 3.7 and 5.3 nm) of the order than excitonic Bohr radius (2.23 nm).
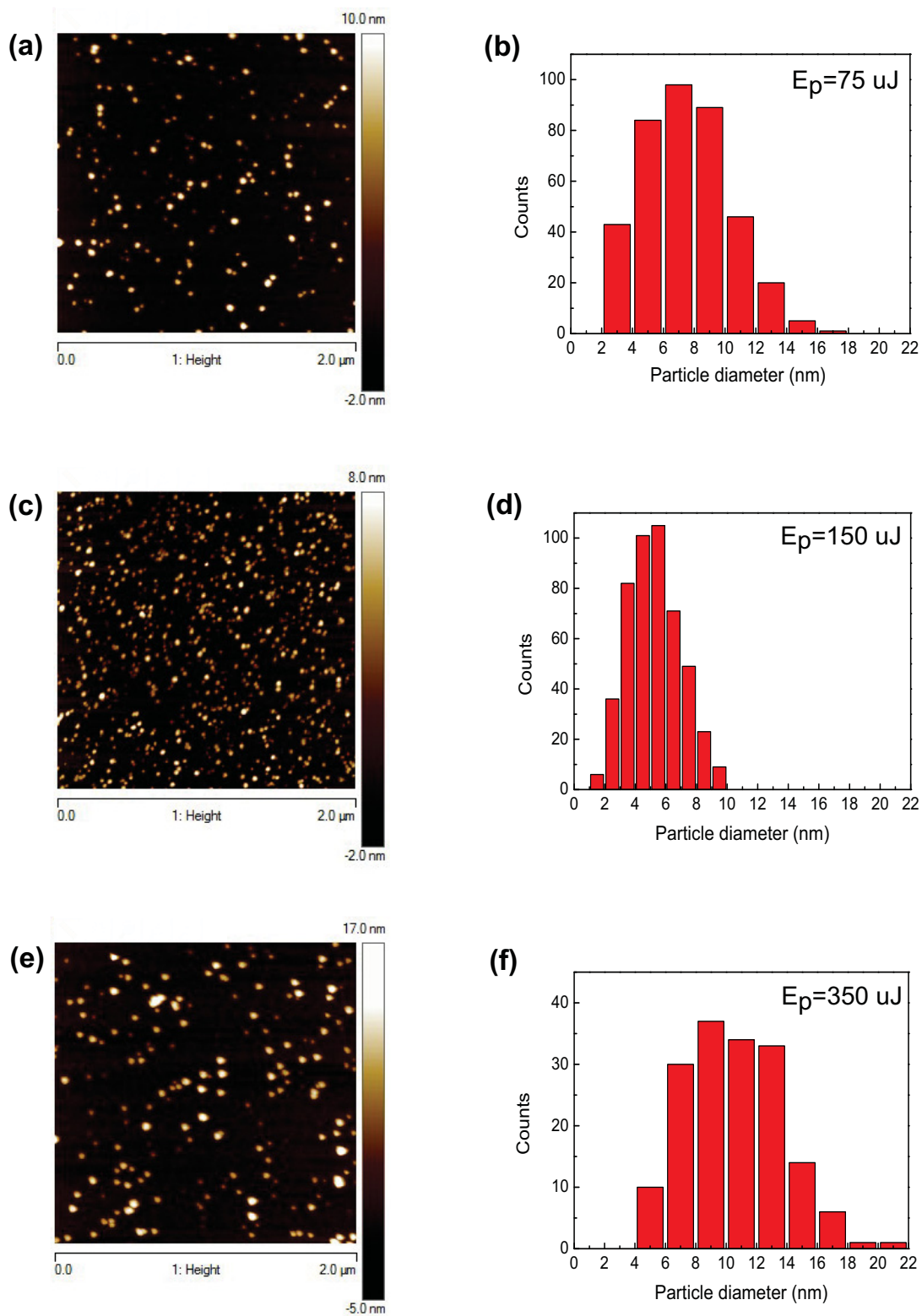
Figure 6.1: (a),(c),(e) AFM image $2 \times 2\ \mu m^2$ of the dried colloidal solution of ZnO NPs produced by PLAL of a zinc plate in water using a fs Ti:Sapphire Laser with energy per pulse of 75, 150 and 350 μJ, respectively; (b),(d),(f) Size distribution calculated from AFM image (a), (c), (e), respectively.

6.3 Optical Properties: Excitons

The purpose of this section is to study the optical properties of ZnO NPs produced by PLAL with different energies of the fs Ti:Sapphire. The OA spectra of ZnO NPs dispersed in water are shown in Fig. 6.2 and show the typical sharp edge of wurtzite ZnO. However, it is evident that the OA edge is located at slightly different spectral positions for the three samples, each characterized by a different size of NPs depending on the laser energy. By Tauc plot we extrapolated the linear region which intersects the energy axis at the band-gap (see the green straight lines in the inset of Fig.6.2), as expected for direct allowed transitions, such as in ZnO. Thereby, we estimated the optical band-gap of 3.41±0.01 eV, 3.45±0.03 eV and 3.50±0.02 eV for the sample with diameter of 10.5, 7.4 and 5.2 nm, respectively. These values are larger than the known E_g for bulk ZnO (3.37 eV) and than obtained value for ZnO NPs prepared with Nd:YAG laser (3.38 eV), which are characterized by average sizes around 20-30 nm, revealing a quantum confinement effect on the ZnO NPs produced by this femtosecond pulses.
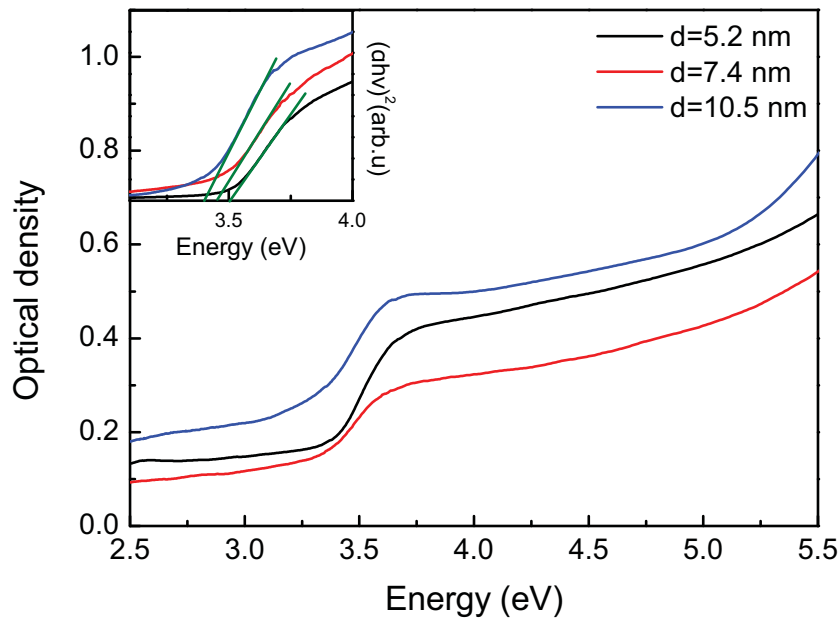
Figure 6.2: UV-Vis optical absorption of the colloidal solution prepared with laser energies of 75 μJ, 150 μJ and 350 μJ per pulse; insets show the Tauc plot of the excitation spectra obtained in the hypothesis of direct band-gap.

In order to deeply study the quantum confinement effect, we report the PL properties of the ZnO NPs. Fig. 6.3 (a) displays an UV emission of the nanoparticles having average size of 5.2, 7.4 and 10.5 nm excited upon UV excitation (4.66 eV) acquired with T_W=10 ns and a time delay T_D=0 ns respect to the arrival of laser pulses. All PL spectra are normalized for the optical density at the excitation energy, that is the spectra are normalized to the ZnO concentration in the samples. The spectra display the Lorentzian line shape of the PL thus supporting its assignment to excitonic emission, in addition they do not show dramatic differences on the PL intensities among the samples. The time decay curve detected in the sample with diameter
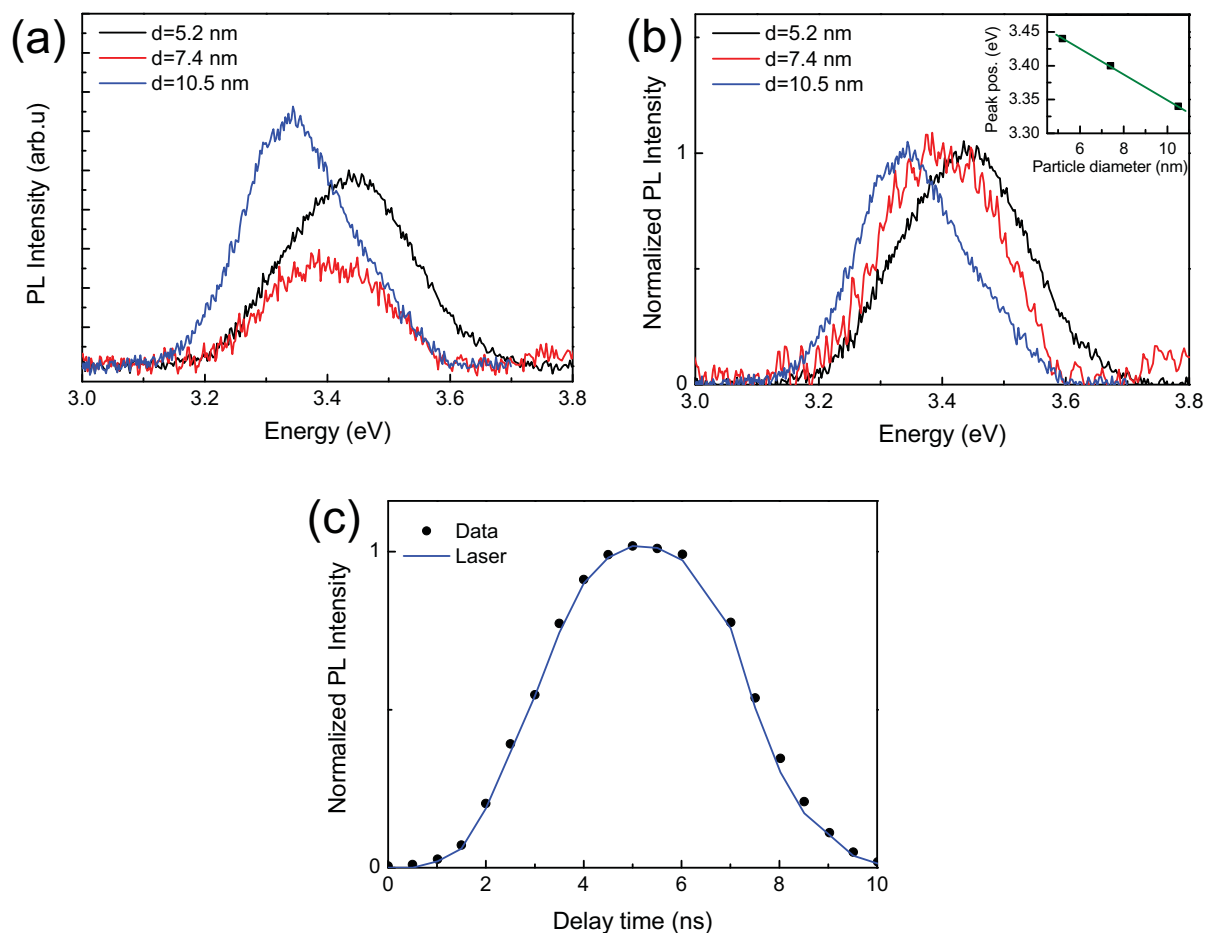
Figure 6.3: (a) ZnO exciton PL of the sample with size of 5.2, 7.4 and 10.5 nm, excited at 4.66 eV. (b) Normalized excitonic PL of the three samples; inset shows the peak positions as a function of the NPs size. (c) Time decay curve of the excitonic PL detected in the sample with diameter of 5.2 nm; the blue smooth line represent the excitation laser pulse.

of 5.2 nm and reported in Fig. 6.3 (c) shows that it follows the laser profile revealing a PL lifetime much shorter than the laser rise time (2 ns). We note that an ultra-short lifetime ($\sim$100 ps) substantially agrees with that in the range of hundreds of picoseconds found in ZnO nanostructures [75, 77–79], thus it provides a further support to the excitonic attribution. In addition, it is shorter than previously shown value of 800 ps revealing a major presence of defects in ZnO NPs. As for ZnO NPs produced by ns pulses, PLE spectrum of excitonic emission is not reported because the emission peak is too close to excitation thus is not possible single out the exciton contribution to the scattered excitation pulse. However, also in this case we observe that its PLE spectrum follows the absorption curve keeping flat at photon energy larger than 4 eV. As shown in Fig. 6.3 (b), the normalized spectra highlight a change of the peak position and FWHM of the excitonic PL on decreasing the NPs sizes. In detail, the peak position was estimated to be 3.34±0.01 eV (10.5 nm), 3.39±0.02 eV (7.4 nm) and 3.43±0.01 eV (5.2 nm), as reported in the inset of Fig. 6.3 (b); interestingly the exciton peaks broaden from 0.21 eV to 0.27 eV on decreasing the NPs diameters.

In the Sec. 1.3 we dealt with the quantum dots both in the strong and in the weak confinement regime, in particular we showed that in the size domain where the dot is smaller than the excitonic Bohr radius, it is plausible that the exciton may not exist and therefore holes and electrons will suffer a strong confinement. Instead, the excitonic emission of ZnO NPs produced by fs pulses suggests that holes and electrons will suffer a weak confinement, hence, it is more correct to use Eq. (6.1), which relates the NPs sizes with the optical band-gap taking into account the exciton binding energy

$$E = E_g + \frac{\hbar^2 \pi^2}{2MeR^2} - E_{ex} \,, \tag{6.1}$$

where M is the translational mass of exciton ($0.69m_0$) obtained by the sum of electron and hole effective mass (m_e=$0.24m_0$, m_h=$0.45m_0$), R is the mean dot size, Eg = 3.369 eV and E_{ex}=59 meV for ZnO. According to this formula, one can calculate the expected optical band-gap for known NPs diameters. Then, replacing the NPs sizes obtained by AFM measurements in Eq. (6.1) we obtained the corresponding E= E_g-E_{ex} values of 3.34±0.01 eV, 3.37±0.01 eV and 3.44±0.01 eV for 10.5, 7.4 and 5.2 nm particle diameter. Comparison between the energy gap obtained by Tauc plot of Fig. 6.2, the estimated parameters of excitonic curves reported in Fig. 6.3 and the excitonic peak position calculated by Eq. (6.1), are reported in Table 6.1.

NPs size (nm)	E_g (eV)	Excitonic peak pos. (eV)	FWHM (eV)	Calc. excitonic peak pos. (eV)
5.2±0.08	3.50±0.02	3.43±0.01	0.27±0.01	3.44±0.01
7.4±0.14	3.45±0.03	3.39±0.02	0.24±0.02	3.37±0.01
10.5±0.2	3.41±0.01	3.34±0.01	0.21±0.01	3.34±0.01
18±2	3.38±0.01	3.32±0.01	0.20±0.01	3.32±0.01

Table 6.1: Comparison between the energy gap obtained by Tauc plot of Fig. 6.2, estimated parameters of excitonic curves reported in Fig. 6.3 and excitonic peak position calculated by Eq. (6.1) for the ZnO NPs produced by fs pulses. For comparison in the last row we report the data on the NPs obtained by ns pulses.

From the comparison in Tab. 6.1 we can infer that calculated excitonic peak position well agrees with that obtained by PL curves, in addition, considering E_{ex}, these values are consistent with the optical band-gap extrapolated by Tauc plot from OA spectra. To easily compare the obtained results in a more general point of view, we also report the data of NPs synthesized by ns pulses taken from Chapter 4. Therefore, this findings demonstrated that ZnO NPs produced by fs pulses are in the weak confinement regime. Moreover, the increasing broadness of the excitonic band on decreasing the NPs size can be attributed to the fact that smaller NPs are more affected by quantum confinement, thus the larger size distribution leads an overlap of excitonic curves peaked at different energy values.

6.4   Optical Properties: Defects

In order to complete the optical characterization of ZnO NPs produced by fs PLAL we investigate the visible emissions related to point defects. Indeed, in addition to the UV excitonic emission,
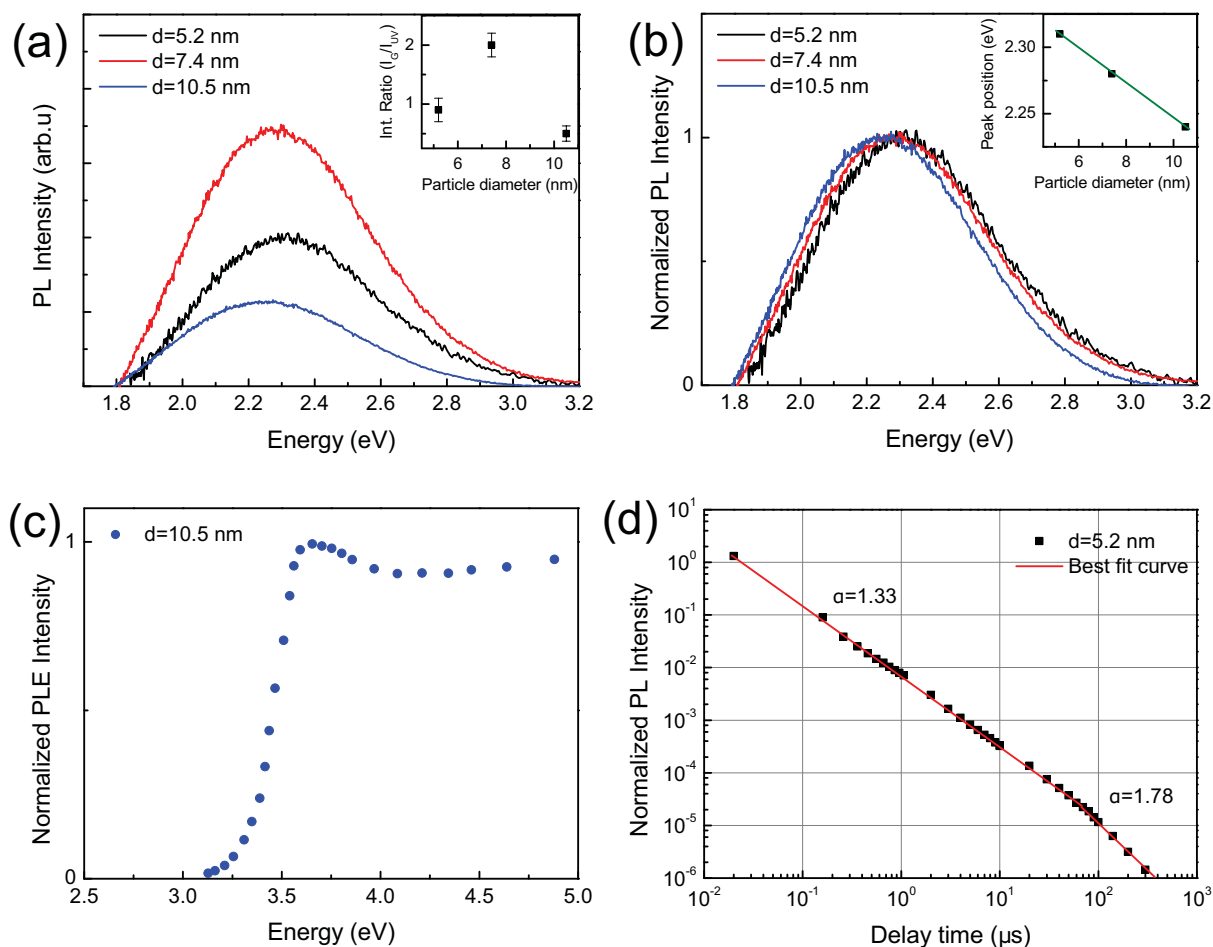
Figure 6.4: (a) Green PL of the sample with size of 5.2, 7.4 and 10.5 nm, excited at 4.66 eV, inset shows the defect/exciton intensity ratio as a function of the NPs size. (b) Normalized defect PL of the three samples; inset shows the peak positions as a function of the NPs size. (c) Excitation spectra of the NPs with average size of 10.5 nm obtained monitoring the defect emission intensity at 2.3 eV. (d) Time decay curve of the defect related PL obtained from NPs with average size of 5.2 nm; the smooth solid line represents the best fit linear curve.

the ZnO NPs here produced have two visible PL peaked in different regions. The first is the broad green emission centered at 2.2-2.3 eV acquired upon UV excitation (4.66 eV) and detected with T_W=10 ms and T_D=20 ns (see Fig. 6.4 (a)). The second is a blue emission peaked at 2.8 eV, which has been never detected in ZnO NPs produced by ns pulses, acquired upon UV excitation (3.76 eV) and detected with T_W=20 ns and T_D=0 ns (see Fig. 6.5 (a)). We note that this blue band is different than that reported in Chapter 5 attributed to surface states in Zn NPs obtained by PLAL in ethanol, in particular it is characterized by a shorter decay time and it is more narrow as will show below. Since the ZnO NPs produced by fs pulses display two emission bands which spectrally overlap in steady state PL measurements, the PL and PLE spectrum here reported were acquired by time resolved apparatus. PLE spectrum was measured manually point by point by fixing the laser energy and normalizing each point to the laser-pulse energy. The green PL, as reported in Fig. 6.4 (a), shows the same features observed in the band

attributed to oxygen vacancies in Chapter 4 and 5, that is, peak position at 2.2-2.3 eV with a FWHM=0.6 eV. Consistently, the three samples with different sizes exhibit similar excitation spectra and decay time curves, as shown in Figs. 6.4 (c) and (d). In fact, the excitation spectrum (PLE) obtained monitoring the emission peak at 2.2 eV exhibits a sharp threshold at ∼3.6 eV and appears almost flat at higher energies (see Fig. 6.4 (c)). This shape is identical in all samples and indicates that the green band is excited only by photon energies larger than the band-gap thus involving band-to-band transitions. Nevertheless, the green PL and PLE spectral features of ZnO NPs produced by fs pulses are the same than those synthesized by ns pulses ablation, we highlight that in this case there is a slight change of peak position as a function of NPs sizes. Fig. 6.4 (b) shows the three normalized green bands of sample with size of 5.2, 7.4 and 10.5 nm. It is evident a blue shift of the peak position on decreasing the NP size. In detail, in the inset we report the peak position of the green band which is estimated to be 2.24±0.02 eV, 2.28±0.02 eV and 2.31±0.02 eV for the samples with NPs having average sizes of 10.5, 7.4 and 5.2 nm, respectively. These blue shift values agree with the optical band-gap energies in the previous section, thus it demonstrates that the intra-gap energy level responsible of the green emission is tightly related to the band-gap value (consistently with excitation spectrum) being about 1.2 eV below the energy minimum of the conduction band (CB). A blue shift of about 0.03 eV is also observed in the PLE of the sample with size 10.5 nm in agreement with the increased optical band-gap and the fact that excitation initially involves a band-to-band transition. The decay time reported in Fig. 6.4 (d) reported in a log/log scale evidences that data follow two different trends consistent with a power law dependence $I \propto t^{-\alpha}$ across five decades in the time scale; the first in region from 20 ns to 60 μs and the second from 60 μs up to 300 μs. By a fitting procedure we get α=1.33±0.07 and α=1.8±0.1 for the two ranges of time, respectively. Therefore, the decay kinetics of the green band follow the same decay function observed for NPs produced by ns PLAL (Chapter 4), but with a larger α value (1.33 with respect to 1.05) in the first time region. Since the green to exciton intensity ratio (inset of Fig. 6.4 (a)) is of the same order of magnitude than that obtained in Chapter 4, one can conclude that these NPs should have the same concentration of oxygen vacancies with respect the total amount of ZnO, thus the same value $\alpha \sim 1$. Nevertheless, this behavior can be tentatively related to a stronger influence of defects on the smaller NPs (from 5.2 to 10.5 nm), which could be responsible of a faster tunneling recombination of trapped electrons and holes. This is a surprising result because indicates that a point defect like oxygen vacancy may be sensitive to the entire NP structure. Because of the green to exciton intensity ratio doesn't show a clear trend as a function of NPs size one reveals that defect-related PL is not sensitive to the surface to volume ratio. Therefore, it supports our claim as discussed in the Chapter 4 that oxygen vacancies lie inside NPs rather than at the surface.

As concerns the blue emission (Fig. 6.5 (a)) comparing the signal of the three samples characterized by NPs with different sizes, we observe that its intensity and its peak position remain almost constant. A blue emission at 2.8 eV has been observed by Zeng et al. [88, 94] in ZnO NPs produced by PLAL of a Zn plate in SDS water solution and associated with zinc
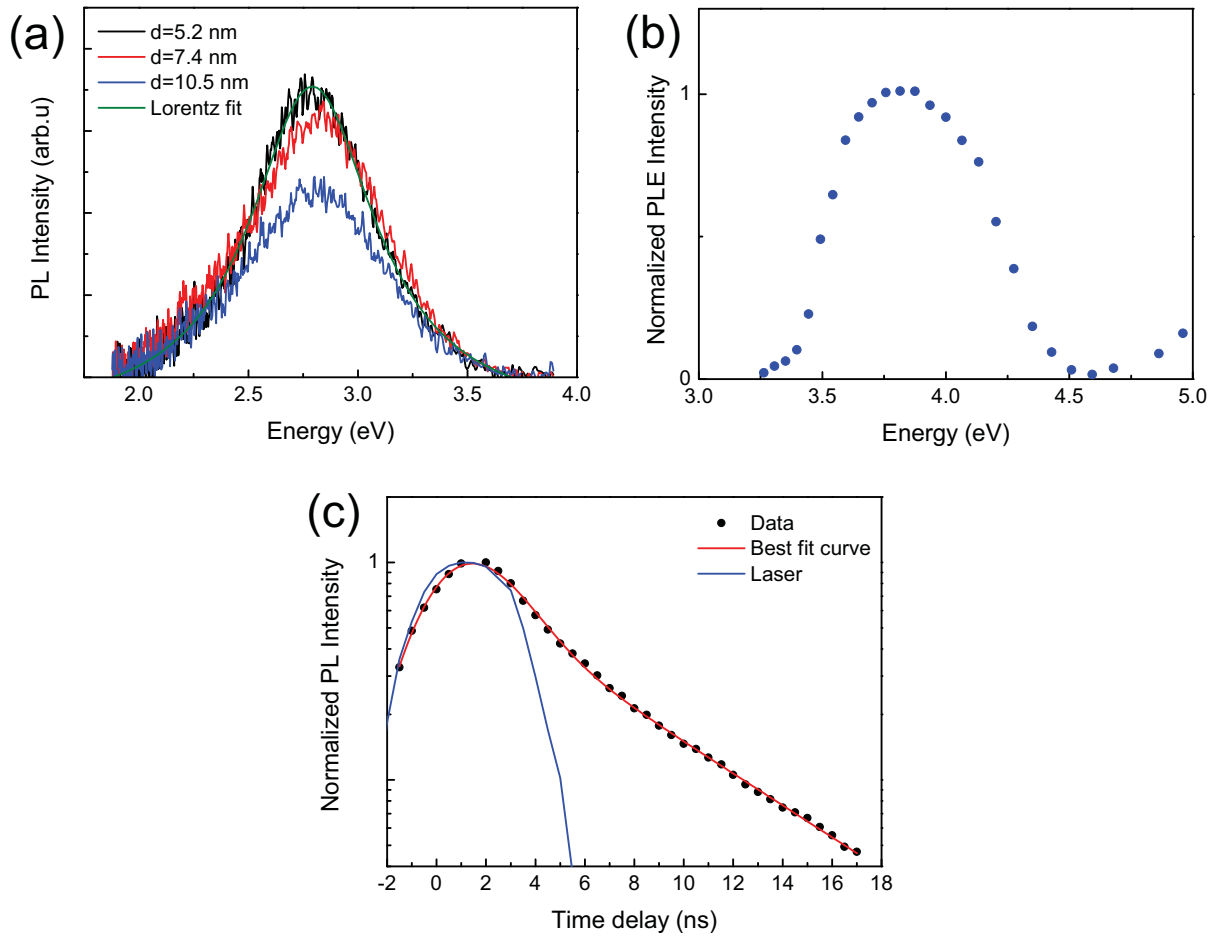
Figure 6.5: (a) Blue PL of the sample with size of 5.2, 7.4 and 10.5 nm, excited at 3.75 eV. (b) Excitation spectra of the NPs with average size of 5.2 nm obtained monitoring the defect emission intensity at 2.8 eV. (c) Time decay curve of the defect related PL; the smooth red solid line represents the best fit curve; the smooth blue solid line represents the laser pulse.

interstitial. However, the reported PLE spectrum exhibits a peak at energy slightly below to the band-gap (3.2 eV) indicating a preferential excitation in an intra-gap state close the CB, which agrees with the shallow donors nature of Zn_i for ZnO, as discussed in the Sec. 1.1.4. In contrast, PLE spectrum acquired in this experiment reveals that the blue band is only excited by photon energy larger than the optical band-gap, thus the excitation initially involves a free electron-hole pair. Besides, it shows a clear Lorentzian shape, centered at 2.80±0.01 eV and with FWHM=0.70±0.03 eV, which suggests the attribution of this PL signal to an excitonic emission rather than to point defects. Despite of this, the PL is peaked about 0.6-0.7 eV belove the optical band-gap which is much larger than the exciton energy bound for ZnO materials (60 meV). The efficiency of excitation reaches a maximum at 3.8 eV and then drops to zero giving rise to a band shape curve peaked at 3.8 eV and with a FWHM=0.75 eV. Therefore, the blue band is preferentially excited in an energy range above the optical band-gap rather than over the absorption edge as for the excitonic PL excited at 4.66 eV and peaked at 3.43 eV discussed above. The extracted time evolution of the luminescence, reported in fig. 6.5 (a), displays a

bi-exponential decay with estimated lifetimes $\tau_1 = 1 \pm 0.2$ ns and $\tau_2 = 6 \pm 0.2$ ns. The existence of two exciton decays with distinctly different lifetimes implies that the emission could be driven by different processes. In any case, it is known that nanosecond lifetimes evidence the presence of free-excitons, as have been argued for bulk ZnO [47, 48] and for ZnO microstructures [49]. Hence, despite NPs produced by fs pulses are in the nanometric regime their excitonic lifetimes of the order of ns evidences the presence of free-excitons in ZnO NPs.

6.4.1 Model for the Blue Band
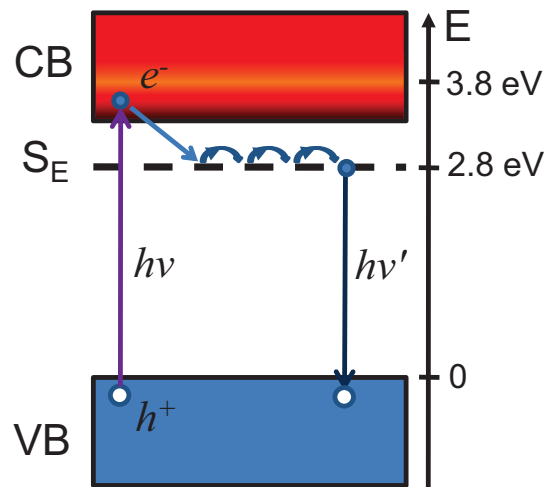
Figure 6.6: Photoluminescent processes suggested for the blue excitonic band of ZnO NPs.

A tentative PL model concerning the blue band at 2.8 eV present in ZnO NPs prepared by PLAL with fs pulses is depicted in Fig. 6.6. Following this model, the blue band is due to a photo-generated electron temporarily trapped in defect states S_E from which it recombines with hole in the valence band, thus producing the PL band peaked at 2.8 eV with lifetimes of 1 ns and 6 ns. Moreover, we suggest that the electron can jump from one state to another keeping the mobile nature of exciton rather than to be localized in the defects. In this way, homogeneous broadening prevails [45, 46] and, since exciton is not trapped in a defect state of quantum dots, we expect a luminescence lifetime larger than ns [75]; indeed, we observed a Lorentzian shape with lifetime of the order of ns. The fact that the exciton peak position is independent of NP size might suggest that defect states responsible of S_E level might be located at the surface of NPs. Since the blue emission is detected only after excitation in a defined energy range above the CB, we can infer that the recombination process is governed by the photon energy transferred to the exciton during the excitation. Then, if the excitation photon provides large enough energy to the electron-hole pair, the recombination mechanisms discussed in Chapter 4 prevail. Hence, the exciton can freely travel through the NP leading the excitonic emission at 3.3-3.4 eV; otherwise the recombination occurs between a hole in the VB and an electron deeply trapped in a singly

ionized oxygen vacancy giving the green PL at 2.2-2.3 eV. This mechanisms producing the blue band at 2.8 eV with ns lifetimes was observed only in ZnO NPs obtained by fs pulses probably due to defects different from oxygen vacancies (probably at the NP surface) which generate S_E states. On the other hand, surface states could to be present in ZnO NPs produced by ns pulses, however, their effect might be sensitive to NPs size and became considerable when size is of the order of excitonic Bohr radius. For this reason we observe this emission in smaller NPs produced by fs pulses.

6.5 Conclusions

ZnO NPs with average sizes from 5 to 10 nm were synthesized by PLAL of a zinc plate in deionized water by using a fs Ti:Sapphire laser. Optical absorption and time resolved PL spectra show the typical absorption edge and the excitonic fast PL of the wurtzite ZnO. The band-gap of ZnO NPs increases on decreasing the NP size, in agreement with the Tauc plot, thus evidencing a quantum confinement effect. Consistently, excitonic peak blue shifts from 3.34 eV up to 3.40 eV and broads from 0.21 eV up to 0.27 eV following the equation which relate the excitonic level to the NP size in the weak confinement regime. In addition to excitonic emission, we observed the visible PL at 2.3 eV due to the presence of oxygen vacancies in ZnO NPs characterized by an excitation spectrum with an edge at about 3.5 eV and a power law decay time which indicates a recombination mechanism driven by tunnelling of trapped electrons to recombination centres randomly distributed in space. Also the green band exhibits a blue shift with the NPs dimensions highlighting its not obvious correlation with the conduction band of ZnO. A further visible PL in the blue region peaked at 2.8 eV and FWHM=0.7 eV was detected. It exhibits typical features of excitonic PL and PLE with two ns bi-exponential lifetimes (τ_1=1 ns and τ_2=6 ns), however is characterized by a large stock shift (0.6 eV). Based on our experimental results we propose a recombination mechanism for the blue PL involving a photo-generated electron which becomes temporarily trapped in a manifold of electronic states S_E localized on different sites, among which the electron can jump from one state to another keeping its mobile nature, then it recombines with hole in the valence band producing the blue emission at 2.8 eV. Summarizing, we have demonstrated that PLAL with fs pulses produces ZnO NPs showing similar optical properties than those produced by ns pulses: optical absorption edge, excitonic emission in the UV region and green emission. Despite of this, we have shown that NPs have a more regular spherical morphology with a much smaller average size which allow us to study the weak confinement effect. If excitation energy falls in the range 3.3-4.4 eV, they exhibit another PL peaked at 2.8 eV, ever reported in literature for ZnO NPs to the best of our knowledge, which can be attributed to a peculiar excitonic emission.

Conclusions

In this thesis we have reported an experimental study on ZnO nanoparticles (NPs) produced by pulsed laser ablation in liquid (PLAL) providing a complete characterization of their morphological, structural and optical properties, as well as a deep insight on the formation processes involved during the NPs synthesis. ZnO NPs are currently the subject of a large scientific interest due to their use in several technological applications including photovoltaics, optoelectronic devices and bioimaging. In addition to the excitonic emission at 3.3-3.4 eV, several visible photoluminescence (PL) bands are commonly attributed to the presence of native defects (zinc vacancies, oxygen antisites, oxygen vacancies, zinc interstitial) in ZnO NPs, one of most debated being a green emission peaked at 2.2-2.4 eV. In the current literature it is known the formation of luminescent ZnO NPs, in crystalline form, by PLAL of a zinc plate in water. However, all experiments reported so far have only used ex situ methods to study the already stabilized ZnO NPs, hence, many questions are still open on the sequence of events producing the oxidized ZnO NPs from the Zn metal target.

Our investigation is founded on the combined use of several experimental techniques including *in situ* optical absorption (OA) and photoluminescence (PL), whereas atomic force microscopy (AFM), high resolution TEM (HRTEM), μRaman and time resolved PL were used for the *ex situ* study. The results here reported enrich the knowledge on the defect responsible for the green emission, thus contributing with elements of novelty deduced by a fine spectroscopic and microscopic analysis. Moreover, by the *in situ* study we clarify the oxidation processes involved during PLAL of zinc in water eventually leading the formation of ZnO NPs.

The main results obtained in this work can be summarized as follows:

- TEM, AFM images and μRaman spectra evidence that ns PLAL, using a Nd:YAG laser, of zinc target in water produces ZnO nanocrystals with an average size of tens of nm having a wurtzite structure. Their UV-Vis absorption curve exhibits the typical edge of wurtzite ZnO and time resolved PL spectra show the corresponding excitonic PL peaked at 3.32 eV with a single exponential lifetime of 800 ps. We also observe the defect-related PL at 2.2 eV characterized by a sharp edged excitation spectrum in agreement with a band-to-band transition that produces a free electron-hole pair, and a power law decay time which suggests a recombination mechanisms where trapped electrons tunnel to recombination centers. The defects are located inside NPs because the green PL is not influenced by the solution pH. Thermal annealing at 300 °C in O_2 atmosphere produces a

contemporary reduction of A_1(LO) Raman mode at 565 cm^{-1}, related to oxygen vacancies, and a decrease of the green PL, demonstrating that its origin is due to oxygen vacancies. Our results allowed us to propose a model for the green PL involving a hole in the VB, recombining with a deeply trapped electron in singly ionized oxygen vacancies. Hence, we provide a significant advance to the research reducing the doubts on the origin and mechanism of the green PL.

- AFM images reveal that by fs PLAL using a Ti:Sapphire laser (pulse width=50 fs) we obtained smaller ZnO NPs having average sizes from 5 up to 10 nm. Tauc plot evidences that the band-gap of ZnO NPs increases on decreasing the NP size; consistently, excitonic peak blue shifts from 3.34 eV up to 3.40 eV and broadens from 0.21 eV up to 0.27 eV demonstrating the quantum confinement effect in the weak confinement regime. We also observe the visible PL at 2.3 eV due to the presence of oxygen vacancies and a further visible PL in the blue region peaked at 2.8 eV. The latter exhibits a Lorentizan shape with two ns bi-exponential lifetimes (τ_1=1 ns and τ_2=6 ns), typical features of an excitonic PL, though it is interestingly characterized by a large Stockes shift (0.6 eV). We have suggested a recombination mechanism which involves a photo-generated electron in a manifold of defect states S_E such that the electron can jump from one state to another keeping its mobile nature, until it finally recombines with hole in the valence band producing the blue emission. We underline that to support this model, it is mandatory to perform further experiments which could provide other more detail on the emission mechanisms. For instance, a study of the effect of pH on the blue PL could give information about the type of defects (S_E) or their location. Moreover, a study as a function of temperature could clarify the trapping and detrapping processes.

- In situ OA and PL measurements during PLAL show a delayed growth of exciton PL signal from the beginning of PLAL demonstrating that the oxidation of the ablated Zn mainly occurs out of the plume region, due to the reaction of Zn NPs with water molecules. In agreement with this finding, online OA spectra exhibit a peak at ∼5 eV coming from surface plasmonic resonance (SPR) of Zn NPs and the typical absorption edge of the wurtzite ZnO, thus revealing transient Zn/ZnO core-shell NPs, which are fully oxidized only several hundreds of seconds after the end of PLAL. Defect-related PL signal arises with a further delay time (100 s) indicating that the earliest oxidation of Zn essentially produces defect-free ZnO. The OA spectra acquired at various laser repetition rates (RR) reveal that the Zn/ZnO ratio at the end of PLAL decreases at lower laser RR, as evidenced by the intensity of the SPR peak at ∼5 eV. Time resolved experiments show that excitonic kinetics is almost independent of the RR, whereas the green emission starts to grow after a number of pulses proportional to the used RR, corresponding to the approximatively constant time delay of ∼100 s. OA and PL spectra acquired on the stable colloidal solution show the typical absorption edge of the wurtzite ZnO and related excitonic PL. All findings can be explained considering that initially produced Zn NPs are oxidized in two phases.

An earliest and superficial oxidation, and a later and slower oxidation which is sensitive to the RR, and it is completed only after the end of ablation thus leading to the complete disappearance of the metal species. The analysis of OA kinetics during PLAL in a mixture of water and ethanol from 0 to 100%, evidence that it is possible to control the oxidation rate of Zn NPs varying from 900 s up to weeks when PLAL is performed in pure water or ethanol, respectively. The enhanced green to UV PL intensity ratio accompanied by the reduction of $A_1(LO)$ mode in the μRaman spectrum prove that the ethanol/water ratio can be also used to control the concentration of oxygen vacancies inside ZnO NPs. These results allow us to put forward an oxidation model that explains the growth of defective ZnO NPs as a result of aqueous oxidation of Zn NPs slowed down and hindered by water diffusion through the ZnO shell. These results underscore the importance of online methods to understand and control the physical processes involved in PLAL experiments, paving the way to use this approach to the PLAL of a variety of other materials.

Overall, our findings provide a significative advance in the knowledge on the PL origin and dynamics of ZnO NPs useful in view of their use in optoelectronic applications.

List of Papers

- L. Vaccaro, P. Camarda, F. Messina, G. Buscarino, S. Agnello, F. M. Gelardi, M. Cannas, and R. Boscaino, *Oxidation of silicon nanoparticles produced by nanosecond laser ablation in liquids*, AIP Conference Proceeding, vol. **174**, p. 1624, 2014.

- P. Camarda, L. Vaccaro, F. Messina, and M. Cannas, *Oxidation of Zn nanoparticles probed by online optical spectroscopy during nanosecond pulsed laser ablation of a Zn plate in H_2O*, Appl. Phys. Lett., vol. **107**, p. 013103, 2015.

- P. Camarda and F. Messina and L. Vaccaro and S. Agnello and G. Buscarino and R. Schneider and R. Popescu and D. Gerthsen and R. Lorenzi and F. M. Gelardi, and M. Cannas, *Luminescence mechanisms of defective ZnO nanoparticles*, Phys. Chem. Chem. Phys., vol. **18**, p. 16237, 2016.

- L. Vaccaro, R. Popescu, F. Messina, P. Camarda, R. Schneider, D. Gerthsen, F. M. Gelardi, and M. Cannas, *Self-limiting and complete oxidation of silicon nanostructures produced by laser ablation in water*, J. Appl. Phys., vol. **120**, p. 024303, 2016.

- P. Camarda, R. Schneider, R. Popescu, L. Vaccaro, F. Messina, G. Buscarino, S. Agnello, F. M. Gelardi, and M. Cannas, *Effect of thermal annealing on the luminescence of defective ZnO nanoparticles synthesized by pulsed laser ablation in water*, Phys. Status Solidi C, vol. **1**, p. 5, 2016.

- P. Camarda, F. Messina, L. Vaccaro, G. Buscarino, S. Agnello, F. M. Gelardi, and M. Cannas, *Controlling the oxidation processes of Zn nanoparticles produced by pulsed laser ablation in aqueous solution*, J. Appl. Phys., vol. **120**, p. 124312, 2016.

Bibliography

[1] K. Kihara and G. Donnay *The Canadian Mineralogist*, vol. 23, p. 647, 1985.

[2] U. Ozgur, I. Alivov, C. Liu, A. Teke, M. A. Reshchikov, S. Dogan, V. Avrutin, S. J. Cho, and H. Morkoc *J. Appl. Phys.*, vol. 98, p. 041301, 2005.

[3] R. Heilbig *J. Cryst. Growth*, vol. 15, p. 25, 1972.

[4] E. Ohshima, H. Ogino, I. Niikura, K. Maeda, M. Sato, M. Ito, and T. Fukuda *J. Cryst. Growth*, vol. 260, p. 166, 2004.

[5] A. Janotti and C. G. V. de Walle *Rep. Prog. Phys.*, vol. 72, p. 126501, 2009.

[6] K. Ellmer, A. Klein, and B. Rech, eds., *Transparent Conductive ZnO*. New York: Springer, 2007.

[7] Y. Ryu, T. Lee, J. Lubguban, H. White, B. Kim, Y. Park, and C. Youn *Appl. Phys. Lett.*, vol. 88, p. 241108, 2006.

[8] S. Choopun, R. Vispute, W. Yang, R.P, Sharma, T. Venkatesan, and H. Shen *Appl. Phys. Lett.*, vol. 80, pp. 1529–1531, 2002.

[9] T. Makino, Y. Segawa, M. Kawasaki, A. Ohtomo, R. Shiroki, K. Tamura, T. Yasuda, and H. Koinuma *Appl. Phys. Lett.*, vol. 78, pp. 1237–1239, 2001.

[10] Z. Zhang and H. Xiong *Materials*, vol. 8, p. 3101, 2015.

[11] J. Song, S. A. Kulinich, J. Li, Y. Liu, and H. Zeng *Angew. Chem. Int. Ed.*, vol. 54, p. 462, 2015.

[12] C. Klingshirn *Chem. Phys. Chem*, vol. 8, p. 782, 2007.

[13] M. S. R. Rao and T. Okada, eds., *ZnO Nanocrystals and Allied Materials*. India: Springer, 2014.

[14] W. L. Bragg *Phil. Mag.*, vol. 39, p. 647, 1920.

[15] Wikipedia, "Zinc oxide — wikipedia, the free encyclopedia," 2016. [Online; accessed 9-October-2016].

[16] C. F. Klingshirn, A. Waag, A. Hoffmann, and J. Geurts, eds., *Zinc Oxide: From Fundamental Properties Towards Novel Applications.* New York: Springer, 2010.

[17] M. Kunish, I. Tanaka, T. Yamamoto, T. Suga, and T. Mizoguchi *J. Phys.: Condens. Matter.*, vol. 16, pp. 3801–3806, 2004.

[18] F. Decremps, J. Zhang, and R. Lieberman *Europhys. Lett.*, vol. 51, p. 268, 2000.

[19] T. Gruber, G. Prinz, C. Kirchner, R. Kling, F. Reuss, W. Limmer, and A.Waag *J. Appl. Phys.*, vol. 96, p. 289, 2004.

[20] R. Callender, S. Sussman, M. Selders, and R. Chang *Phys. Rev. B*, vol. 7, p. 3788, 1973.

[21] C. Arguello, D. Rousseau, and S. Porto *Phys. Rev.*, vol. 181, p. 1351, 1969.

[22] J. M. Calleja and M. Cardona *Phys. Rev. B*, vol. 16, p. 3753, 1977.

[23] F. Decremps, J. Pellicer-Porres, A. Saitta, J. Chervin, and A. Polian *Phys. Rev. B*, vol. 65, p. 092101, 2002.

[24] N. Ashkenov, B. Mbenkum, C. Bundesmann, V. Riede, M. Lorenz, E. Kaidashev, A. Kasic, M. Schubert, M. Grundmann, G. Wagner, and H. Neumann *J. Appl. Phys.*, vol. 93, p. 126, 2003.

[25] J. Zeng, J. Low, Z. Ren, T. Liew, and Y. Lu *Appl. Surf. Sci.*, vol. 197-198, p. 362, 2002.

[26] J. Ye, S. Gu, S. Zhu, T. Chen, W. Liu, F. Qin, L. Hu, R. Zhang, Y. Shi, and Y. Zheng *J. Vac. Sci. Technol.*, vol. A21, p. 979, 2003.

[27] J. Ye, S. Gu, S. Zhu, F. Qin, S. Liu, W. Liu, X. Zhou, L. Hu, R. Zhang, Y. Shi, and Y. Zheng *J. Appl. Phys.*, vol. 96, p. 5308, 2004.

[28] C. Xu and X. Sun *J. Appl. Phys.*, vol. 42, p. 4949, 2003.

[29] Y. Xing, Z. Xi, Z. Xue, X. Zhang, J. Song, R. Wang, J. Xu, Y. Song, S. Zhang, and D. Yu *Appl. Phys. Lett.*, vol. 83, p. 1689, 2003.

[30] Y. Tseng, H. Hsu, W. Hsieh, K. Liu, and I. Chen *J. Mater. Res.*, vol. 18, p. 2837, 2003.

[31] C. Gorla, N. Emanetoglu, S. Liang, W. Mayo, Y. Lu, M. Wraback, and H. Shen *J. Appl. Phys.*, vol. 85, p. 2595, 1999.

[32] K. A. Alim, V. A. Fonoberov, M. Shamsa, and A. A. Balandin *Journ. of Appl. Phys.*, vol. 97, p. 124313, 2005.

[33] R. H. Callender, S. S. Sussman, M. Selders, and R. K. Chang *Phys. Rev. B*, vol. 7, p. 3788, 1973.

[34] Z. Q. Chen, A. Kawasuso, Y. Xu, H. Naramoto, X. L. Yuan, T. Sekiguchi, R. Suzuki, and T. Ohdaira *J. Appl. Phys.*, vol. 97, p. 013528, 2005.

[35] P. K. Giri, S. Bhattacharyya, D. K. Singh, R. Kesavamoorthy, B. K. Panigrahi, and K. G. M. Nair *J. Appl. Phys.*, vol. 102, p. 093515, 2007.

[36] M. Li, G. Xing, G. Xing, B. Wu, T. Wu, X. Zhang, and T. C. Sum *Phys. Rev. B*, vol. 87, p. 115309, 2013.

[37] H. Zeng, X. W. Du, S. C. Singh, S. A. Kulinich, S. Yang, J. He, and W. Cai *Adv. Funct. Mater.*, vol. **22**, p. 1333, 2012.

[38] C. Bundesmann, ed. University of Leipzig, 2006.

[39] N. Ashkenov, B. Mbenkum, C. Bundesmann, V. Riede, M. Lorenz, E. Kaidashev, A. Kasic, M. Schubert, M. Grundmann, G. Wagner, and H. Neumann *J. Appl. Phys.*, vol. 93, p. 126, 2003.

[40] H. Heiland, E. Mollwo, and F. Stockmann *Solid State Phys.*, vol. 8, p. 191, 1959.

[41] A. L. Efros and M. Rosen *Annu. Rev. Mater Sci.*, vol. 30, p. 475, 2000.

[42] C. Klingshirn and U. Rossler, eds., *Semiconductor Optics.* Heidelberg: Springer, 2006.

[43] R. Hauschild, H. Priller, M. Decker, J. BrVckner, H. Kalt, and C. Klingshirn *Phys. Status Solidi C*, vol. 3, p. 976, 2006.

[44] P. K. Basu, ed., *Theory of Optical Processes in Semiconductors: Bulk and Microstructures.* Oxford: Oxford Science Publications, 2003.

[45] Y. Toyozawa, ed., *Optical Processes in Solids.* Cambridge: Cambridge University Press, 2003.

[46] E. Vella, F. Messina, M. Cannas, and R. Boscaino *Phys. Rev. B*, vol. 83, p. 174201, 2011.

[47] T. Koida, A. Uedono, A. Tsukazaki, T. Sota, M. Kawasaki, and S. F. Chichibu *Phys. Status Solidi A*, vol. 201, p. 2841, 2004.

[48] S. F. Chichibu, T. Onuma, M. Kubota, A. Uedon, and T. Sota *J. Appl. Phys.*, vol. 99, p. 093505, 2006.

[49] S. Lee, S. L. Chen, D. Hongxing, L. Sun, Z. Chen, W. M. Chen, and I. A. Buyanova *Appl. Phys. Lett.*, vol. 96, p. 083104, 2010.

[50] D. C. Reynolds, D. C. Look, B. Jogai, J. E. Hoelscher, R. E. Sherriff, M. T. Harris, and M. J. Callahan *J. Appl. Phys.*, vol. 88, p. 2152, 2000.

[51] D. W. Bahnemann, C. Kormann, and M. R. Hoffmann *J. Phys. Chem.*, vol. 91, p. 3789, 1987.

[52] M. Lannoo and J. Bourgoin, eds., *Point Defects in Semiconductors II*. Berlin: Springer, 1983.

[53] M. Stavola, ed., *Identification of Defects in Semiconductors, Semiconductors and Semimetals*. San Diego: Springer, 1999.

[54] G. P. Mohanty and L. V. Azaroff *J. Chem. Phys.*, vol. 35, p. 1268, 1961.

[55] K. Hoffmann and D. Hahn *Phys. Status Solidi a*, vol. 24, p. 637, 1974.

[56] L. S. Vlasenko and G. D. Watkins *Phys. Rev. B*, vol. 72, p. 035203, 2005.

[57] K. I. Hagemark *Phys. Rev. B*, vol. 16, p. 293, 1976.

[58] A. Janotti and C. G. V. de Walle *Phys. Rev. B*, vol. 76, p. 165202, 2007.

[59] A. F. Kohan, G. Ceder, D. Morgan, and C. G. V. de Walle *Phys. Rev. B*, vol. 61, p. 15019, 2000.

[60] S. B. Zhang, S.-H. Wei, and A. Zunger *Phys. Rev. B*, vol. 63, p. 075205, 2001.

[61] F. Oba, S. R. Nishitani, S. Isotani, H. Adachi, and I. Tanaka *J. Appl. Phys.*, vol. 90, p. 824, 2001.

[62] A. Janotti and C. G. V. de Walle *J. Cryst. Growth*, vol. 58, p. 287, 2006.

[63] S. Lany and A. Zunger *Phys. Rev. B*, vol. 72, p. 035215, 2005.

[64] C. H. Patterson *Phys. Rev. Lett.*, vol. 74, p. 144432, 2006.

[65] T. R. Paudel and W. R. L. Lambrecht *Phys. Rev. B*, vol. 77, p. 205202, 2008.

[66] F. O. anf A. Togo, I. Tanaka, J. Paier, and G. Kresse *Phys. Rev. B*, vol. 77, p. 245202, 2008.

[67] A. Janotti and C. G. V. de Walle *Rep. Prog. Phys.*, vol. 72, p. 126501, 2009.

[68] D. G. Thomas *J. Phys. Chem. Solids (USA)*, vol. 3, p. 229, 1957.

[69] J. M. Cho, J. K. Song, and S. Park *Bull Korean Chem. Soc.*, vol. 30, p. 1616, 2009.

[70] Y. Kozuka, A. Tsukazaki, and M. Kawasaki *Appl. Phys. Rev.*, vol. 1, p. 011303, 2014.

[71] L. Kukreja, P. Misra, A. Das, J. Sartor, and H. Kalt *J. Vac. Sci. Technol.*, vol. A29(3), p. 120, 2011.

[72] Y. Kayanuma *Phys. Rev. B*, vol. 38, p. 9797, 1988.

[73] E. Wong, J. Bonevich, and P. Searson *J. Phys. Chem. B*, vol. 102, p. 7770, 1998.

[74] Y. Gong, T. Andelman, G. F. Neumark, S. O'Brien, and I. L. Kuskovsky *Nanosc. Res. Lett.*, vol. 2, pp. 297–302, 2007.

[75] H. C. Hsu, H. Y. Huang, M. O. Eriksson, T. F. Dai, and P. Holtz *Appl. Phys. Lett.*, vol. 102, p. 013109, 2013.

[76] I. Musa, F. Massuyeau, L. Cario, J. L. Duvail, S. Jobic, P. Deniard, , and E. Faulques *Appl. Phys. Lett.*, vol. 99, p. 243107, 2011.

[77] W. M. Kwok, A. B. Djurišić, Y. H. Leung, W. K. Chan, and D. L. Phillips *Appl. Phys. Lett.*, vol. 87, p. 223111, 2005.

[78] S. K. Mohanta, D. C. Kim, X. H. Zhang, C. B. Soh, A. M. Yong, H. K. Cho, and S. Tripathy *J. Cryst. Growth*, vol. 310, p. 5312, 2008.

[79] F. Y. Jen, Y. C. Lu, C. Y. Chen, H. C. Wang, C. C. Yang, B. P. Zhang, and Y. Segawa *Appl. Phys. Lett.*, vol. 87, p. 252117, 2005.

[80] K. Kodama and T. Uchino *Journ. Appl. Phys.*, vol. 111, p. 093525, 2012.

[81] A. Djurišić, A. Ng, and X. Chen *Progr. in Quantum Electr.*, vol. 34, p. 191, 2010.

[82] A. Djurišić, X. Chen, Y. Leung, and A. Ng *J. of Mater. Chem.*, vol. 22, p. 6526, 2012.

[83] M. M. Cluskey and S. Jokela *J. of Appl. Phys.*, vol. 106, p. 071101, 2009.

[84] F. Oba, A. Togo, I. Tanaka, J. Paier, and G. Kresse *Phys. Rev. B*, vol. 24, p. 2452021, 2008.

[85] S. A. M. Lima, F. A. Sigoli, M. J. Jr., and M. R. Davolos *Int. J. Inorg. Mater.*, vol. 3(7), pp. 749–754, 2001.

[86] J. Hu and B. C. Pan *J. Chem. Phys.*, vol. 129, p. 154706, 2008.

[87] P. Erhart, K. Albe, and A. Klein *Phys. Rev. B*, vol. 73, p. 205203, 2006.

[88] H. Zeng, G. Duan, Y. Li, S. Yang, X. Xu, and W. Cai *Adv. Funct. Mater.*, vol. 20, p. 561, 2010.

[89] D. Li, Y. H. Leung, A. B. Djurišić, Z. T. Liu, M. H. Xie, S. L. Shi, S. J. Xu, and W. K. Chan *Appl. Phys. Lett.*, vol. 85(9), pp. 1601–1603, 2004.

[90] J. Qiu, X. Li, W. He, S. J. Park, H. K. Kim, Y. H. Hwang, J. H. Lee, and Y. D. Kim *Nanotecnology*, vol. 20(15), p. 1556031, 2009.

[91] J. P. Kar, M. H. Ham, S. W. Lee, and J. M. Myoung *Appl. Surf. Sci.*, vol. 255(7), pp. 4087–4092, 2009.

[92] K. H. Tam, C. K. Cheung, Y. H. Leung, A. B. Djurišić, C. C. Ling, C. D. Beling, S. Fung, W. M. Kwok, W. K. Chan, D. L. Phillips, L. Ding, and W. K. Ge *J. Phys. Chem. B*, vol. 110(42), pp. 20865–20871, 2006.

[93] A. B. Djurišić, Y. H. Leung, K. H. Tam, Y. F. Hsu, L. Ding, W. K. Ge, Y. C. Zhong, K. S. Wong, W. K. Chan, H. L. Tam, K. W. Cheah, W. M. Kwok, and D. L. Phillips *Nanotecnology*, vol. 18(9), p. 0957021, 2007.

[94] H. Zeng, W. Cai, Y. Li, J. Hu, and P. Liu *J. Phys. Chem. B*, vol. 109, p. 18260, 2005.

[95] K. Kawabata, Y. Nanai, S. Kimura, and T. Okuno *Appl. Phys. A*, vol. 107, p. 213, 2012.

[96] R. S. Ajimsha, G. Anoop, A. Aravind, and M. K. Jayarajz *Electrochem. Solid-State Lett.*, vol. 11, p. k14, 2008.

[97] P. Camarda, L. Vaccaro, F. Messina, and M. Cannas *App. Phys. Lett.*, vol. 107, p. 013103, 2015.

[98] Q. X. Zhao, P. Klason, M. Willander, H. M. Zhong, W. Lu, and J. H. Yang *Appl. Phys. Lett.*, vol. 87, p. 211912, 2005.

[99] B. Lin, Z. Fu, and Y. Jia *Appl. Phys. Lett.*, vol. 79, p. 943, 2001.

[100] F. Fabbri, M. Villani, A. Catellani, A. Calzolari, G. Cicero, D. Calestani, G. Calestani, A. Zappettini, B. Dierre, T. Sekiguchi, and G. Salviati *scientific reports*, vol. 4, p. 5158, 2014.

[101] A. V. Dijken, E. A. Meulenkamp, D. Vanmaekelbergh, and A. Meijerink *J. Lumin.*, vol. 90, p. 123, 2000.

[102] L. Zhang, L. Yin, C. Wang, N. lun, Y. Qi, and D. Xiang *J. Phys. Chem. C*, vol. 114, p. 9651, 2010.

[103] H. Usui, Y. Shimizu, T. Sasaki, and N. Koshizaki *J. Phys. Chem. B*, vol. 109, pp. 120–124, 2005.

[104] C. He, T. Sasaki, H. Usui, Y. Shimizu, and N. Koshizaki *J. Photochem. and Photob. A*, vol. 191, pp. 66–73, 2007.

[105] J. N. Zeng, J. K. Low, Z. M. Ren, T. Liew, and Y. F. Lu *Appl. Surf. Sci.*, vol. 362, p. 197, 2007.

[106] K. Kodama and T. Uchino *Journ. Phys. Chem. C*, vol. 118 (41), p. 23977, 2014.

[107] M. Rahman, N. C. deb Nath, K. M. Noh, and J. J. Lee *Int. Journ. of Phot.*, vol. 23, pp. 1–6, 2013.

[108] A. V. Zvyagin, X. Zhao, A. Gierden, W. Sanchez, J. A. Ross, and M. S. Roberts *J. Biomed. Opt.*, vol. 13, pp. 064031–064039, 2008.

[109] H. Y. Shih, Y. T. Chen, C. M. Wei, M. H. Chan, J. K. Lian, Y. F. Chen, and T. Y. Lin *J. Phys. Chem. C*, vol. 115, p. 14667, 2011.

[110] K. Yang, G. W. She, H. Wang, X. M. Ou, X. H. Zhang, C. S. Lee, and S. T. Lee *J. Phys. Chem. C*, vol. 113, pp. 20169–20172, 2009.

[111] M. W. Ahn, K. S. Park, J. H. Heo, J. G. Park, D. W. Kim, K. J. Choi, J. H. Lee, and S. H. Hong *Appl. Phys. Lett.*, vol. 93, p. 263103, 2008.

[112] H. Huang, S. Mao, H. Feick, H. Q. Yan, Y. Y. Wu, H. Kind, E. Weber, R. Russo, and P. D. Yang *Science*, vol. 292, pp. 1897–1899, 2001.

[113] H. Yan, R. He, J. Johnson, M. Law, R. J. Saykally, and P. Yang. *J. Am. Chem. Soc.*, vol. 125, p. 4728, 2003.

[114] Y. Lu, N. Emanetoglu, and Y. Cheng, eds., *Zinc Oxide. Bulk, Thin films and Nanostructures*. Oxford: Elsevier Press, 2006.

[115] T. Jamieson, R. Bakhshi, D. Petrova, R. Pocock, M. Imani, and A. M. Seifalian *Biomaterials*, vol. 28, pp. 4717–4732, 2007.

[116] H.-M. Xiong *J. Mater. Chem.*, vol. 20, p. 4251, 2010.

[117] L. Schmidt-Mende and J. L. MacManus-Driscoll *Mater. Today*, vol. 10, p. 40, 2007.

[118] B. B. Straumal, S. G. Protasova, A. A. Mazilkin, B.Baretzky, A. A. Myatiev, P. B. Straumal, T. Tietze, G. Schutz, and E. Goering *Mater. Lett.*, vol. 71, p. 21, 2012.

[119] S. C. Singh and R. Gopal *Physica E*, vol. 40, p. 724, 2010.

[120] A. S. Edelstein and R. C. Cammarata, eds., *Nanomaterials: Synthesis, Properties and Applications*. Bristol: Institute of Physics Publishing, 1998.

[121] F. Mafuné, J. Y. Kohno, Y. Takeda, and T. Kondow *J. Phys. Chem. B*, vol. 104, p. 8333, 2000.

[122] F. Mafuné, J. Y. Kohno, Y. Takeda, and T. Kondow *J. Phys. Chem. B*, vol. 107, p. 4218, 2003.

[123] C. Liang, Y. Shimizu, and N. Koshizaki *J. Phys. Chem. B*, vol. 107, p. 9220, 2003.

[124] Z. Yan and B. Chrisey *J. Photochem. Photobiol.*, vol. C13, p. 204, 2012.

[125] V. Amendola and M. Meneghetti *Phys. Chem. Chem. Phys.*, 2013.

[126] S. E. black, ed., *Laser Ablation: Effects and Applications.* New York: Nova Science Publisher, 2011.

[127] A. Menéndez-Manjón, P. Wagener, and S. Barcikowski *J. Phys. Chem. C*, vol. 115, p. 5108, 2011.

[128] N. Barsch, J. Jakobi, S. Weiler, and S. Barcikowski *Nanotechnology*, vol. 20, p. 445603, 2009.

[129] W. T. Nichols, T. Sasaki, and N. Koshizaki *J. Appl. Phys.*, vol. 100, p. 114913, 2006.

[130] A. V. Kabashin and M. Meunier *J. Appl. Phys.*, vol. 94, pp. 7941–7943, 2003.

[131] A. Miotello and R. Kelly *Appl. Phys. A: Mater. Sci. Process.*, vol. 69, pp. 67–73, 1999.

[132] J. C. Miller and R. F. Haglund, eds., *Laser Ablation and Desorption.* San Diego: Academic Press, 2007.

[133] D. Werner, A. Furube, T. Okamoto, and S. Hashimoto *J. Phys. Chem. C*, vol. 115, p. 8503, 2011.

[134] T. Sakka, K. Takatani, Y. H. Ogata, and M. Mabuchi *J. Phys. D*, vol. 35, p. 65, 2002.

[135] T. Tsuji, D. Thang, Y. Okazaki, M. Nakanishi, Y. Tsuboi, and M. Tsuji *Appl. Surf. Sci*, vol. 254, p. 5224, 2008.

[136] D. Perez, L. K. Beland, D. Deryng, L. J. Lewis, and M. Meunier *Phys. Rev. B*, vol. 77, p. 014108, 2008.

[137] R. Intartaglia, K. Bagga, and F. Brandi *Opt. Mater. Express*, vol. 22(3), pp. 3117–3127, 2014.

[138] R. Intartaglia, K. Bagga, M. Scotto, A. Diaspro, and F. Brandi *Opt. Mater. Express*, vol. 2, p. 510, 2012.

[139] E. Fazio, A. Mezzasalma, G. Mondio, F. Neri, and R. Saija *Appl. Surf. Sci.*, vol. 272, p. 30, 2013.

[140] E. Solati *Optic & Laser Technology*, vol. 58, p. 26, 2014.

[141] K. K. Kim, D. Kim, S. K. Kim, S. M. Park, and J. K. Song *Chem. Phys. Lett.*, vol. 511, p. 116, 2011.

[142] R. I. Ismail, A. K. Ali, M. M.Ismail, and K. I. Hassoon *Appl. Nanosci.*, vol. 1, p. 45, 2011.

[143] R. K. Thareja and S. Shukla *Appl. Surf. Sci.*, vol. 253, p. 8889, 2007.

[144] L. V. Zhigilei, Z. Lin, and D. S. Ivanov *J. Phys. Chem. C*, vol. 113, pp. 11892–11906, 2009.

[145] Z. Lin, E. Leveugle, E. M. Bringa, and L. V. Zhigilei *J. Phys. Chem. C*, vol. 114, pp. 5686–5699, 2009.

[146] V. Amendola and M. Meneghetti *Phys. Chem. Chem. Phys.*, vol. 11, pp. 3805–3821, 2009.

[147] Z. Yan, R. Bao, Y. Huang, A. Caruso, S. B. Qadri, C. Z. Dinu, and D. B. Chrisey *J. Phys. Chem. C*, vol. 114, pp. 3869–3873, 2010.

[148] R. Intartaglia, K. Bagga, F. Brandi, G. Das, A. Genovese, E. D. Fabrizio, and A. Diaspro *J. Phys. Chem. C*, vol. 115, pp. 5102–5107, 2011.

[149] C. Sajti, R. Sattari, N. Chichkov, and S. Barcikowski *J. Phys. Chem. C*, vol. 114, pp. 2421–2427, 2010.

[150] V. Amendola, M. Meneghetti, G. Granozzi, S. Agnoli, S. Polizzi, P. Riello, A. Boscaini, C. Anselmi, G. Fracasso, and M. Colombatti *J. Mater. Chem.*, vol. 21, pp. 3803–3813, 2011.

[151] V. Amendola, P. Riello, and M. Meneghetti *J. Phys. Chem. C*, vol. 115, pp. 5140–5146, 2011.

[152] B. E. A. Saleh and M. C. Teich, eds., *Fundamentals of Photonics.* New York: John Wiley and Sons, 1991.

[153] H. Haken, ed., *Light. Volume II - Laser light dynamics.* North Holland: North Holland Physics Publishin, 1985.

[154] F. Messina, ed., *Master's degree Thesis-Role of hydrogen on the generation and decay of point defects in amorphous silica exposed to UV laser radiation.* Dipartimento di Scienze Fisiche ed Astronomiche, Universitá degli studi di Palermo (Italy), 2007.

[155] P. G. Harper and B. S. Wherret, eds., *Nonlinear Optics.* Bristol: Academic Press Inc., 1977.

[156] J. Tauc, R. Grigorovici, and A. Vancu *Phys. Status Solidi*, vol. 15, p. 627, 1966.

[157] E. A. Davis and N. F. Mott *Philos. Mag.*, vol. 22, p. 903, 1970.

[158] B. D. Viezbicke, S. Patel, B. E. Davis, and D. P. Birnie *Phys. Status Solidi B*, vol. 1, p. 11, 2015.

[159] J. R. Lakowicz, ed., *Principles of Fluorescence Spectroscopy.* Singapore: Plenum Press, 1983.

[160] R. Loudon, ed., *The quantum theory of light.* Oxford: Oxford University press, 2000.

[161] G. Pacchioni, L. Skuja, and D. Griscom, eds., *Defects in SiO_2 and related dielectrics: Science and technology.* Springer, 2000.

[162] L. Vaccaro, ed., *Electronic and Vibrational Properties of the Non-Bridging Oxygen Hole Center in the Bulk and at the Surface of Silica.* PhD Thesis, Dipartimento di Fisica e Chimica, Universita degli Studi di Palermo (Italy), 2009.

[163] J. R. Ferraro, K. Nakamoto, and C. W. Brown, eds., *Introductory Raman Spectroscopy.* Boston: Elsevier, 2003.

[164] D. Muller, ed., *Introduction to Electron Microscopy.* Springer, 2003.

[165] J. C. H. Spence, ed., *Experimental high-resolution electron microscopy.* Oxford, UK: Oxford University Press, 1988.

[166] J. Goldstein, D. Newbury, D. Joy, C. Lyman, P. Echlin, E. Lifshin, L. Sawyer, and J. Michael, eds., *Scanning Electron Microscopy and X-Ray Microanalysis.* New York: Springer, 2003.

[167] P. Camarda, F. Messina, L. Vaccaro, S. Agnello, G. Buscarino, R. Schneider, R. Popescu, D. Gerthsen, R. Lorenzi, F. M. Gelardi, and M. Cannas *Phys. Chem. Chem. Phys.*, vol. 18, pp. 16237–16277, 2016.

[168] A. F. Kohan, G. Ceder, D. Morgan, and C. G. V. de Walle *Phys. Rev. B*, vol. 61, p. 15019, 2000.

[169] B. C. Lin, P. Shen, and S. Y. Chen *J. Phys. Chem. C*, vol. 115, p. 5003, 2011.

[170] M. Watanabe, S. Sasaki, and T. Hayashi *Journ. of lum.*, vol. 87, p. 1234, 2000.

[171] D. J. Huntley *J. Phys.: Condens. Matter*, vol. 18, p. 1359, 2006.

[172] V. N. Sigaev, N. V. Golubev, E. S. Ignat'eva, A. Paleari, and R. Lorenzi *Nanoscale*, vol. 6, p. 1763, 2014.

[173] A. Gupta and H. Wiggers *Nanotechnology*, vol. 22, p. 055707, 2011.

[174] P. Camarda, R. Schneider, R. Popescu, L. Vaccaro, F. Messina, G. Buscarino, S. Agnello, F. M. Gelardi, and M. Cannas *Phys. Stat. Sol. C*, vol. 1, p. 5, 2016.

[175] J. Liu, P. Gao, W. Mai, C. Lao, and Z. L. Wang *Appl. Phys. Lett.*, vol. 89, p. 063125, 2006.

[176] L. Yang, P. W. May, L. Yin, and T. B. Scott *Nanotechnology*, vol. 18, p. 215602, 2007.

[177] H. Zeng, X. Ningab, and X. Lia *Phys. Chem. Chem. Phys.*, vol. 17, p. 19637, 2015.

[178] X. Li, J. Song, Y. Liu, and H. Zeng *Curr. Appl. Phys.*, vol. 14, p. 521, 2014.

[179] S. Ramakanth and K. C. J. Raju *Soft Nanosci. Lett.*, vol. 3, p. 32, 2013.

[180] P. Camarda, F. Messina, L. Vaccaro, G. Buscarino, S. Agnello, F. M. Gelardi, and M. Cannas *Journ. Appl. Phys.*, vol. 120, p. 124312, 2016.